DISSERTATION / DOCTORAL THESIS

Titel der Dissertation /Title of the Doctoral Thesis

“Dark matter haloes: The invisible hosts of galaxies probed with dynamics of globular cluster systems”

verfasst von / submitted by

dipl.fiz. Tadeja Veršič, MSc

angestrebter akademischer Grad / in partial fulfilment of the requirements for the degree of

Doktorin der Naturwissenschaften (Dr.rer.nat.)

Wien, 2024 / Vienna 2024

Studienkennzahl lt. Studienblatt / degree programme code as it appears on the student record sheet:	**UA 796 605 413**
Dissertationsgebiet lt. Studienblatt / field of study as it appears on the student record sheet:	**Astronomie**
Betreut von / Supervisor:	**Univ.-Prof. Dr. Petrus Martinus van de Ven**
Betreut von / Supervisor:	**Dipl.-Phys. Dr. Sabine Thater**

"You dig deeper and it gets more and more complicated, and you get confused, and it's tricky and it's hard, but... It is beautiful."

- Brian Cox

Contents

List of Acronyms

ETG . . . . Early-type galaxy (elliptical and lenticular)
LTG . . . . Late type galaxy
S0 . . . . Lenticular galaxy
cD . . . . Central dominant (galaxy)
dSph . . . . Dwarf spheroidal (galaxy)
DM . . . . Dark matter
DMO . . . . Dark-matter-only (simulations)
CDM . . . . Cold dark matter
WDM . . . . Warm dark matter
NFW . . . . Navarro-Frenk-White (profile)
GC . . . . Globular clusters
GCS . . . . Globular cluster system
GCLF . . . . Globular cluster luminosity function
TOM . . . . Turn-over magnitude
PNe . . . . Planetary nebulae
LOS . . . . Line-of-sight
PM . . . . Proper motion
rv . . . . Radial velocity
LOSV . . . . Line-if-sight velocity
LOSVD . . . . Line-if-sight velocity distribution
z . . . . Redshift
IFU . . . . Integral field unit
ACS . . . . Advance camera for surveys
MGE . . . . Multi-Gaussian expansion
JAM . . . . Jeans anisotropic modelling

Declaration of published work and thesis synthesis

This doctoral thesis is a result of the work I carried out in the course of my PhD at the University of Vienna and at the European Southern Observatory in Munich, Germany. My work resulted in two first-author publications and conference proceedings. Therefore, parts of this thesis overlap with published work. The list below summarises which Chapters were based on which published or submitted works. Together with the published work, this dissertation includes yet unpublished results and analysis.

- The work presented in chapter 5 was carried out in collaboration with S. Thater, G. van de Ven, L.L. Watkins, P. Jethwa, R. Leaman and A. Zocchi and has been published as: Veršič et al. (2024) “Total mass slopes and enclosed mass constrained by globular cluster system dynamics” in A&A.
- The work presented in chapter 6 has been completed in collaboration with M. Rejkuba, M. Arnaboldi, O. Gerhard, C. Pulsoni, L.M. Valenzuela, J. Hartke, L.L. Watkins, G. van de Ven and S. Thater. It has been accepted as conference proceedings Veršič et al. (2023) of the 379 IAU Symposium *“Dynamical Masses of Local Group Galaxies”* and has been submitted to A&A for review as Veršič et al. (subm.) “Shapes of dark matter haloes with discrete globular cluster dynamics: The example of NGC 5128 (Centaurus A)”.
- Parts of chapter 1, 2 and 7 are also adapted from published or submitted work (Veršič et al., 2023, 2024, subm.).

Tadeja Veršič
Vienna, January 2024

Chapter 1

Introduction

"Nobody ever told us all matter radiated.
We just assumed it."
- Vera Rubin

Declaration of published work

This chapter includes text already published or submitted to a journal. Specifically, the introductory sections in Veršič et al. (2023, 2024, subm.) were adapted for the thesis. As a result, there may be partial overlap with those publications.

A SHORT ORIGIN OF DARK MATTER STUDIES

The term **dark matter (DM)** has been used since ancient times to describe the celestial bodies that were too faint to be observed and were therefore referred to as "dark" (Bertone and Hooper, 2018). In the 17th century, the discovery of Newton's law of universal gravity opened up a new possibility to use the motions of stars to infer the gravitational pull that kept them in orbit. Lord Kelvin was among the first to attempt a dynamical mass estimate of the Milky Way in the hopes of determining the dark matter mass at the beginning of the 20th century. He applied his theory of gasses to the stars moving under the influence of gravity and predicted 10^9 stars within 1 kpc of the Sun. The early 20th century saw numerous attempts to determine the local dark matter density, including those of James Jeans, always with the assumption that DM was made of faint stars.

Zwicky (1933) demonstrated that dark matter is also needed to explain the motions of galaxies in galaxy clusters and in much greater quantity than reported for the Milky Way. Over several decades the presence of DM was quantified by the dynamical mass-to-light $(M/L)_{\rm dyn}$ ratio and its existence was neither accepted nor disregarded. Researchers studied the assumptions in dynamical modelling approaches to determine if they could result in biased measurements of $(M/L)_{\rm dyn}$. However, the nature of dark matter could not be explained. Rubin and Ford (1970) presented the most detailed measurements of the rotation curve of M31, our closest massive neighbor. They confirmed that the rotation curve of M31 flattens in the outer regions, even beyond the radius at which the density profile of the luminous[1] matter declines. The flattening of the rotation curves became the strongest evidence for the presence of non-luminous matter.

In parallel, a field of cosmology was emerging after Einstein formulated the theory of general relativity at the beginning of the 20th century. This made it possible to construct a predictive and testable model of the Universe for the first time, where everything started with the Big Bang. The technological advances in observations of the late 20th century gave rise to deep wide-field surveys of galaxy distributions such as SDSS[2]. They confirmed that the Universe is isotropic and galaxies are distributed along filaments and nodes of the cosmic web. Space-based telescopes sensitive to microwave radiation mapped the first light of the Universe, the Cosmic Microwave Background (CMB), originating in the very early universe, around 300 000 years after the Big Bang at the redshift of $z \sim 1000$. Probes such as WMAP[3] and the Planck telescopes detected temperature fluctuations in the CMB, which can be interpreted as random density fluctuations of matter that seeded the first galaxies. To explain these observations the presence of non-baryonic matter was necessary, i.e. - dark matter. Such DM only interacts with baryonic matter through gravity and is one of the key components in the *Standard model of cosmology*, a model of the Universe that is best supported by observational evidence (Dodelson, 2003). According to the latest results of Planck Collaboration et al. (2020) the universe is spatially flat and is dominated by dark energy (Λ, responsible for driving the accelerated expansion of the Universe) and dark matter, respectively comprising 68% and 27% of energy density in the Universe. Even though baryonic matter represents only a small ($\sim$ 5%) component in the mass and energy budget of the Universe, by observing it we can gather information about the dominating dark components.

While the term dark matter initially referred to objects too faint to observe, the advent of dynamical modelling and the field of cosmology fundamentally reshaped how we understand it today, and brought us to consider it **as a non-baryonic component of the Universe that enabled the formation of galaxies** (Mo et al., 2010). Great advances have been made in the past century to understand dark matter, but many key questions remain unanswered: *What is the nature of dark matter?*, *How is dark matter distributed in galaxy haloes?* and *What are the shapes of dark matter halos?*. In this thesis, we address some of these questions using the dynamical modelling of globular clusters (GCs) in the haloes of galaxies.

In this chapter, we provide an overview of relevant developments in the field of cosmology to clarify how the radial distribution of dark matter in haloes and their shapes can be used to

[1] In this thesis we will use the terms luminous and baryonic as well as dark and non-baryonic matter interchangeably.
[2] Sloan Digital Sky Survey.
[3] Wilkinson Microwave Anisotropy Probe.

shed light on its nature. In Sect. 1.1 we summarise results from cosmologies based on different particle nature of DM and from dark-matter-only (DMO) cosmological simulations. In Sect. 1.2 we focus on two diagnostics that have been used in the literature to probe the interplay between baryons and DM. In Sect. 1.2.3 and Sect. 1.3 we summarise the core-cusp problem and studies of the DM halo shapes; these properties are particularly interesting because they are influenced by the nature of dark matter particles and the baryonic feedback. In Sect. 1.4 we introduce GCs, their properties, the properties of the globular cluster systems (GCSs), and their connection with the dark matter content of their host galaxy. The open questions addressed in this thesis are summarised in Sect. 1.5.

1.1 COSMOLOGY AND DARK MATTER MODELS

Einstein's field equations enabled us for the first time to study the evolution of the Universe as it expands adiabatically. The discovery of the CMB gave us an insight into the initial conditions of the early Universe, which can be well described by a Gaussian random field. The discovery of CMB confirmed that the Universe is isotropic on large scales, however matter is clustered in local overdensities. Self-gravity promotes the growth of the overdensities, while the internal pressure acts to remove matter. At a critical size, an overdensity becomes dominated by self-gravity and decouples from the expanding Universe. Such virialised haloes are hosts of galaxies, galaxy groups and galaxy clusters at $z = 0$ (present). The critical size evolves with redshift and depends on the cosmological model.

The key components of the Universe are radiation, matter (baryonic and non-baryonic), the cosmological constant Λ and the curvature of space. Varying the energy density of the four components results in a different abundance of overdensities at $z = 0$ and this information is encoded in the matter power spectrum (Dodelson, 2003). For example, low mass DM particle candidate results in a "top-down" formation of structure. Where large galaxies formed first and then fragmented to form smaller, dwarf galaxies, such DM is referred to as **warm** DM (WDM). Similarly, the absence of the cosmological constant results in a "top-down" formation of galaxies. In contrast, a massive DM particle candidate results in a "bottom-up" formation, where low-mass galaxies form first, such DM is referred to as **cold** DM (CDM). Therefore, comparing the observed galaxy mass function and matter power spectrum helps to constrain the cosmological models. The *Standard model of cosmology*, the model best supported by observations of large-scale structure is a **flat ΛCDM model** of the Universe (Alam et al., 2017; Betoule et al., 2014; Planck Collaboration et al., 2020).

Tests of the *Standard model of cosmology* have seen great development owing to the increased computational resources enabling cosmological numerical simulations of the large-scale structure of the Universe. These simulations have provided crucial insight into the nonlinear regime of structure formation, that is inaccessible with any other method (e.g., Springel et al., 2006, Vogelsberger et al., 2020, and references therein). Simulations like the *Millennium simulations*[4] and Bolshoi[5] have sufficient spatial and temporal resolution that we can investigate the internal properties of DM haloes, their **size**, **orientation**, **internal density distribution** and **intrinsic shape** over time. The most prominent particle candidate for CDM are weakly-interactive massive particles (WIMP Ellis et al., 1984) with masses $\mathcal{O}$(GeV - TeV). However, no such particles have been detected either directly or indirectly (Aprile et al., 2018). Therefore it is worth looking into simulations of alternative theories on the particle nature of DM.

In the regime of bright galaxy satellites ($M_\star \geqslant 10^5$ M$_\odot$) Forouhar Moreno et al. (2022) find a suppression of the number of satellites in the WDM compared with CDM. For DM haloes formed under the assumption of a self-interacting DM (SIDM) the authors find structural changes, that are restricted to the centre of the halo. SIDM haloes form density cores in the very centres, whose size depends on the interaction cross-section. They also note that baryonic process can wash away a lot of the differences between the CDM and SIDM models. SIDM and CDM models show similar

[4]https://wwwmpa.mpa-garching.mpg.de/galform/virgo/millennium/
[5]https://hipacc.ucsc.edu/Bolshoi.html

Table 1.1: Mass and circular velocity scales of typical virialised structures observed in the Universe.

	M_{200} [$\mathrm{M}_\odot$]	V_{200} [km s^{-1}]
Dwarf galaxies	10^9	10
Milky Way	10^{12}	100
Galaxy clusters	10^{15}	1000

behaviour on large scales (Rocha et al., 2013), but the type of interactions that occur in SIDM models (elastic or inelastic scattering) results in different inner slopes of the DM haloes compared with CDM (O'Neil et al., 2023).

There are many open questions around ΛCDM, chief among them are the nature of dark matter and dark energy. In this thesis, we focus on the former by probing the spatial distribution of DM in galaxies with discrete dynamical modelling of galactic haloes. Therefore, we focus on two properties of DM haloes that we constrain with GC dynamics: **internal density distribution** and **intrinsic shape**.

1.1.1 Definition of dark matter halo mass

To measure the mass of a DM halo, we first have to define it. Most commonly, the density contrast $\Delta = \overline{\rho(r_\Delta)}/\rho_{\rm crit}$ is used to define a halo of size r_Δ, with the mean density of $\overline{\rho(r_\Delta)}$. $\rho_{\rm crit} = 3H_0^2/(8\pi G)$ is the critical density of the Universe at $z = 0$, H_0 is the Hubble constant and G is the gravitational constant (Mo et al., 2010). In this thesis we use the latest results from Planck Collaboration et al. (2020) for the value of the Hubble constant $H_0 = 67.4\ \mathrm{kms^{-1}Mpc^{-1}}$[6]. The halo is thus defined as a spherical overdensity, with spherically averaged density $\Delta \times \rho_{\rm crit}$ within a radius r_Δ. While there are other definitions of the halo radius, we consider here a density contrast of $\Delta = 200$ and $r_\Delta = r_{200}$ (Wechsler and Tinker, 2018, and references therein). With such a definition for the halo, its total mass is calculated as:

$$M_{200} = \frac{4\pi}{3}\, 200\rho_{\rm crit}\, r_{200}^3 \tag{1.1}$$

The circular velocity of such haloes is then defined as:

$$V_{200} = \left(\frac{GM_{200}}{r_{200}}\right)^{1/2} \tag{1.2}$$

Based on these definitions the typical mass and velocity scales of structures in the Universe at $z \approx 0$ are summarised in Table 1.1.

The concentration of the haloes is defined as:

$$c_{200} \equiv \frac{r_{200}}{r_{-2}}\ , \tag{1.3}$$

where r_{-2} is the radius where the local power-law slope is -2.

These definitions do not depend on the assumed dark matter density profile or cosmology, and have been used extensively in the literature to compare different cosmological models with observations. We acknowledge here that the $\rho_{\rm crit}$ is implicitly dependent on the redshift through the Hubble constant. However, throughout this thesis, we study nearby systems and therefore we strongly limit the discussion on the redshift evolution of M_{200} and c_{200} in this chapter.

[6]It is important to note that in the past years, tension has emerged in the values of H_0 based on measurements from independent and we refer the interesting reader to Di Valentino et al. (2021) for a review on this problem and possible solutions.

1.1.2 RADIAL PROFILES OF PURE DM HALOES

The simplest treatment of halo formation is to consider a spherical collapse of a density perturbation (matter overdensity). Such simple assumption leads to a mass profile:

$$\rho(r) \propto r^{-\gamma} \,, \tag{1.4}$$

where γ is the power-law slope and for the value of $\gamma = 2$ this results in an *isothermal sphere* characterised by a constant constant circular velocity (Mo et al., 2010). However, the process of gravitational collapse is nonlinear and to accurately characterise the internal density profile numerical simulations are needed.

The spatial resolution of large cosmological simulations is not sufficient to study the radial distribution of matter in haloes. Instead, a re-simulation is needed to account for physics on smaller scales, such as tidal interactions that affect the internal mass distribution of interacting haloes. Navarro et al. (1997) employed this technique to explore the spherically averaged density distribution in DMO simulations for different cosmological parameters. They found a universal spherically averaged density profile of DM haloes that form through dissipationless hierarchical clustering which is independent of their mass or cosmology. The Navarro-Frenk-White profile (Navarro et al., 1996, NFW) is characterised by a cusp in the centre, with a slope of -1 and in a steeper declining outer density with a slope of -3:

$$\rho = \rho_s \left(\frac{r}{r_s} \left(1 + \frac{r}{r_s} \right)^2 \right)^{-1} \,, \tag{1.5}$$

where ρ_s is the scale density and r_s the scale radius.

In recent years, the improvements in the simulations have shown that the halo structure is sensitive to the cosmological parameters and that fitting an NFW profile to the simulations results in a large scatter for haloes with $M_{200} \leqslant 10^{12}\ h^{-1}\ \mathrm{M}_{\odot}$[7] (Macciò et al., 2008). Navarro et al. (2004) find that with NFW profile DM is underestimated in the inner regions of haloes. An alternative profile was introduced to reduce scatter when fitting the simulations, the Einasto profile (Einasto, 1965), which has an additional free parameter α modulating the transition between the inner and outer slope:

$$\rho_{\mathrm{EIN}}(r) = \rho_{-2} \exp\left\{ -\frac{2}{\alpha} \left[\left(\frac{r}{r_{-2}} \right)^{\alpha} - 1 \right] \right\} \,, \tag{1.6}$$

where r_{-2} is the radius where the local density slope is -2 (scale radius) and ρ_{-2} is the density at this scale radius.

A comparison between the NFW and Einasto profiles is shown in Fig. 1.1, where the logarithmic density slope $d\ln(\rho)/d\ln(r)$ and the density profile $\rho(r)$ are shown in the left and right panels, respectively. The solid black lines show the NFW profile, with an inner slope of -1 and an outer slope of -3. The coloured lines correspond to Einasto profiles with different values of the shape parameter α. For CDM haloes the typical values of this parameter are $0.12 \leqslant \alpha \leqslant 0.35$. The Einasto profile is very flexible as it can also be reduced to the form of an isothermal sphere for $\alpha = 0$ or of a Gaussian profile for $\alpha = 2$. Galaxy mass haloes have a typical value of $\alpha \sim 0.16$ (cyan) and galaxy cluster mass haloes agree better with ~ 0.3 (yellow/green; Gao et al., 2008, see their Eq. 5). The mass dependency originates from the different ρ_{crit} at the formation time of the halo (less massive haloes form earlier). The Einasto profile is therefore more flexible in reproducing DM profiles in DMO simulations that naturally arise in hierarchical structure formation.

Despite the inconsistencies between the NFW profile and simulations at higher resolution, most dynamical modelling studies assume a NFW profile.

[7] $h = H_0/(100\ \mathrm{km\ s^{-1}\ Mpc^{-1}})$.

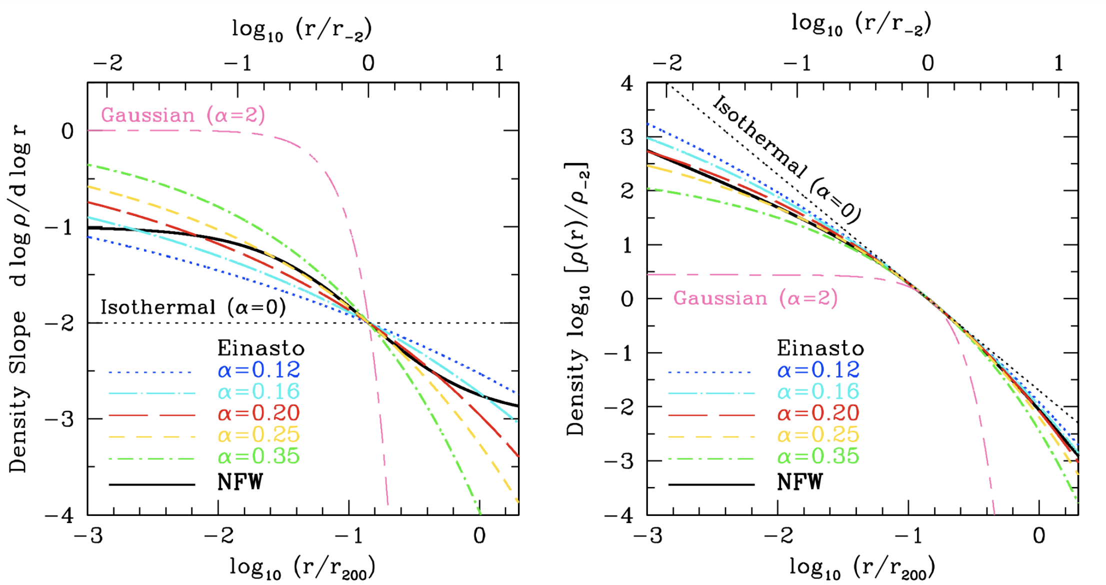

Figure 1.1: Comparison between the different profiles that have been used to fit DM haloes. The solid black lines show the NFW profile and the coloured lines show Einasto profiles with different values of the shape parameter α. Figure taken from Dutton and Macciò (2014).

1.1.3 Mass - concentration relation

The concentration is defined with Eq. 1.3 and the NFW profile is completely described by specifying the total mass M_{200} and concentration c_{200}. Navarro et al. (1997) showed that the concentration of a halo depends on its formation timescale. Haloes formed at lower redshift have lower concentrations (e.g. Wechsler et al., 2002; Zhao et al., 2003). Prada et al. (2012) analysed different cosmological simulations and found consistent results in the $M_{200} - c_{200}$ relation. However, the normalisation of the relation depends on the assumed cosmology, with *Planck* cosmology showing a 20% increase with respect to WMAP cosmology (Dutton and Macciò, 2014). The $M_{200} - c_{200}$ relation is a function of redshift. Haloes are more concentrated at $z = 0$ and the slope of the relation increases with redshift (Dutton and Macciò, 2014).

The formation history of haloes is imprinted in the value of its concentration. Out of equilibrium haloes, those that are still forming or have experienced recent major mergers have on average lower concentration (Neto et al., 2007). Haloes that have experienced longer quiescent periods are found to be more concentrated.

1.2 The influence of baryons on dark matter

Until now we have focused on the dark matter content of galaxies and we have presented conclusions based on DMO simulations. DM haloes provide potential wells for gas to coalesce to form stars and galaxies at their centres. The difference in the spatial distribution of DM and stars is clearly demonstrated in the hydrodynamic simulations, with an example shown in Fig. 1.2. Baryonic physics impacts the internal properties of DM haloes by redistributing mass and angular momentum of DM. Therefore, it is important to understand the connection between luminous and non-luminous components of galaxy haloes. Here, we focus on two observed properties: the stellar-halo-mass ratio (SHMR) and the bulge-halo conspiracy.

In the current cosmological framework, galaxy formation is driven by the coalescence of gas in the dark matter overdensities of the large-scale structures (White and Rees, 1978). This connection between luminous and dark matter is for example manifested in the correlation between the star formation history and their halo mass, as recently identified by Scholz-Díaz et al.

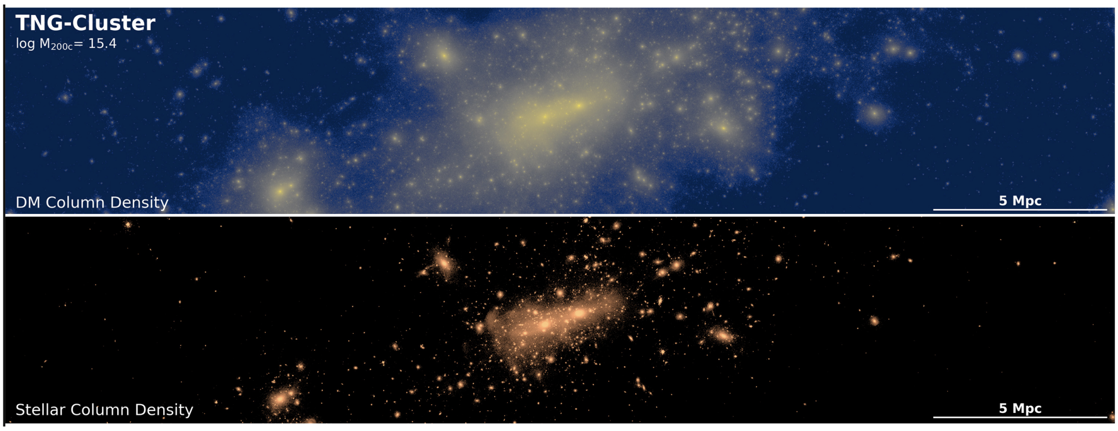

Figure 1.2: Dark matter and stellar distribution from the TNG-Clusters simulation (Nelson et al., 2023). The top figure shows the distribution of dark matter, the bottom one that of the stars. Figure taken from https://www.tng-project.org/cluster/#images.

(2023). Hydrodynamic simulations fold the baryonic physics into the DMO simulations using different astrophysically informed prescriptions for processes, such as SF, AGN and SN feedback, magnetic fields and metallicity enrichment. By comparing the results with the observed properties of galaxies (e.g., colour, age, size and morphology, luminosity function and metallicity) we can gain deeper insight into the physics of galaxy formation (Crain and van de Voort, 2023, and references therein).

Historically two classes of galaxies are observed, whose names refer to their proposed evolutionary pathways: **early-type galaxies** (ETGs, lenticulars S0 and ellipticals E) are red in colour, show low star formation rate (SFR) and are elliptical in projection; **late-type galaxies** (LTGs, spirals) are bluer in colour, have active SF and show prominent spiral arms in their thin gas disk. In this thesis, we focus on ETGs, because they have a larger number of GCs, see Sect 1.4.

1.2.1 STELLAR-HALO-MASS RATIO

DMO simulations predict the mass distribution of dark matter halos; the simplest method to populate the haloes with real galaxies is based on the assumption that the most massive galaxies reside in the most massive DM haloes. This approach is referred to as "abundance matching" (Wechsler and Tinker, 2018, and reference therin) and can be used to determine SHMR in a statistical way. An overview of literature studies using different techniques to determine the SHMR is shown in Fig. 1.3 for central galaxies.While the normalisation and the exact location of the peak of this relation differ between the different literature studies, they all show consistent trends. The SHMR is characterised by a peak $M_h \sim 10^{12}$ M$_\odot$ ($M_h \approx M_{200}$), where the haloes are the most efficient in transforming baryons into stars, and by a drop at lower and higher masses. At the low mass end, SN and stellar winds are very efficient at removing gas from the galaxy and the potential well is not sufficient to retain the out-flowing gas. At the high mass end, AGNs powered by the supermassive black holes in the centre provide sufficient kinetic energy to remove the gas and quench SF.

The SHMR is thus dependent on both cosmology and baryonic physics, and observation constraints of this relation are not trivial, mainly because DM is not directly observable and its presence can only be inferred from the gravitational influence it exerts on the luminous matter. In galaxy clusters, the temperature of X-ray emitting intercluster gas can be used, as well as strong gravitational lensing and thermal Sunyaev-Zel'dovich effect[8]. For the individual galaxies in the nearby Universe, dynamical modelling of the stellar line-of-sight (LOS) velocity distribution or gas rotation curves are used to constrain the total mass. However, as it can be seen in Fig. 1.2, the

[8]Distortion of CMB spectra due to inverse Compton scattering on free electrons in galaxy clusters.

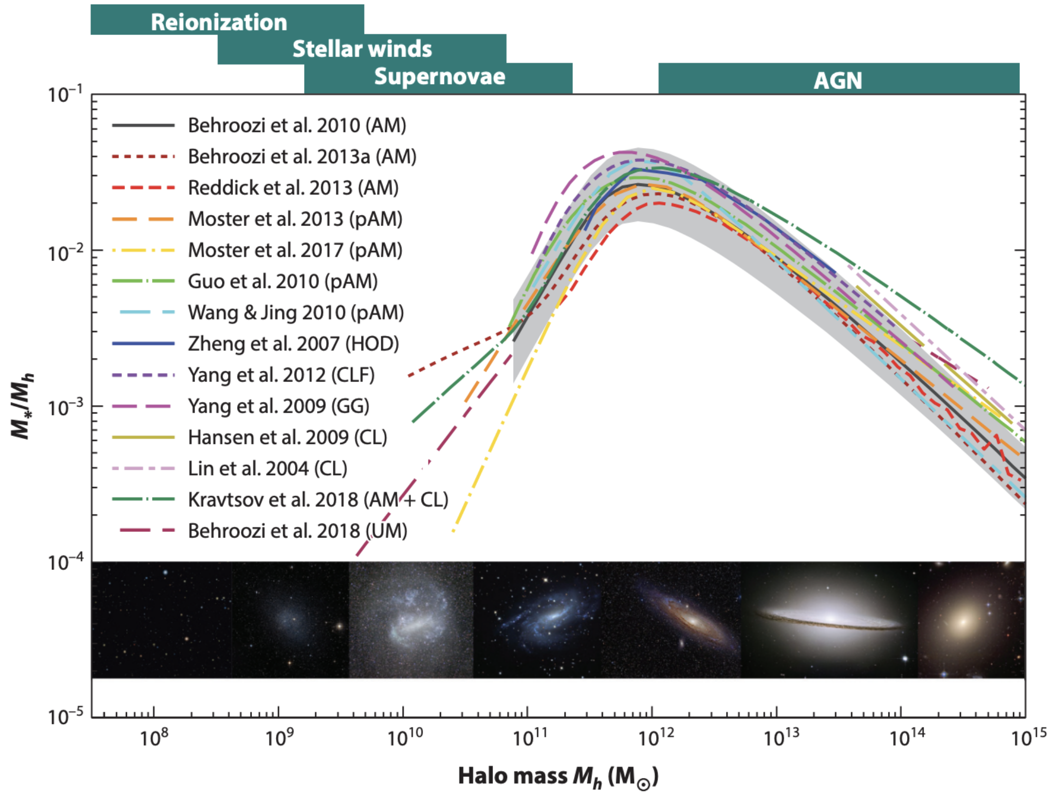

Figure 1.3: Compilation of literature SHMR relations for central galaxies. Figure taken from Wechsler and Tinker (2018).

stars are concentrated in the very inner regions of the haloes, and therefore the M_{200} resulting from such measurements is obtained by extrapolation.

Observations have already revealed a large scatter in the SHMR and measured a deviation from the predicted relation for the most massive spiral galaxies (Posti et al., 2019). Posti and Fall (2021) also found evidence for morphology-dependant SHMR, with ETGs in their sample closely following SHMR and most massive LTGs showing higher than expected stellar mass. Both these studies used kinematic tracers that are more spatially extended than the stellar component, such as gas rotation curves of LTGs and globular clusters (GCs) for ETGs. They demonstrate the need for larger samples of dynamical mass measurements constrained with extended kinematic tracers.

1.2.2 Singular isothermal sphere

First studies with gravitational lensing of ETGs found that the total mass distribution within the Einstein radius ($\sim R_e/2$) can be well approximated by a single power law with a narrow scatter and a profile that is slightly steeper than an isothermal sphere with a slope of -2 (Auger et al., 2010; Barnabè et al., 2011; Sonnenfeld et al., 2013). This trend was initially determined for the strongest gravitational lenses, i.e. the most massive galaxies. Subsequently, a similar trend was confirmed for lower-mass galaxies using dynamical modelling (e.g. Alabi et al., 2016; Poci et al., 2017; Bellstedt et al., 2018, hereafter A16; B18; P17). In the case of ETGs, the apparent tendency that two non-isothermal distributions of stars and dark matter "conspire" in a slope of close to isothermal has been a point of great discussion. The "bulge-halo" conspiracy was found to hold only on certain mass scales, suggesting that galaxy feedback processes might play a role (Dutton and Treu, 2014, and references therein).

The flat velocity dispersion profile found within 1 R_e of ETGs has been linked to dry major mergers as the main formation channels of these gas-poor systems. Through simulated binary mergers, Remus et al. (2013) showed that the inner slope $\gamma_\mathrm{tot} \sim -2$ acts as a natural attractor and once in place only a major merger with high gas fraction can modify the total mass density slope. They found that the larger the fraction of in-situ formed stars the steeper the total density profile. They link this with the dissipational nature of gas, which sinks in the centre of the merged galaxy to form a new population of more centrally concentrated stars, thereby steepening the total mass slope.

1.2.3 CORE-CUSP PROBLEM

Observations of galaxy rotation curves found that a cuspy NFW profile cannot reproduce well the central kinematics. Instead, a flattening of DM, i.e., a "core" ($\rho_\mathrm{DM} \propto r^{-\gamma}$, $\gamma \approx 0-0.5$), resulted in a better fit to the observations (e.g. de Blok et al., 2001, 2008; Simon et al., 2005). While baryonic feedback in hydrodynamic simulations has helped to explain this for Milky Way mass galaxies, that are baryon-dominated in their centres, it remains an issue on the small scales ($M \lesssim 10^{11}$ M$_\odot$). Its strength depends on the fraction of DM in a stellar system as well as the duration and burstiness of star formation (e.g. Read et al., 2019). The so-called *core-cusp problem* is only one of the small-scale challenges of ΛCDM and we defer an interested reader to the review by Bullock and Boylan-Kolchin (2017) for a broader discussion on this topic.

As shown in Fig. SHMR, DM haloes below 10^12 are increasingly dark matter dominated. They host dwarf galaxies with stellar masses $M_\star \leqslant 10^9$ M$_\odot$ and as low as $M_\star \leqslant 10^{2-5}$ M$_\odot$ (Simon, 2019) and thus initial dynamical mass models estimated a mass-to-light radio of 100. Therefore, they are expected to be DM-dominated at all radii. Due to their shallower gravitational potential, stellar feedback and supernovae more efficiently strip gas from the galaxy, halting star formation and preserving the primordial distribution of DM. Observations of bright dwarf galaxies ($M_\star \approx 10^{7-9}$ M$_\odot$) found that their density profiles are more consistent with a constant core in the centre, or even show varied central slopes (e.g. Simon et al., 2005). Dutton et al. (2019, 2020) analysed the NIHAO suite of simulations and found that the implementation of subgrid physics alters the central slope in low mass systems. Vogelsberger et al. (2016) show that DM physics can partially elevate the "core-cusp" problem. This further motivates the recovery of DM density profiles in low-mass systems, to test both DM and galaxy formation models.

Nearby dwarf galaxies are ideal environments to probe this question (Tolstoy et al., 2009). Because of their proximity, low mass dwarfs and gas-poor dwarfs can be observed in great detail. As their individual stars are resolved we can measure their individual LOS velocities (LOSVs) and proper motions (PMs) providing 3D kinematics of stars in these systems. For example, Walker et al. (2009) measured LOS velocities of ~7000 individual red giant branch (RGB) stars in 4 nearby dwarf spheroidal (dSph) galaxies. Owing to their proximity, proper motions of stars can be measured to provide 3D motions of stars in these systems (Massari et al., 2020a,b). Despite the improvement in the sample size and precision of the kinematic samples, a conclusive answer to the question of whether these systems have cored or cusped DM profiles is still missing. One of the biggest challenges is the low-velocity dispersion of these systems ~ 10 km s^{-1}, which require high precision of velocity measurements.

1.3 SHAPES OF DARK MATTER HALOES

Understanding the intrinsic shape of galaxies is essential to prevent biased conclusions when interpreting results derived from dynamical modelling. The shape is quantified by the axis ratios of a 3D ellipsoid, $p = b/a$ and $q = c/a$, where $a > b > c$ are semi-major, intermediate and minor axes. A shape characterized by $a > b = c$ is considered prolate, a shape with $a = b > c$ is considered oblate and, otherwise, the shape is triaxial. A sketch of prolate, spherical and oblate distributions is shown in Fig. 1.4.

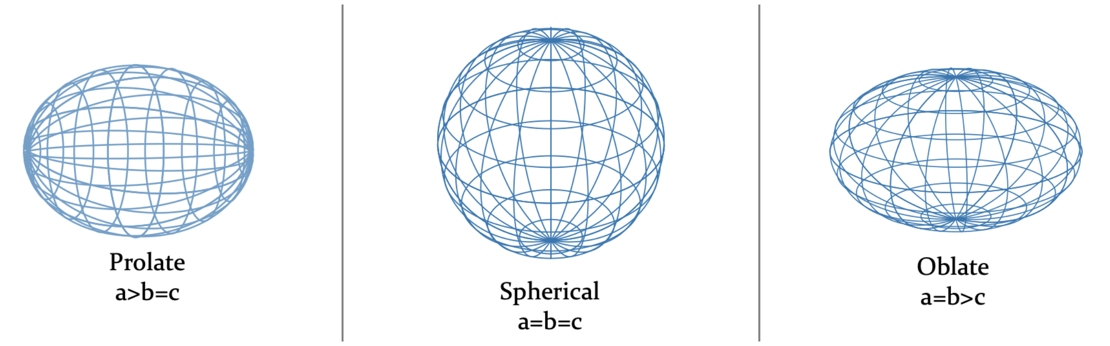

Figure 1.4: Sketch of prolate, spherical and oblate distributions (from left to right).

Observations of the luminous components of ETGs have revealed that stars show oblate, prolate, or even triaxial distributions (Ene et al., 2018; Foster et al., 2017; Foster et al., 2016; Pulsoni et al., 2018; Weijmans et al., 2014). These studies used photometry and kinematics to constrain the shapes and found a link between the amount of rotational support and the degree of triaxiality, with more rotation favouring oblate distributions, but not excluding triaxial shapes. Further, more oblate-axisymmetric distribution of stars can be embedded within a triaxial DM halo (see for example the results from the TNG simulations by Pulsoni et al., 2020). The Milky Way and its satellites are the only galaxies where we have detailed 6D phase-space information for a sufficiently large sample of tracers with which we can reconstruct the shape of the total mass distribution, including both luminous and dark matter (e.g., Sesar et al., 2011; Debattista et al., 2013; Posti and Helmi, 2019; Iorio and Belokurov, 2019; Naidu et al., 2021; Han et al., 2022). Beyond the Local Group, we rely on projected quantities only. Because of the random orientation of galaxies, we observe these intrinsic distributions projected along a line-of-sight (LOS), which makes the recovery of intrinsic shape very challenging, especially for ETGs with non-regular rotation (Krajnović et al., 2005; van den Bosch and van de Ven, 2009).

While great advances have been made in recent years on the intrinsic shapes of the central stellar components of ETGs with dynamical modelling (Jin et al., 2020; Santucci et al., 2022; Thater et al., 2023), much less is known about the haloes, where non-luminous matter dominates. In this domain, cosmological simulations have been the source of insight into the intrinsic shapes of the dark matter haloes (e.g., Cole and Lacey, 1996; Allgood et al., 2006; Prada et al., 2019; Chua et al., 2019). N-body simulations in the ΛCDM framework have shown strong radial dependence on the halo shape, with a preference for prolate haloes in the inner regions $r < 0.1r_{\rm vir}$, that become increasingly triaxial in the outer regions (e.g. Bailin and Steinmetz, 2005; Hayashi et al., 2007). The inclusion of baryonic physics acts to make the haloes rounder at all radii and the exact prescription of the baryonic feedback impacts the triaxiality of galaxies (e.g., Kazantzidis et al., 2004; Bryan et al., 2013; Tenneti et al., 2015; Chua et al., 2019). Studies of N-body dissipationless simulations found a strong dependence of the halo shape with the different cosmological parameters and the dark matter fraction (Allgood et al., 2006). For example, haloes in WDM cosmology are found to be rounder than CDM haloes (e.g. Bullock, 2002; Mayer et al., 2002). Directly observed measurements of the dark matter halo shape can thus provide additional constraints for cosmological simulations.

The inner regions of luminous galaxies are typically dominated by baryons, while in the outer regions, dark matter becomes the dominant contributor to the mass distribution (e.g., Deason et al., 2012; Cappellari et al., 2013). In the case of ETGs, the DM fraction at 5 $R_{\rm e}$ has been found to be 30-80% (Gerhard, 2013, and references therein). Harris et al. (2020) found a median DM fraction of 80-90% for galaxies with $M_\star > 10^{10}$ M$_\odot$. For the recovery of galaxy DM distribution and shapes, we need luminous tracers in the regions where DM dominates. Specific features such as stellar streams and polar rings have been used to put observational constraints on the 3D distribution of the dark matter (e.g., Iodice et al., 2003; Varghese et al., 2011; Khoperskov et al., 2014; Pearson et al., 2015; Leung et al., 2021). Weak lensing provides constraints on the projected flattening of DM haloes on a statistical basis (e.g. Robison et al., 2023).

1.4 GLOBULAR CLUSTERS AS TRACES OF DARK MATTER

Globular clusters are old ($\gtrsim 10$ Gyrs) dense stellar systems populating the haloes of every large galaxy (Brodie and Strader, 2006, and references therein). They can be observed beyond 5 $R_{\rm e}$ and are thus unique tracers of the DM (e.g. Brodie et al., 2014). There is empirical evidence that the total mass in GC systems (GCSs) is a better tracer of the total halo mass of its host galaxy rather than its stellar mass (Blakeslee, 1997; Spitler and Forbes, 2009; Georgiev et al., 2010; Hudson et al., 2014; Harris et al., 2017a). Thanks to their compact sizes and relatively high luminosities, individual GCs can be observed in galaxies at distances up to a few 100 Mpc with the *Hubble Space Telescope* (HST; e.g, see Jordán et al., 2009; Jordán et al., 2015; Harris, 2023) and in nearby groups and clusters from ground-based surveys (e.g. Taylor et al., 2016). Spectroscopic observations needed to measure radial velocities (RVs) are however limited to a few nearby groups and clusters (Brodie et al., 2014; Chaturvedi et al., 2022).

Deep observations of GCs in the nearby Universe have revealed that the magnitude distribution of GCs around galaxies follows a nearly universal shape (e.g. Harris et al., 2014; Jordán et al., 2006; Rejkuba, 2012). The GC luminosity function (GCLF) for ETGs is well approximated by a Gaussian distribution (Rejkuba, 2012, and references therein). The mean absolute magnitude of the GCLF, the turn-over magnitude (TOM), is constant for massive ETGs within ± 0.2mag (e.g., Harris et al., 2014; Villegas et al., 2010) and has been used to determine precise distances to galaxies (e.g. Jordán et al., 2005). The width of the GCLF, $\sigma_{\rm GCLF}$, depends on the total mass of the galaxy with a significant scatter at the faint end (Villegas et al., 2010).

The most massive, often central galaxies in galaxy clusters, can host ~ 1000 GCs, while the number drops to around 100 GC around Milky Way mass galaxies and less than 10 for dwarf spheroidals. A recent study of GCS of Milky Way-like simulated galaxies suggests that a large fraction of in-situ GCs are tidally disrupted by $z = 0$. They also found a connection between the total stellar mass of the galaxy and the present-day mass of the GCS (Bastian et al., 2020).

GCSs of all large galaxies show bi- or multi-modal colour distribution, because most GCs are old the colour can be seen as a proxy for metallicity and the presence of bimodality has been linked to the distinct origin of both populations (Brodie and Strader, 2006). With blue GCs being metal-poor and red metal-rich. Redder GCs are often more centrally concentrated and on more disk-like orbits because they were likely formed in situ. Blue GCs on the other hand are thought to originate from other galaxies that have merged with the host galaxy at some point throughout its lifetime. Hence, they are often found in the outer halo on more radial orbits. The different spatial distribution and orbital properties of the two populations have been used in the literature in the dynamical modelling of massive ETGs (e.g. Romanowsky et al., 2009; Zhu et al., 2016). While the two populations of the most massive galaxies show such distinct behaviour for most galaxies, the rotation amplitude and dispersion of blue and red GCs are consistent as found by Fahrion et al. (2020). Therefore they can be modeled as a single population (Veršič et al., 2024).

1.5 OPEN QUESTIONS THAT WILL BE ADDRESSED IN THIS THESIS

In this thesis, we investigate the internal properties of the dark matter haloes, in particular, the radial distribution of mass and shape of dark matter haloes. To that end, we use the discrete dynamical modelling (chapter 2) of GCSs in ETGS to trace the mass distribution in the regions dominated by DM. In particular, we address the following questions:

- What are the properties of the dataset, in terms of spatial extent and precision, to discriminate between cored and cusped DM profiles in low mass systems $(v_{200}) \sim 10$ km s^{-1}? (chapter 3)
- Advantages and biases when modelling GCS of ETG galaxies? (chapter 4)

- Are total mass profiles consistent with a single power law profile with an isothermal slope of -2? (chapter 5)
- Are DM haloes of ETGs spherical? (chapter 6)

This work highlights the advantages of using discrete dynamical modelling to put accurate constraints on the properties of DM haloes.

Chapter 2

Discrete dynamical modelling

"The proper method for inquiring after the properties of things
is to deduce them from experiments."
- Isaac Newton

Declaration of published work

This chapter includes text already published or submitted to a journal. Specifically, sections on methodology in Veršič et al. (2023, 2024, subm.) were adapted for the thesis. As a result, there may be partial overlap with those publications.

2.1 Introduction

Stellar dynamics describes the motion of stars within a stellar system in a statistical way under the influence of the gravitational potential in which they orbit. Dynamical modelling uses the observed motions of stars to infer the enclosed mass (gravitational potential) and orbital properties of the stars (rotation and velocity anisotropy) (Binney and Tremaine, 2008). Historically, dynamical modelling has been applied to binned stellar kinematics or light integrated along the line-of-sight. In this thesis, I take advantage of the novel measurements of discrete sources (GCs or stars) and carry out *discrete dynamical modelling*. It offers a unique opportunity for dynamical modelling of sparsely populated regions, such as galaxy haloes. There are three main advantages of the discrete approach over binning velocities in radial bins: the number of kinematic data points constraining the model is higher, biases due to an arbitrary binning strategy are removed, and contaminants, that could bias binned velocity moments, can be self-consistently modelled (e.g. Hénault-Brunet et al., 2019; Watkins et al., 2013).

Discrete dynamical modelling uses the velocities of individual tracers (stars, GCs or PNe) to constrain their orbital properties and gravitational potential as seen in Fig. 2.1. The individual velocities can be understood as single samples drawn from the underlying local LOSVD. This is conceptually different from how integrated stellar spectra of galaxies are modelled, where the moments of the LOSVD can be derived from spectra (e.g. Bellstedt et al., 2018; Cappellari et al., 2013; Poci et al., 2017). Fig. 2.1 demonstrates the discrete dynamical modelling approach for an example of GCs in NGC 5128 that we model in chapter 6. The top panel shows the individual GCs coloured by their LOSV wrt the systemic velocity of the galaxy and with the star symbols we highlight two GCs that we compare throughout the figure. In the central panels, we show the moments of the LOSVD (mean velocity on the left and velocity dispersion on the right) predicted by CJAM for a given gravitational potential and orbital properties. The locations that correspond to the stars in the top panel are shown here with black circles. The discrete approach uses the moments of the projected velocity distribution highlighted with black circles to construct a Gaussian likelihood as seen on the bottom two panels for the blue and red-shifted GC respectively. The bottom panels show the model LOSVD in black and the discrete velocity of a GC with the width corresponding to the LOSV measurement uncertainty. The discrete dynamical modelling approach combines the likelihood at the position of each tracer to constrain the model parameters (gravitational potential and orbital properties).

In this thesis, I present a series of dynamical studies all based on the methodology outlined in this chapter but with specific adaptations for each of the scientific questions. The dynamical modelling tool used through this thesis is *Jeans Anisotropic MGE*[1] (JAM) models, a dynamical modelling framework introduced by Cappellari (2008). In this chapter,outline how we constructed an accurate characterisation of the spatial distribution of the discrete kinematic tracers, i.e. tracer density profile, and how we introduced the gravitational potential in JAM. Lastly, it describes the statistical approach we adopted to recover the best-fit parameters.

In chapter 3 we study mock datasets of Milky Way dSph, for which we use projected 5D phase-space information: two positions in the plane of the sky (α, δ), LOS velocity $v_{\rm LOS}$ as well as the two proper motion components: (μ_α, μ_δ). In chapter 4, 5 and 6 we study extragalactic objects where three projected phase-space components are observed for discrete tracers: $(\alpha, \delta, v_{\rm LOS})$.

2.2 Jeans Anisotropic MGE modelling

Most stellar systems are an ensemble of a large number of stars, with galaxies like the Milky Way hosting $\sim 10^{11}$ stars (Binney and Tremaine, 2008). Modelling the system as a whole is therefore more practical than following the orbit of each star. One such method, the Jeans equations (Jeans,

[1]Multi Gaussian Expansion (Emsellem et al., 1994).

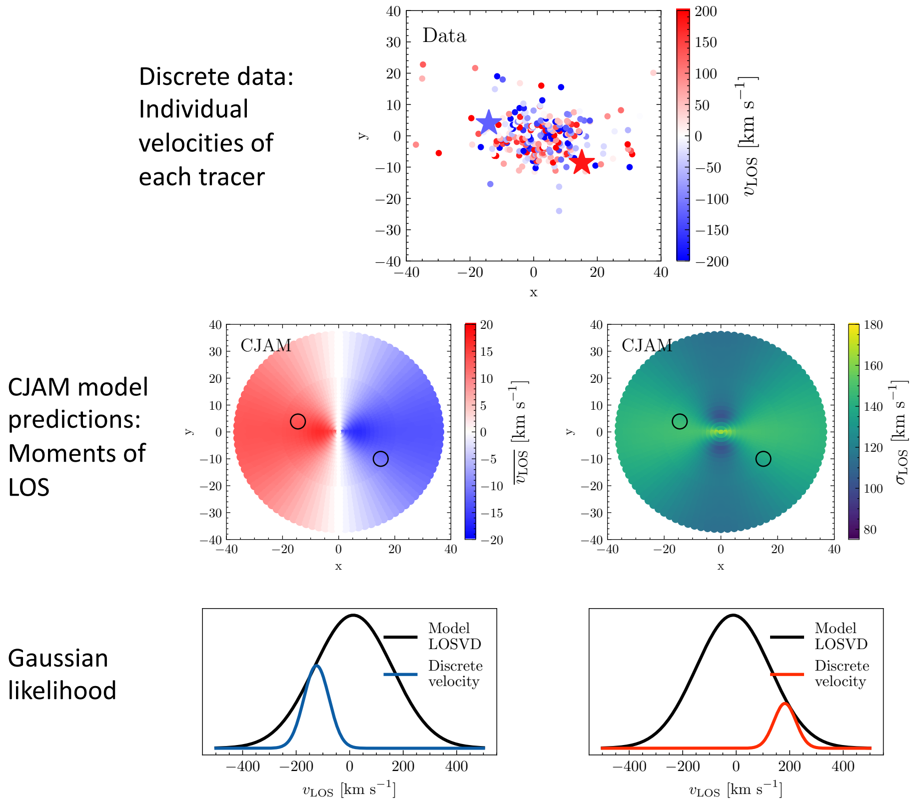

Figure 2.1: Sketch of the discrete dynamical modelling approach for an example of blue GCs in NGC 5128 presented in chapter 6. The top panel shows the individual GCs colour-coded based on their LOSV. The star symbols highlight two GCs we picked to demonstrate the modelling approach. The middle panels show the mean LOSV on the left and velocity dispersion on the right predicted by CJAM. The locations of the GCs highlighted as stars on the top panel are shown with black circles here. In the bottom panels, we compare the Gaussian LOSVD given by CJAM predictions with black lines and the velocity of individual GCs in coloured lines.

1922), is based on the collisionless Boltzmann equations for a system in a steady state:

$$\sum_{i=1}^{3}\left(v_i\frac{\partial f}{\partial x_i}-\frac{\partial \Phi}{\partial x_i}\frac{\partial f}{\partial v_i}\right)=0, \tag{2.1}$$

where f is the 6D distribution function (indicating the probability of finding a star at any given phase-space location), Φ is the gravitational potential, v_i are the velocity components and x_i are the spatial components in the phase space. Both assumptions (collisionless systems in steady state) are reasonable for the inner regions of most galaxies, where the two-body relaxation time is longer than the age of the Universe. However, the first assumption can break down in very dense stellar systems such as centres of galaxies and globular clusters (Binney and Tremaine, 2008). The second assumption is not valid in the outer regions of the galactic haloes and for actively merging systems.

2.2.1 JAM FORMALISM

The JAM formalism has been extensively used to model ETGs with stars and GCs as tracers to derive dark matter fraction, stellar M/L and dark matter density profile (e.g. Bellstedt et al., 2018; Cappellari et al., 2013; Poci et al., 2017; Zhu et al., 2023). As discussed in Sect. 1.3 most

ETGs can be well approximated as axisymmetric systems in the inner regions, with both stellar and DM haloes showing triaxial shapes.

To link the observable moments of the velocity distribution $(\overline{v}, \sigma)$ with the gravitational potential, the Jeans equations are derived in a coordinate system that best corresponds to the intrinsic geometry of the stellar system (spherical, axisymmetric or triaxial). JAM is only available for spherical and axisymmetric potentials and we use the axisymmetric formalism in cylindrical polar coordinate system (R, φ, z) as implemented by Watkins et al. (2013, CJAM).

Starting from Eq. 2.1 assuming cylindrical geometry, the axisymmetric assumptions imposed by $\frac{\partial f}{\partial \varphi} = \frac{\partial \Phi}{\partial \varphi} = 0$ simplifies the equation to:

$$v_R \frac{\partial f}{\partial R} + v_z \frac{\partial f}{\partial z} + \left(\frac{v_\varphi^2}{R} - \frac{\partial \Phi}{\partial R} \right) \frac{\partial f}{\partial v_R} - \frac{\partial \Phi}{\partial z} \frac{\partial f}{\partial v_z} - \frac{v_R v_\varphi}{R} \frac{\partial f}{\partial v_\varphi} = 0 \, . \tag{2.2}$$

Multiplying Eq. 2.2 by v_R and v_z and integrating over the velocities we arrive at the two Jeans equations, that connect the components of the velocity dispersion tensor with the gravitational potential:

$$\begin{aligned} \frac{\nu\left(\overline{v_R^2} - \overline{v_\varphi^2}\right)}{R} + \frac{\partial(\nu \, \overline{v_R^2})}{\partial R} + \frac{\partial(\nu \, \overline{v_R v_z})}{\partial z} &= -\nu \, \frac{\partial \Phi}{\partial R} \\ \frac{\nu \, \overline{v_R v_z}}{R} + \frac{\partial(\nu \, \overline{v_z^2})}{\partial z} + \frac{\partial(\nu \, \overline{v_R v_z})}{\partial R} &= -\nu \, \frac{\partial \Phi}{\partial z} \, , \end{aligned} \tag{2.3}$$

where ν represents the number density of the kinematic tracers, $\overline{v_R^2}$, $\overline{v_\varphi^2}$, and $\overline{v_z^2}$ are the second velocity moments and $\overline{v_R v_z}$ is the cross term of the second moment tensor. Once both the gravitational potential Φ and tracer density profile ν are known, the two Jeans equations (Equation 2.3) have four free parameters: to obtain a unique solution, further assumptions on the second moment tensor are needed. The cross terms of the second moment tensor are 0 when we make an assumption that the velocity ellipsoid is aligned along a particular coordinate system.

The axisymmetric JAM models assume an astrophysically-motivated cylindrical alignment of the velocity dispersion tensor (for more details see discussion in Sect. 2.3 in Cappellari, 2008). Such alignment assumes that the vertical and radial oscillations of the kinematic tracers are independent in the meridional plane (R, z): $(\overline{v_R v_z} = 0)$. By additionally assuming a constant anisotropy quantified as $\overline{v_R^2} = b \, \overline{v_z^2}$ we arrive to the two Jeans equations:

$$\begin{aligned} \frac{\nu \, \left(b \, \overline{v_z^2} - \overline{v_\varphi^2}\right)}{R} + \frac{\partial(b \, \nu \, \overline{v_z^2})}{\partial R} &= -\nu \, \frac{\partial \Phi}{\partial R} \\ \frac{\partial(\nu \, \overline{v_z^2})}{\partial z} &= -\nu \, \frac{\partial \Phi}{\partial z} \end{aligned} \tag{2.4}$$

with two free variables $\overline{v_\varphi^2}$ and $\overline{v_z^2}$. Such a system of equations can be solved numerically and $\overline{v_R^2}$ is evaluated through the anisotropy parameter b.

MGE formalism

Both the mass distribution, which generates the potential Φ, as well as the tracer density ν, are incorporated in the JAM models as MGE. This choice has the advantage of being computationally efficient, as the projection and deprojection of the Gaussians are analytic when translating the observed 2D to intrinsic 3D quantities. As well as flexible since they can incorporate a large range of radial profiles and can accurately reproduce the surface brightness profiles of real galaxies.

The projected surface brightness or tracer distribution (Σ) at each position in the plane of the sky (x', y'), with x' aligned with the major axis, is expressed as:

$$\Sigma(x', y') = \sum_{k=1}^{N} \frac{L_k}{2\pi\sigma_k^2 q_k'} \exp\left[-\frac{1}{2\sigma_k^2} \left(x^{'2} + \frac{y^{'2}}{q_k^{'2}} \right) \right] \tag{2.5}$$

where N is the number of Gaussian components, L_k is the total luminosity (or number of tracers) of each component, σ_k is the width (dispersion) along the major axis, and q'_k the projected axis ratio of the major and minor axis, also called the flattening.

The projected quantities are analytically linked to the intrinsic axisymmetric density profile $\nu(R, z)$:

$$\nu(R, z) = \sum_{k=1}^{N} \frac{L_k}{(\sqrt{2\pi}\sigma_k)^3 q_k} \exp\left[-\frac{1}{2\sigma_k^2} \left(R^2 + \frac{z^2}{q_k^2} \right) \right] \tag{2.6}$$

where q_k is the deprojected flattening:

$$q_k = \frac{\sqrt{q_k'^2 - \cos^2(inc)}}{\sin(inc)} \tag{2.7}$$

obtained with the inclination angle inc[2] (90^o is edge-on and 0^o face-on).

The drawback of using MGEs is that the decomposition of the profile is not unique because Gaussians are not eigenfunctions and the number of Gaussian components can be non-trivial. Additionally, in the outer regions of the fitted profile, the Gaussians will fall off faster than most literature profiles used to describe the distribution of matter. Similarly, in the innermost regions, MGEs can better describe cored profiles and a large number of Gaussians are needed to accurately represent a cuspy profile. Therefore, when using MGE decomposition, great care has to be placed on the choice of the radial region over which the profile is fitted as well as the number of Gaussian components. With these mitigations, the drawbacks are slight while the advantages are great, as MGEs represent efficient and effective solutions that are useful for our purposes in this thesis. Throughout this thesis, we use *mgefit* implementation of the MGE algorithm by (Cappellari, 2002).

VELOCITY ANISOTROPY AND FIRST VELOCITY MOMENT

Using MGEs also enables the modelling of anisotropy gradients by allowing each Gaussian component k to have a different value b_k. When these components are different the global anisotropy can be computed weighted by the tracer density ν_k:

$$\beta_z \equiv 1 - \frac{\overline{v_z^2}}{\overline{v_R^2}} \approx 1 - \frac{\sum_k \nu_k}{\sum_k b_k \nu_k} \tag{2.8}$$

that corresponds to radial anisotropy for $\beta_z > 0$, characteristic for strongly eccentric orbits, vertical anisotropy for $\beta_z < 0$, and semi-isotropy for $\beta_z = 0$. Since one of the second moments is not accounted for in the β_z as seen in Eq. 2.8 the interpretation of its value may not be as straightforward, especially for systems with strong rotational signature.

The Jeans equations provide a prediction for the second velocity moments. To obtain a unique solution for the first velocity moments, additional assumptions must be made to connect the relative contributions of ordered and random motions:

$$\kappa_k = \frac{[\overline{v_\varphi}]_k}{\sqrt{[\overline{v_\varphi^2}]_k - [\overline{v_R^2}]_k}} \tag{2.9}$$

where $\overline{v_\varphi}$ is the first moment in the tangential coordinate φ. It is helpful to think of κ_k as a proxy for rotation, and $\kappa_k = 0$ when the kth Gaussian component is non-rotating. The global mean velocity can be computed by summing the contributions from the individual Gaussian components:

$$\nu\, \overline{v_\varphi} = \left[\nu \sum_{k=1}^{N} \kappa_k^2 \left([\nu \overline{v_\varphi^2}]_k - [\nu \overline{v_R^2}]_k \right) \right]^{1/2} \tag{2.10}$$

Both b_k and κ_k define the velocity ellipsoid and are needed to interpret the intrinsic velocity anisotropy.

[2]In this thesis we adopt inc for the inclination to avoid confusion with the indexing used for iterations in chapter 6.

2.3 CONSTRUCTING THE TRACER DENSITY PROFILE

As can be seen in Eq. 2.4, 2.8 and 2.10, the tracer density profile ν acts as a weighing function in the JAM models. Therefore, its accurate characterisation is crucial for unbiased predictions of the projected velocity moments that are compared with observations. Typically, dynamical modelling studies of the stellar kinematics in the central 1-2 R_{e} of galaxies use integrated surface brightness profiles based on photometric imaging (e.g. Cappellari et al., 2013; Thater et al., 2023; Zhu et al., 2023). However, the types of kinematic tracers used in this thesis require a different approach to recover ν. This is needed for kinematic tracers that are intrinsically sparse, such as extragalactic GCs, as well as when the proximity of the stellar system or its low surface brightness hinders deep imaging, such as for Galactic GCs or dwarfs. In such systems where only the positions of individual tracers are available, binning is required to recover their spatial distribution.

When using individual photometric sources, removing foreground and background contamination can be non-trivial. Recent works from Taylor et al. (2017, hereafter T17) and Hughes et al. (2021, hereafter H21) demonstrated this for GC candidates of NGC 5128, a nearby elliptical galaxy. The methodology we developed to establish a sample of GCs least affected by observational biases for GCS is explained in Sect. 4.4. Here, we outline how to create an MGE input of the tracer density profile for CJAM once a clean sample of discrete sources is available.

2.3.1 POSITION ANGLE AND FLATTENING

The analysis is performed in the projected Cartesian coordinate system (x', y'), where x' is in the direction of West and y' North. When needed, we transform the equatorial coordinates of the discrete tracers (α_i, δ_i) (van de Ven et al., 2006):

$$\begin{aligned}
\Delta\alpha &= \alpha - \alpha_0 \\
\Delta\delta &= \delta - \delta_0 \\
x' &= -r_0 \cos(\delta)\sin(\Delta\alpha) \\
y' &= r_0\big(\sin(\delta)\cos(\delta_0) - \cos(\delta)\sin(\delta_0)\cos(\Delta\alpha)\big) \ ,
\end{aligned} \tag{2.11}$$

where α_0, δ_0 are the coordinates of the centre of the galaxy hosting the tracers. The scale factor $r_0 = 180/\pi \times 3600$ converts the x', y' from radians to arcsec.

In the projected Cartesian coordinate system, position angle PA[3] and flattening q' are computed by constructing an inertial tensor $I_{i,j}$. The eigenvectors of the tensor are aligned along the semi-major axis. We use the following equations to compute both quantities:

$$I_{ij} = \frac{\sum_{n=1}^{N} x_{i,n} x_{j,n}}{N} \tag{2.12}$$

where i, j are the projected coordinates x', y'. Then the position angle is given by

$$\mathrm{PA} = \frac{1}{2}\arctan\left(\frac{2\, I_{x'y'}}{I_{x'x'} I_{y'y'}}\right). \tag{2.13}$$

The semi-major a and semi-minor b axis lengths and the ellipticity e are given by

$$a = \frac{I_{x'x'} + I_{y'y'}}{2},\ b = \left[\left(\frac{I_{x'x'} - I_{y'y'}}{2}\right)^2 + I_{x'y'}^2\right]^{1/2}, \qquad e = 1 - \left[\frac{a-b}{a+b}\right]^{1/2}, \tag{2.14}$$

and, finally, the projected flattening is connected with the ellipticity e by

$$q' = 1 - e. \tag{2.15}$$

[3]Increasing from North to East.

To ensure a robust result for a given set of discrete tracers, we apply the above-outlined procedure to a subset of sources within an increasing radius. We compute the PA and q' in running radial shells of width ΔR, as is done for shapes of simulated galaxies (e.g. Pulsoni et al., 2021; Zemp et al., 2011). This is achieved by setting the width of the shell and the step size d ($d < \Delta R$) by which we move outward such that the centre of the $(n+1)$ shell is at $R_{n+1} = R_n + d$. This increases the number of sources in each shell and avoids nonphysical sudden changes in the recovered parameters due to the stochasticity of the discrete dataset.

Both the step size and shell size are adjusted for individual galaxies to yield robust results depending on the number of photometric sources. Additionally, when modelling GCSs (chapter 4, 5 and 6), the PA is compared with that of the stellar distribution $\mathrm{PA}_\star$ to further verify the robustness of the results.

2.3.2 Fitting an analytic profile

To construct the MGE of the tracer density profile, we could bin the photometric data for each galaxy and fit the MGEs to the binned profile. However, binned profiles are stochastic and the number of bins is often small. So instead we choose to fit an analytic function to the binned data as an intermediate step. Throughout this work, we fit three different kinds of tracer density profiles:

$$\text{Power-law:} \quad \Sigma_\mathrm{P}(R) = \Sigma_{\mathrm{P},0}\ R_1^{\alpha} \tag{2.16}$$

$$\text{Broken power-law:} \quad \Sigma_\mathrm{BP}(R) = \Sigma_{\mathrm{PB},0} \begin{cases} \left(\frac{R}{R_\mathrm{PB}}\right)^{\alpha_2} & : R \leqslant R_\mathrm{PB} \\ \left(\frac{R}{R_\mathrm{PB}}\right)^{\alpha_3} & : R > R_\mathrm{PB} \end{cases} \tag{2.17}$$

$$\text{Sérsic:} \quad \Sigma_\mathrm{S}(R) = \Sigma_{\mathrm{S},0}\ \exp\left(-b_n\left(\left(\frac{R}{R_e}\right)^{1/n} - 1\right)\right) \tag{2.18}$$

where $\Sigma_{\mathrm{P},0}$, $\Sigma_{\mathrm{PB},0}$ and $\Sigma_{\mathrm{S},0}$ are the normalising constants $[N_\mathrm{tracers}\ \mathrm{arcsec}^{-2}]$, and α_1, α_2, and α_3 are the power law slopes. For the Sérsic profile (Sersic, 1968), n is the Sérsic index, and to compute b_n we used the asymptotic expansion $b_n = 2n - 1/3 + 4/(405n) + 46/(25515n^2)$ from Ciotti and Bertin (1999). The parameter R_PB is the break radius of the broken power-law and R_e is the effective radius. The choice of fitting function depends on the intrinsic and observed properties of the system we are modelling, as we will discuss further in each chapter.

To account for the flattening of the discrete tracers, we do not bin in spherical radii, instead, we use the elliptical radius $R_\mathrm{ell} = \sqrt{x'^2 + y'^2/q'^2}$. We investigate two binning strategies: logarithmically-spaced bins and bins with an equal number of tracers. For each binning strategy, we additionally create 5 different binned profiles, varying the number of bins or number of tracers per bin. To each of the binned profiles we fit an analytic function and compare the recovered parameters to ensure the binning is minimally impacting the resulting tracer density. This step is motivated by the large variation in the number of tracers per galaxy we modelled throughout the thesis work. This approach yields good results even in the presence of low-number statistics.

To fit the analytic profile, we use a Bayesian framework, with flat priors on the free parameters and a Gaussian likelihood. The best-fit parameters and the posteriors are sampled using EMCEE (Foreman-Mackey et al., 2013) a python implementation of the Goodman and Weare (2010) affine-invariant Markov Chain Monte Carlo (MCMC) ensemble sampler.

2.3.3 MGE decomposition

The last step is to represent the tracer density profile in the MGE format required for the dynamical models we will use later. We draw samples of the modelled parameters from their posteriors and use them to evaluate the profile at each radius. This step mimics observational noise and provides a more realistic treatment of the tracer density profile.

2.4 Gravitational potential in JAM

A different set of Gaussians can describe the total mass density of the galaxy that generates the gravitational potential:

$$\rho(R,z) = \sum_{j=1}^{M} \frac{M_j}{(\sqrt{2\pi}\sigma_j)^3 q_j} \exp\left[-\frac{1}{2\sigma_j^2}\left(R^2 + \frac{z^2}{q_j^2}\right)\right] \tag{2.19}$$

where M_j is the total mass in the Gaussian and q_j its intrinsic flattening. Galaxies consist of different components, such as stars, gas[4] and DM. Their relative contributions to the gravitational potential can be accounted for in JAM by combining their MGEs.

The mass distribution of stars can be obtained by scaling the stellar surface brightness MGEs in a given photometric band b with mass-to-light ratio $M_\star/L_b$[5]. We arrive at the total mass density of a galaxy by adding the stellar mass density to the adopted dark matter density (for discussion on the dark matter distributions see Sect. 1.1.2):

$$\rho_{\rm tot} = (M_\star/L_{\rm b}) \times \nu_b + \rho_{\rm DM} \tag{2.20}$$

where $\nu_{\rm b}$ is the MGE representation of the deprojected luminosity density and $\rho_{\rm DM}$ the MGE representation of the DM component.

A central supermassive black hole can also be incorporated into the JAM models through a Keplerian potential. However, the systems modelled throughout this work are not sensitive to the potential in the innermost regions of galaxies and we, therefore, do not include it in our analysis.

2.5 Discrete likelihood analysis

Once both the observed velocities and model predictions are available, we use discrete likelihood analysis to recover best-fit parameters. The kinematic tracers used throughout my work are discrete, such as individual stars and GCs, as opposed to integrated stellar light or gas kinematics where, from their spectra, the moments of LOSVD can be recovered. The discrete tracers on the other hand are a single sample drawn from an underlying velocity distribution. Discrete modelling has several key advantages, the main among them is that it avoids the need for arbitrary spatial binning. This means we can trace the mass distribution out to the outermost measured position. Moreover, past studies have shown that contaminants can greatly impact binned statistics.

In this thesis, we adopt two main approaches to finding the best-fit parameters: **Bayesian analysis** and χ^2. Where possible, we employ the former as it can self-consistently account for prior information on the free parameters of our model and degeneracies in the modelling parameters, and results in a full posterior distribution in the multi-dimensional parameter space. However, it can be more time-intensive, particularly when the model is computationally intensive. Exploring a χ^2 surface on a predefined grid of parameters can significantly reduce the computational time while still yielding comparable results. Throughout this thesis, we use Gaussian likelihood to compare the model predictions $(\overline{v}, \sigma)$ with the observed velocities (both proper motions and LOS). The computational simplicity and flexibility to account for measurement uncertainties make this functional form a very practical choice with minimal bias. For a tracer n with velocity component $v_{i,n}$ and measurement uncertainty $\epsilon_{i,n}$, the likelihood is given by:

$$\ln \mathcal{L}_n = -\frac{1}{2}\ln\left(2\pi(\sigma_{i,n}^2 + \epsilon_{i,n}^2)\right) - \frac{(v_{i,n} - \overline{v_{i,n}})^2}{2(\sigma_{i,n}^2 + \epsilon_{i,n}^2)}, \tag{2.21}$$

where i stands for the three projected components of the velocity $(\mu_\alpha, \mu_\delta, v_{\rm LOS})$. For computational efficiency, we use the logarithm of the likelihood. The chosen functional form of the likelihood directly relates to the χ^2:

$$\chi^2 = -2\ln\mathcal{L} \tag{2.22}$$

[4]The galaxies we model have negligible gas content, so we ignore it.

[5]Throughout this work the mass-to-light ratio is in solar units [$\mathrm{M_\odot L_\odot^{-1}}$] and for clarity of the text we omit it.

This enables consistent methodology among both approaches.

2.5.1 BAYESIAN ANALYSIS

In the Bayesian framework, the posterior distribution of the parameters is:

$$\mathcal{P}(\Theta|\mathrm{data}_i)\propto\mathcal{L}(\mathrm{data}_i|\Theta) \times p(\Theta) \tag{2.23}$$

where Θ is a vector of model parameters, $\mathcal{L}(\mathrm{data}_i|\Theta)$ is the likelihood of the data given the model, $p(\Theta)$ represents the prior, and data_i the ith data point. Additionally, we can reasonably assume the measurements are independent and for computational simplicity, we write the combined posterior as:

$$\ln(\mathcal{P}(\Theta|\mathrm{data}))\propto\sum_{i}^{\mathrm{data}}\ln\mathcal{L}(\mathrm{data}_i|\Theta) + \ln p(\Theta) \tag{2.24}$$

Throughout the thesis, we used a mix of uninformative (flat) and informative priors. For the informative priors, we choose to use Gaussian priors for their simplicity and computational efficiency. From the sample returned by EMCEE, we estimate the best-fit parameters and their confidence intervals. The number of walkers and steps is adjusted for each analysis.

2.5.2 χ^2 ANALYSIS

Where it is computationally impractical to adopt the Bayesian analysis, we evaluate χ^2 on a grid of parameters. The best-fit solution is found at the location of the minimum of the statistics. The caveat is that when there are N free parameters constructing an N dimensional grid can be just as computationally expensive as full posterior sampling. The solution therefore is to evaluate the χ^2 for one parameter at a time and keep the other $(N-1)$ fixed, thereby evaluating a slice of the N dimensional χ^2 surface. Far from the global minimum, the best solution for any given parameter will strongly depend on the values of the other $(N-1)$ parameters. That is why careful iterations need to be employed to find the global minimum.

The computational efficiency and simplicity of χ^2 analysis also offer a unique opportunity to coarsely explore the parameter space and refine the initial guesses for the Bayesian analysis.

Chapter 3

Mock data to resolve the core-cusp problem

"So important is this dark matter to our understanding of the size, shape, and ultimate fate of the universe that the search for it will very likely dominate astronomy for the next few decades."
- Vera Rubin

3.1 Introduction

Galactic dwarf spheroidal galaxies are ideal systems in which to address the question of whether DM-dominated systems are hosted in a primordial cuspy or cored DM halos as introduced in Sect. 1.2.3. The typical velocity dispersion of dwarfs $\sigma \sim 10$ km s^{-1} requires a large number of velocity measurements with a precision of the $\mathcal{O}(\epsilon_i)$ km s^{-1}, which is observationally challenging. Here we focus on observational guidelines motivated by the limitations of current ground- and space-based facilities for systems analogous to Galactic dSphs.

In this chapter, we consider what observational data is needed—in size, spatial coverage, and precision—to make advances in answering this question. To do this, we create a series of mock kinematic datasets of dSph galaxies, attempt to recover the intrinsic galaxy properties with CJAM (Sect. 2.2), and then assess which of the mock datasets were able to recover the properties correctly. From this, we provide observational guidelines for what data is needed to break this longstanding problem.

We start by introducing the discrete dynamical approach in Sect. 3.2. Followed by the description of how we generate mock observations in Sect. 3.3. The results are presented in Sect. 3.4.

3.2 Discrete dynamical modelling

Dwarf spheroidal galaxies are well approximated as axisymmetric systems in a steady state. Observations have also found evidence of deviations from isotropic orbital configuration (e.g. Massari et al., 2018, 2020b). As we discussed in Sect. 3.3.1, the mock datasets we generate are spherical and isotropic. However, we model them with a dynamical modelling approach that can account for velocity anisotropy and flattening in the spatial distribution to prepare for future application to real systems and to ensure that the models can constrain the isotropy and sphericity. For the nearby dSph galaxies, the kinematic tracers of the potential are discrete velocities of stars. Henceforth, when we discuss tracers and tracer number density we mean the individual stars and their spatial distribution.

We use CJAM, introduced in Sect. 2.2, to predict velocity moments for both the LOS velocities and PMs. Through the use of Gaussian likelihood (Eq. 2.21) we use Bayesian analysis to find the best-fitting model parameters and sample the posterior. The methodology closely follows the approach outlined in chapter 2 and in this section, we further explain the steps we adapted for application to mock dSph datasets.

Mass density profile

This work aims to identify the observing strategy needed to discriminate between cored and cusped DM profiles at the low mass end of the galaxy mass function. The systems we are modelling are DM-dominated at all radii, therefore the mass model we adopt only takes the dark component of the potential into account as the source of the gravitational potential.

The mass density profile could be fit parametrically, where we adopt a functional form to which we fit an MGE, or non-parametrically, where we fit the MGE parameters directly. We elect to do the former as it significantly reduces the number of free parameters in our models.

We adopt a generalized Hernquist profile (Read et al., 2021) to characterize the DM density profile:

$$\rho_{\rm DM}(r) = \rho_{\rm DM,0} \left(\frac{r}{r_{\rm DM}}\right)^{-\gamma_{\rm DM}} \left[1 + \left(\frac{r}{r_{\rm DM}}\right)^{\alpha_{\rm DM}}\right]^{\frac{\gamma_{\rm DM}-\beta_{\rm DM}}{\alpha_{\rm DM}}}, \tag{3.1}$$

where $\rho_{\rm DM,0}$ is the central DM density, $r_{\rm DM}$ is the scale radius of DM, $\alpha_{\rm DM}$ is the "sharpness" of the transition between the inner $\gamma_{\rm DM}$ and outer logarithmic slope $\beta_{\rm DM}$. This profile has variable inner and outer slopes, making it very flexible; such profiles have been used in the literature to describe the density of MW dwarfs (e.g. Hayashi et al., 2020).

Additionally, as we will see in Sect. 3.3, the literature dataset, which we down-sample to create different mock datasets, was generated assuming the same functional form for the mass distribution. Our primary goal is to see how well we can recover the overall shape of the mass profile regardless of the particulars of its parameterisation, but it is nevertheless useful to see how well we can recover the generalized Hernquist parameters as well.

TRACER DENSITY PROFILE

Similarly to the mass density, we elect to perform a parametric fit to the tracer density profile, whereby we adopt a functional form and then fit to it an MGE. We also adopt a generalized Hernquist profile here, but with an independent set of parameters[1]. So for the tracer density, we have,

$$\nu(r) = \nu_0 \left(\frac{r}{r_\star}\right)^{-\gamma_\star} \left[1 + \left(\frac{r}{r_\star}\right)^{\alpha_\star}\right]^{\frac{\gamma_\star - \beta_\star}{\alpha_\star}}, \tag{3.2}$$

where ν_0 is the central number density of the luminous component, $r_\star$ the scale radius, $\gamma_\star$ and $\beta_\star$ the inner and outer slope respectively and $\alpha_\star$ the transition.

Again, the simulated dataset we use in this work used a generalised Hernquist profile to generate the tracer population of luminous matter. So although the focus of this work is to recover the shape of the overall tracer profile, with this choice we will be able to investigate how well we can recover the true parameters as well.

ANISOTROPY AND ROTATION

Real stellar systems are characterised by the radial variation of their velocity anisotropy, which reflects their dynamical state and formation history (Eggen et al., 1962). Here we also assume anisotropy is not constant. To reduce the number of free parameters and impose a continuously-varying anisotropy profile, we assume Osipkov-Merritt form (OM, Merritt, 1985; Osipkov, 1979) for the anisotropy,

$$\beta = \beta_0 + (\beta_\infty - \beta_0)\,\frac{r^2}{r^2 + r_{\rm ani}^2}, \tag{3.3}$$

where β_0 and β_∞ are the values of velocity anisotropy in the centre and the outskirts respectively, and $r_{\rm ani}$ is the transition radius. This form has been widely used for dispersion-dominated systems and is typically used to describe systems with radially-biased orbits in the outskirts ($\beta_\infty \sim 1$) and isotropic central regions ($\beta_0 \sim 0$). For each Gaussian component, we compute the local velocity anisotropy $[\beta_z]_k = \beta(s_k)$, where s_k stands for the dispersion of the kth MGE component of the tracer density.

The models do allow for rotation, however, we know that these are non-rotating mock systems, and adding rotation significantly increases the computation time. So we elect here to assume that the models are not rotating. Or more correctly, we assume that the rotation profile is flat $[\kappa]_k = \kappa(s_k) = \kappa$, which is the same for each tracer Gaussian component.

3.2.1 BAYESIAN ANALYSIS

Now that we have described the models, we can move on and fit them to the datasets. We follow the basic approach outlined in Sect. 2.5.1 and here we offer more details on the aspects particular to this chapter.

[1]In general (and in our mocks) the tracer and mass distributions can be very different in dwarf galaxies, so it is important to fit their parameters independently.

Table 3.1: Limits of the uniform priors and initial guesses for the free parameters in the models. The † denotes the parameters specific for the cored model and * for the cuspy.

parameter	lower limit	upper limit	initial guess
$\gamma_{\rm DM}$	-0.1	2	$0^\dagger/1^\star$
$\log_{10}\rho_{\rm DM,0}$	0	1	$-0.4^\dagger/-1.19^\star$
$\log_{10} r_{\rm DM}$	0	3	1
$\alpha_{\rm DM}$	0	2	1
$\beta_{\rm DM}$	2.5	3.5	3
β'_0	-1	1	0
β'_∞	-1	1	0

Free parameters

In principle, we have 14 free parameters: five for the mass profile, five for the tracer profile, three for the anisotropy, and one for the rotation. However, for real stellar systems, we can typically measure the surface brightness profiles very well and when the stars are used as kinematic tracers the surface brightness profile is a proxy for the tracer number density needed for JAM. So we choose to fix the tracer parameters in Eq. 3.2, which reduces the number of parameters by five. By assuming the stellar system is not rotating ($\kappa = 0$) we further reduce the number of free parameters by one.

Although we do not fit for rotation, we do fit for anisotropy. Mass and anisotropy are tightly linked. Real systems have been shown to deviate from isotropy, and incorrect measurements of velocity anisotropy can lead to biased inferences about the cored or cusped nature of the mass profile (e.g. Binney and Tremaine, 2008; Read et al., 2021). So even though we are investigating isotropic models, we do fit the anisotropy to ensure that the models can recover the isotropy (and mass) correctly when both profiles are left free. However, we further assume that the anisotropy profile follows the tracer distribution and set the anisotropy radius $r_{\rm ani} = r_\star$, where $r_\star$ is the scale radius of the tracer distribution from Eq. 3.2, reducing the number of free parameters by one.

For the practicalities of fitting, we apply mathematical transformations that improve the convergence of the MCMC chains to some of the free parameters. We sample the $\rho_0^{\rm DM}$ and $r_{\rm DM}$ in log space; this allows them to efficiently span many orders of magnitude, and also ensures that both values are always positive. The anisotropy parameters β_0 and β_∞ are defined from 1 to $-\infty$. To symmetrise the sampling of these parameters, and to make their range finite, we instead reparameterize them following Read et al. (2006) so that

$$\beta' = \frac{\beta}{2-\beta}, \tag{3.4}$$

where now β' is defined between 1 and -1.

So we are left with **7 free parameters**: 5 corresponding to the DM profile ($\log\rho_{\rm DM,0}$, $\log r_{\rm DM}$, $\alpha_{\rm DM}$ and $\beta_{\rm DM}$, $\gamma_{\rm DM}$) and 2 to characterize the velocity distribution (β'_0 and β'_∞).

Priors

All the priors are set to be uniform, returning 0 within the prior limits and $-\infty$ otherwise. The cored and cusped models have the same priors. They were chosen such that the true values, known from the simulated dataset, were roughly in the centre of the prior limits, but still provide enough freedom for the walkers to explore the parameters space and find the maximum likelihood region. The priors and initial guesses for the parameters are summarised in Table 3.1 with the second and third columns including the limits.

We explored different ranges in priors as well as different initial positions and found they have negligible impact on our results.

LIKELIHOOD

The one-dimensional projected velocity distribution can be well approximated by a Gaussian function as introduced in Sect. 2.5 and we assume that the uncertainties are uncorrelated. At the position of each discrete tracer n, the Gaussian velocity distribution informs the likelihood of the measured velocity - $(v_{i,n}, \epsilon_{i,n})$, for the ith velocity component, given the free parameters - Θ as shown in Eq. 2.21.

POSTERIOR

In this work, we combine the priors and the likelihood as given in Eq. 2.24. Owing to the independent samples of PM and LOS velocities we compute the posterior separately for LOS velocities and both PM components before combining them into a joint posterior. As outlined in Sect. 2.5.1 we use EMCEE to find and explore the best-fitting region of parameter space. From the resulting samples, we estimate the best parameters and their confidence intervals. We use 100 walkers and we adjust the number of steps (~ 2000) such that the parameters converge. We inspect the evolution of the walkers to determine the convergence.

3.3 MOCK OBSERVATIONS

In this section, we will introduce the mock datasets used in this work. The mock datasets were constructed from simulated samples from the *Gaia* Challenge[2]. In the discussion that follows we will adopt the terms: **simulated dataset or simulations** when referring to the literature dataset and **mock observations or datasets** when referring to datasets generated in our work from them.

The methodology for obtaining the velocity measurements along the line-of-sight and in the plane of the sky (PM components) are very different. With the former requiring spectroscopic observations and the latter photometry over a long temporal baseline. That is why an observed sample with measured LOS velocities and PM can have a low number of overlapping sources for a given stellar system and therefore, the assumption on uncorrelated velocities is reasonable.

We first introduce the simulations, then explain how we computed the tracer density, and lastly, describe how the simulated data was down-sampled to generate mock kinematics, and how observationally-motivated errors were incorporated.

3.3.1 SIMULATED DATASET: *Gaia* CHALLENGE

The simulated datasets were sampled from distribution functions constructed for different tracer densities, gravitational potentials and velocity anisotropies aimed at generating realistic dSph galaxies (as described in Read et al., 2021). Here we will briefly summarize the properties of the simulated datasets used in this work.

The full simulation suite spans a wide range dSph properties and is more comprehensive than we need for this work.

We use a subset of the full simulation suite that best mimic real dwarf spheroidal galaxies. The parameters of the two models are summarized in Table 3.2.

The simulated datasets are provided in different sample sizes and we use the largest with 10^4 tracers with and without measurement errors. For the greatest flexibility and reproducibility, we use only the largest dataset to generate the mock observations.

3.3.2 TRACER DENSITY PROFILE

As described in Sect. 2.3, we require the tracer density profile in the form of an MGE. Dwarf spheroidal galaxies have been extensively studied since their discovery and the distribution of the stellar component is often well understood (e.g., Moskowitz and Walker, 2020).

[2] http://astrowiki.ph.surrey.ac.uk/dokuwiki/doku.php?id=tests:sphtri:spherical

Table 3.2: Parameters of the two models used in this work for tracer density profile and DM profile.

	core	cusp
$\gamma_{\rm DM}$	0	1
$\rho_{\rm DM,0}$ [M/pc^3]	0.400	0.064
r_* [kpc]	1.0	0.25

To mimic the observations we can expect the sample of photometric candidates of Galactic dwarfs to be much larger both in the photometric depth and spatial extent than the spectroscopic. Hence we treat the tracer density profile separately from the kinematic dataset. We assume the tracer density profile is known from literature studies and use the exact functional form from the simulations of the tracer density to decompose it in the series of Gaussians.

3.3.3 Kinematic Catalogues

To provide guidelines for observers, we focus on three properties of kinematic datasets:
- the number of the kinematic tracers,
- their spatial distribution,
- the precision of the velocity measurements.

We will consider these properties for LOS velocities and PM datasets separately. We create 3 different subsets of mocks that consider each these key properties. The overall properties of the mock catalogues are given in Table 3.3.

Briefly, the A datasets investigate the effect of including PMs, and the effect of PM uncertainty size. All have LOSVs typical of current catalogues in terms of sample size, spatial coverage, and uncertainty. A3 has no PMs, A2 has PMs with uncertainties typical of current catalogues (and is the closest to a realistic present-day mock), and A1 has smaller PM uncertainties.

The B datasets investigate the effect of increasing the precision and sample size of the LOSVs. B1 is similar to A2 but with smaller LOSV uncertainties. B2 is similar to A2 but with a 3$\times$ larger sample of LOSV.

The C datasets investigate the LOSV sample size and uncertainty for stars near the centres of the dSphs that will be most sensitive to the inner profile shape, and the uncertainties of stars in the outermost parts of the dSph that will constrain the outer shape. C1 has no LOSV for stars near the centre and small LOSV uncertainties for the outer stars. C2 is the same as C1 but with LOSVs for stars at the centre. C3 is the same as C2 but with larger LOSV uncertainties in the outer regions.

Now we describe in detail how we generate each mock dataset.

Mock radial velocities

When making the LOS sample we defined three radial regions motivated by potential observational limitations: $R/R_c \leqslant 0.2$ - *inner*, $2.5 < R/R_c \leqslant 8$ - *intermediate* and $2.5 < R/R_c \leqslant 8$ - *outer*. The choice to define these three regions was motivated by the fact that central regions tend to be affected by crowding and intrinsically sparse outer regions require many telescope pointings with few targets. These arguments also motivated the choice of the velocity uncertainties assigned to the mock velocities.

We defined the different radial ranges in multiples of the core radius R_c because it is one of the quantities that can be robustly measured from the light profile. The core radius is defined as $\Sigma(R_c) = \Sigma_0/2$[3] and, in our approach, it is computed from the MGE of the tracer density profile. We randomly sampled a fixed number of stars from the simulated dataset and projected the positions edge-on at a typical distance of Galactic dwarf galaxies of 100 kpc. The number of expected targets was informed by the existing radial velocity datasets (e.g. Walker et al., 2009). The radial ranges and number of tracers in each range are shown in Table 3.3.

[3] Σ stands for projected surface density of the tracers.

3

Table 3.3: Details of the mock datasets generated in this work. Column 1 shows the name of the mock dataset with datasets **A** targeted at the effects of the PMs. Datasets **B** compare increased precision in LOSVs (B1) and an increase in the sample size of LOSVs (B2). Datasets **C** explore the effect of varying the mean velocity uncertainty in different radial ranges of the LOSV samples. The med(ϵ_i) in Column 5 is in units km s^{-1} for the LOS samples and mas yr^{-1} for PM samples. The velocity dispersion of this mock stellar system is ~ 25 km s^{-1}.

Mock (1)	i (2)	Region (3)	# tracers (4)	med(ϵ_i) (5)
A1	LOS	inner	20	3.5
	LOS	intermediate	1100	2.6
	LOS	outer	250	2.4
	PM	$R/R_c \leqslant 8$	100	0.01
A2	LOS	inner	20	2.0
	LOS	intermediate	1100	2.6
	LOS	outer	250	2.7
	PM	$R/R_c \leqslant 8$	100	0.35
A3	LOS	inner	20	3.5
	LOS	intermediate	1100	2.6
	LOS	outer	250	2.4
	PM	–	–	–
B1	LOS	inner	20	1.2
	LOS	intermediate	1100	1.7
	LOS	outer	250	1.8
	PM	$R/R_c \leqslant 8$	100	0.37
B2	LOS	inner	60	2.4
	LOS	intermediate	3300	2.7
	LOS	outer	750	2.6
	PM	$R/R_c \leqslant 8$	100	0.48
C1	LOS	inner	0	–
	LOS	intermediate	2200	1.2
	LOS	outer	60	1.1
	PM	$R/R_c \leqslant 8$	100	0.02
C2	LOS	inner	30	3.9
	LOS	intermediate	2200	1.2
	LOS	outer	60	1.2
	PM	$R/R_c \leqslant 8$	100	0.02
C3	LOS	inner	30	3.4
	LOS	intermediate	2200	1.2
	LOS	outer	60	4.6
	PM	$R/R_c \leqslant 8$	100	0.02

MOCK PROPER MOTIONS

The *Gaia*[4] mission has provided the largest sample of stars with precise positions and PM for stars brighter than $G \sim 21$ mag. Along with the census of the Galactic stars, it has also provided positions and velocities for the brightest stars in the nearby dwarfs. The survey nature of the mission means the spatial coverage of the PM catalogue will most likely not be matched in the foreseeable future. Recent data releases (Gaia Collaboration et al., 2018, 2021) have already demonstrated that the measurements can be used to study the internal kinematics of dwarf galaxies (e.g. Massari et al., 2020a). End-of-mission measurements will further reduce uncertainties and increase the sample size.

At a distance of 100 kpc the apparent magnitude range in the *Gaia* G-band for stars from the horizontal branch (HB) up to the tip of the red giant branch (RGB) spans $20 \gtrsim G \gtrsim 16$, meaning that the brightest stars in these old stellar systems are within the detection limits, with the survey completeness dropping sharply below 21 magnitude. Another consideration can be done on the spatial extent: while spectroscopic observations tend to be targeted and hence warrant the split in different radial ranges as mentioned in the chapter above, *Gaia* is an all-sky survey and we assume a small number of brightest stars will be observed over the whole body of the galaxy. The

[4] https://www.cosmos.esa.int/gaia

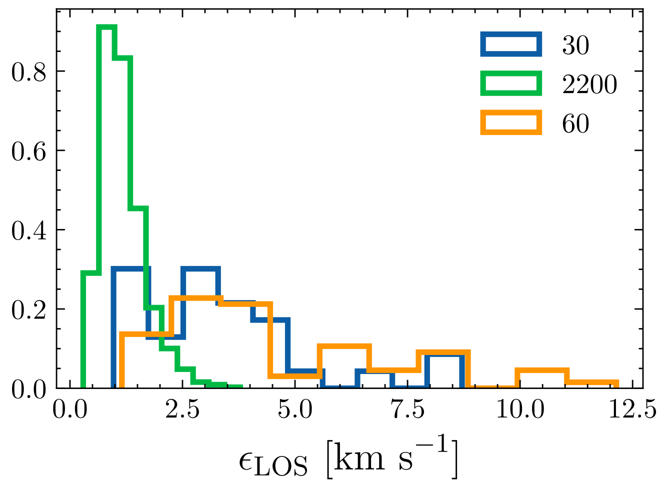

Figure 3.1: An example of the error distribution for the LOS tracers of sample C3 from Table 3.3. The blue histogram corresponds to the inner region with 30 tracers, the orange one to the outer region with 60 tracers, and the green one to the intermediate region, where the largest amount of tracers are located.

spectroscopic and proper-motion observations are independent and hence we draw at random 100 stars from the simulated dataset.

Simulating observational velocity uncertainties

Once we have created a sample of LOSVs and PMs, we proceed to add observationally-informed uncertainties. The error distribution of observed LOS velocity measurements follows a log-normal distribution (e.g. Walker et al., 2009), which is parameterised by a mean and dispersion. We use this to simulate the observational uncertainties. To guide our adopted values for the moments of the distribution, we use the observations of LOSVs of stars in Milky Way dwarfs from Walker et al. (2009) with a median uncertainty of 2.1 km s^{-1} and for PMs of RGB stars at a distance of 100 kpc we use projected end-of-mission uncertainties for the *Gaia* mission.

To simulate real observations, we first generate a distribution of uncertainties with a log-normal distribution and randomly assign them to each mock tracer. A new velocity is then sampled by randomly drawing a velocity from a Gaussian distribution centered at the velocity given by the simulation and with a specific dispersion, that represents the measurement uncertainty.

To investigate the effect of velocity error on the recovery of the DM density profile, we scale the mean LOSV uncertainty in individual ranges as shown in Col. 5 of Table 3.3. The fiducial mean LOSV uncertainty of ~ 2.1 km s^{-1} is taken from Walker et al. (2009). To simulate a more or a less precise dataset we multiply the mean uncertainty by a factor of 0.5 and 2 respectively. An example of the mock uncertainty distribution for the LOSV sample is shown in Fig. 3.1 for a cored mock, where each colour corresponds to the error distribution in different radial ranges for the C3 dataset.

For the PM sample, we use the *pygaia*[5]. The PM measurements depend on the magnitude and colour of the stars and Galactic latitude. To simulate the uncertainties we use the magnitude range of the RGB above the horizontal branch at the distance of 100 kpc, colour $\min(V-I) > -0.2$ and Galactic latitude of $b = 45^\circ$ (similar to Sculptor dSph). The *pygaia* package computes the uncertainties of the instrument for different planned data releases. We use end-of-mission projections for the most precise PM measurements. At the distance of 100 kpc, the typical velocity dispersion of the dSph ($\sim$20 km s^{-1}) results in the PM $\mu \sim 0.042$ mas yr^{-1}. The typically end-of-mission uncertainties are 5 times larger than the expected velocity dispersion of a dSph like

[5] https://github.com/agabrown/PyGaia

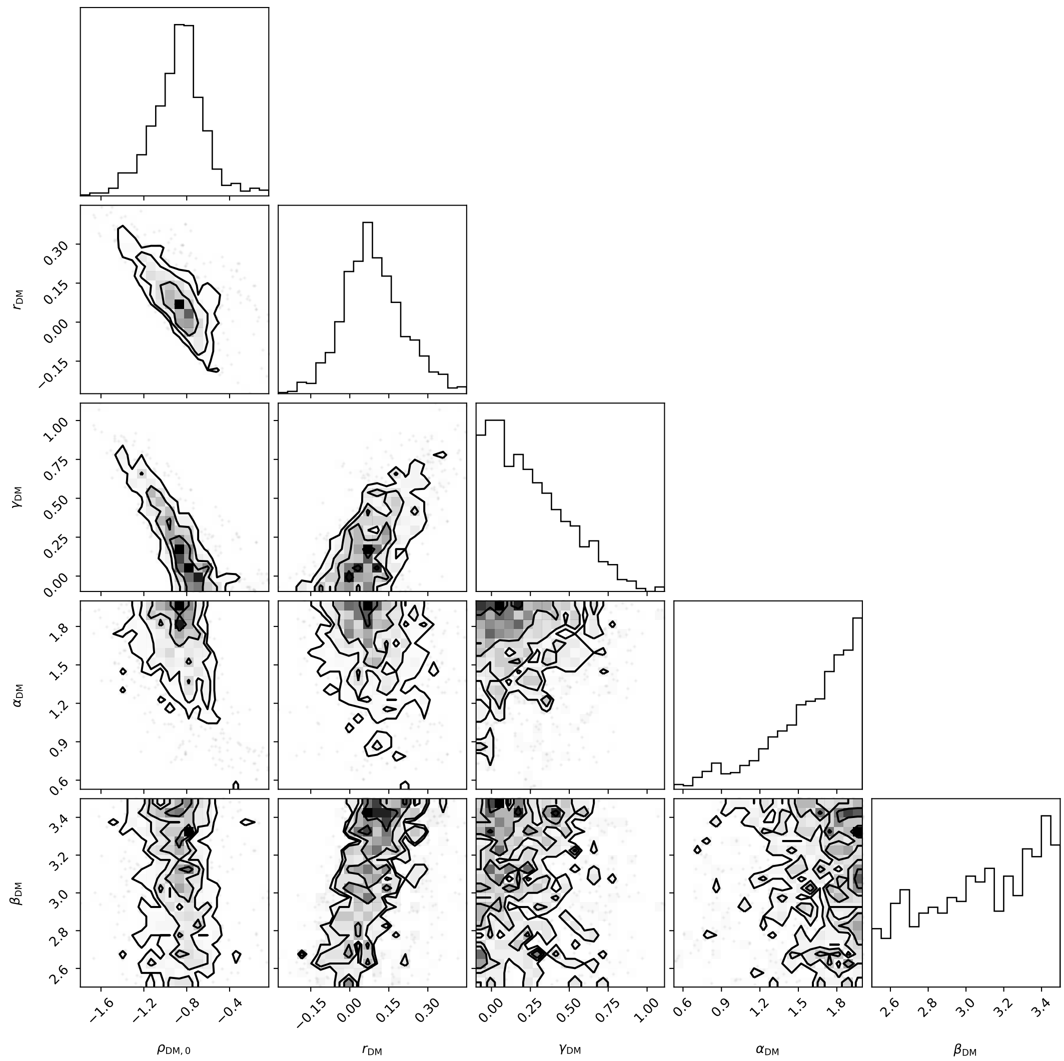

Figure 3.2: The post burn-in posterior from the dataset **C3** for the parameters of the DM density profile.

Sculptor (Tolstoy et al., 2009, and reference therein), that is why we reduce the PM uncertainties in models **A1** and **C**.

3.4 Results

Now we have described the details of the model fitting and the suite of mock catalogues, we can proceed to fit the models to the catalogues. We run model fits independently for each of the mock catalogues in Table 3.3, analyze the quality of each fit, and then compare the relative performance of all the fits.

3.4.1 Posteriors

First, let us look at a typical posterior distribution for a model fit – we choose the fit to the C3 catalogue as our example. Fig. 3.2 shows the 5 parameters of the DM density profile from Eq. 3.1. Fig. 3.3 shows the two parameters that describe the velocity anisotropy profile.

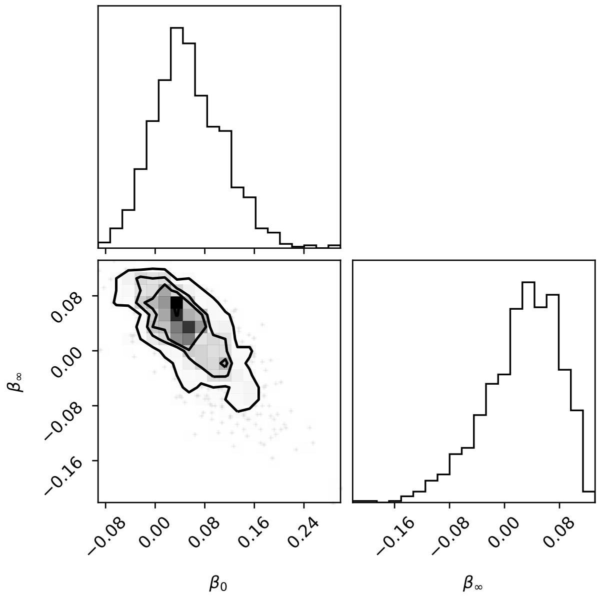

Figure 3.3: The post burn-in posterior from the dataset **C3** for the parameters of the inner (β'_0) and outer(β'_∞) velocity anisotropy.

The central density and scale radius are constrained, with clear degeneracy in the two parameters. The inner $\gamma_{\rm DM}$ and outer slopes $\beta_{\rm DM}$ as well as the transition $\alpha_{\rm DM}$ do not show a clear peak and reach the prior limit. Only $\gamma_{\rm DM}$ shows anti-correlation with $\rho_{\rm DM,0}$ and correlates with $r_{\rm DM}$, other two parameters show negligible correlation with the scale density and radius.

Both parameters of the velocity anisotropy are well constrained as seen in Fig. 3.3 and are consistent with isotropy.

3.4.2 Recovered dark matter profile

Our primary goal is to see how well we can recover the underlying DM potential of each mock dSph, which we do by fitting an analytic function. In Sect. 3.2, we intentionally chose this function to have the same form as the function used to generate the mocks so we can compare the fitted parameters with the generating parameters. However, the generating parameters do not uniquely define the profile shape. So while it can be instructive to see how well we can recover the input parameters, investigating how well we can recover the DM potential is our focus here.

We chose to show the resulting best-fit profile constrained by the **C3** dataset. We draw 100 random samples from the posterior of dataset **C3** and evaluate the DM density profile for each parameter set. We show the resulting profiles in the left panel of Fig 3.4. The black line shows the true profile with grey-shaded regions showing the 16th and 84th percentile. The true profile used to make the simulated dataset is shown in red. The right panel of Fig. 3.4 shows the distribution of the tracers in the position-velocity diagram with the dispersion profile from the best-fit parameters shown in red. The blue points show the LOSV dataset and the binned velocity dispersion is shown in black to guide the reader. We use these to compare how close the resulting profile is to the true profile shown with the solid black line. The model can reproduce the dataset very well at all radii.

3.4.3 Inner and outer slope of the dark matter profile

For an individual mock catalogue, we can investigate the fit of the whole DM profile. To compare the fits for different mocks, it is useful to consider specific quantities rather than a whole profile.

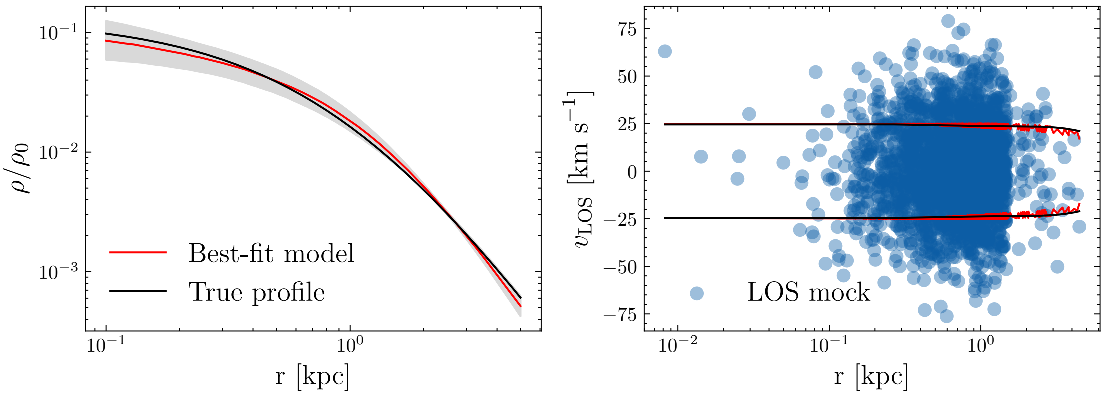

Figure 3.4: The left panel shows the comparison between the true profile in black and the recovered profile shown in red the grey shaded regions highlight the 1σ uncertainty intervals. The right panel shows the distribution of the positions and LOS velocities for the mock dataset **C3**. The dispersion profile computed from the data is shown in black and the resulting best-fit model in red.

To that end, for the 1000 samples drawn from each posterior, we compute the local slope of the DM density $d\ln\rho_{\rm DM}/d\ln r$ at the locations of the innermost ($r_{\rm min}$) and outermost ($r_{\rm max}$) kinematic tracers. The results for the different datasets are shown in Fig. 3.5. The left column shows the distributions of $r_{\rm min}$ slopes and the right column shows the distributions of $r_{\rm max}$ slopes. The true slopes are shown as vertical black dashed lines in each panel.

The top row shows the **A** datasets, which explore the effect of using PMs and the uncertainty on the PMs. The A3 model (orange) has LOSVs only. We see that this is unable to recover the central cored shape of the profile as the range of central slopes is very broad. The A2 model (green) has PMs included, with typical uncertainties from present datasets. This distribution is very similar to the A3 distribution, showing that A2 also cannot recover the core, and that the PMs have made little difference to this fit. The A1 model (blue) has PMs with better-than-present-day uncertainties. We see that this model has successfully recovered the central cored shape. All 3 models are able to recover the outer shape equally well.

The middle panels compare the effect of sample size and precision of LOSV sample in datasets **B** and can be most closely compared with dataset **A2** in the panels above. The reduced uncertainties of dataset **B1** (red) wrt with dataset **A2** (green, above) do not improve the fit in a meaningful way. The posterior of the outer slope is not affected, while the mean inner slope from dataset **B1** is slightly shallower (more consistent with a cored) compared with the **A2**. The increase in the sample size of dataset **B2** (purple) wrt with dataset **A2** (green, above), similarly does not improve the fit.

The bottom panels show datasets **C** that explore the radial variation of the precision in the LOS samples. Dataset **C1** (dark grey) has no LOSV in the inner region. It has a $2\times$ larger LOSV sample compared with datasets **A** and the same precision in PMs as dataset **A1**. The resulting posteriors show negligible difference wrt to the datasets **A2** and **A3**. Particularly the absence of central LOSVs worsens the fit of the inner slope wrt to the dataset **A1**. Dataset **C2** (light grey) introduces the central LOSVs with the mean uncertainty $2\times$ the fiducial value from Walker et al. (2009). This results in improved recovery of the inner slope, however, the mean recovered slope is still too steep. Dataset **C3** (light blue) has the same LOSV sample in the inner and intermediate region as dataset **C2**, but increased LOSV uncertainties in the outer regions by a factor of 2. The inner and outer slope constrained by this dataset can best recover the true inner and outer slope of the dark matter density distribution.

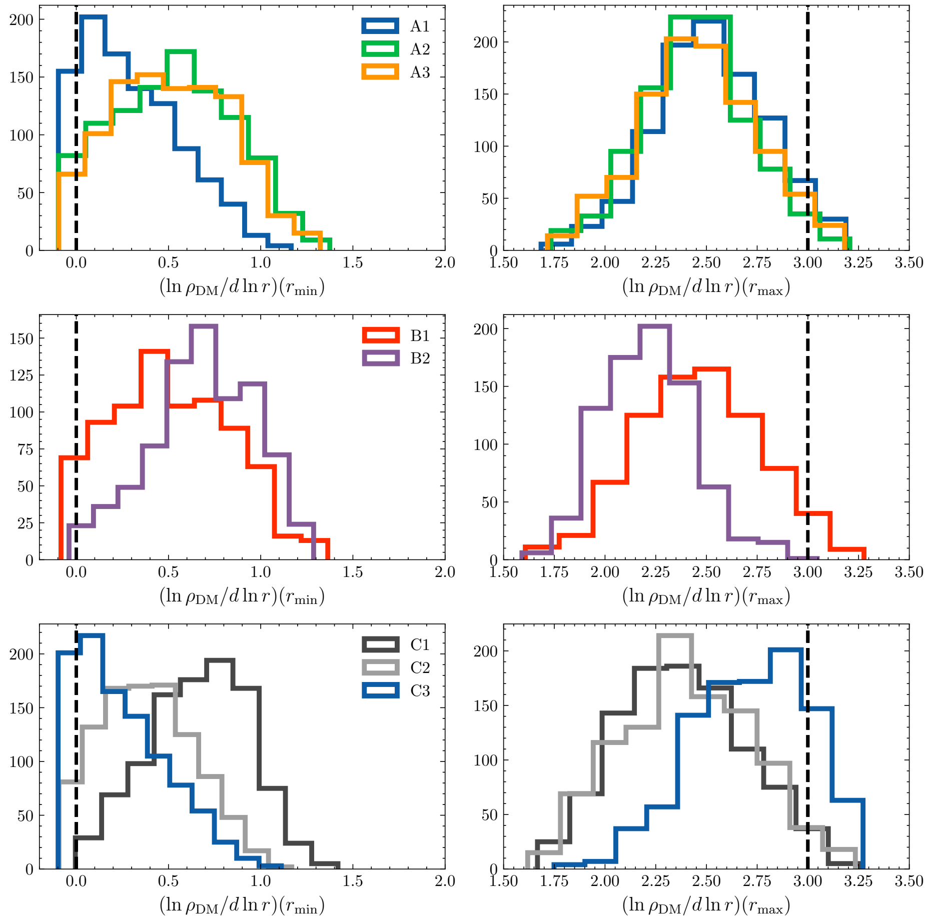

Figure 3.5: The distribution of the local logarithmic slope at the location of the inner and outermost kinematic tracer is shown in the left and right columns, respectively. The top 2 panels correspond to datasets **A** in Table 3.3, the middle panels to datasets **B** and the bottom to datasets **C**. The vertical black dashed lines show the location of the inner slope γ_{DM} in the left column and of the outer slope β_{DM} in the right column.

3.5 Conclusions

Current datasets of LOSVs of nearby dwarfs contain $\sim$1000 measured velocities with a median precision of $\sim$2.1 km s^{-1}. However, the dynamical modelling based on such datasets cannot discriminate between a cored or cuspy DM profile. Here we constructed 8 mock datasets (Table 3.3) of LOSV and PM to address the question of what datasets are needed to discriminate between cored and cuspy profiles. Specifically, we varied the number of LOSVs and their precision. Additionally, we investigated the importance of PMs and their precision in recovering the inner and outer slope of the DM potential.

We find that precise proper motions are needed to constrain the inner slope as seen in dataset **A1**. A sample of 100 measured PMs uniformly distributed across the body of the galaxy is sufficient to improve the constraints on the inner slope. Our mock datasets varied the number and precision of LOSVs in three radial regions: inner, intermediate and outer. We find that a sample size of $\sim$2000 LOSVs is needed to improve the constraints on the inner and outer slope. Uncertainties of LOSV that are not the same between the different radial regions improve the fit. Specifically, larger uncertainties (by a factor of 2 wrt to Walker et al., 2009) in radial regions that have intrinsically fewer stars (inner and outer) and smaller uncertainties (by a factor of 0.5 wrt to Walker et al., 2009) in the region where most of the stars are observed results in the best fit.

These results suggest that with an increase of a factor 2 in the sample of LOSVs, a factor 10 improvement in PM uncertainties and factor 2 improvement in LOSV uncertainties, we predict we will be able to determine whether dSph halos have cusps or cores. The next step is to run these tests on cuspy models and verify that this conclusion holds.

Chapter 4

Impact of the kinematic dataset on recovered gravitational potential - NGC 1380

"You're unlikely to discover something new without a lot of practice on old stuff, but further, you should get a heck of a lot of fun out of working out funny relations and interesting things."

\- Richard P. Feynman

4.1 Introduction

The goal of this work was to take advantage of the novel precise LOSV measurements of GCs in the Fornax cluster galaxies and map their mass distribution. We focused on the NGC 1380 (FCC 167) galaxy, an S0 galaxy in the Fornax cluster that experienced the last major mergers 10 Gyrs ago (Zhu et al., 2022). This suggests that the population of halo tracers is reasonably relaxed and therefore suitable for dynamical modelling. It is at a distance of 21.2 ± 0.7 Mpc (distance modulus $=31.632 \pm 0.075$) (Blakeslee et al., 2009), has a stellar mass of 9.85×10^{11} $M_{\odot}$ ($M_{\star}/L_i = 1.1$), $R_{\rm e}= 60$ arcsec (6.17 kpc) in the i photometric band and ellipticity of 0.49 at 1 $R_{\rm e}$ (Iodice et al., 2019a). The central dust ring in the inner 0.1 arcmin enables geometric determination of the inclination angle, and Viaene et al. (2019) determined it to be $77^{\circ} \pm 18^{\circ}$. The galaxy is at 0.21 Mpc from the cluster centre (Iodice et al., 2019b) and doesn't have many nearby neighbours. This makes it easier to assign membership probabilities to GCs based on their position and kinematics. The virial mass is estimated to be $M_{200} = 6.4 \times 10^{12}$ $M_{\odot}$ (Sarzi et al., 2018) this galaxy is expected to host 555 GCs (Kissler-Patig, 1997).

Within the Fornax 3D survey (Sarzi et al., 2018) 33 galaxies (23 ETGs) were observed with MUSE IFU instrument down to $\mu_B \geqslant 25$ mag arcsec^{-2} and with a mean spectral resolution of 2.5Å. Fahrion et al. (2020) measured LOSV of 722 GCs in 32 galaxies; due to the observational footprint of the survey, most of the GCs are at $R < 3$ $R_{\rm e}$ from their host galaxy, with a typical velocity uncertainty of $\langle \epsilon_{\rm rv} \rangle < 20$ km s^{-1} (up to > 50 km s^{-1} for faint GCs with low S/N). In this work, we complimented this precise and centrally concentrated sample of GCs with a less precise literature dataset from Puzia et al. (2004) that covered a larger area. Additional kinematic information from the PNe tracing the stellar kinematics were taken from Spriggs et al. (2020). An overview of the datasets used is presented in Sect. 4.2.

4.2 Data

To construct a tracer density profile we followed the methodology outlined in Sect. 2.3, and we used the photometric catalogue of candidate GCs from ACS[1] Fornax cluster survey (Jordán et al., 2007a). The LOSV measurements came from three literature studies of GCs and PNe (Fahrion et al., 2020; Puzia et al., 2004; Spriggs et al., 2020). This heterogeneous kinematic dataset is especially adequate to constrain the gravitational potential both in the inner and outer regions of the galaxy. The kinematics were corrected for the systemic velocity of the galaxy $v_{\rm sys} = 1878 \pm 2$ km s^{-1} (Iodice et al., 2019b).

4.2.1 Photometric dataset

Owing to the proximity of the Fornax cluster, the brightest GCs are spatially resolved with space-based HST[2] observations. This enables us to better remove foreground and background contamination to get a high-fidelity sample of GCs. Jordán et al. (2015) compiled a sample of 558 GC candidates within 150 arcsec (i.e., within around ~ 2 $R_{\rm e}$). This dataset is the largest and deepest sample of GCs around this galaxy. Together with positions (α, δ), magnitudes (F475W $\approx$ *Sloan* g and F850LP $\approx$ *Sloan* z) and half-light radii from a fitted King profile, the catalogue also provides a probability of a source to be a bona fide GC. The survey extends more than 2 mag below the TOM and 368 GC candidates have membership probability $p_{\rm GC} > 0.8$. In what follows we used these highest probability members.

The colour distribution of the GCs in NGC 1380 shows clear bimodality, but it is dominated by red GCs, with less than 1/3 having $(g - z) < 1.15$. This is consistent with the findings by Zhu et al. (2022), suggesting very quiescent past $\sim$10 Gyrs, with few mergers. Fahrion et al. (2020) find consistent rotation in both blue and red GCs, but systematically higher velocity dispersion in the red compared with the blue GCs.

[1] Advance Camera for Surveys.
[2] Hubble Space Telescope.

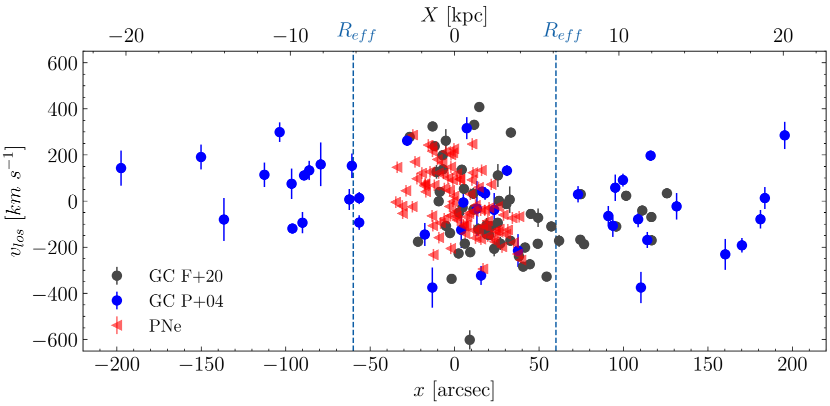

Figure 4.1: Distribution of the velocities with corresponding uncertainties and position along the major axis of the galaxy. The three kinematic datasets used in this work are shown here: GCs with velocities from Fahrion et al. (2020) are indicated with black circles, less precise (and more spatially extended) measurements coming from Puzia et al. (2004) with blue circles, and PNe with red triangles Spriggs et al. (2020). The light blue dashed lines show the stellar R_e of the galaxy.

Table 4.1: Overview of the kinematic datasets used in this work.

Source	Tracer	$N_{\rm tracers}$	$\langle\epsilon\rangle$ [km s^{-1}]	$R_{\rm min}$ [R_e]	$R_{\rm max}$ [R_e]
Fahrion et al. (2020)	GC	59	10	0.13	2.4
Puzia et al. (2004)	GC	43	47	0.24	3.8
Spriggs et al. (2020)	PNe	91	25	0.08	0.77

Column 1 shows the source of the dataset, Col. 2 indicates the type of tracers included in the sample (GCs or PNe), Cols. 3 and 4 show the number of kinematic tracers and the median LOSV uncertainty. The last two columns show the minimum and maximum extent of the tracers.

4.2.2 Kinematic datasets

The summary of the kinematic datasets is presented in Table 4.1 and the positions and velocities of all tracers are shown in Figure 4.1, where GCs are indicated with circles and PNe with triangles. The positions along the semi-major axis, corrected for the PA of the stellar component, are shown on the x-axis and the LOSVs corrected for the systemic velocity of the galaxy are shown on the y-axis. The dataset from Fahrion et al. (2020), shown with black points, is not symmetric with respect to the centre of the galaxy (as also seen in Fig. 3 of Sarzi et al., 2018) and extends up to $\sim 2\ R_e$ on the North side of the galaxy. The GCs measured by (Puzia et al., 2004), indicated with blue circles in Figure 4.1, are evenly distributed on both sides of the galaxy. Both samples show the presence of rotation, which has also been analysed and reported in Fahrion et al. (2020). The rotation signature is also evident in the PNe (Spriggs et al., 2020), which are mainly located in the very inner regions of the galaxy. For the GCs, we combined the samples from Fahrion et al. (2020) and Puzia et al. (2004) and for overlapping GCs, we used the LOSV measurement from the former, with smaller uncertainty.

4.3 Dynamical modelling

We adopted a similar modelling approach as outlined in Sect. 2.2, 2.5 and 2.3 and explored the impact of different kinematic samples and gravitational potentials on the models.

4.3.1 Anisotropic Jeans modelling

To characterise both the stellar contribution to the gravitational potential and the tracer density of the PNe we used the stellar surface brightness MGE obtained from the F3D (Fornax 3 D) survey (Ding et al., 2023). To find the best-fit parameters we employed a similar methodology as explained in Sect. 2.5. We used CJAM with 100 walkers and 2000 steps. This choice was a compromise between the computational run-time and convergence of the MCMC sampling.

4.3.2 Modelling set-up

We explored different modelling set-ups in terms of datasets used (GCs vs PNe) and the gravitational potential (without DM, NFW, Eq. 1.1.2 and Einasto profiles Eq. 1.6). Owing to the increased precision of the measurements we adopted the LOSV measurements from Fahrion et al. (2020) as the fiducial sample and additionally explored how the recovered best-fit values change when the Puzia et al. (2004) and Spriggs et al. (2020) datasets are added. This enabled us to study the impact of precision and spatial extent on the recovery of different parameters. As the PNe dataset has only a characteristic uncertainty of 25 km s^{-1} reported, we use this value but also explored the impact varying the uncertainty by a factor 2 and 3 has on the results. To investigate how well the gravitational potential can be constrained we explored models **without DM** but with constant or varying $M_\star/L$ and models **with DM** focusing on Einasto and NFW profiles to investigate which parameters can be constrained.

To describe the gravitational potential of dark matter we use a more general form of the NFW profile:

$$\rho(r) = \frac{\rho_s}{(r/r_s)^\gamma \, (1 + (r/r_s)^\eta)^{(3-\gamma)/\eta}} \,, \tag{4.1}$$

where ρ_s and r_s are the scale density and radius and η and γ the inner and outer slope, respectively. The classical NFW cusped profile can be recovered with $\eta = \gamma = 1$. To reduce the number of free parameters we additionally used the literature relation between the halo mass and its concentration (see Sect. 1.1.3). We use the literature relation from Dutton and Macciò (2014) to compute the value of c_{200} (see their Eq. 8) for the results from *Planck* cosmology.

We explored the following modelling set-ups:

1. **Gravitational potential:** How well can different parameters of the gravitational potential be recovered?
   - 1.1 Constant $M_\star/L$ and no DM
   - 1.2 Radially varying $M_\star/L$[3]
   - 1.3 Impact of including a central black hole $M_{\rm BH} = 1.47 \times 10^8$ M$_\odot$ (Kabasares et al., 2022)
   - 1.3 Constant $M_\star/L$ and DM parametrised with NFW for both Eq. 4.3.2 and classical NFW parametrised only by M_{200}
   - 1.4 Constant $M_\star/L$ and Einasto DM profile
2. **Effect of different datasets:** What impact do different datasets have on the recovered parameters?
   - 2.1 GCs from Fahrion et al. (2020)
   - 2.2 GCs from Puzia et al. (2004)
   - 2.3 GCs from Fahrion et al. (2020) and PNe from Spriggs et al. (2020)

4.4 Tracer density profile

This work was the basis on which we established a 2 step approach to identify the sample of GCs that are least affected by survey incompleteness and observational footprint as introduced in Sect. 2.3. Here, we did not use theoretical GCLF, as the incompleteness of the survey was extensively studied in Jordán et al. (2009) and we used their results to analyze incompleteness

[3] This is done by independently assigning a value of $M_\star/L$ to each of the surface brightness MGE components.

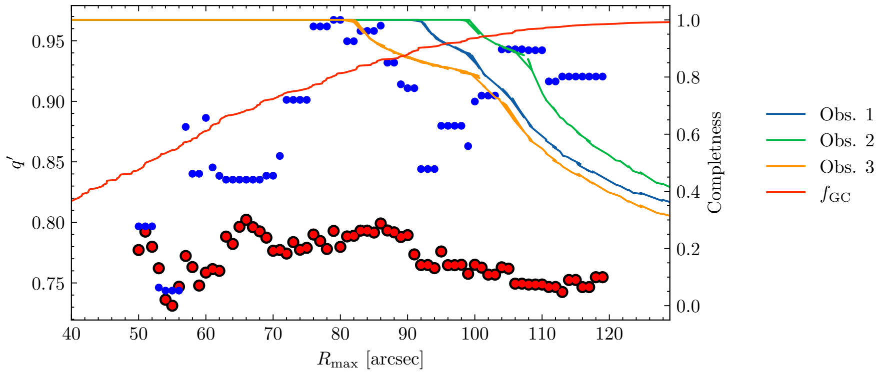

Figure 4.2: Radial variation of flattening for the whole GC population in black, red population ($(g-z) > 1.1$) in red and blue ($(g-z) \leqslant 1.1$) in blue. For all samples, only those clusters with $p_{GC} > 0.8$ are used. The red curve corresponding to the axis on the right shows the cumulative number of GCs. Light blue, orange and light green show the observational footprint for the 3 different HST pointings used in the survey.

4

based on background surface brightness - I_b, half-light radius of the fitted King profile[4] - r_h and magnitude of the cluster. Additionally, we explored different fitting functions for the binned tracer density profile that we will present here.

4.4.1 Incompleteness of the photometric data

There are two sources of incompleteness in the ACSFCS[5] dataset. Firstly, there is an **observational footprint** corresponding to the 202 arcsec $\times$ 202 arcsec field-of-view of the WFC[6] on the Hubble Space Telescope. In order to understand how important spatial incompleteness is we used the location of image vertices as provided in the HST Legacy archive. We create concentric annular bins, centred on NGC 1380, and determine the fraction of each annulus not observed due to the observational polygon as a function of radius - *incompleteness*. As can be seen in Fig. 4.2 with light blue, orange, and green lines this incompleteness has a significant effect on the observations $R > 90$ arcsec, where there is more than 90% of the GCs in our dataset.

Secondly, the **survey incompleteness** can be assigned to each globular cluster based on the value of I_b, r_h and mag by interpolating on the grid presented in Jordán et al. (2009). Using the following selection we maximized the number of GCs to which the value of incompleteness can be assigned as well as the spatial extent of the photometric data used to obtain the tracer density profile: $R \geqslant 6.1$ arcsec, $p_{GC} > 0.8$, $g_{\rm mag} \leqslant 25.29$ mag, 0.0128 arcsec$\leqslant r_h(g) \leqslant 0.077$ arcsec. We adopted the photometric filter g, but the results are consistent when photometry from the photometric band z is used.

After establishing a sample of GCs least affected by **survey incompleteness**, we used Eq. 2.12, Eq. 2.13, Eq. 2.14 and Eq. 2.15 to compute the radial variation of PA and q'. Starting with the minimal radius of 50 arcsec where $\sim 85\%$ of the highly probable members are located, we computed the PA and q' moving outward by 1 arcsec at each step. The results for the flattening are shown in Fig. 4.2, with blue and red points for blue and red GC populations respectively and black points for the whole sample.

This approach was repeated for all clusters, as well as the blue and red populations separately. We use $(g-z) = 1.1$ to split the blue and red population. In Fig. 4.2 we can see that there is a non-negligible amount of flattening in the red population, while the blue population shows a preference for a more spherical distribution. Such trends have consistently been found in the literature (e.g. Brodie and Strader, 2006). The radial variation of the flattening q' demonstrates

[4] In the survey the parameters of the GCs were extracted such that a King profile was fitted to sources on the HST image.
[5] Advanced Camera for Surveys Fornax Cluster Survey.
[6] Wide-field camera.

Table 4.2: Table with recovered flattening and position angle for GCs ($p_{GC} > 0.8$) in the ACSFCS survey around NGC 1380.

	q'	PA [°]	$\alpha_{1\mathrm{GCS}}$	$\alpha_{2\mathrm{GCS}}$	R_s
all	0.78 ± 0.02	172.3 ± 2.2	$0.9^{+0.1}_{-0.1}$	$5.8^{+1.3}_{-0.9}$	$84.5^{+7.4}_{-6.2}$
red	0.78 ± 0.02	172.3 ± 2.2	–	–	–
blue	0.87 ± 0.06	193 ± 21	–	–	–

the effect of the observational footprint on this parameter. The value of q' is constant in the radial ranges $65 < R < 90$ arcsec and starts to show progressively flatter distribution $R > 90$ arcsec. This coincides with the drop in the spatial completeness of observational fields 1 and 3, in blue and green respectively, which results in the distribution appearing flatter. We use such rapid changes in the q' to determine the maximal radius up to which the sample is minimally impacted by the observational footprint. Similar trends are seen in the PA determination. We use $R < 100$ arcsec to compute both orientation and shape parameters and present them in Table 4.2. Iodice et al. (2019b) measured the stellar PA (measured N-E) of $186^\circ \pm 1^\circ$ and our measurements for the GC PA are consistent as seen in Table 4.2.

In the following analysis, we do not model blue and red GCs separately, as the number of kinematic tracers would limit robust results, and instead, we adopt the values of q' obtained for the whole dataset. The latter value is very similar to that of the red population, which is not surprising, given that this is the dominant population.

4.4.2 Fitting analytic tracer density profile

To fit an analytic profile we first corrected the positions for the PA and computed the R_{ell} with the value of q' presented in Table 4.2. We modelled only the whole population of GCs because splitting them based on colour reduced the number of GCs too much for a robust number density fit. The GCs were then binned in such R_{ell} such that 15 GCs were in each bin, ensuring a sufficient number of GCs in each bin. We explored different binning strategies and found they have negligible impact on the final profiles. Following the literature reports of GCS fitting functions we used single power-law, broken power-law (Eq. 2.17) and a Sérsic function (Eq. 2.18). Using a Gaussian likelihood and uninformative priors we found best-fit parameters in a Bayesian approach and EMCEE to efficiently sample the posterior. The best-fit profiles are shown in Fig. 4.3 and the best-fit parameters for the Sérsic fit are presented in the last three columns of Table 4.2.

The single power-law fit overestimates the number of GCs in the centre, which would result in biased measurements. Both the Sérsic and the broken power-law agree reasonably well with the observed distribution, and we adopt the latter as the fiducial tracer density profile.

4.4.3 MGE decomposition

As the final step, we used the posterior of the Sérsic fitting function to compute the parameters of the MGE as explained in Sect. 2.3.

4.5 Results

4.5.1 Gravitational potential

In the model set-ups 1.1-1.4 we only use Fahrion et al. (2020) as tracers of the potential. The parameters of the DM are not constrained in any of the setups, but the orbital properties of the GCs and the $M_\star/L$ have converged. The latter did not converge in the case of 1.2 (varying $M_\star/L$), likely due to the lack of kinematic data.

Figure 4.4 shows the posterior distributions for three parameters of interest obtained from different model set-ups. The posteriors for the orbital properties are consistent among the different

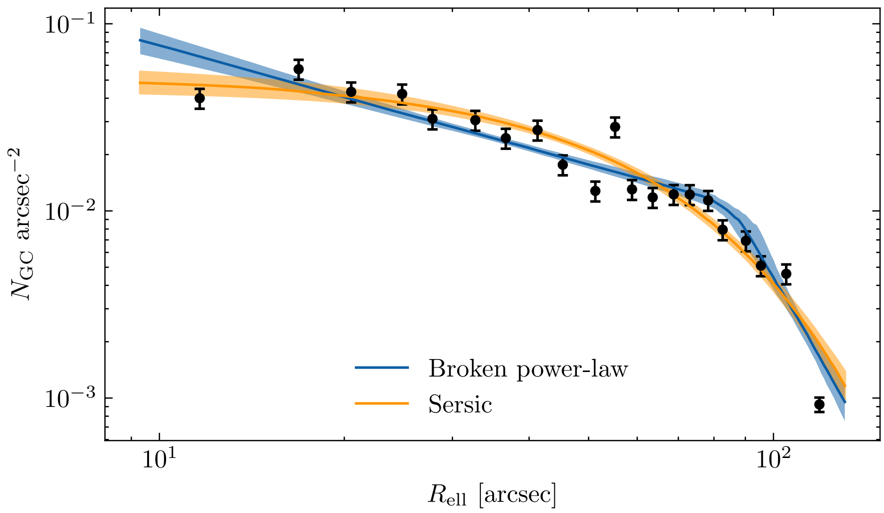

Figure 4.3: The binned profile and the two fitting functions used in this work. The black points show the binned profile with corresponding uncertainties, due to the Poisson noise. The coloured lines show the different fitting functions, the broken power-law in blue and the Sérsic in orange with associated 1σ uncertainty intervals.

set-ups, with all models showing clear signs of bimodality in β' and an asymmetric distribution in κ. The mass-to-light ratio $M_\star/L$ shows a slightly different behaviour for each of the four different model set-ups. The NFW (with ρ_s and r_s as free parameters) and Einasto profiles to represent the DM halo both favour lower values of $M_\star/L$, compared with models in which a central SMBH or the relation $M_{200} - c_{200}$ are taken into account. It is worth noting that the recovered values of $M_\star/L$ are all higher than those found by Zhu et al. (2022). The presence of the bimodality in β' is of particular interest and in what follows we explore it further.

4.5.2 Effect of the dataset

The limiting radial extent and strong observational footprint of the Fahrion et al. (2020) catalogue motivated us to study the effect of different kinematic datasets. The posteriors in the model set-up with DM parameterised with NFW and $M_{200} - c_{200}$, constant $M_\star/L$ and orbital properties for the three different kinematic tracers are shown in Figure 4.5. We show here models 2.1 in grey, 2.2 in blue and 2.3 in red. For model 2.3 we omit the orbital properties of the PNe for clarity.

The total DM mass (M_{200}) is not constrained, but the posterior is narrower than the priors when Fahrion et al. (2020) is not the only dataset that constrains the model. The bimodality in $\beta'_{\rm GC}$ is weaker when PNe are used together with GCs (red contours) and almost disappears when only Puzia et al. (2004) is considered. Similarly, the posterior in the κ parameter shows reduced asymmetric feature, at stronger values of rotation, when PNe are also considered. Puzia et al. (2004) further favours the lower value of the rotation parameter, which is more consistent with a slower rotation of the GCSs.

The value of $M_\star/L$ is consistent between the two GC datasets, but it is systematically lower when PNe are included. In the latter case, the resulting $M_\star/L$ is consistent with the findings from Zhu et al. (2022) based on the dynamical modelling of the stellar population. PNe are mainly located at $R <\sim 0.5\ R_{\rm e}$, this may explain the added constraining power they provide in the regions where the stellar component is expected to dominate the gravitational potential.

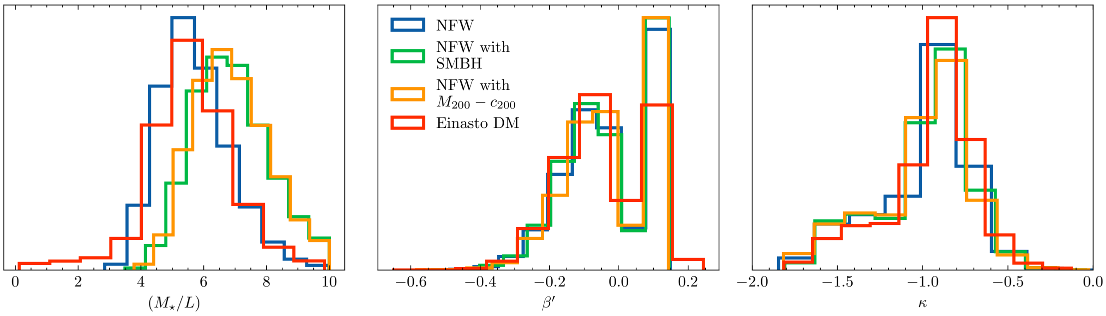

Figure 4.4: Posteriors for the different model set-ups 1.3, 1.4 and 1.5. The left panel shows the posterior of the constant stellar mass-to-light ratio $M_\star/L$, the middle panel the posterior of the velocity anisotropy β', and the right panel the posterior of the rotation parameter κ. The blue line shows the results when the classical NFW profile is used and ρ_s and r_s are free parameters. The orange line shows the model that additionally includes a central SMBH. The model shown with the green line uses the literature $M_{200} - c_{200}$ relation to reduce the number of free parameters. Finally, the red line shows the model where the Einasto profile was used to generate the DM potential.

Table 4.3: Results for the three models shown in the corner plot in Fig. 4.5. The median values with the 16th and 84th percentile are shown.

	kin.	$\beta_{\rm GC}$	$\kappa_{\rm GC}$	$(M_\star/L)$	$\beta_{\rm PNe}$	$\kappa_{\rm PNe}$
2.1	Fahrion et al. (2020, F+20)	$-0.04^{+0.13}_{-0.11}$	$-0.94^{+0.17}_{-0.41}$	$6.85^{+1.33}_{-1.14}$	–	–
2.2	Puzia et al. (2004)	$-0.10^{+0.06}_{-0.08}$	$-0.60^{+0.13}_{-0.11}$	$6.50^{+1.06}_{-0.91}$	–	–
2.3	F+20 & Spriggs et al. (2020)	$-0.07^{+0.06}_{-0.07}$	$-0.86^{+0.16}_{-0.13}$	$4.60^{+0.59}_{-0.47}$	$-0.03^{+0.17}_{-0.17}$	$-0.97^{+0.13}_{-0.11}$

4.6 Conclusions

Fahrion et al. (2020) presented a kinematic study of the galaxy, finding that the globular cluster system rotates with $v_{GCS} = 117.4^{+27.5}_{-26.8}$ km s^{-1} and has a velocity dispersion of $\sigma = 172.4^{+17.5}_{-15.4}$ km s^{-1}. In addition to the global properties, the authors also present kinematic properties for blue and red populations of GCs, finding higher dispersion for red GCs and lower for blue, while the rotation velocities are similar.

These results suggest that in the particular case of NGC 1380 a secondary population of GCs may be hiding and coincidently the observational footprint of F3D survey captured it. It is worth noting that in the area observed by the survey, long-slit observations of the stellar kinematics along the semimajor axis have reported a drop in the velocity dispersion at around 70 arcsec (Bedregal et al., 2006). Recently deep observations with IFU from F3D survey have revealed a complex kinematic and chemical behaviour of this galaxy (Martín-Navarro et al., 2019; Zhu et al., 2022). The 2D maps of the mean velocity and velocity dispersion show a distinct feature at the same location, that coincides with younger stellar populations and higher metallicity. These signatures could be caused by a foreground or background dwarf galaxy. Any GCs that belong to such a galaxy would not be tracing the potential of NGC 1380 and could result in the bimodality in β' that is most prominent when F3D kinematics is used. The biased dataset could be hindering the constraints on the DM mass. Discrete dynamical modelling is sensitive to the presence of outliers and using different kinematic tracers enables us to identify when our modelling is biased and study the reason for it.

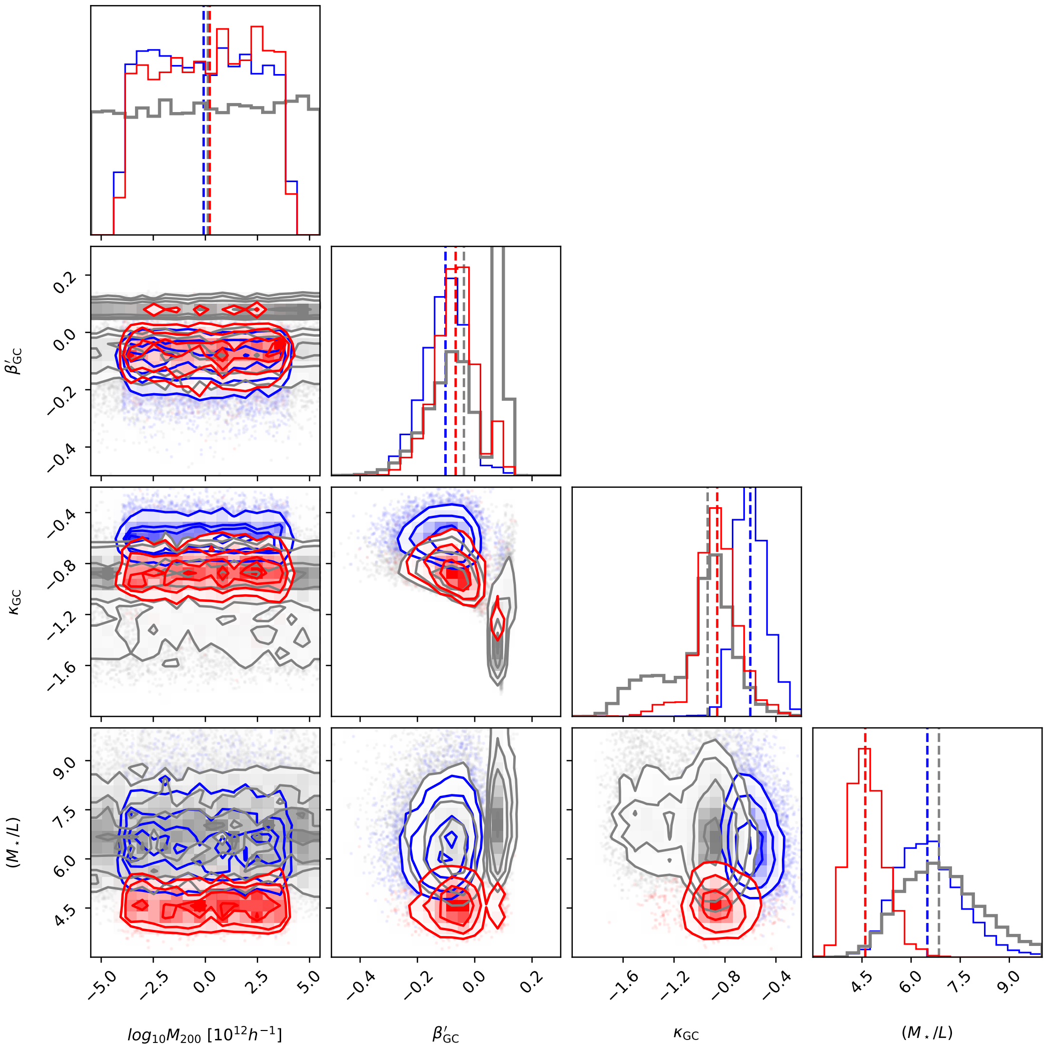

Figure 4.5: Posterior plots for the NFW DM and $M_{200} - c_{200}$ model set-up, where different kinematic datasets were used. Grey contours correspond to the results obtained when considering only the dataset from Fahrion et al. (2020), blue to results obtained with the dataset from Puzia et al. (2004) alone, and red for the results obtained when both Fahrion et al. (2020) and Spriggs et al. (2020) data were used. The dashed vertical lines show the location of the median of each distribution.

Chapter 5

Galaxy halo masses and slopes constrained by globular cluster system dynamics

"There are two types of people in the world.
Those who can extrapolate from incomplete data."
- Anonymous

Declaration of published work

This chapter includes text already published in Veršič et al. (2024) and was partially adapted for this thesis.

5.1 Introduction

Early analytic efforts to characterize the mass distribution within ETGs were based on the dynamical formalism of Jeans equations (Jeans, 1922) and implementing the effects of violent relaxation (Lynden-Bell, 1967). With additional assumptions of spherical symmetry and isotropic orbital distribution, the resulting radial density profile for both dark matter and baryons was found to have a power-law distribution $\rho(r) \propto r^{\gamma_{\rm tot}}$ with the slope of -2. A similar "isothermal" distribution was also found for gas-rich late-type galaxies (LTGs) (see the review from Courteau et al., 2014) and it results in their flattening of the circular rotation curves first reported by Rubin and Ford (1970).

P17 investigated the correlations between the inner slope and stellar kinematic properties and found that for galaxies with $\log \sigma_{\rm e} \gtrsim 2.1$ (where $\sigma_{\rm e}$ is the velocity dispersion at 1 $R_{\rm e}$), the stellar velocity dispersion at 1 $R_{\rm e}$, the inner slope is constant. Recently, Zhu et al. (2023) extended the study to late-type galaxies (LTGs) and found morphological and mass dependence of the $\gamma_{\rm tot}$ in the sample of MANGA galaxies. LTGs with $\log \sigma_{\rm e} < 2.2$ show an increasingly shallower total mass-density profile in contrast with ETGs. They also found a steeper slope with increasing age of the stellar component at a fixed value of $\sigma_{\rm e}$.

The goal of this chapter is to constrain the total mass and the inner slope of the total mass profile of ETGs for $R > 5\ R_{\rm e}$. These regions of ETGs are dominated by dark matter and we use discrete dynamical modelling of GCs to trace the gravitational potential. In this chapter, we carry out discrete anisotropic Jeans modelling accounting for the observed flattening of the GC systems (GCS) to investigate the inner slope of the total mass profile and the virial mass. In Sect. 5.2 we introduce the sample of GCs used throughout the paper and discuss the source of photometry and kinematics. Then we discuss the modelling of the tracer density profile in Sect. 5.3, one of the key components of the dynamical modelling. We introduce the dynamical modelling approach we adopt, focusing on the Bayesian inference and different modelling set-ups in Sect. 5.4, followed by a discussion of the results and exploration of potential biases in our modelling approach in Sect. 5.5. In Sect. 5.6 we compare the results with literature values and discuss our results in Sect. 5.7. Sect. 5.8 presents our main conclusions.

5

5.2 Sample of globular cluster systems

In this section, we will introduce the data used throughout this work. For dynamical modelling, we need kinematic data as well as information on the spatial distribution of the tracer population. We use the sample of the GC radial velocities (RV) from the SAGES Legacy Unifying Globulars and GalaxieS (SLUGGS; Brodie et al., 2014) survey that observed 27 nearby galaxies. First, we will discuss the properties of the RV sample and define kinematic flags based on the visual inspections of the GC velocities. Secondly, we will present the sources of GC photometry for 21 galaxies used to determine the tracer density profile in Sect. 5.3. Observed properties of the 21 galaxies we modelled in this work are presented in Table 5.1.

Table 5.1: Basic information for the 21 galaxies from the SLUGGS survey modelled in this work. Column (1) gives the NGC identifier of each galaxy. Columns (2)-(7): distance, stellar mass, stellar effective radius in angular and physical units, environment (F - field, G - group, C - cluster), systemic velocity of the galaxy, all taken from Forbes et al. (2017) and references therein. Columns (8) and (9) show the inclination (sources listed below) and the number of GCs used in the dynamical modelling, respectively. Column (10) gives the kinematic quality flags discussed in Sect. 5.2.2. In column (11) we list the source of GCs photometry, and with the symbol $^{a)}$ we highlight the galaxies for which only the tracer density profile is available in the literature.

NGC (1)	d Mpc (2)	$\log_{10} M_*$ $M_\odot$ (3)	R_e arcsec (4)	R_e kpc (5)	env (6)	v_{sys} $km\,s^{-1}$ (7)	i $^\circ$ (8)	N_{GC} (9)	kin. flags (10)	Photometry source (11)
720	26.9	11.27	29.1	3.8	F	1745	$90.0^\ddagger$	65	Good	SLUGGS (Kartha et al., 2014)$^{a)}$
821	23.4	11.0	43.2	4.9	F	1718	$75.0^\dagger$	58	Good w. rot.	SLUGGS (Forbes et al., 2017)
1023	11.1	10.99	48.0	2.6	G	602	$74.0^\ddagger$	113	Good w. rot.	Forbes et al. (2014)
1400	26.8	11.08	25.6	3.3	G	558	$32.5^\star$	69	Pecul.	SLUGGS (Forbes et al., 2017)
1407	26.8	11.6	93.4	12.1	G	1779	$30.3^\star$	356	Subpop.	SLUGGS (Forbes et al., 2017)
2768	21.8	11.21	60.3	6.4	G	1353	$90.0^\dagger$	106	Good	SLUGGS (Forbes et al., 2017)
3115	9.4	10.93	36.5	1.7	F	663	$90.0^\dagger$	149	Good w. rot.	SLUGGS (Forbes et al., 2017)
3377	10.9	10.5	45.4	2.4	G	690	$89.0^\dagger$	122	Good	SLUGGS (Forbes et al., 2017)
3607	22.2	11.39	48.2	5.2	G	942	$46.0^\ddagger$	39	Good	SLUGGS (Kartha et al., 2016)$^{a)}$
3608	22.3	11.03	42.9	4.6	G	1226	$88.0^\ddagger$	29	Good	SLUGGS (Kartha et al., 2016)$^{a)}$
4278	15.6	10.95	28.3	2.1	G	620	$88.0^\ddagger$	256	Good	SLUGGS (Forbes et al., 2017)
4365	23.1	11.51	77.8	8.7	G	1243	$88.0^\ddagger$	251	Good	SLUGGS (Forbes et al., 2017)
4374	18.5	11.51	139.0	12.5	C	1017	$88.0^\ddagger$	41	Pecul.	Jordán et al. (2009)
4459	16.0	10.98	48.3	3.7	C	1192	$48.0^\ddagger$	36	Pecul.	Jordán et al. (2009)
4473	15.2	10.96	30.2	2.2	C	2260	$81.0^\dagger$	105	Good	Jordán et al. (2009)
4486	16.7	11.62	86.6	7.0	C	1284	$84.0^\ddagger$	650	Subpop.	Jordán et al. (2009)
4494	16.6	11.02	52.5	4.2	G	1342	$86.0^\ddagger$	105	Good	Humphrey (2009)
4526	16.4	11.26	32.4	2.6	C	617	$77.0^\ddagger$	107	Pecul.	Jordán et al. (2009)
4564	15.9	10.58	14.8	1.1	C	1155	$76.0^\ddagger$	26	Good w. rot.	Jordán et al. (2009)
5846	24.2	11.46	89.8	10.5	G	1712	$89.0^\ddagger$	176	Subpop.	SLUGGS (Forbes et al., 2017)
7457	12.9	10.13	34.1	2.1	F	844	$74.0^\ddagger$	21	Pecul.	SLUGGS (Forbes et al., 2017)

References. † Bellstedt et al. (2018); ‡ Cappellari et al. (2013); * HyperLeda (http://leda.univ-lyon1.fr/).

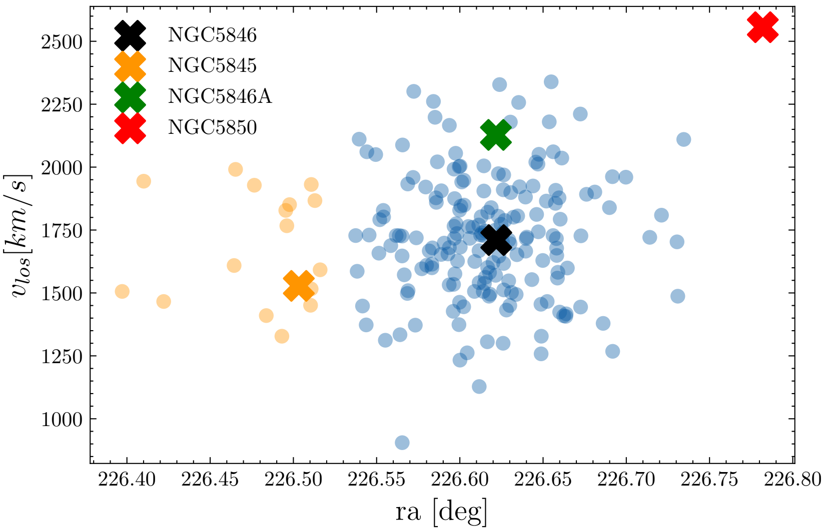

Figure 5.1: The position of GCs from SLUGGS survey is shown in blue and orange points. The orange points are selected based on their position to be more likely belonging to NGC 5845 and blue points show NGC 5846 GCs used in this work. The positions and systemic velocities shown as coloured crosses for the 4 galaxies are taken from Simbad (https://simbad.unistra.fr/simbad/).

5

5.2.1 Kinematic datasets

The kinematic tracers from the SLUGGS dataset have a typical spatial extent of $\sim 8\ R_{\rm e}$ up to $R_{\rm max} \sim 15\ R_{\rm e}$ and a median of 80 GCs per galaxy, varying from 20 to 600 GCs per individual galaxy. The median error of the radial velocities is 10-15 km s^{-1}, representing around 10% of the typical velocity dispersion of a GCS for SLUGGS galaxies. The SLUGGS catalogue excludes foreground stars and background galaxies based on the phase-space diagram (Forbes et al., 2017). Additionally, ultra-compact dwarfs (UCDs) are flagged and we exclude them from the following analysis. UCDs can be misidentified as the bright tail of the GCs due to their compact size and magnitude but they have a different origin, and therefore different spatial distribution and orbital properties (e.g. UCDs in NGC 5128: Dumont et al., 2022).

NGC 5846

A special remark is needed for galaxy NGC 5846, which is the brightest cluster galaxy and has 3 bright companions (NGC 5846A, NGC 5845 and NGC 5850). The projected phase space distribution of GCs belonging to NGC 5846 from the SLUGGS survey and the locations of all 4 galaxies are shown in Fig. 5.1. The right ascension and RV of the GCs are presented with the blue (GCs belonging to NGC 5846) and orange (GCs belonging to NGC 5845) points, the 4 galaxies are presented with coloured crosses.

The spatial and velocity distribution of NGC 5846A and NGC 5845 overlap with those of NGC 5846. In Fig. 5.1 there is a clear elongation of the GCS in the direction of NGC 5845, but the contamination from NGC 5846A is not so apparent in this phase space diagram. To estimate the contamination of the GC catalogue for NGC 5846 we first estimated the number of GCs for each of these galaxies based on their absolute V-band magnitude. We used the observed correlations between the number of GCs and the absolute V band magnitude of its host galaxy in high-density cluster environment (e.g. Kissler-Patig, 1997; Zepf et al., 1994). We estimate that NGC 5846A hosts fewer than 100 GCs, for NGC 5845 we estimate ~ 300 GCs and NGC 5846 is expected to host ∼2500 GCs. The GCs from NGC 5845 thus have a much stronger contribution to the contamination than the GCs from NGC 5846A: to remove potential GCs belonging to NGC 5845 we remove clusters at $\alpha < 226.52°$ from the kinematic dataset of NGC 5846. A more sophisticated selection and additional removal of NGC 5846A GCs is beyond the scope of this work.

5.2.2 KINEMATIC FLAGS

Strong rotation, substructures (non-relaxed populations), and a low number of kinematic tracers or GC subpopulations with distinct kinematics can bias the results of the dynamical modelling. Before proceeding with the modelling we visually inspect the velocity distribution of the GCS for all galaxies.

We focused on the radial variation of mean velocity and velocity dispersion as well as the 2D velocity field of the GCs, like the one shown in the left panel of Fig. 5.2 for NGC 3377. We visually inspected the regularity of the velocity field looking for the presence of strong rotation signatures, cold comoving groups, observationally biased sparse sampling or other peculiar features.

Focusing on these features we defined 4 flags: *Good* (9/21) and *Good w. rot.* (4/21) for GCSs showing a highly regular velocity field and either being dispersion-dominated or showing non-negligible rotation respectively. Galaxies flagged as *Subpop.* (subpopulations, 3/21) show distinct kinematic subpopulations (such as the blue and red GC populations in NGC 1407, Romanowsky et al., 2009) or cold comoving groups that can inflate their velocity dispersion. Lastly, galaxies flagged as *Pecul.* (peculiar, 5/21) have on average the lowest number of GCs among the SLUGGSs galaxies and show an irregular velocity field. Galaxy flags are shown in column 10 of Table 5.1.

5.2.3 PHOTOMETRIC DATASETS

5

One of the inputs for the dynamical modelling is the spatial distribution of the kinematic tracers, i.e. *tracer density profile* and we use the approach outlined in Sect. 2.3 to construct it.

The SLUGGS catalogue provides photometry in the Sloan g and z bands that can be used to construct accurate tracer density profiles for 12 galaxies. For the remaining galaxies we utilized either literature photometry, when available, or the parameters of the fitted number density profile. With the literature photometric information, we could construct the tracer density profiles for additional 9 galaxies. The source of photometry or tracer density profile for each of the galaxies is presented in the last column of Table 5.1.

Eight galaxies in the SLUGGS survey belong to the Virgo galaxy cluster. This nearby galaxy cluster ($d \simeq 16.5$ Mpc) has been extensively studied with the HST Advanced Camera for Surveys (ACS) as part of the ACSVCS survey (Côté et al., 2004). We used the photometry in the F475W (≃Sloan g) and F850LP (≃Sloan z) bands of 6 galaxies in the survey. ACSVCS targeted only the innermost regions of the galaxies and the spatial extent of their tracers is limited to $R_{\rm max} \sim 100$ arcsec, which translates to $\sim 3\ R_{\rm e}$ for a typical galaxy in our sample. For three of the galaxies that we model, only the best-fitting parameters of the tracer density profile were available.

5.3 MODELING TRACER DENSITY PROFILE

The key component of any dynamical modelling is an accurate spatial distribution of the tracer population. For the dynamical modelling approach used in this work, the input tracer density profile is needed in the form of Multi-Gaussian Expansion (MGE, Emsellem et al., 1994) and in this section, we explain how we construct MGEs for the SLUGGS galaxies.

We applied the analysis to the 18 SLUGGS galaxies, for which the photometry of the GCs is available in the literature (see Table 5.1). The sources of photometry used in this work are heterogeneous and assessing magnitude completeness and observational footprint from the photometric images was not possible. That is why we use the observed GC luminosity function (GCLF) to asses the magnitude completeness and radial variation of $\mathrm{PA_{GCS}}$ for spatial completeness. Both steps are applied only to the photometric dataset as dynamical modelling is less sensitive to incompleteness in the kinematic sample.

ETGs show the presence of multiple populations of GCs (Jordán et al., 2007b, and references therein) found in their colour distribution.

Building on those findings and the work done by A16, Posti and Fall (2021) and Bílek et al. (2019), we treat the red and blue GCs as one population in our dynamical modelling. Notable

Table 5.2: Results from the analysis of the tracer density profile fitting and completeness. Column (1) lists the NGC identifier of the galaxy, column (2) the limiting magnitude for completeness as determined using GCLF, (3) the outer radial limit for spatial completeness as described above in units of R_e of the stellar component of the galaxy. Columns (4) and (5) show the best-fit position angle and flattening for the magnitude complete sample of GCS. Columns (6) and (7) show the best-fit effective radius $R_{e,GCS}$ and Sérsic index and $n_{e,GCS}$ of the number density of the GCS with associated 16th and 84th percentile. Galaxies NGC 720, NGC 3607 and NGC 3608 have only tracer density profiles presented in the literature and we used those Sérsic parameters to perform the MGE for the dynamical models.

NGC	$mag_{\rm lim}$	$R_{\rm e,max}$ arcsec	$\rm PA_{GCS}$ °	$q_{\rm GCS}$	$R_{\rm e,GCS}$ arcsec	$n_{\rm GCS}$
(1)	(2)	(3)	(4)	(5)	(6)	(7)
720	—	—	50.0	0.77	$118.2 \pm 20.4^{a)}$	$4.16 \pm 1.21^{a)}$
821	23.79	10.0	56	0.77	$147.31^{+78.24}_{-34.79}$	$2.74^{+1.47}_{-1.25}$
1023	23.87	8.0	67	0.75	$104.40^{+7.57}_{-7.49}$	$1.16^{+0.33}_{-0.23}$
1400	23.34	8.0	26	0.71	$247.53^{+76.70}_{-88.55}$	$3.21^{+1.21}_{-1.42}$
1407	22.94	6.0	165	0.87	$276.13^{+116.57}_{-53.12}$	$2.32^{+1.20}_{-0.76}$
2768	22.9	10.0	52	0.74	$92.61^{+20.89}_{-19.08}$	$2.75^{+0.83}_{-0.84}$
3115	22.35	6.0	40	0.8	$214.53^{+98.07}_{-85.19}$	$3.66^{+1.54}_{-1.73}$
3377	22.89	8.0	36	0.82	$160.60^{+104.70}_{-40.32}$	$3.14^{+1.95}_{-1.51}$
3607	—	—	$109 \pm 8^{b)}$	$0.61^{b)}$	$119.4 \pm 17.4^{b)}$	$1.97 \pm 1.19^{b)}$
3608	—	—	$66 \pm 7^{b)}$	$0.8^{b)}$	$90 \pm 9^{b)}$	$0.93 \pm 0.56^{b)}$
4278	22.53	12.0	168	0.93	$213.84^{+203.95}_{-69.11}$	$2.53^{+1.78}_{-1.12}$
4365	22.83	10.0	39	0.73	$175.68^{+26.30}_{-20.36}$	$2.45^{+0.86}_{-0.65}$
4374	25.5	1.0	140	0.89	$71.69^{+5.33}_{-3.60}$	$0.69^{+0.17}_{-0.13}$
4459	24.57	2.0	46	0.85	$59.45^{+72.52}_{-24.48}$	$4.13^{+1.33}_{-1.93}$
4473	24.86	3.0	110	0.82	$170.63^{+65.81}_{-65.77}$	$2.67^{+0.84}_{-0.92}$
4486	25.85	1.0	19	0.94	$162.46^{+64.84}_{-59.52}$	$1.17^{+0.32}_{-0.39}$
4494	23.58	10.0	10	0.75	$119.95^{+15.63}_{-13.71}$	$1.90^{+0.96}_{-0.58}$
4526	24.54	3.0	128	0.74	$106.35^{+111.41}_{-46.06}$	$1.64^{+1.28}_{-1.03}$
4564	24.4	8.0	48	0.67	$80.98^{+65.95}_{-28.44}$	$3.07^{+0.67}_{-1.06}$
5846	22.25	10.0	12	0.87	$254.20^{+19.51}_{-16.18}$	$0.49^{+0.21}_{-0.14}$
7457	22.28	6.0	131	1.0	$173.58^{+108.52}_{-103.14}$	$3.58^{+1.67}_{-1.89}$

References. [a] Kartha et al. (2014), [b] Kartha et al. (2016)

exceptions, where such treatment breaks down, are the central dominant galaxies NGC 1407, NGC 4486 and NGC 5846. Such galaxies have been shown to have very different accretion histories than other galaxies (e.g. De Lucia and Blaizot, 2007; Oliva-Altamirano et al., 2015) and much richer population of GCs (Harris et al., 2017b). As Chaturvedi et al. (2022) showed in a study of the central galaxy of the Fornax cluster, these galaxies host a population of blue (metal-poor) GCs that trace better the group or cluster potential. We discuss these three galaxies further in Sect. 5.7.2.1.

For the 3 galaxies with literature studies on the GCs number density profile, we use the parameters of the fit. In Sect. 5.3.4 we focus on a close pair of Leo II galaxies, for which the GC density profile was investigated with 2 different methods in Kartha et al. (2016).

5.3.1 Magnitude completeness

We use the observed GCLF to determine the limiting magnitude. Sources fainter than the limiting magnitude are strongly affected by incompleteness. Including them in the analysis of the tracer density profile would introduce a bias by mimicking a shallower profile close to the centre of the galaxy as the galaxy light becomes brighter than the faint GCs.

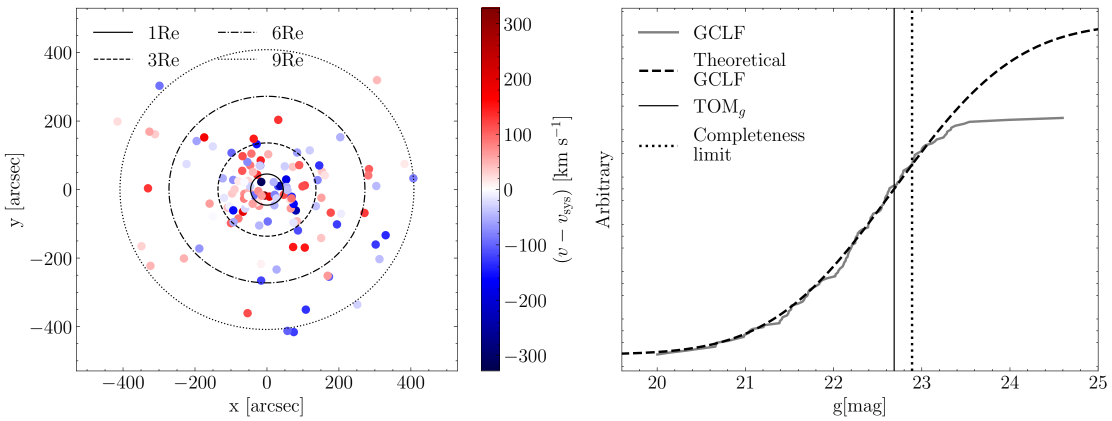

Figure 5.2: An example of spatial and magnitude distribution of the kinematic tracers. We used both to determine an observationally unbiased sample of GCs to construct the tracer density profile for each galaxy. The left panel shows the spatial distribution of the GCs in NGC 3377 centred at the coordinates of the host galaxy and aligned with the photometric position angle. The GCs are colour coded by their velocity corrected for the systemic velocity of the galaxy. The kinematic tracers extend beyond 9 $R_{\rm e}$. The solid grey line in the right panel shows the GCLF of NGC 3377. The dashed black curve shows the arbitrarily scaled theoretical GCLF, with the turn-over magnitude marked with a vertical solid black line. The dotted vertical line shows the magnitude completeness of the sample, determined as described in the text.

To determine a magnitude-complete sample of GCs, we compare the observed cumulative GCLF with the theoretical Gaussian function, assuming $\rm TOM_V$ =-7.5 mag or $\rm TOM_z$ =-8.5 mag and a spread of $\sigma_{\rm GCLF} \sim 1.2$ mag computed from the absolute magnitude of the galaxy in the B band and relation found in Jordán et al. (2007b). The theoretical luminosity function is normalized to match the number of clusters up to the limiting magnitude in an iterative approach. For each galaxy, we compute the square of the residuals between the observed cumulative GCLF and theoretical function and we set the magnitude limit where the residuals exceed 1σ. This is shown in the right panel of Fig. 5.2 for NGC 3377. The observed GCLF of this galaxy becomes strongly affected by the incompleteness at the limiting magnitude of 23.8, shown with the vertical dotted line in the right panel of Fig. 5.2. The limiting magnitudes and radial truncation for all of the galaxies are presented in Table 5.2 together with the results of the Sérsic fit.

5.3.2 SPATIAL COMPLETENESS

After determining the magnitude limit we analyze the radial variation of $\rm PA_{GCS}$ (increasing North to East) and flattening defined as $q'_{\rm GCS}$ to understand the spatial completeness and measure both parameters. We follow the methodology outlined in Sect. 2.3.1 assuming an oblate distribution of GCs.

We assume that the intrinsic position angle of each GCS is constant with radius and that any deviations we measure are introduced by the observational footprint in the SLUGGS survey. We take the radius where the $\rm PA_{GCS}$ and $q'_{\rm GCS}$ change rapidly as the maximal completeness radius and we present it in column (3) of Table 5.2 in units of $R_{\rm e}$; columns (4) and (5) of this table show the recovered $\rm PA_{GCS}$ and $q'_{\rm GCS}$ of the spatially and magnitude complete sample.

5.3.3 SÉRSIC FITS

After establishing a spatially and magnitude complete sample we could bin the photometric data for each galaxy and fit the MGEs to the binned profile. However, binned profiles are stochastic and the number of bins is often small. So instead we choose to fit an analytic Sérsic function (Eq. 2.18) to the binned data as an intermediate step as described in Sect. 2.3.2.

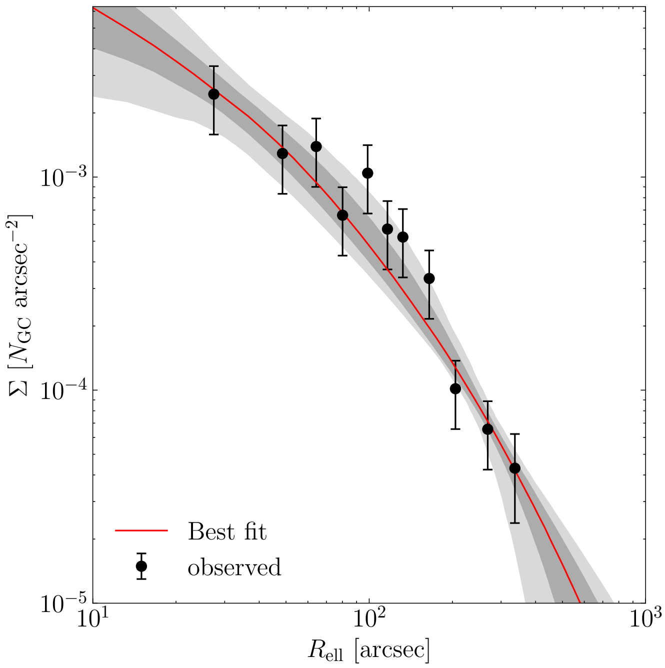

Figure 5.3: Sérsic fit to the binned tracer density profile for NGC 3377 in elliptical radius. The binned profile is represented by black points. The best-fit model is shown with the solid red line with 1 and 3σ uncertainty regions indicated with dark and light grey shaded regions, respectively.

To fit the Sérsic function we use a Bayesian framework, with flat priors on the free parameters: $n_{\rm GCS}$ and $R_{\rm e,GCS}$ and a Gaussian likelihood. The best-fit parameters and the posteriors are sampled using EMCEE ensemble sampler.

As an example, the best-fit Sérsic model for NGC 3377 is shown in Fig. 5.3. The black points with respective uncertainties represent the binned data. The solid red line is the best-fit model and grey-shaded regions are 1σ and 3σ uncertainty regions. Full results of the fits are presented in Table 5.2 in columns (6) and (7).

5.3.4 MGE decomposition

The last step is to represent the tracer density profile in the MGE format required for the dynamical models we will use later. For the 18 galaxies to which we have fit Sérsic profiles directly, we draw samples of the Sérsic parameters from their posteriors and use them to evaluate the profile at each radius as discussed in Sect. 2.3.3.

Three galaxies, NGC 720, NGC 3607 and NGC 3608, have only parameters of the Sérsic profile reported in the literature and do not have GCs photometry available. For these we do not have posteriors to draw from, so our approach is necessarily different. We generated random samples of n and $R_{\rm e}$ assuming a Gaussian distribution centred at the best-fit values presented in the literature, generate the perturbed Sérsic and proceed in the same way as before. For these galaxies, we take PA$_{\rm GCS}$ from the main stellar component and $q_{\rm GCS}$ from the literature studies. These quantities are listed in Table 5.1.

NGC 3607 and NGC 3608

NGC 3607 and NGC 3608 are part of the Leo II group. They are a close pair with a projected distance of 39 kpc and a relative difference in the systemic velocity of $\sim$260 km s^{-1}(Brodie et al., 2014). The velocity dispersion of the GCS, of the order of 150 km s^{-1}(Kartha et al., 2016), means that membership cannot be assigned based on velocities alone. To that end, we use the results from Kartha et al. (2016), where the properties of GCS were investigated in a systematic way and two different methods were used to determine the distribution of GCS in both galaxies (see their section 4). The authors find that $\mathrm{PA_{GCS}}$ and e_{GCS} for NGC 3607 are consistent between the different methods. The recovered $\mathrm{PA_{GCS}}$ for NGC 3608 does differ by more than 2σ between the two methods. We adopt the results from their major-axis method (see their section 4.2) for both galaxies and we use the Sérsic parameters computed with this method as presented in Table 5.2. We found this method better matched our analysis of the $\mathrm{PA_{GCS}}$ of NGC 3608 based on the kinematic sample.

5.4 Discrete dynamical modeling

In this section, we will introduce the dynamical modelling approach used in this work. The method was introduced in chapter 2 and here we emphasise aspects unique to this work. First, we will present the anisotropic Jeans models followed by the Bayesian inference to find best-fit parameters. The results and robustness test against the modelling assumptions are presented in the next section.

5.4.1 Axisymmetric Jeans Anisotropic MGE models

Most ETGs in the nearby universe are well approximated as axisymmetric systems in a steady state. Jeans equations derived from the collisionless Boltzmann equation in cylindrical coordinates (R, z, φ) have been used extensively in the literature to determine the dynamical properties and mass profiles of galaxies using a variety of different tracers (PNe, GCs, stellar and gas kinematics). The recent study of simulated GCS by Hughes et al. (2021b) investigated the accuracy of Jeans models applied to these discrete potential tracers of LTGs and showed its robustness in recovering the enclosed mass.

We use CJAM implementation of axisymmetric Jeans Anisotropic MGE modelling. The models provide the first and second velocity moments $\overline{v_i}$, $\overline{v_i^2}$ at a given position on the plane of the sky. The velocity dispersion is given by: $\sigma_i^2 = \overline{v_i^2} - \overline{v_i}^2$. This enables discrete dynamical modelling, through the assumption of local LOSVD as outlined in Sect. 2.5. This simplified assumption is reasonable given the quality and size of the dataset and has been used in the literature to model discrete kinematic datasets (e.g. Zhu et al., 2016). Read et al. (2021) compared different modelling techniques on simulated datasets (spherical Jeans equations, distribution function models and higher virial moments) and found good agreement in the recovered mass profile for the different modelling techniques.

5.4.2 Gravitational potential

In this work, the total mass in a galaxy (luminous and dark matter) is assumed to follow a spherical double power-law profile (as done in Bellstedt et al., 2018; Cappellari et al., 2013, 2015; Poci et al., 2017). We assumed the following functional form:

$$\rho_{\mathrm{tot}}(r) = \rho_s \left(\frac{r}{r_s}\right)^{\alpha} \left(\frac{1}{2} + \frac{r}{2r_s}\right)^{-\alpha-3}, \tag{5.1}$$

where ρ_s represents scale density and r_s scale radius. The inner total mass slope, parameterized by α, transitions to an outer slope fixed at -3. The potential is incorporated into CJAM through MGE components as discussed in Sect. 2.4.

5.4.3 Bayesian inference

We use Bayesian inference to find the best-fit models as described in Sect. 2.5.1. Each GC is treated independently and no binning in velocities is used to obtain the mean velocity and velocity dispersion profile.

Table 5.3: The overview of the priors for different set-ups. Parameters with uninformative priors (α and κ) have lower and upper limits (min/max). The other three parameters ($\log_{10}\rho_s$, $\log_{10} r_s$, and β_z) have Gaussian priors characterized by mean $\mu_{\rm prior}$ and spread $\sigma_{\rm prior}$. The models A and B have anisotropy and rotation fixed to 0, these assumptions are relaxed in model C.

	$\log_{10}\rho_s$ [$M_\odot$ pc^{-3}]		$\log_{10} r_s$[kpc]		α		β_z		κ		Comments
	$\mu_{\rm prior}$	$\sigma_{\rm prior}$	$\mu_{\rm prior}$	$\sigma_{\rm prior}$	min	max	$\mu_{\rm prior}$	$\sigma_{\rm prior}$	min	max	
A	-3	1.5	1.78	1	-5	0	–		–		Narrow priors
B	-3	4.5	1.78	3	-5	0	–		–		Wide priors
C	-3	1.5	1.78	1	-5	0	0.0	0.2	-1	1	Rotating model

Likelihood

Gaussian likelihood is used as given in Eq. 2.21. At the position of each GC, this constitutes the likelihood of the measured velocity $(v_i, \delta v_i)$ given the free model parameters Θ.

Priors and summary of the modelling set-ups

In this analysis, we use both uninformative, flat priors and informative, Gaussian priors. The informative priors were necessary to break the degeneracy in the modelled parameters (in particular between ρ_s and r_s) without the need for fixing one of them. The Gaussian function was chosen for its simplicity and symmetry. To test and ensure that the priors are not driving the resulting posteriors, we run two models with different prior widths.

We consider three different model set-ups: models A, B and C. They differ in the number of free parameters and the widths of Gaussian priors. In models A and B we vary only the three parameters of the total mass profile in Equation 5.1 (ρ_s, r_s, and α) and change the prior widths between the two models. In model C we additionally vary rotation and velocity anisotropy and thus have 5 free parameters: ρ_s, r_s, α, β_z, and κ. The modelling set-ups and choices of priors are summarised in Table 5.3.

The assumption of no rotation and isotropy in models A and B are motivated by the substantial increase in the computational time of the models when $\beta_z \neq 0$ and $\kappa \neq 0$. Before proceeding with models A and B we explored the variation of the likelihood on a small grid of models by varying β_z and κ. We found that the peak of the likelihood corresponds to very mild radial anisotropy ($\beta_z > 0$) and that the galaxies which were flagged as having strong rotation signatures in Sect. 5.2.1 have a prominent non-zero peak. We discuss the impact of these assumptions on the recovered parameters of the total mass density in Sect. 5.5.2.

The parameters ρ_s and r_s can vary by several orders of magnitude and to sample the posterior more efficiently they are sampled in logarithmic space. Other parameters are dimensionless and even though anisotropy is a strongly asymmetric variable[1], we do not reparametrize it as GCSs show only mildly anisotropic orbital distributions, as discussed in Sect. 5.5.2. The effect our choice of priors has on the posteriors is discussed in Sect. 5.5.1.

Posterior

Having defined the likelihood and priors, the Bayes theorem gives the expression for the posterior, as shown in Eq. 2.24.

MCMC set-up

To explore the parameter space and sample the region of best-fitting parameters we use the EMCEE package, a Python implementation of an affine-invariant ensemble sampler for Markov chain Monte Carlo (MCMC). For models A and B (isotropic and non-rotating) we use 100 walkers and 6000 steps and for model C (free β_z and κ) 100 walkers and 2000 steps, due to the increase in the computational time. In both set-ups, 600 steps are discarded as a burn-in phase. We

[1] Velocity anisotropy varies between 1 and $-\infty$ for extremely radial and vertically anisotropic systems respectively.

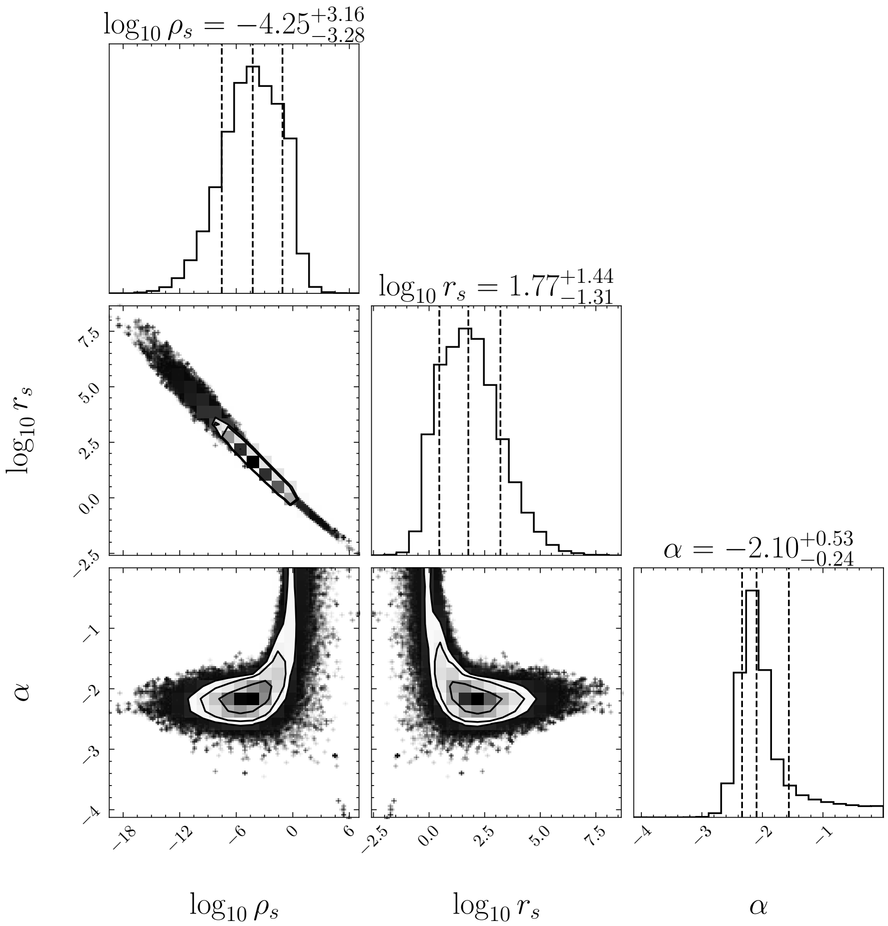

Figure 5.4: Posterior of model B for NGC 3377. The median and the 1σ percentiles are shown as dashed lines on each of the marginalized posteriors and the corresponding values are written on the top of each panel.

verified that this set-up is longer than several auto-correlation times and we visually inspected the convergence of the chains. The initial conditions are the same in all runs: $\log_{10}\rho_s = -4\ \mathrm{M_{\odot}pc^{-3}}$, $\log_{10} r_s = 1.3$ kpc, $\alpha = -1.5$, for model C: $\beta = 0.01$, $\kappa = 0.1$. These initial conditions were informed by prior dynamical modelling of GCs in FCC 167, an ETG of the Fornax galaxy cluster. Given its properties, the modelled galaxy is a good representative of the ETGs in the SLUGGS sample. We explored the robustness of the posteriors against the variations in the initial conditions and found a negligible effect.

5.5 RESULTS: FIDUCIAL MODEL AND ROBUST SAMPLE

Now that we have described the dataset and laid out the models we can apply the models to the data. We applied models A, B and C to all 21 galaxies in our sample and found that all MCMC chains converged and all posteriors were unimodal. As an example, we show the corner plot for NGC 3377 for the model B set-up in Fig. 5.4. The ρ_s and r_s are strongly anti-correlated and the informative priors we impose help to constrain both but cannot break the degeneracy. The inner slope α is not degenerate with the scale density and radius but has a tail towards shallower profiles. At such shallow profiles, $r_s \sim$1 kpc (within the innermost kinematic tracer), therefore in these cases the density is effectively a single power-law profile with the slope of -3 (see Equation 5.1).

Table 5.4: The summary of the posterior results from the fiducial set-up, model B. We list the median and the 16th and 84th percentile on the parameters of the total mass slope. We also report the value of the quality flag in the last column.

NGC	$\log_{10}\rho_s$ [$\mathrm{M_\odot\,pc^{-3}}$]	$\log_{10} r_s$ [kpc]	α	Flag
(1)	(2)	(3)	(4)	(5)
720	$-0.95^{+2.58}_{-4.59}$	$0.53^{+1.39}_{-0.94}$	$-2.36^{+1.42}_{-1.24}$	Good
821	$-1.57^{+3.08}_{-4.56}$	$0.65^{+1.49}_{-1.08}$	$-2.46^{+1.28}_{-1.26}$	Good w. rot.
1023	$-3.65^{+2.39}_{-3.23}$	$1.87^{+1.72}_{-1.14}$	$-1.64^{+0.69}_{-0.34}$	Good w. rot.
1407	$-5.2^{+1.17}_{-1.71}$	$4.42^{+1.57}_{-1.06}$	$-1.06^{+0.09}_{-0.09}$	Subpop.
2768	$-1.09^{+1.24}_{-3.18}$	$0.66^{+1.25}_{-0.54}$	$-1.55^{+1.04}_{-0.75}$	Good
3115	$-1.29^{+2.29}_{-4.5}$	$0.67^{+1.66}_{-0.91}$	$-2.13^{+1.21}_{-0.54}$	Good w. rot.
3377	$-4.25^{+3.16}_{-3.28}$	$1.77^{+1.44}_{-1.31}$	$-2.1^{+0.53}_{-0.24}$	Good
3608	$-2.79^{+2.73}_{-3.45}$	$1.36^{+1.94}_{-1.22}$	$-1.61^{+1.0}_{-1.34}$	Good
4278	$-3.0^{+2.05}_{-3.7}$	$1.54^{+1.69}_{-0.9}$	$-1.85^{+0.93}_{-0.29}$	Good
4365	$-5.54^{+2.3}_{-2.67}$	$2.95^{+1.38}_{-1.1}$	$-1.87^{+0.2}_{-0.14}$	Good
4374	$-3.58^{+2.07}_{-2.71}$	$2.65^{+1.85}_{-1.29}$	$-1.29^{+0.57}_{-0.47}$	Pecul.
4459	$-4.27^{+2.03}_{-2.59}$	$2.57^{+1.8}_{-1.27}$	$-1.28^{+0.5}_{-0.38}$	Pecul.
4473	$-2.3^{+1.7}_{-3.87}$	$1.12^{+1.7}_{-0.76}$	$-1.77^{+1.05}_{-0.43}$	Good
4486	$-4.72^{+1.52}_{-2.15}$	$3.49^{+1.67}_{-1.05}$	$-1.21^{+0.16}_{-0.1}$	Subpop.
4494	$-3.84^{+2.31}_{-3.4}$	$1.73^{+1.71}_{-1.06}$	$-1.72^{+0.76}_{-0.34}$	Good
4526	$-4.47^{+2.01}_{-2.43}$	$2.81^{+1.78}_{-1.27}$	$-1.26^{+0.41}_{-0.28}$	Pecul.
4564	$-2.09^{+3.53}_{-4.51}$	$0.53^{+1.59}_{-1.21}$	$-2.51^{+1.12}_{-1.32}$	Good w. rot.
5846	$-4.05^{+0.97}_{-1.69}$	$3.37^{+2.02}_{-1.24}$	$-0.61^{+0.35}_{-0.43}$	Subpop.
7457	$-3.51^{+2.27}_{-2.92}$	$1.6^{+2.14}_{-1.29}$	$-1.27^{+0.77}_{-0.87}$	Pecul.

We adopt model B as the fiducial model, following the arguments laid out in this section; the robust sample of galaxies are the ones with the flags *Good* and *Good w. rot.* as introduced in Sect. 5.2.2. We present the best-fit values of the total mass density profile for the fiducial model in Table 5.4 for the 19 galaxies we modelled. NGC 1400 and NGC 3607 were not modelled due to the literature value of the inclination, which was not consistent with the projected flattening of their GCSs.

5.5.1 Effect of informative priors

To test the robustness of the results against our choice of priors we discuss the marginalized posteriors of models A and B, the two isotropic and non-rotating set-ups, in this section. We focus only on the parameters with informative priors $\log_{10}\rho_s$ and $\log_{10} r_s$ as the prior for α is the same in both set-ups (see Table 5.3). The posteriors for both set-ups are shown in Fig. 5.5. The top row shows the results for model A and the bottom row for model B (fiducial model) as described in Sect. 5.4.3. Each column corresponds to a different free parameter of the total density profile: $\log_{10}\rho_s$ on the left and $\log_{10} r_s$ on the right. The solid grey lines show the marginalized posteriors for each of the modelled galaxies and priors are shown with coloured lines: the blue line shows prior for model A and the orange for model B.

The posteriors and priors show similar widths on the top panels for model A making it unclear whether the data or prior are driving the posterior distribution in this case. This motivated us to test the robustness of the informative priors to ensure our choice of prior was not driving the posterior. To that end, we increased the widths of the Gaussian priors on the $\log_{10}\rho_s$ and $\log_{10} r_s$ parameters and on the bottom row for model B the prior is wider than the posteriors. This indicates the data is driving the posterior for this choice of prior. Thus we adopted model B as the fiducial set-up. This effect is most strongly seen for the $\log_{10}\rho_s$ parameter, while the posteriors in $\log_{10} r_s$ are narrower than the prior in both instances. For clarity, the inner slope

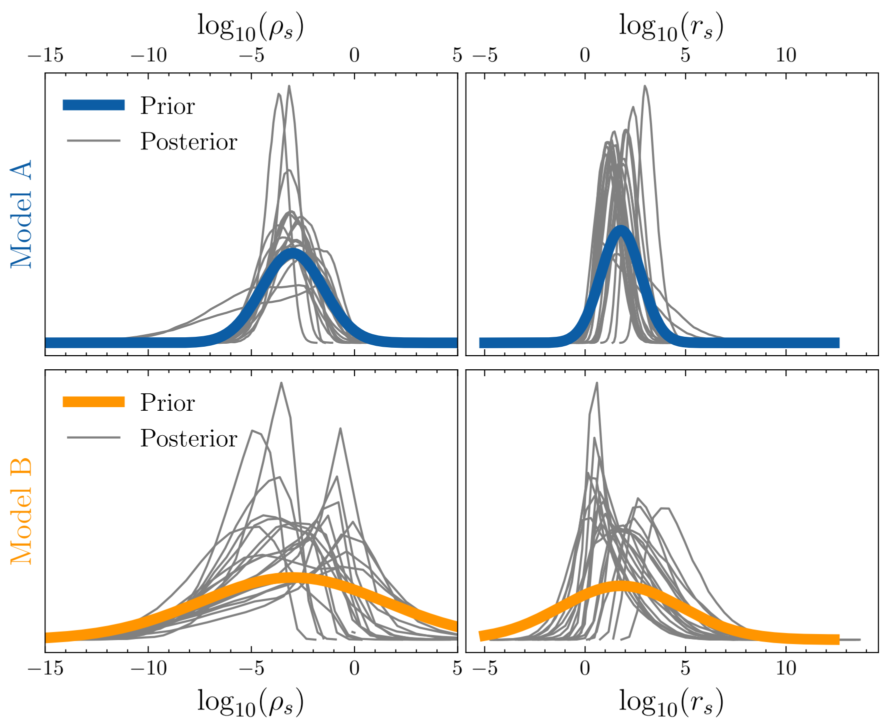

Figure 5.5: Comparison between the informative priors for $\log_{10}\rho_s$ and $\log_{10}r_s$ in coloured lines for model A and model B and posteriors for each of the 21 modelled galaxies in grey. In the fiducial model B the widths of the posteriors are narrower than those of the priors, which indicates that the data (and not the prior) is driving the posterior.

α is not shown in Fig. 5.5. We compared the values of the slope among both set-ups and found minimal differences in their posteriors.

We did the same investigation for model C, which includes rotation and anisotropy and found similar behaviour of the posteriors as for model A.

We further explored the impact of informative priors by comparing the resulting enclosed mass for models A and B. To compute the enclosed mass we numerically integrate Equation 5.1. We randomly drew 1000 samples from the posterior, computed the enclosed mass profile and determined the uncertainties at fixed radii: 1 R_e, 5 R_e and at the radius of the maximal extent of the tracers for literature comparison. In the integration, we excluded profiles with α steeper than -3. These result in infinite enclosed mass, and with $\lesssim$0.5% of the chains having such extreme values we considered this selection did not impact our results and conclusions.

The enclosed mass measurements for model B are presented in Table 5.5 and the comparison between the fiducial and narrow set-up is presented in Fig. 5.6 within 5 R_e. Different symbols correspond to the kinematic flags defined in Sect. 5.2.2. The black points show galaxies flagged as *Good* or with strong rotation signatures, red open symbols denote the galaxies with strong subpopulations and blue open symbols peculiar galaxies with apparent peculiar velocity fields. The dashed line shows the 1-1 relation to guide the eye, and is not fit to the points. This figure demonstrates the negligible effect the prior widths in models A and B have on the enclosed mass. The same is found for enclosed mass at all radii we investigated, with the uncertainties increasing with increasing radius, and it also holds for model C.

5.5.2 EFFECTS OF ROTATION AND VELOCITY ANISOTROPY

After investigating the effects of informative priors on the posterior and enclosed mass we discuss the impact of anisotropy and rotation of the GCS on the parameters of the total mass distribution.

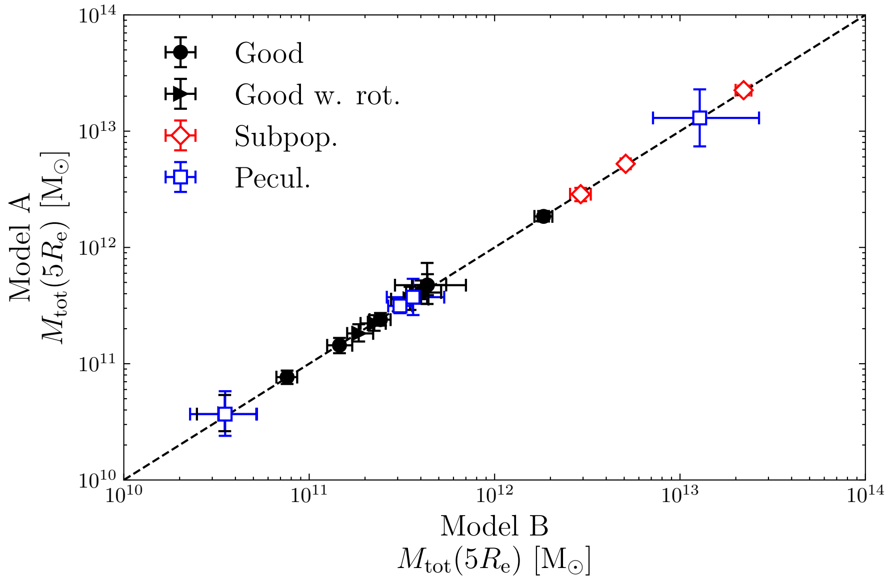

Figure 5.6: The effect of informative priors on the enclosed mass within 5 $R_{\rm e}$. The black dots and triangles show galaxies flagged as *Good* and *Good w. rot.*, respectively, as defined in Sect. 5.2.2. The measurements for these galaxies are robust. Open red diamonds and blue squares highlight galaxies flagged as *Subpop.* and *Pecul.*, respectively, and for which the measurements are not robust. The dashed line is a 1-1 line for reference.

We find the enclosed mass and inner slopes α are consistent between models A, B and C, suggesting that velocity anisotropy and rotation have a negligible impact on the recovered properties of the total mass profile. A16 studied the GCs of the SLUGGS galaxies and using a Tracer Mass Estimator (TME, e.g. Watkins et al., 2010)[2] they found minimal contribution ($\sim$ 6%) to the pressure-supported mass estimate due to rotation (see their Figure 7) and $\sim 5\%$ when different velocity anisotropy for GCs is assumed (see the right panel of their Figure 5).

This can be seen in Fig. 5.7 for NGC 3115; we chose this galaxy as it shows signs of strong rotation in the kinematics of its GCs. In the figure, we compare the velocity moments computed from the best-fit parameters of models B (in black) and C (in red). Blue squares and triangles show the binned velocity dispersion and rotation of the GCs: they are only shown for visualisation purposes and were not used in the dynamical modelling. To obtain the binned profiles we assumed a point-symmetric velocity field, characteristic of a relaxed axisymmetric system, and symmetrised the velocities to reduce the noise in each radial bin. We imposed a constant number of GCs in each bin along the semi-major axis and computed robust mean velocity and velocity dispersion, i.e. $\sigma_k^2 = \overline{v_k^2} - \overline{v_k}^2$, for the kth bin. The drop in the velocity dispersion close to the centre of the galaxy is not realistic, but is due to incompleteness in radial velocity measurements in the galaxy inner region.

In this galaxy, the rotation of the GCs in the outer parts is $\overline{v_{\rm LOS}} \sim 100$ km s^{-1} and velocity dispersion is $\sigma_{\rm LOS} \sim 130$ km s^{-1}. The results for model B are shown with black dashed lines and the velocity moments from CJAM for model C are shown as solid red curves. In the top panel, we see that model C can reproduce the observed rotation well, which by construction is not the case for model B. The velocity dispersion profile is very well matched by model B in the bottom panel and model C agrees within the 1σ uncertainties of the data. We can see that, both models B and C agree with the velocity dispersion profile as seen on the bottom panel.

[2]The method assumes spherically symmetric tracer and mass distributions to evaluate pressure-supported mass estimates and, through additional correction, provides mass corrections due to flattening of the tracer distribution, rotation and velocity anisotropy.

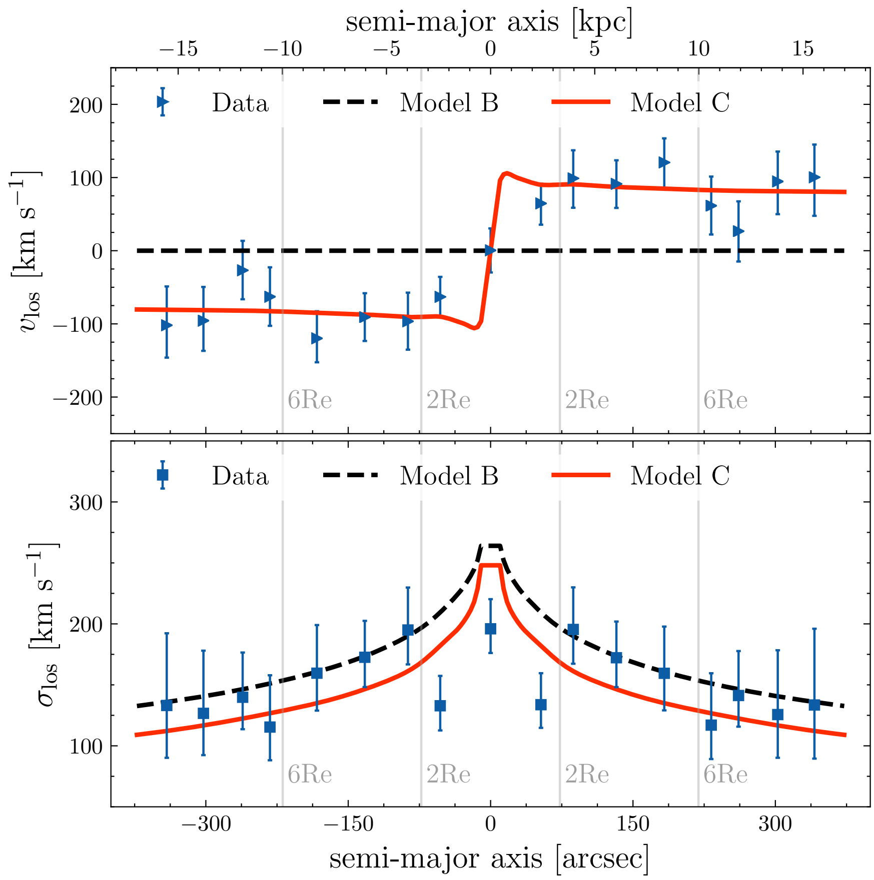

Figure 5.7: Comparison between the best-fit results from models B and C and the data for NGC 3115 along the semi-major axis of the galaxy. The top panel shows the mean velocity and the bottom the velocity dispersion. The blue triangles and squares show the mean velocity and velocity dispersion of the GCs, respectively. The black dashed lines show the profiles computed with the best-fit parameters of model B, the solid red lines those of model C. The vertical grey lines show multiples of the stellar effective radius for comparison.

Velocity anisotropy and rotation measurements

In Fig. 5.8 we show the anisotropy (top panel) and rotation (bottom panel) parameters. We find that most galaxies have velocity anisotropy consistent with zero, consistent with the assumptions in models A and B. NGC 1023 and NGC 2768 deviate at the level of 3σ, showing more radial orbits ($\beta_z > 0$). We also find that most GCs are consistent with having negligible rotation, with the exception of those we flagged as having strong rotation signatures, highlighted with black triangles. Two galaxies were not flagged as showing a strong rotation signature in the velocity field of their individual GCs (NGC 2768 and NGC 4494), but the model prefers strong $\kappa \neq 0$.

5.5.3 Definition of the robust sample

In this work, we present robust results for 12 galaxies out of the initial 21. These are flagged as *Good* (8 galaxies) and *Good w. rot.* (4 galaxies) in Table 5.5 and in this chapter we refer to these as robust measurements.

In our analysis, we identified galaxies with strong rotation signatures, low number of GCs or strong presence of subpopulation in their GCS. Three galaxies, NGC 1407, NGC 4486 (M87) and NGC 5846, are central galaxies of their respective groups and literature studies have identified a strong presence of dynamically distinct populations. We flagged them as *Subpop.* (Subpopulations)

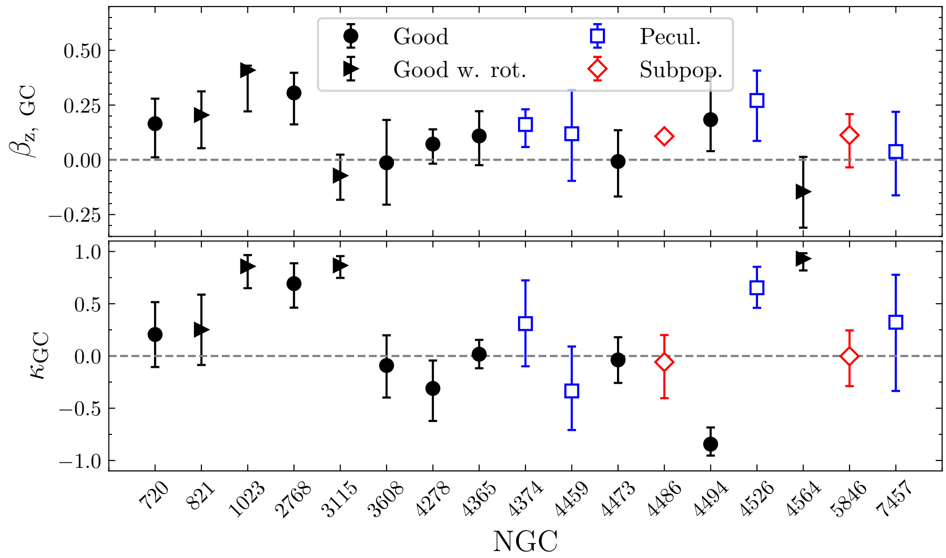

Figure 5.8: The best-fit velocity anisotropy and rotation from model C. The symbols match those in Fig. 5.6, with black points highlighting the galaxies with robust measurements and open symbols those without. The top panel shows the velocity anisotropy for each galaxy and the bottom panel shows the rotation parameter κ. The error bars represent the 16th and 84th percentile uncertainties on the measurement. The dashed grey line shows the isotropic $\beta_z = 0$ and non-rotating $\kappa = 0$ values for reference.

based on the differences in the kinematic properties between the red and blue GCs. We flag four galaxies, NGC 4374, NGC 4459, NGC 4526 and NGC 7457, as *Pecul.*, owing to the peculiar signatures in the kinematics of their GCs. We will discuss individual galaxies with these flags in more detail in Sect. 5.7.2. In the analysis that follows we show the results for these two classes with open symbols for completeness.

5.5.4 Single power law slope of the total mass density

The key advantage of this work is the large spatial distribution of the tracers, which enables us to place robust constraints on the total mass profile. To compare the inner mass slope obtained in this work with literature studies, we fit a single power law with slope $\gamma_{\rm tot}$ in different radial ranges to our best-fit models, and present the results in Table 5.6. The radial ranges were selected based on literature measurements.

To determine the single power-law slope, we first randomly draw 10000 samples of the total mass parameters from the post-burn-in posterior of each galaxy. This represents 25% of the total posterior sample and changing the number of samples affected the final results in a negligible way. For each set of parameters we solve for the single power-law slope by computing the least square solution of equation: $\log\rho = \gamma_{\rm tot}\log r + A$, with the logarithmic slope $\gamma_{\rm tot}$ and scaling A. The median and 16th and 84th uncertainty intervals for $\gamma_{\rm tot}$ are then computed and are presented in Table 5.6 for the 5 different radial ranges we considered.

To illustrate the method an example of the fit to NGC 3377 is shown in Fig. 5.9. The red solid line and red shaded regions show the median and 1σ percentiles of the total density profile. The vertical red dashed line shows the location of the median scale radius of the total mass density for reference. For comparison, we chose the $\gamma_{\rm tot}$ and A obtained from the fit in the range $0.1 < r/R_{\rm e}< 4$ (same as B18). The black solid line shows the power-law with the median and grey-shaded regions highlighting the uncertainty. The vertical orange lines show the multiples of the $R_{\rm e}$, and the small vertical blue lines indicate the projected positions of the GCs.

Depending on the radial region over which we fit the single power-law profile the resulting power-law slope will vary as also commented on in B18. The larger the radial extent the more

Table 5.5: Results from the fiducial run (model B set-up). Columns (2) and (3) show the total enclosed mass within specific radii in units of $10^{11}\mathrm{M}_{\odot}$. The results are given as the median and the uncertainties are computed as 16th and 84th percentile. For reference columns (4) and (5) give the effective radii of the galaxy's stellar component in angular and physical units and column (6) includes the quality flags introduced in the text. Two galaxies (NGC 1400 and NGC 3607) do not have results due to the literature value of the inclination being inconsistent with the flattening of the GCS.

NGC	$M_{\mathrm{tot}}(1\ R_{\mathrm{e}})$ [$10^{11}\mathrm{M}_{\odot}$]	$M_{\mathrm{tot}}(5\ R_{\mathrm{e}})$ [$10^{11}\mathrm{M}_{\odot}$]	R_{e} [arcsec]	R_{e} [kpc]	Flag
(1)	(2)	(3)	(4)	(5)	(6)
720	$1.01^{+2.08}_{-0.8}$	$3.43^{+1.58}_{-0.7}$	29.1	3.8	Good
821	$1.0^{+1.52}_{-0.56}$	$2.81^{+1.53}_{-0.63}$	43.2	4.9	Good w rot
1023	$0.22^{+0.24}_{-0.09}$	$1.89^{+0.69}_{-0.32}$	48.0	2.58	Good w rot
1407	$8.76^{+2.31}_{-1.15}$	$202.53^{+40.28}_{-20.16}$	93.4	12.14	Subpop.
2768	$1.15^{+0.79}_{-0.33}$	$3.66^{+1.89}_{-0.72}$	60.3	6.37	Good
3115	$0.37^{+0.73}_{-0.26}$	$1.63^{+0.51}_{-0.24}$	36.5	1.66	Good w rot
3377	$0.15^{+0.14}_{-0.06}$	$0.67^{+0.2}_{-0.1}$	45.4	2.4	Good
3608	$0.3^{+1.48}_{-0.49}$	$3.05^{+4.27}_{-1.31}$	42.9	4.64	Good
4278	$0.3^{+0.36}_{-0.15}$	$2.13^{+0.65}_{-0.28}$	28.3	2.14	Good
4365	$2.71^{+1.07}_{-0.5}$	$16.46^{+3.96}_{-1.9}$	77.8	8.71	Good
4374	$10.47^{+7.74}_{-3.24}$	$72.89^{+185.51}_{-56.83}$	139.0	12.47	Pecul.
4459	$0.2^{+0.23}_{-0.09}$	$2.58^{+2.76}_{-1.09}$	48.3	3.75	Pecul.
4473	$0.19^{+0.29}_{-0.12}$	$1.24^{+0.47}_{-0.22}$	30.2	2.23	Good
4486	$2.41^{+0.96}_{-0.49}$	$47.78^{+6.66}_{-3.05}$	86.6	7.01	Subpop.
4494	$0.18^{+0.17}_{-0.07}$	$1.15^{+0.51}_{-0.23}$	52.5	4.23	Good
4526	$0.13^{+0.19}_{-0.08}$	$2.68^{+0.89}_{-0.39}$	32.4	2.58	Pecul.
4564	$0.07^{+0.2}_{-0.07}$	$0.26^{+0.27}_{-0.09}$	14.8	1.14	Good w rot
5846	$0.52^{+0.9}_{-0.3}$	$25.4^{+7.85}_{-3.66}$	89.8	10.54	Subpop.
7457	$0.02^{+0.08}_{-0.02}$	$0.23^{+0.31}_{-0.11}$	34.1	2.13	Pecul.

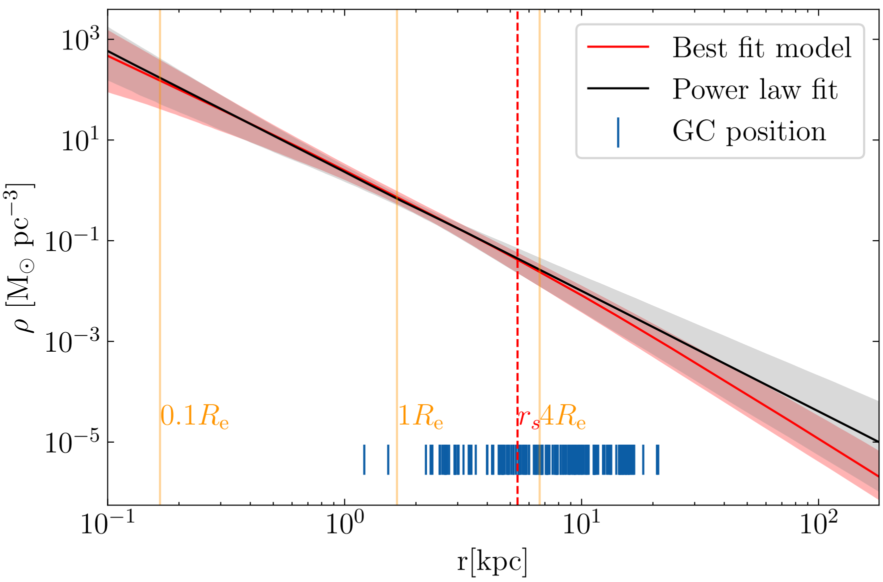

Figure 5.9: Total mass density of NGC 3115 from the fiducial model. The red solid line with the associated shaded region shows the median, 16th and 84th percentile of the total mass density profile. The red vertical dashed line shows the median scale radius of the total mass density profile. The black solid line and grey shaded regions show the resulting single power-law fit in the region $0.1 < r/R_e < 4$ and 1σ uncertainties as explained in Sect. 5.5.4. Orange vertical lines show the locations of multiples of the stellar effective radius and blue lines indicate the positions of the tracers for reference.

Table 5.6: The single power-law slope of total mass density profile in different radial ranges, where $x_r = r/R_\mathrm{e}$. Kinematic flags are also listed in the last column.

	γ_tot					
NGC	$x_r < 1$	$x_r < 4$	$0.1 < x_r < 1$	$0.1 < x_r < 4$	$R_\mathrm{min} < r < R_\mathrm{max}$	Flag
720	$-2.56^{+0.94}_{-1.0}$	$-2.59^{+0.78}_{-0.92}$	$-2.69^{+0.67}_{-0.69}$	$-2.76^{+0.56}_{-0.53}$	$-2.89^{+0.36}_{-0.28}$	Good
821	$-2.57^{+0.81}_{-0.98}$	$-2.62^{+0.71}_{-0.89}$	$-2.73^{+0.61}_{-0.66}$	$-2.8^{+0.54}_{-0.51}$	$-2.89^{+0.46}_{-0.32}$	Good w. rot.
1023	$-1.64^{+0.56}_{-0.32}$	$-1.67^{+0.44}_{-0.3}$	$-1.69^{+0.39}_{-0.29}$	$-1.74^{+0.29}_{-0.27}$	$-1.91^{+0.28}_{-0.28}$	Good w. rot.
1407	$-1.06^{+0.1}_{-0.08}$	$-1.06^{+0.09}_{-0.08}$	$-1.06^{+0.09}_{-0.08}$	$-1.07^{+0.09}_{-0.08}$	$-1.07^{+0.09}_{-0.08}$	Subpop.
2768	$-1.87^{+0.72}_{-0.51}$	$-1.96^{+0.56}_{-0.45}$	$-2.14^{+0.38}_{-0.4}$	$-2.28^{+0.28}_{-0.35}$	$-2.47^{+0.27}_{-0.28}$	Good
3115	$-2.21^{+0.78}_{-0.51}$	$-2.25^{+0.62}_{-0.48}$	$-2.3^{+0.54}_{-0.46}$	$-2.36^{+0.4}_{-0.43}$	$-2.61^{+0.32}_{-0.31}$	Good w. rot.
3377	$-2.11^{+0.37}_{-0.24}$	$-2.12^{+0.3}_{-0.23}$	$-2.13^{+0.26}_{-0.23}$	$-2.17^{+0.21}_{-0.23}$	$-2.28^{+0.19}_{-0.23}$	Good
3608	$-1.84^{+0.89}_{-1.15}$	$-1.89^{+0.84}_{-1.1}$	$-2.0^{+0.9}_{-0.99}$	$-2.11^{+0.92}_{-0.89}$	$-2.21^{+0.91}_{-0.79}$	Good
4278	$-1.87^{+0.72}_{-0.25}$	$-1.88^{+0.59}_{-0.25}$	$-1.89^{+0.55}_{-0.24}$	$-1.93^{+0.38}_{-0.21}$	$-2.12^{+0.19}_{-0.18}$	Good
4365	$-1.87^{+0.2}_{-0.14}$	$-1.88^{+0.19}_{-0.14}$	$-1.88^{+0.18}_{-0.14}$	$-1.9^{+0.14}_{-0.13}$	$-1.92^{+0.13}_{-0.13}$	Good
4374	$-1.32^{+0.45}_{-0.43}$	$-1.35^{+0.43}_{-0.43}$	$-1.43^{+0.45}_{-0.41}$	$-1.51^{+0.43}_{-0.42}$	$-1.57^{+0.45}_{-0.48}$	Pecul.
4459	$-1.3^{+0.42}_{-0.37}$	$-1.32^{+0.4}_{-0.36}$	$-1.34^{+0.41}_{-0.34}$	$-1.38^{+0.37}_{-0.34}$	$-1.44^{+0.36}_{-0.35}$	Pecul.
4473	$-1.78^{+0.8}_{-0.39}$	$-1.83^{+0.65}_{-0.36}$	$-1.86^{+0.59}_{-0.34}$	$-1.96^{+0.41}_{-0.28}$	$-2.17^{+0.23}_{-0.28}$	Good
4486	$-1.21^{+0.16}_{-0.1}$	$-1.21^{+0.15}_{-0.1}$	$-1.21^{+0.15}_{-0.1}$	$-1.22^{+0.13}_{-0.1}$	$-1.26^{+0.08}_{-0.08}$	Subpop.
4494	$-1.76^{+0.62}_{-0.31}$	$-1.77^{+0.48}_{-0.31}$	$-1.8^{+0.35}_{-0.29}$	$-1.87^{+0.29}_{-0.28}$	$-2.02^{+0.27}_{-0.3}$	Good
4526	$-1.28^{+0.39}_{-0.28}$	$-1.29^{+0.38}_{-0.28}$	$-1.29^{+0.37}_{-0.28}$	$-1.3^{+0.33}_{-0.27}$	$-1.38^{+0.25}_{-0.25}$	Pecul.
4564	$-2.66^{+0.9}_{-1.06}$	$-2.68^{+0.8}_{-0.95}$	$-2.74^{+0.77}_{-0.87}$	$-2.8^{+0.71}_{-0.7}$	$-2.92^{+0.59}_{-0.41}$	Good w. rot.
5846	$-0.65^{+0.29}_{-0.41}$	$-0.66^{+0.28}_{-0.41}$	$-0.68^{+0.28}_{-0.4}$	$-0.72^{+0.3}_{-0.37}$	$-0.76^{+0.32}_{-0.38}$	Subpop.
7457	$-1.42^{+0.7}_{-0.87}$	$-1.46^{+0.66}_{-0.88}$	$-1.5^{+0.69}_{-0.93}$	$-1.6^{+0.71}_{-0.89}$	$-1.68^{+0.73}_{-0.93}$	Pecul.

sensitive we are to the transition from the inner slope α to the outer, fixed to -3. While the profiles agree within the 1σ uncertainty, it is clear that using the single power-law profile will result in a higher density and larger enclosed mass in the outer regions of the galaxy.

5.6 Comparison with literature

In this section, we compare the results from this work with the literature measurements obtained with different dynamical modelling methods and kinematic tracers. We focus on the comparison of the enclosed mass and the slope of the total mass profile. We discuss the results for all 19 galaxies we modelled but focus on the sample of 12 galaxies with robust measurements as determined in Sect. 5.5.3.

We compare our results with three different studies that have systematically investigated the total mass profile of a large subset of SLUGGS galaxies: A16, P17 and B18. Their overlapping science goals but different kinematic tracers or methodologies make them uniquely suitable for comparison with our work. A16 determined the enclosed mass with GCs from the SLUGGS survey. They used TME which assumes spherically symmetric tracer and mass distribution. The inner slope γ_tot was studied by P17 and B18 with stellar kinematics and axisymmetric JAM. The former used stellar kinematics from Atlas$^\mathrm{3D}$ survey Cappellari et al. (2011) which extends out to 1 R_e and the latter combined the central Atlas$^\mathrm{3D}$ kinematics with extended stellar kinematics from the SLUGGS survey out to 4 R_e. The summary of the literature studies is presented in Table 5.7.

5.6.1 Enclosed mass

We compute the enclosed mass at different radii from model B as discussed in Sect. 5.5 and compare it to literature results from A16. The study modelled 18 of the galaxies presented in this work and used GCs with TME. It assumes that both mass density and the tracer density profile are spherically symmetric with a power-law distribution. The slopes are not free parameters in their modelling. Instead, for the GC tracer density slope the authors use literature studies to build an observed correlation between the stellar mass of the host galaxy and the power-law slope of the GCS. To get the slope of the total mass density the study uses simulated ETGs and observations to

Table 5.7: The properties of the different dynamical studies from the literature in comparison with this work.

	Potential tracers	R_{max} $[R_{\mathrm{e}}]$	Modelling tool	Symmetry	Tracer density	Mass density	r_s	κ, β
This work	individual GCs	$4-8$	CJAM	axisymmetry	Sérsic	Eq. 5.1	free	free
A16	ensemble GCs	$4-8$	TME	spherical	power law	power law	–	0
P17	unresolved stars	~ 1	JAM	axisymmetry	SB MGE†	Eq. 5.1	fixed (20 kpc)	free
B18	unresolved stars	~ 4	JAM	axisymmetry	SB MGE†	Eq. 5.1	fixed (20 kpc)	free

† SB MGE - stellar surface brightness multi Gaussian expansion

determine the correlation between the logarithmic slope and stellar mass of the galaxy. In their modelling, they find that the steeper the slope of either profile the larger the recovered mass, and their treatment of the tracer density profile could result in biased measurements.

Figure 5.10 shows the enclosed mass within 5 R_{e} as computed from the fiducial set-up described in Sect. 5.5, on the x-axis, and the values from A16 on the y-axis. We use the A16 masses corrected for flattening, rotation and presence of kinematic substructures. The dashed line shows the 1-1 line as a guide. Solid black points show galaxies with robust measurements and we highlight the galaxies with strong rotation signatures as triangles. These galaxies show no systematic difference in the enclosed mass compared with the galaxies that do not show a strong rotation signature. The biggest outlier is NGC 4564 with mass measurement more than 1σ lower than the literature value. NGC 4365 shows more than 1σ higher value of the total mass.

The red diamonds and blue square open symbols indicate the galaxies with strong subpopulations or other complications in the dynamical modelling. These galaxies deviate most from the 1-1 relation. Blue points highlight three galaxies: NGC 4374, NGC 4526, and NGC 7457. A16 found that NGC 4526 and NGC 7457 have a very large number of GCs in kinematic substructures, 25 out of 107 measured GCs and 6 out of 21, respectively. We did not remove such kinematic substructures and in the dynamical modelling framework used in this work, the substructures bias the measurements. NGC 4374 is one of the most massive galaxies in the sample, but it has only 41 observed GCs. A16 do not find strong corrections due to rotation, flattening or kinematic substructures for this galaxy. They compare their measurement with the literature and find a range of enclosed mass values, suggesting that this galaxy requires great care when inferring its total mass. For our measurement, we conclude that the low number of kinematic tracers is the main driver of the difference with the literature values, but a full investigation is beyond the scope of this work. NGC 4526 shows peculiar kinematics but has twice the number of GCs than the other two galaxies. With 107 GCs Jeans modelling can reasonably constrain the enclosed mass, but the inner slope is a factor of 2 shallower than the literature studies. Owing to their complex kinematic properties and observational caveats the measurements of these three galaxies are not robust.

5.6.2 THE POWER-LAW SLOPE OF THE TOTAL MASS PROFILE

To compare the single power-law profiles with the literature we chose B18 (their model **I**) and P17 (their model 1). Both studies used integrated stellar kinematics in different radial ranges. P17 used central kinematics out to 0.9 R_{e} and B18 extended the measurements to 4 R_{e}. They both used JAM modelling with cylindrically aligned velocity ellipsoid and the same total mass-density profile to which they fit a single power-law slope. The spatial extent of their data does not allow to constrain r_s so they fix it to 20 kpc. B18 explored how their constraints on the γ_{tot} change when r_s is left to vary freely. They claim that in this case, the measurements agree within the 1σ uncertainties. Their similar methodology makes these studies ideal for comparison. We find that our results agree within 1σ for the robust sample of galaxies, however, our measurements

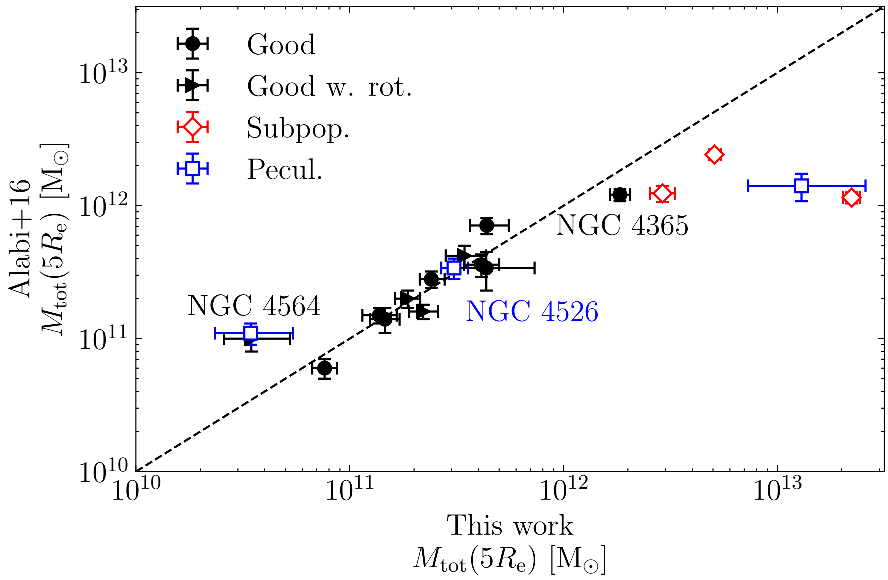

Figure 5.10: Comparison between the enclosed mass within 5 $R_{\rm e}$ measured using GC kinematics presented in this work and A16. The measurements on the x-axis were obtained with axisymmetric Jeans models assuming general NFW total mass density; on the y-axis we report the values from the literature study, which used spherical TME with power-law total mass density distribution. The colours and shapes of the points correspond to the ones used in other figures. The dashed line is a 1-1 line for comparison and not a fit to the data. We find consistent enclosed mass for galaxies with robust measurement, with the exception of NGC 4564 and NGC 4365, highlighted in the figure, which show more than 1σ lower and higher values than those reported in the literature, respectively.

5

have a larger spread. We postulate that this could be a consequence of a more flexible modelling approach and fewer data points used to constrain the model.

The comparison of individual galaxies between this work on the x-axis and literature on the y-axis is shown in Fig. 5.11. The top panel shows the comparison with P17 for the logarithmic slope within 1 $R_{\rm e}$ and on the bottom panel the comparison with B18 within 4 $R_{\rm e}$. The symbols correspond to the ones in Fig. 5.6. The black points highlight the galaxies with robust measurements and within 1σ uncertainties they agree with the literature value. NGC 1023 is more than 1σ from the dashed 1-1 line and is highlighted in the figure.

The values of the slope are systematically lower than the literature values for galaxies shown as blue open squares and red open diamonds similarly as found for the enclosed mass measurement (discussed in Fig. 5.6). We highlight galaxy NGC 4526, which shows enclosed mass measurements consistent with the literature in Fig. 5.10 but the inner slope is more than 1σ shallower than both literature studies. This justifies the exclusion of this galaxy from our robust sample and further supports our initial assignment of kinematic flags.

5.6.3 Mean value of the inner slope and the intrinsic scatter

After determining the samples with robust measurements we investigate the mean value of the inner slope. We consider both the logarithmic power-law values $\gamma_{\rm tot}$ in different radial ranges and the intrinsic inner slope α. The mean values with respective uncertainties are presented in Table 5.8 together with a summary of literature results. The first two rows summarise our results and are followed by literature values determined using different methodologies and tracers. The first row summarises the results only for galaxies without strong rotation signatures and the second row includes the galaxies with strong rotation signatures of the GCS. The third column shows the mean values and 1σ error for the intrinsic inner total mass density slope α. The fourth column is the mean value of the single power-law fit within 1 $R_{\rm e}$, for comparison with P17, who

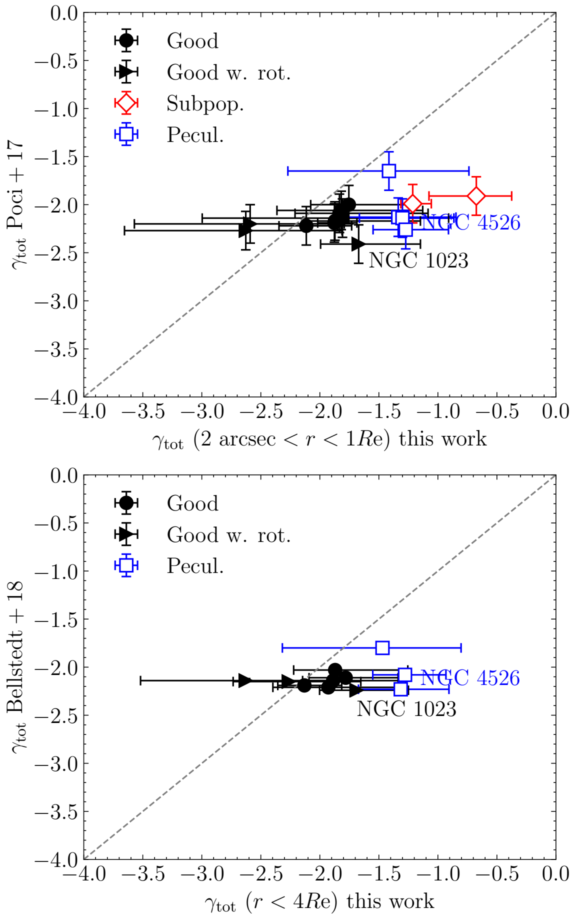

Figure 5.11: Comparison of the logarithmic slope of the total mass-density profile presented in this work on the x-axis and literature studies on the y-axis. The top panel shows the comparison with model 1 from P17, the bottom one with model **I** from B18; the dashed grey line is a 1 to 1 line. The colours and symbols match those of Fig. 5.6 with solid symbols showing robust measurements and open symbols galaxies excluded from the final analysis. The error bars correspond to the 16th and 84th percentile as presented in Table 5.6. In both analyses JAM with integrated stellar kinematics was used; moreover, this work uses GC kinematics while literature studies used stellar kinematics. Within the uncertainties, the measurements of the robust sample agree with the literature.

determined an inner slope of $\langle\gamma_{\rm tot}\rangle_1 = -2.193 \pm 0.016$. The last column shows the mean value for the power-law slope within 0.1-4 $R_{\rm e}$, comparable with $\gamma_{\rm tot} = -2.24 \pm 0.05$ found by B18.

Table 5.8: Mean values of the inner slope and the observed root-mean-square scatter for the robust sample of galaxies from this work and literature studies. The first two rows contain results from this work and are followed by 6 literature investigations using different potential tracers and techniques for z=0 galaxies. For the results from this work, the subsamples used to compute the mean values are highlighted in the first column, with the number of galaxies in that subsample in the second column. The third and fourth columns show the statistics of the intrinsic inner slope with 1σ uncertainties. The 5th and 6th columns list the mean and root-mean-square scatter for the logarithmic slope within $0.1-1\ R_\mathrm{e}$, and the last two columns show the same for the fit in $0.1-4\ R_\mathrm{e}$ as explained in Sect. 5.5.4. The last 6 rows contain the values from the literature studies computed in different radial ranges.

Sample	# gal.			$0.1-1\ R_\mathrm{e}$		$0.1-4\ R_\mathrm{e}$	
		$\overline{\alpha}$	σ_α	$\langle\gamma_\mathrm{tot}\rangle_1$	$\sigma_{\gamma_\mathrm{tot},1}$	$\langle\gamma_\mathrm{tot}\rangle_2$	$\sigma_{\gamma_\mathrm{tot},2}$
good	8	-1.76±0.01	0.83±0.01	-2.03±0.18	0.53±0.19	-2.12±0.16	0.48±0.17
good + w. rot	12	-1.88±0.01	0.94±0.01	-2.14±0.16	0.64±0.16	-2.22±0.14	0.58±0.15
Auger et al. (2010)	73	–	–	-2.078 ± 0.027^1	0.16 ± 0.02^1	–	–
Cappellari et al. (2015)	14	–	–	-2.15 ± 0.03	0.1	2.27 ± 0.06^2	$0.16^\dagger$
Serra et al. (2016)	16	–	–	-2.18 ± 0.03^1	$0.11^{1,\dagger}$	–	–
Poci et al. (2017)	142	–	–	-2.193 ± 0.016^3	$0.15^\dagger$	–	–
Yıldırım et al. (2017)	16	–	–	–	–	-2.25	–
Bellstedt et al. (2018)	21	–	–	-2.12 ± 0.05	–	–	–

[1] Single power law profile used in the fit. [2] In radial range $r<4\ R_\mathrm{e}$. [3] For model **I**. [†] Estimated intrinsic scatter σ_γ.

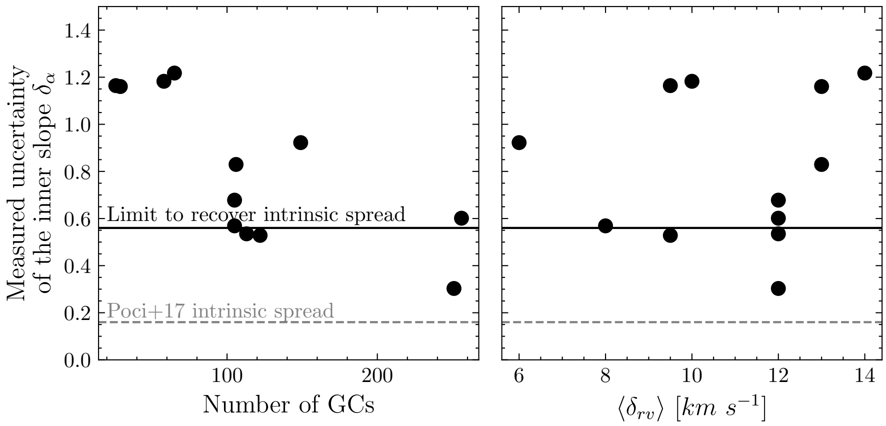

Figure 5.12: Correlation between the measurement uncertainty of the inner slope (from model B) and the number of GCs per galaxy on the left panel, and the median error of the RV on the right panel. The grey dashed line indicates the intrinsic scatter of the inner slope of 0.16 as determined by P17 and Auger et al. (2010). In order to constrain the intrinsic slope on the same level the black solid line indicates the maximal measurement uncertainty needed when using ∼10 galaxies.

Including only the measured slopes of galaxies flagged as *Good* results in a slightly shallower slope than when galaxies with strong rotational signatures are included. When investigating the effect of rotation and velocity anisotropy we did not find evidence linking rotation to a steeper profile and we conclude that our kinematic classification is not linked to the measured values. Our measurements are in broad agreement with these literature studies. Auger et al. (2010) finds slightly shallower slopes, which could be a result of the systematically more massive galaxies that were probed in this study with gravitational lensing. P17 and Yıldırım et al. (2017) use central stellar kinematics, B18 and Cappellari et al. (2015) used extended stellar kinematics and Serra et al. (2016) combined the central stellar kinematics with extended gas measurements; they all agree within 1σ uncertainties.

The literature studies disagree on the value of the $\sigma_{\gamma_{\rm tot}}$, with Cappellari et al. (2015) and Serra et al. (2016) preferring even smaller intrinsic scatter than Auger et al. (2010) and Serra et al. (2016). This low intrinsic spread has been linked with the universality of the inner total mass slope over several magnitudes in stellar mass. With the novel measurements presented in this work, we attempted to constrain the intrinsic spread of the inner slope σ_α (e.g. Kirby et al., 2011, eq. 8). We find that the measurement uncertainties δ_α are such that the intrinsic spread cannot be recovered. This is mainly driven by the low average number of GCs per galaxy, which is strongly correlated with the resulting measurement uncertainty as seen on the left panel of Fig. 5.12. The figure shows how the δ_α for each galaxy is correlated with the number of kinematic tracers on the left panel and the median RV error for GCs on the right panel. The measurement uncertainty is strongly correlated with the number of kinematic tracers while up to a median RV error of 14 km s^{-1} δ_α is not correlated with the velocity errors. The dashed grey line indicates the literature value of the $\sigma_{\gamma_{\rm tot}} \sim 0.16$ consistently found by Auger et al. (2010) and (P17). We investigated what is the limiting precision of α needed to constrain the intrinsic scatter at the same level with 10 galaxies by artificially scaling δ_α. The estimate of that limiting precision is shown with the solid black line highlighting that at least 100 kinematic tracers per galaxy are needed for sufficient precision. For galaxies with fewer observed GCs the modelling has to be supplemented by stellar kinematics or other halo tracers such as planetary nebulae to provide sufficient constraints on the α to recover the intrinsic scatter. Increasing the number of galaxies will have an impact on the recoverability of the σ_α but more detailed quantification of the observing guidelines is beyond the scope of this work.

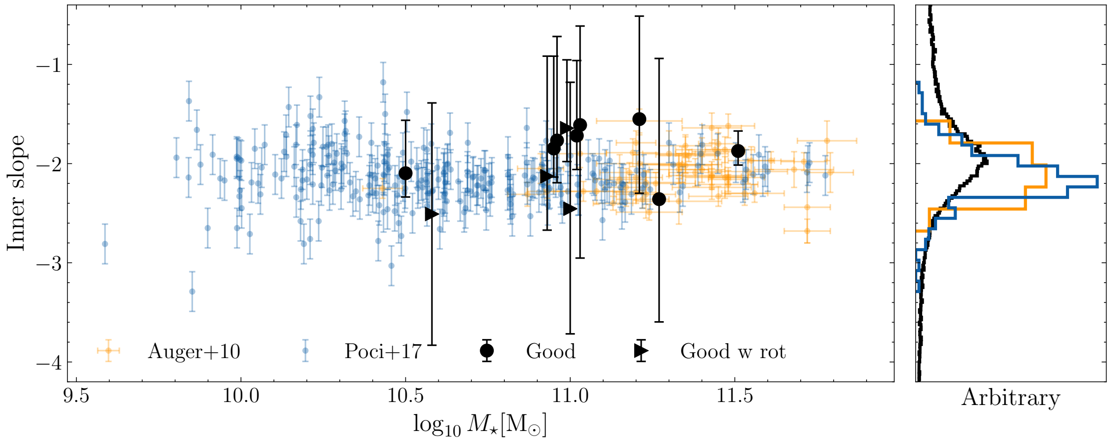

Figure 5.13: Relation between the stellar mass and inner slope on the left panel and distribution of the slopes as determined by this work and literature samples in the right panel. Measurements from this work show the intrinsic inner slope - α of a generalised NFW and literature shows the single power-law slope - $\gamma_{\rm tot}$. The black-filled circles and triangles show the galaxies with robust measurements representing the inner mass slope α as measured in this study from the GC kinematics, extending out to $\sim$8 $R_{\rm e}$. Symbols correspond to those of Fig. 5.6. Large literature samples focused on the single power-law slope only; results from Poci et al. (2017) and Auger et al. (2010) are shown as blue and orange points, respectively. The gravitational lensing from the former study constrained the slope within 0.5 $R_{\rm e}$ and the latter used stellar kinematics within ~ 0.9 $R_{\rm e}$. The arbitrary scaled distribution of the measurements on the right panel shows the distribution of the slopes with colours corresponding to that of the left panel.

5

5.6.4 The relation between the inner slope and stellar mass

Several relations have been reported in the literature linking $\gamma_{\rm tot}$ to different properties of the galaxy. Due to the limited number of galaxies with robust measurements, we focus only on the relation between the stellar mass and inner slope and present our measurements of the intrinsic inner slope α in Fig. 5.13. The literature values in light blue from P17 were computed with the central stellar kinematics with median radius probed 0.9 $R_{\rm e}$. Similarly, the orange points show measurements with gravitational lensing (Auger et al., 2010) with median radius probed 0.5 $R_{\rm e}$.

We do not observe a statistically significant trend of α with the stellar mass. A similar behaviour has been reported by B18 and has also been found in the Magneticum simulations[3] (Remus et al., 2017). Tortora et al. (2014) used spherical isotropic Jeans equations to carry out dynamical modelling of SPIDER galaxies over large mass range and found that $\gamma_{\rm tot}$ becomes progressively shallower with increasing stellar mass, a trend not observed by our study nor by Cappellari et al. (2015).

The large spatial extent to which the discrete dynamical modelling of GCS is sensitive means that we have tracers beyond the scale radius of the total mass profile. Therefore, the SLUGGS GCs are sensitive to the intrinsic inner total mass slope α and we can compare α to the values from the power-law studies of the inner mass slope, but its interpretation is not straightforward.

5.7 Discussion

Comparing with the literature results from A16, P17 and B18 we investigated various properties of the galaxies for potential trends with the environment (field, group, cluster), baryonic content (stellar mass), $(v_{\rm rot}/\sigma)_{\rm GCS}$ as reported by A16, flattening of the GCSs and a number of dynamical tracers on $\Delta\gamma_{\rm tot}$. We did not identify any parameters correlated with systematic offset for any of the 3 literature datasets.

[3] www.magneticum.org

5.7.1 THE LINK BETWEEN INNER SLOPE AND GALAXY FORMATION

The apparent universality of $\gamma_{\rm tot} \sim -2$ has been linked to the formation history of the ETGs. Remus et al. (2013) found in merger simulations that dry major mergers redistribute baryonic and dark matter such that the resulting total mass distribution follows a singular isothermal sphere. This configuration is very stable and only the accretion of large amounts of gas can modify the inner slope. Major mergers were more frequent in the earliest phases of galaxy cluster assembly and Derkenne et al. (2021, 2023) recently studied redshift evolution of $\gamma_{\rm tot}$ finding shallower profiles in cluster galaxies compared to those in intermediate density environments at $z \sim 0.3$. With the trend persisting to $z = 0$ and galaxies in intermediate density environments, that experience fewer major mergers, show negligible evolution of $\gamma_{\rm tot}$ in the past 3-4 Gyrs. Recently, Zhu et al. (2023) showed a strong dependence of the inner slope on the $\sigma_{\rm e}$ and morphological type.

Different galaxy simulations disagree on the values for the inner slope. B18 found that EAGLE[4] simulations (Schaye et al., 2015) produce galaxies with profiles shallower by $\sim 0.3 - 0.5$ than Magneticum simulations (Remus et al., 2017). Galaxies in the latter simulation additionally show anticorrelation between the stellar mass and the inner slope $\gamma_{\rm tot}$ that is not observed in real galaxies. Moreover, Remus et al. (2017) studied the correlations between the galaxy properties and $\gamma_{\rm tot}$ for three different simulations that vary in whether they incorporate active galactic nuclei (AGN) and star-formation feedback. They find that the AGN feedback in their simulations acts to erase the correlation between the slope and stellar mass of the simulated ETGs. When comparing the results for galaxies from the Magneticum simulation with those from the Oser simulations (Oser et al., 2012) that do not include AGN feedback, they find large discrepancies and systematically steeper values of $\gamma_{\rm tot}$ for Oser simulated ETGs. The study also finds evidence that the slope in simulated galaxies is steeper at higher redshift and a strong anti-correlation between the central stellar surface brightness and $\gamma_{\rm tot}$.

Literature investigations have repeatedly found a narrow intrinsic spread in $\gamma_{\rm tot}$ (with $\sigma_\gamma^{\rm int.} \sim 0.16$) for ETGs (P17, Auger et al., 2010). Two studies with extended potential tracers found an intrinsic spread of 0.11 for ETGs using stellar kinematics out to 4 $R_{\rm e}$ (Cappellari et al., 2015) and coupling central stellar kinematics with HI circular velocity out to 6 $R_{\rm e}$ (Serra et al., 2016). Studies have found that bulge-halo conspiracy requires a non-universal stellar initial-mass function and feedback mechanisms to counteract dark matter contraction resulting from dark matter cooling (e.g. Dutton and Treu, 2014). However, observations have primarily relied on gravitational lensing or IFU-based dynamical modelling. Both provide information well within 1 $R_{\rm e}$, where dark matter fraction is on average $< 15\%$. While Auger et al. (2010) used a single power-law slope for the total mass density, P17 had a more realistic double power-law profile with a fixed transition radius. B18 used extended stellar kinematics out to 4 $R_{\rm e}$. However, the spatial extent of the tracers was not sufficient to freely vary the scale radius of the total mass profile.

Recently, Derkenne et al. (2023) showed that fixing the scale radius has a systematic impact on the recovered slope α. We have also shown that the radial region where the inner slope $\gamma_{\rm tot}$ is fit will impact the recovered value of the parameter as seen in Table 5.8, a trend commented also by B18. With discrete dynamical modelling of the GCs we have shown in this work that it is possible to recover the intrinsic inner slope of the total mass profile, relaxing the assumption on the scale radius. This opens an avenue for dynamical studies of a larger number of galaxies to probe the intrinsic slope α and better understand the interplay between the baryonic and dark matter physics in the process of galaxy formation.

In this work, we agree with the literature studies and find the mean inner slope $\gamma_{\rm tot}$ is steeper than isothermal, but the exact value of the profile is strongly dependent on the radial range where the profile is fit. Additionally, because of our flexible modelling approach and the large spatial extent of our tracers, our results are sensitive to the intrinsic inner slope of the double power-law profile α. As can be seen on Fig. 5.9 the projected positions of the GCs in NGC 3377 can also be found around the best-fit scale radius of the total mass profile, meaning that there is enough power in the data to constrain the intrinsic inner slope.

[4] Evolution and Assembly of GaLaxies and their Environments.

5.7.2 Limitations of our modeling approach

Discrete dynamical modelling is very flexible, yet great care is needed to understand the intrinsic and observational properties of the GCs. Kinematically cold substructures or biased sampling of the underlying velocity field can result in the biased inference of the modelled parameters, an effect that is strongly dependent on the number of the kinematic tracers.

5.7.2.1 Effect of subpopulations

A subset of galaxies shows the presence of strong subpopulations that are not relaxed or trace the group/cluster potential instead of the galaxy potential. These galaxies were identified by the rising or constant velocity dispersion out to 7 $R_{\rm e}$ from the centre without a strong presence of rotation. NGC 1407, NGC 4486 (M87) and NGC 5846 are all the central galaxies of their group and NGC 4486 is the second brightest galaxy of the Virgo cluster. Their GCS have been extensively studied in the literature.

Zhu et al. (2016) and Napolitano et al. (2014) showed how the velocity dispersion of red GCs in NGC 5846 rises in the outskirts of the galaxy. Both red and blue GCs also show distinct orbital anisotropy with blue showing mild radial anisotropy and red tangential anisotropy in the outskirts. Similarly, Pota et al. (2015) found a kinematically distinct red and blue population of GCs in NGC 1407, with the velocity dispersion of blue GCs increasing towards the outskirts. Strader et al. (2011) carried out a comprehensive kinematic and dynamical study of M87 (NGC 4486), revealing complexity and strong presence of substructures in the GCS of the galaxy pointing to active assembly.

NGC 1407

To investigate whether the presence of subpopulations is causing the systematic offsets we modeled separately the blue and red populations of GCS in NGC 1407 as a test case. Romanowsky et al. (2009) carried out a kinematic analysis of the red and blue populations using the colour information $(g' - i') = 0.98$ to separate the populations. They found that the dispersion profile decreases up to $R \sim 20$ kpc and then starts to increase. They report low v_{rot}/σ in the outer parts and find signs of misaligned rotation signature between the red and blue population with hints of tangentially biased orbits in the outer regions. The blue population shows the presence of a cold moving group around $R \sim 40$ kpc.

We used the photometry and kinematics from the SLUGGS survey, which has 356 kinematic members NGC 1407 and a median uncertainty on the velocity measurements of 15 km s^{-1}. To separate the blue and the red subpopulations we used the literature value of $(g - i)_0 = 0.98$ (Romanowsky et al., 2009), resulting in 49% of blue and 51% of red GCs. The colour distribution is shown in the left panel of Fig. 5.14 with clear bimodality highlighted by the two Gaussian components. Then we carry out the same completeness and tracer density analysis as described in Sect. 5.3 and re-run the dynamical modelling.

After subtracting the systemic velocity of the galaxy ($v_{\rm sys} = 1779$ km s^{-1}, see Table 5.1) We binned the GCs in radius and used Bayesian approach to evaluate the mean velocity and dispersion in each bin. We compare the individual velocities of GCs with the radial trend of $v_{\rm rms}$ to investigate the behaviours of the two subpopulations shown in the right panel of Fig. 5.14. The blue points and lines correspond to the results for the blue GCs and show an increasing $v_{\rm rms}$ with radius. In comparison, the red GCs show a flat $v_{\rm rms}$ within 1 $R_{\rm e}$and a mildly declining profile at larger distances. This different behaviour suggests that the red GCs are tracing the potential of their host galaxy. In comparison, the rising $v_{\rm rms}$ of blue GCs in the outskirts could be due to the blue GCs tracing the potential of the galaxy group, as also commented by Chaturvedi et al. (2022). This trend further motivates separate treatment of both subpopulations in the dynamical modelling of this galaxy.

We show the resulting best-fit parameters of the total mass profile from dynamical modelling of the red and blue populations in Fig 5.15. The black points show the results when both GC populations are modelled as one, the blue and red points show the results from modelling the

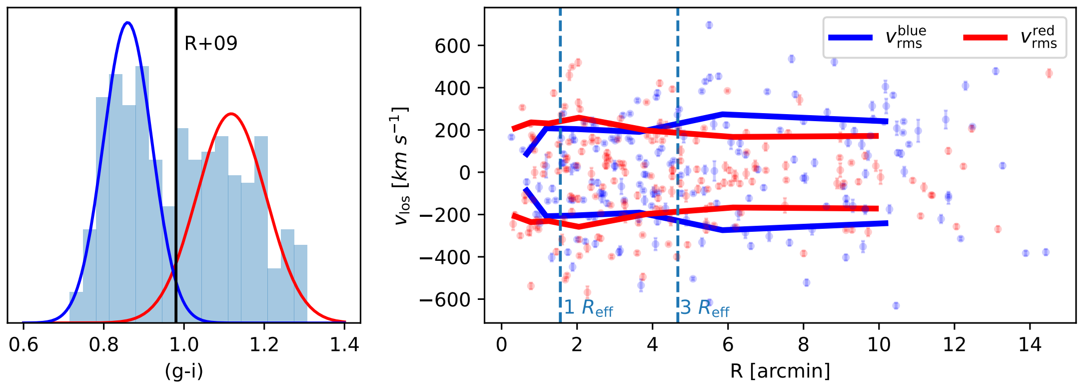

Figure 5.14: Colour and velocity distribution of GCs in NGC 1407. The left panel shows the colour distribution and the vertical line highlights the separation between the two subpopulations as identified by Romanowsky et al. (2009). The overplotted Gaussians in corresponding colours are computed based on the moments of the blue and red GCs' colour distributions. The velocities of individual GCs on the right panel are shown as points with associated measurement uncertainties and radial trend of the $v_{\rm rms} = \sqrt{\overline{v_{\rm los}}^2 + \sigma_{\rm los}^2}$ as solid lines of the blue and red GCs, in respective colours. The light blue dashed lines highlight the 1 $R_{\rm e}$ and 3 $R_{\rm e}$ of the stellar component for reference (see Table 5.1.)

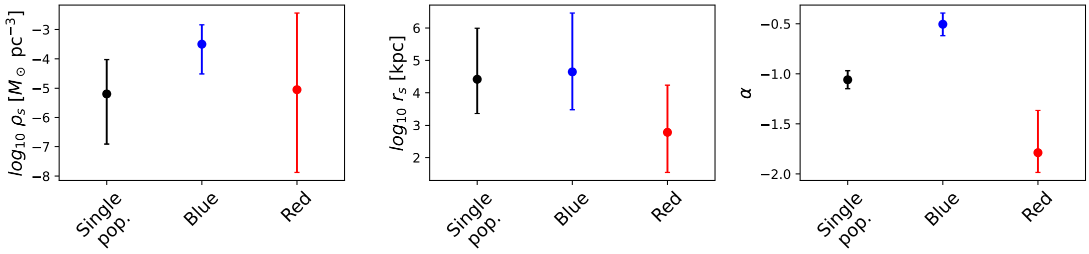

Figure 5.15: The best-fit parameters of the total mass profile when GCs are modelled as single (in black) or two different populations (red and blue in respective colours). The error bars show the associated 16th and 84th-percentile uncertainties.

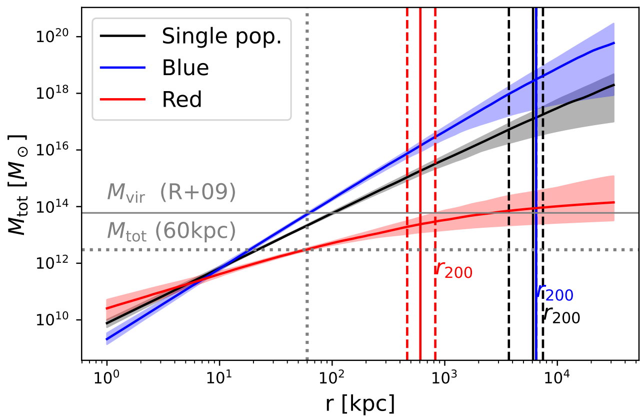

Figure 5.16: Comparison between the enclosed mass when blue and red GCs are modelled separately (shown in respective colours) and when they are treated as a single population (in black). The solid grey line shows the virial mass found by (Romanowsky et al., 2009) and the dotted line the total mass within 60 kpc.

corresponding GC population. The effect of the two populations is seen on the middle and right panel for the r_s and α respectively. The red population results in smaller r_s and a steeper profile compared with the blue population.

A similar trend is seen in Fig. 5.16. Where by modeling only the red populations the resulting enclosed mass is consistent with literature studies and the results using blue GCs have enclosed mass at the order of galaxy clusters. This supports our hypothesis that the subpopulations are driving the discrepancies in pour measurements of galaxies flagged as *Subpop.*

Peculiar GCs

A subset of galaxies, NGC 4374, NGC 4459, NGC 4526, and NGC 7457 showed peculiar trends in their velocity field. All but NGC 4526 have fewer than 40 GCs sparsely populating their halo. NGC 4526 has a peculiar velocity field in the GCS with the central region showing strong rotation and the outer region showing a velocity offset. This particular galaxy has twice the number of GCs compared with the other galaxies flagged as *Subpop.* and the recovered enclosed mass is consistent with the literature studies by A16, as highlighted in Fig. 5.10. However, the inner slope is more sensitive to the peculiar features in the observed GC velocity field, resulting in a biased measurement of the inner slope α shown on Fig. 5.11.

To understand the discrepancy with the literature studies we explored trends with the galaxy stellar mass, environment, and rotation parameter as reported by A16, the Sérsic index and the number of tracers. We found the latter has the strongest impact together with a non-uniform spatial distribution of the tracers. These observational effects result in the shallower profile and overestimated mass when using discrete dynamical modelling. As for the galaxies discussed in Sect. 5.7.2.1, we consider our measurements for galaxies flagged as *Subpop.* not robust.

5.8 Summary and future work

We carried out the discrete dynamical modelling of a large number of GCSs from the SLUGGS survey. Detailed analysis of the tracer density profile and the investigation of the GC velocity field limited the number of galaxies we modelled from 27 to 21 and we present robust measurements for 12 galaxies. These galaxies have a sufficiently large number of kinematic tracers without a strong observational footprint or presence of subpopulations. We used Bayesian inference and MCMC sampler to efficiently sample the posterior and find the best-fit parameters. We find that informative priors on $\log \rho_\mathrm{s}$ and $\log r_\mathrm{s}$ can help break the degeneracy in these parameters.

We explore 3 different model set-ups (A, B, C) to investigate how the modelling assumptions impact the best-fit parameters. Models A and B assume non-rotating and isotropic GCs and model C explores the impact of velocity anisotropy and rotation on the recovered parameters of the total mass profile. We find that β_z and κ have a negligible impact on the enclosed mass and inner slope. We identify model B as the fiducial model and find that the logarithmic inner slope of the 12 galaxies with robust measurements is $\langle\gamma_\mathrm{tot}\rangle = -2.22 \pm 0.14$ in the range 0.1-4 R_e. These values agree within the uncertainties but our values are systematically shallower than the literature measurements. This could be a result of our more flexible modelling approach. The large spatial extent of the kinematic tracers in tandem with the discrete modelling approach enables us to constrain the transition radius of the total mass slope and measure an intrinsic inner slope $\overline{\alpha} = 1.9 \pm 0.01$ that is shallower than γ_tot.

We find a large rms scatter in the inner slope which is in part driven by the large measurement uncertainties. We demonstrate that in order to constrain the intrinsic scatter at the level of 0.16 at least 100 kinematic tracers are needed per galaxy.

In Sect. 5.7.2.1 we have shown that the modelling results of dispersion-dominated systems with CJAM are minimally affected by rotation and anisotropy when the number of tracers is sufficiently large, but providing quantitative guidelines is beyond the scope of this work. Modelling merger remnants and GCS with a strong presence of distinct subpopulations leads to biased results.

Namely, the enclosed mass is overestimated by several orders of magnitude and the density profile is biased towards shallower inner slope α.

Both simulations and observations provide strong evidence that the total mass slope cannot be extrapolated with a single power-law profile at a large spatial extent and new observations will enable both larger photometric and kinematic samples of discrete tracers in the nearby universe. We can use them to characterize the mass distribution on large scales and constrain structure formation models. This work highlights the benefits and caveats of using sparse dynamical tracers in the haloes of the galaxies. Combining integrated stellar kinematics in the inner regions with more extended halo tracers can provide stronger constraints on the central mass distribution. Our work can be expanded by including higher Gauss-Hermite moments or assuming an intrinsic 3D Gaussian velocity distribution instead of the 1D projected.

With the upcoming wide-field photometric surveys, larger samples of extragalactic GCs will be observed and this will open an avenue for more studies of these low surface-brightness diffuse haloes that contain rich information on the total mass content of galaxies. With the full mass profiles, dark matter content can also be investigated over large galactocentric radii. We would also like to further explore methods to improve the precision of the modelling results and better account for the kinematic substructures.

Chapter 6

Dark matter halo shape in NGC 5128 with GCS

"We should not fear questioning our beliefs, for only through questioning can we truly understand and advance our understanding of the world."
- Steven Weinberg

Declaration of published work

This chapter includes text already published or submitted (Veršič et al., 2023, subm.). The text was adapted for this thesis and as a result, there may be partial overlap with those publications.

6.1 Introduction

As discussed in Sect. 1.3 understanding the intrinsic shape of galaxies is essential to prevent biased conclusions when interpreting results derived from dynamical modelling. In this work, we use the dynamical modelling approach outlined in chapter 2 to constrain the shape of the dark matter halo hosting the NGC 5128 galaxy.

NGC 5128 is the closest ETG to us classified as giant Elliptical or S0 (Harris, 2010) and has clear evidence of a recent accretion history or possibly a major merger (Wang et al., 2020, and references therein). It has a stellar mass of 1.6×10^{11}M$_{\odot}$ (Hui et al., 1995) and is estimated to host up to 2000 GCs (e.g Harris et al., 2006). It hosts the radio source Centaurus A and, for simplicity, we will refer to the galaxy as CenA. Its proximity has enabled detailed studies of the resolved red giant branch (RGB) stars out to more than 25 $R_{\rm e}$ (140 kpc) (Rejkuba et al., 2022), providing constraints on the density distribution of the stellar halo. Spectroscopic observations of a large population of PNe (Peng et al., 2004a; Walsh et al., 2015) and GCs (Hughes et al., 2022; Peng et al., 2004b; Woodley et al., 2010b) over a vast halo area provide a necessary sample of kinematic tracers for dynamical modelling that we are exploiting in this work. Several literature studies took advantage of these kinematic samples to measure the spherical mass distribution of this galaxy (Dumont et al., 2023; Hughes et al., 2021b; Peng et al., 2004a; Woodley et al., 2007, 2010b). Observational evidence from PNe kinematics (Hui et al., 1995; Peng et al., 2004a; Pulsoni et al., 2018) however supports strong triaxiality of the CenA stellar component and the gravitational potential. In this work, we aim to test the validity of the assumption of spherical symmetry of the CenA DM halo by means of axisymmetric dynamical modelling.

We utilise the large photometric and kinematics datasets of GCs recently compiled to determine the shape of DM halo of NGC 5128. Throughout the chapter, we adopt the following properties: distance $D = 3.8$ Mpc (Harris et al., 2010)[1], stellar effective radius of $R_{\rm e}= 5$ arcmin and position angle PA = 35^o (Dufour et al., 1979), and systemic velocity $v_{\rm sys} = 541$ km s^{-1} (Hui et al., 1995). In Sect. 6.2 we introduce the photometric and kinematic datasets used in this work. In Sect. 6.3 we present a careful analysis of both datasets. The aim of the analysis is to determine the population of GCs that is consistent with being dynamically relaxed in the gravitational potential of CenA. We describe the dynamical modelling tool used in this work in Sect. 6.4 and the statistical approach to find the best-fit parameters in Sect. 6.5. We present the results of the modelling in Sect. 6.6 and discuss the findings in Sect. 6.7.

6.2 Data

6.2.1 Photometric dataset

In this work, we use the photometric catalogue from Taylor et al. (2017) (hereafter T17) with multi-band *u'g'r'i'z'* photometry based on the observational programme aiming to characterise the baryon structures around CenA with the *Dark Energy Camera* (DECam, Taylor et al., 2016). T17 used 500,000 detected sources within ∼140 kpc of CenA and covering ∼21 deg^2. To remove fore- and background contamination, the authors used measurements of full width at half maximum (FWHM) together with the location of kinematically-confirmed GCs from Woodley et al. (2010a) in the $(u' - r')_0$ - $(r' - z')_0$ plane. The GCs are well separated from Milky Way stars at the red end of the colour-colour plane, however, the confusion increases for blue GCs (see their Fig.2). The final dataset of ~ 3200 candidate GCs is therefore still affected by contamination, which we discuss in more detail in Sect 6.3.

We excluded GCs that did not have photometry in all of the photometric bands and selected those within $5 < R < 130$ arcmin, to remove the impact of the inner polar dust ring and observational footprint. Additionally, we corrected the online catalogue for extinction. We use the

[1] At the distance of CenA, 1 arcmin corresponds to 1.1 kpc.

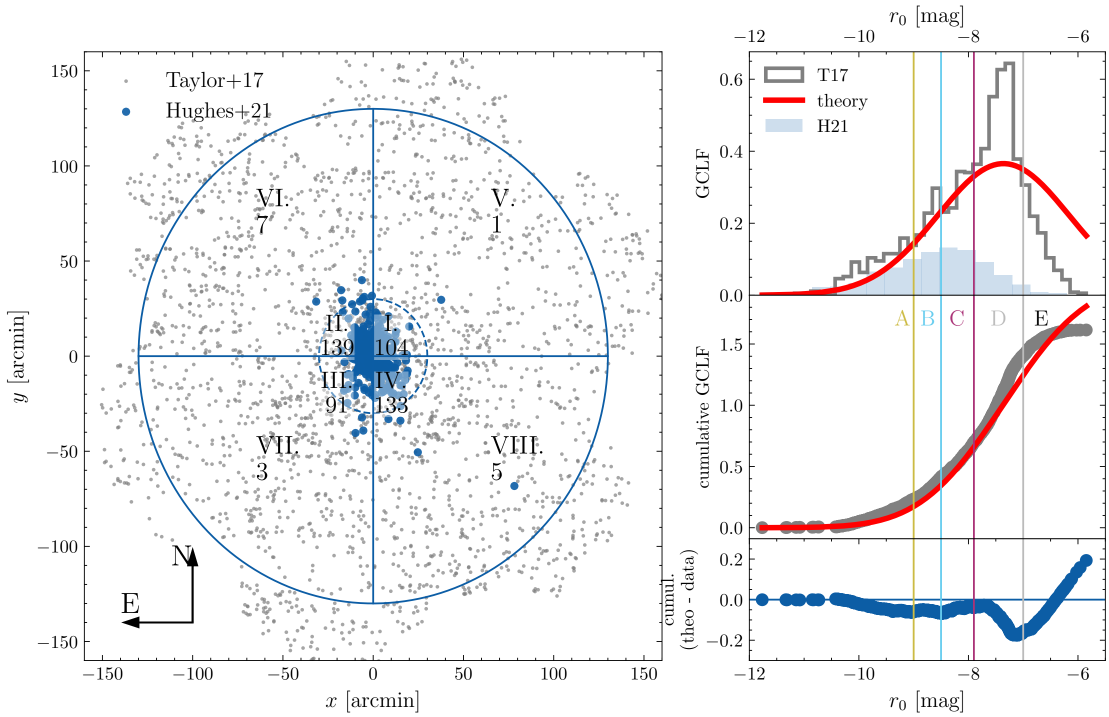

Figure 6.1: The spatial (left panel) and magnitude (right panels) distribution of the photometric and kinematic datasets. The photometric GC candidates from T17 are shown in grey and the kinematic dataset from H21 in blue. The blue circles and lines on the **left panel** delimit the inner and outer quadrants. The Roman numerals indicate the number of the respective quadrant, the Arabic numbers indicate the number of GCs with kinematic measurements in the corresponding quadrant. The **right panels** show the comparison between the observed and theoretical GCLF. The top panel shows the GCLF and the middle panel the cumulative GCLF, which allows for more precise determination of the magnitude subsamples. Both theoretical GCLFs are scaled, to match the total observed number of GCs in regions A-C. The bottom panel is based on the cumulative GCLF from the middle panel and it shows the difference between the theoretical and observed distributions. The coloured vertical lines delineate different magnitude subsamples labelled with A-E in corresponding colours.

online tool IRSA[2] to obtain the reddening correction $E(B-V)_{\rm SFD}$[3] at the location of each GC. We combine these with $A_b/E(B-V)_{\rm SFD}$ values from Schlafly and Finkbeiner (2011, see Table 6) for $R_V = 3.1$ in relevant SDSS bandpasses (b) to compute the colour excess A_b. The reddening corrected magnitude is then $b_0 = b - A_b^{\rm SFD}$.

6.2.2 Kinematic catalogue

In this work, we use a heterogeneous compilation of literature kinematic measurements of GCs as presented in H21 (see their Sect. 3 and Table 4). Together with the positions and velocities the authors also report their g and r-band photometry. Out of the whole sample of 557 GCs only 482 have both photometric and kinematic information and we use this subset of GCs in the following analysis and dynamical modelling. This is the largest sample of kinematic measurements for CenA GCs in the literature and the authors carefully matched the different datasets. The 482 GCs span a magnitude range $-11 < r_0 < -6$ mag and have a median radial extent of 8 arcmin (9 kpc, 1.6 $R_{\rm e}$) with 95% of the GCs within 25 arcmin (27 kpc, 5 $R_{\rm e}$). The median velocity uncertainty is 33 km s^{-1}.

[2]https://irsa.ipac.caltech.edu/applications/DUST/
[3]SFD stands for the dust corrections from Schlegel et al. (1998).

The spatial distributions of both the kinematic and photometric catalogues used in this work are shown on the left panel of Fig. 6.1. The dashed and solid blue circles mark the radius of 30 arcmin and 130 arcmin respectively and they delimit the quadrants used in Sect. 6.3.1 to determine the magnitude-selected subsample of GC candidates from T17 that are consistent with a relaxed axisymmetric distribution. The photometric dataset extends much further than the kinematic one. The photometric dataset at $R > 130$ arcmin clearly shows the observational footprint. The kinematic sample is concentrated in the inner 30 arcmin ($\sim$6 $R_{\rm e}$), with a few GCs located in the outer halo. It also shows an elongation in the NE - SW direction, with a larger number of GCs in the II. and IV. quadrants compared with I. and III. in the inner halo. The same trend is also seen in the outer halo, but the number of GCs there is significantly lower.

6.3 Selection of the relaxed tracer component

The dynamical models used in this work (see Sect. 2.2) assume that the kinematic tracers are relaxed and fully phase-mixed in the gravitational potential. Additionally, they require accurate characterization of their spatial distribution, the tracer density profile.

The presence of shells, streams and a young population of halo stars all support a recent merger scenario of CenA (e.g. Crnojević et al., 2016; Malin et al., 1983; Rejkuba et al., 2011; Rejkuba et al., 2005). Recently Wang et al. (2020) used an N-body simulation that can reproduce several observed features of the galaxy. The major merger scenario dates the merger back to $\sim$6 Gyrs, with the final fusion of the progenitors $\sim$2 Gyrs ago. Woodley et al. (2010a) found that CenA's globular cluster system is dominated by old GCs ($\tau > 8$ Gyrs) and has evidence of intermediate age ($5 < \tau < 8$ Gyrs) and young ($\tau < 5$ Gyrs) populations. The metallicities and ages of the GCs and halo stars suggest that few minor mergers took place after the bulk of the galaxy was assembled $\sim$10 Gyrs ago (e.g. Beasley et al., 2008; Woodley et al., 2010a). Such timescales suggest that a population of GCs may not be completely phase-mixed in the CenA potential and necessitates a careful photometric and kinematic analysis to determine the relaxed population of GCs for the modelling.

In this section, we present our analysis of the photometric GC candidates from T17 to identify the relaxed population. Furthermore, we analysed the kinematic GC catalogue from H21 and used the smooth component of the PN velocity field as determined by Pulsoni et al. (2018) to investigate the possible presence of prominent non-relaxed features. Lastly, we present how we build the tracer density profile used for dynamical modelling.

6.3.1 Analysis of the photometric dataset

To build up the tracer density profile of the relaxed GC population we followed the two-step approach presented in Veršič et al. (2024). In the first step, we select a subsample of GCs that is complete up to a limiting magnitude and radius and in the second step we fit an analytic function to the complete subsample. A hallmark of a clean and dynamically-relaxed sample of GCs is that the magnitude distribution should closely follow a lognormal globular cluster luminosity function (GCLF) up to the completeness limit of the survey and the spatial distribution should be close to point symmetric. For CenA we adopt literature values TOM_r =-7.36 and σ_r =1.2.

Comparison between observed and theoretical GCLF

Deep observations of GCs in the nearby Universe have revealed that the magnitude distribution of GCs around galaxies follows a nearly universal shape (e.g. Harris et al., 2014; Jordán et al., 2006; Rejkuba, 2012). The Gaussian shape of the GCLF is characterised by a peak turnover magnitude (TOM_r) and a spread (σ_r). The values of these parameters mildly depend on the mass of the host galaxy (Villegas et al., 2010) and, for CenA, we adopt literature values TOM_r =-7.36 and σ_r =1.2. In the first step of the analysis, we leverage the universality of the GCLF to further remove contaminants from the T17 catalogue of GC candidates.

Table 6.1: Overview of the different magnitude ranges defined in this work. The subsample name is shown in Col. 1. The r_0 band magnitude range of the corresponding subsample is in Col. 2 with the number of candidate GCs from the T17 dataset in Col. 3 and theoretical prediction based on the work by H21 in Col. 4. The ratio between the number of theoretically predicted GCs and candidate GCs ($N_{\rm GC}^{\rm theo}/N_{\rm GC}$) is shown in Col. 5. The last column shows the fraction of red GCs based on the separating magnitude of $(u-z) = 2.6$.

	Mag cut	$N_{\rm GC}$	$N_{\rm GC}^{\rm theo}$	$N_{\rm GC}^{\rm theo}/N_{\rm GC}$	$f_r^{\dagger}$
all	–	2341	1450 ± 160	0.62 ± 0.07	0.48
A	$r_0 < -9$	338	124 ± 13	0.37 ± 0.04	0.36
B	$-9 \leqslant r_0 < -8.5$	259	123 ± 13	0.48 ± 0.05	0.41
C⋆	$-8.5 \leqslant r_0 < -7.9$	412	225 ± 24	0.55 ± 0.06	0.53
D	$-7.9 \leqslant r_0 < -7$	1029	422 ± 46	0.41 ± 0.05	0.56
E‡	$r_0 \geqslant -7$	303	554 ± 61	1.83 ± 0.2	0.35

† Fraction of GCs with $(u-z)_0 \geqslant 2.6$.
⋆ The most relaxed sample of GCs.
‡ This subsample is strongly affected by the magnitude completeness limit of the survey.

To remove the effect of the central polar dust ring and the observational footprint of DECAM (as seen in Fig. 6.1), we additionally limited the sample to 4 arcmin $\leqslant R \leqslant 130$ arcmin (4.4 kpc $\leqslant R \leqslant$ 143 kpc). By comparing the theoretical GCLF and the observed magnitude distribution, we identified 5 different photometric subsamples, which we labelled A-E. The observed GCLF corrected for distance and extinction is compared with the theoretical GCLF. The right panels in Fig. 6.1 show the two GCLFs together with the delineation of the different magnitude subsamples. The limiting magnitudes that correspond to the different subsamples are shown in Table 6.1. Column 3 shows the number of candidate GCs in the corresponding magnitude range and in Column 4 we computed the estimated number of GCs based on the lognormal GCLF and a total of $N_{\rm CG} = 1450 \pm 160$ as estimated by H21.

Based on the strong deviations from the theoretical GCLF, we refer to all sources with $r_0 > -7.9$ (D, E) as **faint** and $r_0 \leqslant -7.9$ (A-C) as **bright** in the following discussion. The brightest GC bin A is expected to have the lowest contamination fraction, with the contamination expected to increase in fainter magnitude bins; a trend that is observed in subsamples D and E. Subsample D shows the largest excess of observed GCs with respect to the theoretical GCLF, and the completeness limit of the survey is evident in subsample E, with the number of GCs dropping rapidly towards the fainter magnitudes. The faint sources are progressively affected by the survey's incompleteness and contamination, therefore we excluded them from the subsequent analysis.

On the bright end, we observe less strong deviations between the observed and theoretical GCLF. The brightest magnitude bin A has potential contributions from ultra-compact dwarfs (UCDs, Dumont et al., 2022), that have distinct origins from GCs (Haşegan et al., 2005; Mieske et al., 2008; Voggel et al., 2020), therefore they could bias the GC tracer density profile. There is an unexpected overdensity of sources in subsample B that deviates from the theoretical GCLF. Identifying whether this is a real feature or the result of the GC candidate selection process is beyond the scope of this work.

Among all of the samples, subsample C shows the best agreement between the theoretical and observed GC numbers. The values in Cols. 4 and 5 of Table 6.1 should be taken as guidelines and not as exact contamination fractions, since different studies estimate the total number of GCs in CenA from 1000 to 2000 GCs (Harris et al., 2010; Harris et al., 2006), which would alter the exact values of the fraction, although the general trends would remain.

POINT SYMMETRY OF MAGNITUDE SELECTED SUBSAMPLES

To further investigate whether the bright GC subsamples are consistent with being dynamically relaxed, we investigate the azimuthal variation of GCs in 8 quadrants as shown in Fig. 6.1. Guided by the findings of Rejkuba et al. (2022), who reported a transition between the inner and outer halo of RGB stars at $R \sim 30$ arcmin, we separately inspected the number of sources in 4 quadrants

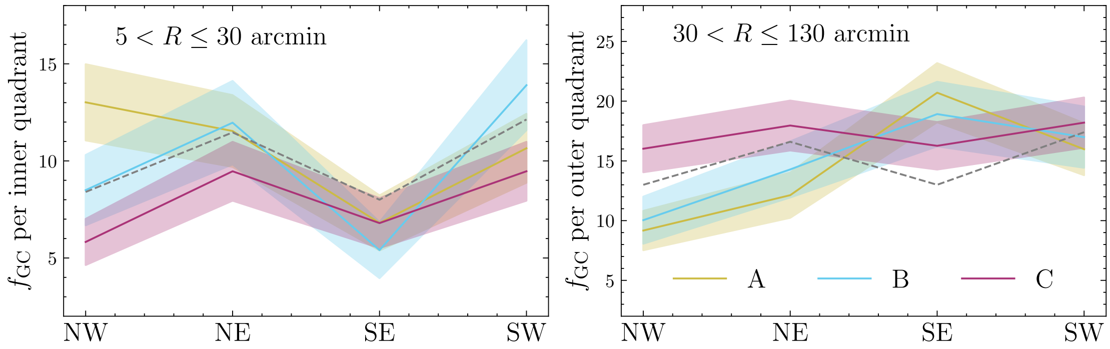

Figure 6.2: The fraction of candidate GCs in each of the 8 angular bins as shown on the left panel in Fig. 6.1. We focus on the subsamples A, B and C in yellow, light blue and purple, respectively as defined on the right panels in Fig. 6.1 and Table 6.1. The left panel shows the azimuthal variation of the fraction of GCs in the inner halo ($5 < R < 30$ arcmin) and the right panel the outer halo ($30 < R < 130$ arcmin). The shaded regions show the associated 1σ uncertainties. The stellar position angle is along NE - SW. To guide the eye, the grey dashed lines show an azimuthal variation for a mock ellipsoidal distribution of points aligned along the CenA stellar PA.

of the inner ($5 < R \leqslant 30$ arcmin) and outer ($30 < R \leqslant 130$ arcmin) regions. These regions are shown in Fig. 6.1 as solid and dashed lines for the outer and inner halo regions, respectively.

The azimuthal variation of the fraction of GCs for the subsamples A, B and C in each of the 8 quadrants is shown in Fig. 6.2. A flattened point-symmetric distribution of tracers will show an increased fraction along the major axis of the flattened system. For comparison, we also sampled positions of mock GCs from an elliptical distribution aligned with the stellar PA. The azimuthal variation of such a point-symmetric distribution is shown with a grey dashed line. The coloured lines show the fraction of GCs compared with the subsample as $f_{\rm GC} = N_{i,\rm quad.}/N_i$ [%], where i stands for A, B and C, coloured yellow, light blue and purple, respectively. The shaded regions highlight the corresponding 1σ uncertainty region. The orientation of the stellar major axis is along the NE - SW direction and the magnitude-selected population C agrees best with the same alignment both in the inner and outer halo regions. This subsample exhibits a higher than 1σ difference in the fraction of the sources along the major and minor axis.

Subsample A shows deviations from point symmetry both in the inner and outer halo indicating a strong presence of non-relaxed features. Subsample B does show signs of point symmetry in the inner regions, however in the outer regions the behaviour mimics that of subsample A. There has been recent observational evidence supporting the presence of a younger and brighter population of GCs that might not be fully relaxed, which might explain the trends we observe (Dumont et al., 2022; Voggel et al., 2020). However, as is evident from Table 6.1, there might still be substantial contamination and it is beyond the scope of this work to identify whether the source of the deviation from point symmetry in subsamples A and B is intrinsic or observational. Therefore, we adopt subsample C as the most relaxed sample of candidate GCs from T17 and use it to determine the tracer density profile.

6.3.2 PNe vs GCs velocity field

Radial velocity measurements in the H21 dataset offer the possibility to investigate whether this sample of kinematic tracers is phase-mixed in the galactic potential. Non-relaxed structures, originating in a recent interaction, appear as overdensities in phase space or perturbations of a point-symmetric velocity field (e.g. Coccato et al., 2013). In this section, we investigated whether the kinematic sample of GCs is consistent with a smooth, point-symmetric velocity field or whether there are substructures that sample a broader range of magnitudes. We investigate both the whole kinematic sample as well as the magnitude selected subsample C. The magnitude distribution of the kinematic sample is shown in Fig. 6.1 as a light blue histogram on the top right panel.

Table 6.2: Percentage and absolute number of GCs outside of the n$\times\sigma$ range of the PN velocity field. 1σ [32%] 2σ [5%] 3σ [0.2%].

sub sample	Per. of n$\times\sigma$ outliers			No. of n$\times\sigma$ outliers			$N_{\mathrm{GC,tot}}$
	1σ	2σ	3σ	1σ	2σ	3σ	
All	30.3	4.1	0.2	146	20	1	482
All blue	30.4	3.5	0.4	78	9	1	257
All red	30.2	4.9	0.0	68	11	0	225
C	34.7	6.6	0.8	42	8	1	121
C blue	32.3	3.1	1.5	21	2	1	65
C red	37.5	10.7	0.0	21	6	0	56

Compared with the photometric dataset it samples a narrower range in magnitude, due to the brighter limiting magnitude of the spectroscopic observations.

To investigate the presence of such features, we take advantage of the results from Pulsoni et al. (2018). The authors used the PN catalogue from Walsh et al. (2015) as tracers of the stellar halo kinematics to determine the minimum relaxed velocity and velocity dispersion fields. Non-relaxed structures are higher-level perturbations of the relaxed field and the authors found evidence for deviation from a point-symmetric velocity field at all radii. In this work, we consider the point-symmetric model fitted to the PNe as a good proxy for the mean velocity field of the relaxed population and thus use it for comparison with the GCs.

We carry out this analysis by using the entire sample of GCs with velocity measurements as well as separating them by colour. A more detailed discussion on the colour distribution follows in the next section and here we adopt a colour cut of $(g-r)_0$ = 0.74 to separate the blue and red GCs. We used this combination of photometric bands because it was available for the whole kinematic sample and a two-component Gaussian mixture model to determine the colour cut.

To compare the GC velocities with the PN velocity field, we used the radial variations of the harmonic expansion coefficients to generate the moments of the smooth PN LOS velocity field at the position of each GC. The coefficients were computed in fixed annular bins and we used a linear interpolator to compute the values of these parameters for arbitrary radii within the extent of the literature measurements. Using higher-order interpolators resulted in unrealistic radial variations of the coefficients.

The point-symmetric PN velocity field from Pulsoni et al. (2018) is plotted in Fig. 6.3 in the background and the individual GC velocity measurements used in this work are shown with coloured points. The stellar photometric PA and the kinematic PA show clear signs of misalignment which is a signature of triaxiality. However the amplitude of rotation ~ 50 km s^{-1} is much smaller than the velocity dispersion ~ 150 km s^{-1}, which supports the axisymmetry assumption in the dynamical modelling approach we use in this work (Sect. 6.4.1).

For each GC, we use the interpolated moments of the velocity field to compute the local LOS velocity field (LOSVD). Then, we determine the probability of observing a GC with a velocity as extreme as measured assuming a local Gaussian LOSVD. This assumption is reasonable for discrete halo tracers and has been used in the literature (e.g. Zhu et al., 2016). By investigating the spatial distribution of outliers greater than 1, 2 and 3σ from the PN velocity field we find no discernible overdensity or trend with magnitude or colour out to $R \sim 40$ kpc. We find that the individual GCs are consistent with being randomly drawn from a local Gaussian LOSVD, where the mean and σ are informed by the PN velocity field and convolved with the measurement error. The fractions of the GCs with velocities more extreme than 1, 2 and 3σ from the local LOSVD are given in Table 6.2. We repeated the analysis for the whole kinematic sample and again for the kinematic sample in the magnitude range of subsample C. In both cases, we redid the analysis for the whole subsample as well as the colour-selected subsample. Given that the local Gaussian LOSVD is informed by the point-symmetric velocity and dispersion field our investigation justifies dynamical modelling of the whole kinematics sample of GC based on the assumption of dynamical equilibrium.

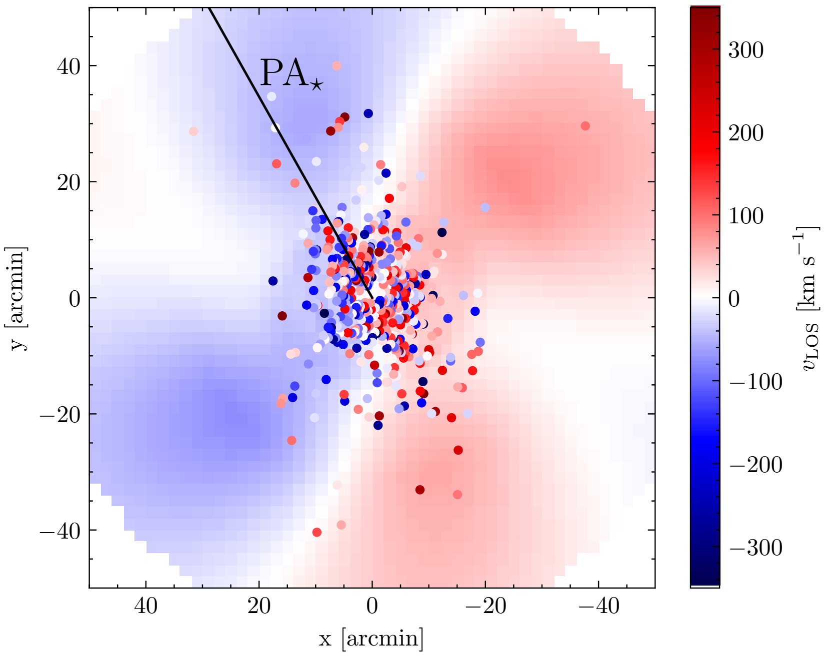

Figure 6.3: The mean velocity field of the PNe in the background obtained with harmonic expansion (Pulsoni et al., 2018) in comparison with the individual kinematic measurements of GCs. The photometric position angle of the stellar component is shown with a black solid line (Dufour et al., 1979).

These results expand the findings of Peng et al. (2004b) to $R \sim 40$ kpc. These authors determined a significant correlation between the GC and PN velocity field, finding that the red GCs correlate more strongly with the velocity field of the PN. They also observed a mild rotational signature both around the major and minor axis for the GCs. A rotation signature was also identified in Hughes et al. (2022), where the velocity field was investigated with a constant kinematic position angle and a constant rotation. The authors similarly find a stronger rotation signature for red GCs than blue GCs further motivating the modelling of the blue and red populations separately.

6.3.3 Tracer density profile

In the dynamical modelling used in this work (see Sect. 6.4.1), GCs are used as massless tracers of the gravitational potential. An essential input for the modelling is an accurate description of their spatial distribution. In this section, we will build the tracer density profile of the relaxed GCs subsample (the subsample C) in the form of multi-Gaussian expansion (MGE, Emsellem et al., 1994). We also considered separately GCs according to their colour as independent tracer populations as described in the following section.

Color distribution

GCSs of all large galaxies show bi-modal colour distribution as discussed in Sect. 1.4 and here we determine the colour separation for the magnitude-selected population C. To separate the GCs into red and blue populations we use Gaussian mixture model algorithm implemented in Python package *sklearn*. As already pointed out in T17 the largest separation is in $(u-z)_0$ colour, owing to the large wavelength baseline, therefore we use this combination of magnitudes. We determine the separation of the 2 components as the colour where the probability of belonging to either component is equal. We use bootstrap with replacements to provide uncertainties and determine

Table 6.3: Best fit results of the analytic tracer density profile for the blue and red GCs of the magnitude selected subsample C, corresponding to Fig. 6.4. The results show 16th and 84th percentile uncertainties.

i	$\Sigma_{e,i}$ $[N_{\rm GC}$ arcsec$^{-2}]$	$R_{e,i}$ [arcmin]	n_i	A_i $[N_{\rm GC}$ arcsec$^{-2}]$	α_i
blue	$10.01^{+6.61}_{-7.06}$	$4.44^{+2.27}_{-2.65}$	$0.67^{+0.28}_{-0.29}$	$0.004^{+0.008}_{-0.003}$	$1.08^{+0.12}_{-0.13}$
red	$6.95^{+4.95}_{-5.1}$	$3.65^{+4.17}_{-2.37}$	$0.7^{+0.28}_{-0.3}$	$0.005^{+0.012}_{-0.004}$	$1.1^{+0.14}_{-0.15}$

the separation to be $(u-z)_0 = 2.69^{+0.04}_{-0.03}$. Reassuringly, a similar separating colour was found by Hughes et al. (2021a).

Position angle and flattening

In the next sections, we investigate the position angle PA and projected flattening q' of the red and blue GCs for which we followed the method described in Sect. 2.3.1. For different magnitude regions, we compared the recovered flattening in the 4 radial regions informed by the overdensity in GC candidates observed in T17 ($R/R_e \leqslant 9$ and $9 < R/R_e \leqslant 17$), as well as the radial regions noted in the RGBs by Rejkuba et al. (2022) ($R \leqslant 30$ kpc and $R > 30$ kpc).

For subpopulation C, we observe that the flattening and PA are consistent within all the radial regions. A comparison of the red and blue GCs shows that the red GCs prefer a more flattened distribution with $q'_{\rm GCS,\ red} = 0.72^{+0.08}_{-0.08}$ and blue a more spherical distribution with $q'_{\rm GCS,\ blue} = 0.82^{+0.01}_{-0.02}$. Within the uncertainties, the PAs of the two components agree with the photometric position angle of the main body stellar component of the galaxy at 35^o: ${\rm PA}_{\rm GCS,\ red} = 46.0^{+10.5}_{-10.5}$ and ${\rm PA}_{\rm GCS,\ blue} = 30.2^{+8.0}_{-8.0}$.

6

To correct for the PA and rotate the sample to a common PA, we use the literature results from the main stellar component of the galaxy PA $= 35°$. This ensures the potential generated by the stars and the kinematics of the GCs are aligned with the same PA as required by the axisymmetric dynamical models used in this work.

Fitting an analytic tracer density profile

Based on the colour, and as discussed in Sect. 6.3.3, we split the GCs in subsample C into blue and red. To build the tracer density profile that will be an input to the dynamical modelling, we first fit the observed number density profile of the GCs with an analytic function and then decompose it in a series of Gaussians utilising *mgefit* as described in Sect. 2.3.3. Assuming the PA of 35°, we align the major axis of the GCS with that of the main body of the galaxy. To account for the flattened spatial distribution of GCs, we assume the density is constant on confocal ellipses $R_{\rm ell}^2 = x^2 + (y/q)^2$ and use this to make a binned profile with 16 logarithmically-spaced bins. Bins with fewer than 3 GCs are removed because of low statistical significance. We explored different binning strategies to ensure the best-fit profile is minimally affected by it.

To find the best-fit parameters we use a Gaussian likelihood and uninformative (flat) priors on the modelled parameters ($\Sigma_{\rm S,0}$, $R_{{\rm e},i}$, n_i, $\Sigma_{\rm P,0}$ and α_1) as described in Sect. 2.3.2. The priors for the fitting of the analytic profile are uniform in the following regions: $\log R_{\rm e} \in [1, 3]$ arcsec, $\alpha_1, n \in [0.2, 6]$ and $\log \Sigma_{\rm S,0}$, $\log \Sigma_{\rm P,0} \in [-10, 3]$ arcsec^{-2}. The slope and Sérsic index were sampled in linear space and $\Sigma_{\rm S,0}$, $R_{\rm e}$ and $\Sigma_{\rm P,0}$ in logarithmic space as they can span multiple orders of magnitude and such transformation results in a more efficient sampling of the parameter space.

We sample the posterior, find the maximum likelihood region and explore the parameter space with EMCEE (see Sect. 2.3.2). The posteriors on each of the 5 free parameters are unimodal with the weakest constraints on the Sérsic index. The chains were allowed to evolve for 12000 steps to ensure convergence of the best-fit parameters, the first 1000 were discarded as burn-in.

The best-fit parameters for different subpopulations are shown in Table 6.3. The Sérsic profile can better capture the behaviour of the density profile in the inner regions and the single power

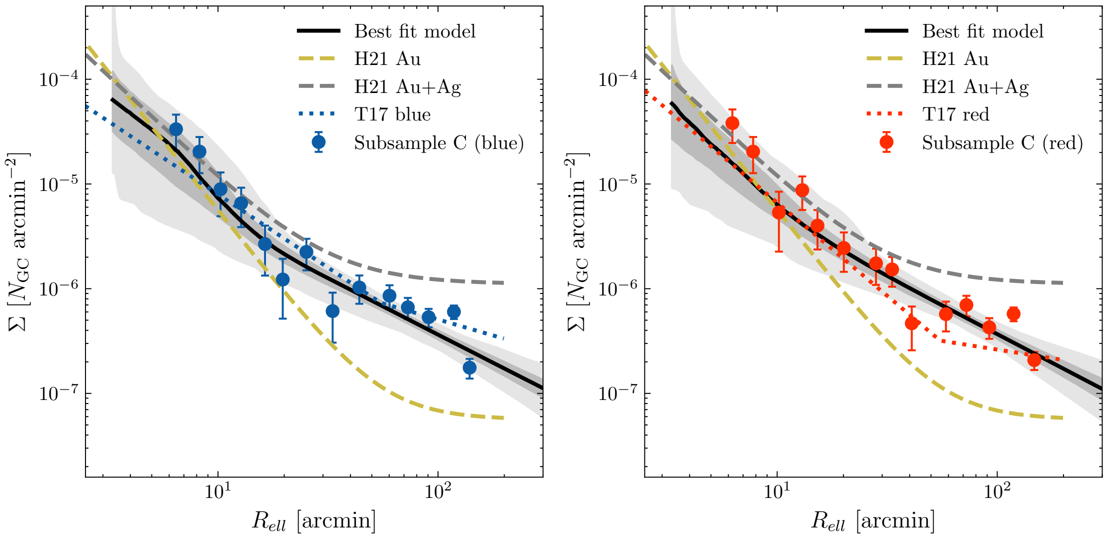

Figure 6.4: Tracer density distribution for population C of GCs. The left figure shows the blue and the right the red population. The blue and red points with associated uncertainties indicate the binned profile computed for the respective sub-population GCs. A solid black line shows the best-fit model to the data, and dark and light grey shadings show 1 and 3σ uncertainties computed as the 16th and 99.7th percentiles from the posterior. The dotted blue and red lines show the best-fit double power law from T17 for each population. H21 used different datasets to determine three different stages of the clean photometric datasets. They refer to the best sample as golden (Au) and the next best sample as the silver (Ag) sample. The dashed yellow line shows the best-fit model of the golden sample from H21 and the dashed grey line the silver and golden combined. The two literature results are arbitrarily scaled for comparison.

law in the outer regions. Because of the choice of the fitting function, the interpretation of the individual best-fit parameters is not straightforward, especially in reference to literature studies. We note that the blue population shows a slightly shallower Sérsic and power law slope and a larger R_e compared to the red population, which is consistent with the literature.

The resulting profiles for the blue and red C subpopulations are shown as solid black lines in Fig. 6.4, with dark and light shaded regions corresponding to 1 and 3 σ uncertainties. The left panel shows the blue GC data as blue points and the associated best-fit model. The right shows the same for the red population. Arbitrarily-scaled dashed and dotted profiles show the literature results.

The dashed H21 results were computed without the colour selection. Our profile in the inner regions ($R \leqslant 30$ arcmin) is steeper than their silver sample (Au+Ag) for both the blue and red populations. The blue population profile shows a slope more consistent with their higher purity (gold) sample, which is shown as a dashed orange line. In the outer regions ($R > 30$ arcmin) our best-fit profile drops off faster than the literature results. The latter might not be surprising as they impose a constant background.

The dotted lines show the broken double power-law fits presented in T17. In the inner region, we find a consistent slope for the red GCs and a steeper slope for the blue GCs, while in the outer region our best-fit profile shows a steeper slope compared with T17 profiles.

In general, our profiles lie within the literature results and show the main characteristics that have been observed for the GCS of CenA. The differences stem from the different methods of selecting a high-purity and high-completeness sample of GCs and different fitting functions.

MGE decomposition

In the last step, we constructed an MGE representation of the number density profiles separately for the blue and red GCs of subsample C (as defined in Fig. 6.1). Such a representation is necessary

Table 6.4: MGE for the **blue** GCs of subpopulation C in the input format needed for CJAM. The first column shows the sorted number of the Gaussian components. Column 2 the central number density, Column 3 the major axis dispersion of the Gaussian and Column 4 the projected flattening.

n	$N_{\rm GC}$ pc^{-2}	arcsec	q'
1	1.352e-07	70.71	0.82
2	5.567e-08	119.24	0.82
3	1.423e-09	192.91	0.82
4	1.090e-07	230.29	0.82
5	1.062e-08	436.06	0.82
6	2.145e-09	470.45	0.82
7	1.405e-09	779.61	0.82
8	1.831e-09	1012.21	0.82
9	1.373e-09	1939.49	0.82
10	7.152e-10	4612.45	0.82
11	3.477e-10	18257.41	0.82

Table 6.5: MGE for the **red** GCs of subpopulation C in the input format needed for CJAM. The column structure corresponds to that of Table 6.4.

n	$N_{\rm GC}$ pc^{-2}	arcsec	q'
1	2.241e-07	72.37	0.72
2	9.751e-08	137.25	0.72
3	3.466e-08	216.51	0.72
4	1.886e-08	277.48	0.72
5	9.599e-09	482.48	0.72
6	3.424e-09	878.25	0.72
7	7.064e-10	1182.39	0.72
8	2.624e-11	1635.44	0.72
9	1.589e-09	1972.49	0.72
10	8.265e-10	4678.81	0.72
11	3.952e-10	18257.41	0.72

for the dynamical modelling used in this work and is obtained by following the procedure outlined in Sect. 2.3.3. Lastly, we also accounted for the flattening of both the blue and red GC systems. The MGE components for blue and red GCs are given in Table 6.4 and Table 6.5.

6.4 Dynamical modeling with GCs

To model the GCs, we use the axisymmetric JAM formalism introduced by Cappellari (2008) and described in Sect. 2.2. In this section, we describe how we use it to reproduce the GC kinematics and spatial distribution, and, thus, derive the mass distribution of CenA.

6.4.1 CJAM

As we need to reproduce the flattening of the tracer density distribution and the stellar and dark matter distributions, we use axisymmetric models. We use the C implementation of the JAM model CJAM. In principle, these models have two free angular parameters that describe the orientation of the galaxy: the PA and the inclination angle i. In Sect. 6.3.3, we discussed the PA, and we henceforth keep this fixed. The main rotation of the galaxy is along the photometric major axis, which supports our choice of symmetry axis coinciding with the minor axis of the stellar and GC distribution.

The inclination angle is used to connect the intrinsic 3D quantities from the model with the observables (density profiles and velocity components) projected on the sky, where $i = 0^\circ$ for a face-on system and $i = 90^\circ$ for an edge-on system. We will keep this parameter free in some of our models.

6.4.2 Stellar surface density

To construct the stellar surface density profile, we combine the stellar surface brightness in the inner 1 R_e from Dufour et al. (1979) with the appropriately scaled halo RGB number counts from Rejkuba et al. (2022).

Accounting for the inner dust disk the stellar surface brightness in the range 70 arcsec$\leqslant R \leqslant 255$ arcsec (0.2 - 0.8 R_e) is best represented by the de Vaucouleurs profile in the B-band magnitude (Dufour et al., 1979, eq. 12) :

$$I_\mathrm{B} = 8.32\left[\left(\frac{R}{R_{e,\mathrm{B}}}\right)^{1/4} - 1\right] + 22.94 \,, \tag{6.1}$$

where I_B is in mag arcsec^{-2} and $R_{e,\mathrm{B}} = 305$ arcsec is the effective radius in the B band. We adopt a position angle of 35° East of North and a flattening of $q_{\star,\ \mathrm{main}}$ = 0.93 from Dufour et al. (1979).

Assuming the distance modulus of $(\mathrm{m} - \mathrm{M}) = 27.88$ mag (Harris et al., 2010) and absolute Solar magnitude $M_{\odot,\mathrm{B}} = 5.48$ (Binney and Tremaine, 2008), the B-band magnitude is converted to surface brightness [$\mathrm{L}_\odot$ arcsec^{-2}]:

$$L_\mathrm{B} = 10^{-0.4\left(I_\mathrm{B} - (\mathrm{m}-\mathrm{M}) - M_{\odot,\mathrm{B}}\right)} \,. \tag{6.2}$$

Rejkuba et al. (2022) used *HST* images to study the properties of resolved stellar halo of Cen A out to 30R_e. Constructing deep colour-magnitude diagrams (CMDs) that contained individual bright RGB stars enabled the authors to remove fore- and background contamination and construct the stellar number density profile from 28 individual *HST* pointings across the galaxy. Using the RGB number counts in the range $0.23 < R/R_\mathrm{e} < 30$ they find the tightest fit to the number density profile of RGB stars by fitting both a single power-law and a de Vaucouleurs profile with an increased flattening in the outer stellar halo corresponding to $q'_{\star,\ \mathrm{halo}} = 0.54 \pm 0.02$. We adopt the best fit de Vaucouleurs profile from Rejkuba et al. (2022):

$$\log \Phi_\mathrm{RGB} = 7.685 - 3.008(a/R_\mathrm{e})^{1/4} \,, \tag{6.3}$$

where a is the semi-major axis position. The authors convert the number counts to luminosity and provide a shift to match the inner stellar surface brightness profile from Dufour et al. (1979), thereby extending the inner stellar surface brightness out to 30 R_e. By integrating the combined functions, we recover the total luminosity of $L_\mathrm{B} \sim 0.3 \times 10^{11}\mathrm{L}_\odot$ corresponding to $M_\mathrm{B} = -20.7$ mag, consistent with $B_\mathrm{T} = 7.84$ mag ($M_\mathrm{B} = -20.6$ mag), the measurements in the Third Reference Catalogue of Bright Galaxies (de Vaucouleurs et al., 1991).

To obtain the stellar surface brightness we combine the profile from Dufour et al. (1979) and Rejkuba et al. (2022). To account for the difference in the flattening when making the MGE of the galaxy's baryonic component, we generate a 2D image using Eq. 6.2 and Eq. 6.3 in their respective radial regions. We do not have information on the radial variation of the flattening, so we keep q' fixed to 0.93 within 0.8 R_e (the inner region) and to 0.54 in the outer region beyond 1.5 R_e. In the regions defined by both profiles, we assign the mean luminosity between both models. We decompose the image with *mgefit* and the resulting components are shown in Table 6.6. The profiles along the major and minor axes together with the MGE components are shown in Fig. 6.5. The blue points show the observed stellar surface density along the major and minor axis in the left and right panels, respectively. The individual Gaussian components are shown with faint coloured lines and the cummulative profile is shown with a solid red line. The discontinuities along the minor axis reflect the transition region where both profiles are evaluated as a result of the different flattenings of the main stellar body and the halo RGBs.

Table 6.6: The moments of the MGE components for the combined stellar density in the form required by the modelling tool. The sorted number of a component is in Col. 1, the central surface brightness is in Col. 2, the major axis dispersion is in Col. 3 and the projected flattening is in the last column.

n	$L_\odot\,\mathrm{pc}^{-2}$	arcsec	q′
1	1432.364	34.54	0.93
2	453.59	64.24	1.0
3	307.05	119.78	0.89
4	73.88	253.33	0.49
5	21.45	444.91	0.54
6	6.18	637.61	0.54
7	4.19	962.74	0.54
8	1.08	1710.16	0.54
9	0.13	3515.16	0.51
10	0.02	3515.16	0.83

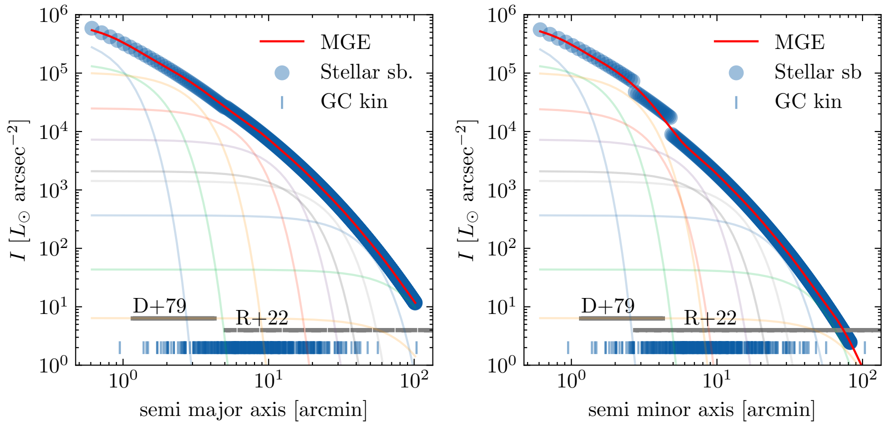

Figure 6.5: Combined stellar surface brightness profile of CenA from Dufour et al. (1979) and Rejkuba et al. (2022) and its MGE decomposition. The left panel shows the profile along the semi-major axis and the right along the semi-minor axis. The blue points show the observed 2D profile we generated with Eq. 6.1 in the region highlighted by the grey horizontal solid line (D+79 fitting region) and Eq. 6.3 in the outer regions highlighted with the grey horizontal dashed line (R+22 fitting region). The red line shows the resulting MGE fit to the profile and the faint coloured lines are the individual Gaussian components. The blue vertical bars at the bottom of the figure show the positions of the kinematic tracers.

6.4.3 Dark matter

For the dark matter potential, we assume an NFW profile (Eq. 1.1.2) in elliptical coordinates m: $m^2 = x^2 + y^2 + z^2/q_{\mathrm{DM}}^2$, where q_{DM} is the intrinsic flattening of the dark matter profile. It is important to emphasize that we fix the axis of symmetry to the stellar component. Therefore, the oblate and prolate shapes of dark matter haloes have the same symmetry axis in our modelling approach. We parameterise the profile with the total mass M_{200}, defined as the mass within a sphere of radius r_{200} and an average density 200 times the critical density of the Universe (ρ_{crit}), and concentration $c_{200} = r_{200}/r_s$ as introduced in Sect. 1.1.1.

Similar to the stellar density profile, the dark matter profile is parametrised as an MGE to generate the input for CJAM. We decompose the 1D radial profile and account for the intrinsic flattening of the dark matter. Finally, q_{DM} is projected based on the inclination $q'_{\mathrm{DM}} = \sqrt{q_{\mathrm{DM}}^2 \sin^2 i + \cos^2 i}$ and on the central surface density of the Gaussian components.

6.5 Discrete likelihood analysis

To compare our models with the data, we follow the discrete likelihood analysis approach described in Sect. 2.5. Instead of the Bayesian analysis (see Sect. 2.5.1) carried out in chapter 3, chapter 4 and chapter 5, here we employ the χ^2 described in Sect. 2.5.2. Gaussian likelihood is used as given in Eq. 2.21 which directly relates to the χ^2 as seen in Eq. 2.22. In our modelling, we use 7 free parameters: 3 to describe the dark matter (M_{200}, c_{200} and $q_{\rm DM}$), one to scale the stellar surface density $M_\star/L_{\rm B}$, one to characterise the inclination (inc), and two to describe the orbital properties of the tracer population (β_z and κ).

This 7-dimensional parameter space is explored by evaluating CJAM models on a fixed grid. Each grid point represents a combination of model parameters. Due to the computational time intensity of the CJAM models, we computed the likelihood and χ^2 statistics on this grid instead of full posterior sampling. We carried out the analysis in two steps. First, to find the rough location of the global minimum, we varied only one parameter, keeping the others fixed. Second, to find the best-fit parameters as well as to investigate their covariances and quantify uncertainties, we varied 2 parameters at a time keeping the others fixed. We carried out the analysis separately for the blue and red GCs to get independent constraints on each of the parameters.

We found the best-fit solution through a series of iterations. Not all 7 parameters were explored in each of the iterations. For each parameter (or parameter pair) that is explored, we evaluate the likelihood on a grid; while one of the parameters (or two) was varied the rest were kept fixed to the initial guess at the corresponding iteration. The initial guess of each successive iteration is determined from the output of the previous iteration based on the likelihood that was also used to determine the convergence of the best-fit solution. As the last step of the analysis, we derive both the best-fit parameters and the uncertainties by combining the constraints from the individual 2D grids.

6

6.5.1 Finding a approximate location of the global minimum

At each iteration step n, we compute the χ^2 curve for each of the parameters θ_i that is varied while keeping the other parameters $\theta_j^{(n,\mathrm{fix})}$ (for $j \neq i$) fixed. We adopted initial estimates for the two components of the gravitational potential from previous investigations: $\log M_{200}$ =12[4], c_{200}=10 (Peng et al., 2004a), and the dynamical $(M/L)_{\rm B}$ = 3.9 (Hui et al., 1995). Our initial estimate for the inclination was inc= 75^o, and for the orbital parameters we used $\beta_z = 0$ and $\kappa = 0$.

We used 20 grid points for each parameter as a compromise between the computational time and the coarseness of the grid. For each free parameter θ_i, we evaluated the CJAM model, calculated the $\chi^2(\theta_i)$, and determined the minimum $(\chi^2)_i^{(n)}$ that corresponds to the solution $\theta_i^{(n)}$. We used two criteria to inform the location of the global minimum as shown in Fig. 6.6. One is related to the difference of the minimum χ^2 of the two subsequent iterations. The second is related to the difference in the value of the solution $\theta_i^{(n)}$ between two subsequent iterations ($\Delta\theta_i = \theta_i^{(n+1)} - \theta_i^{(n)}$). Figure 6.6 shows a sketch of χ^2 for two iteration steps and demonstrates these two criteria. Between steps n and $n+1$ we modified parameters $\theta_j^{n+1,\,\mathrm{fix}}$; $(j \neq i)$ and the resulting minimum of χ^2 statistic is lower than the minimum at the previous step: $\chi^2(\theta_i^{(n+1)}) < \chi^2(\theta_i^{(n)})$. This negative difference in the minimal χ^2 value indicates that parameters $\theta_j^{n+1,\,\mathrm{fix}}$ are closer to the best-fit parameters than $\theta_j^{n,\,\mathrm{fix}}$. Additionally, the value of the parameter at the minimum is different: $|\theta_i^{(n+1)} - \theta_i^{(n)}| >> \Delta\theta_i$, meaning that the $\theta_i^{(n+1)}$ is closer to the best-fit parameter than $\theta_i^{(n)}$. Therefore we considered the solution has converged once $\Delta\theta_i$ was a few grid step sizes and $(\chi^2)_i^{(n+1)} \approx (\chi^2)_i^{(n)}$. Because of the correlations in 7D parameter space, $\theta_i^{(n)}$ will depend on the values of all other parameters $\theta_j^{(n)}$, $j \neq i$.

[4]In the following text $\log M_{200}$ is in units [$\mathrm{M}_\odot$] and for clarity of the text we omit the unit.

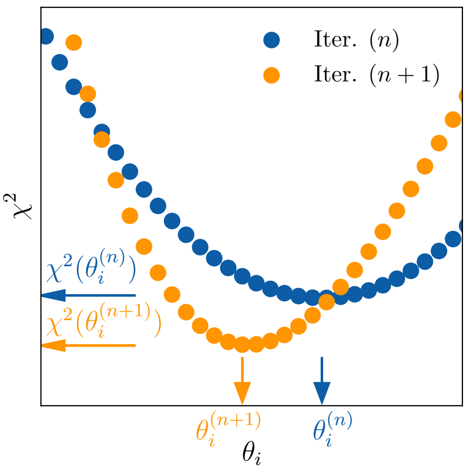

Figure 6.6: A sketch of a variation of χ^2 statistics as a function of parameter θ_i for iteration step n in blue and $n+1$ in orange. Circles represent the grid points in θ_i, with a grid step size of $\Delta\theta_i$, where the χ^2 is computed. The coloured arrows highlight the value of the parameter at the minimum of the χ^2 statistics on the x axis and the absolute value of the statistics on the y axis.

As the result of the above iterative procedure, we identify the following best-fit parameters that are close to the global minimum and use them for the initial estimates for the next step of the analysis. These were: $\log M_{200} = 12$, $c_{200} = 10$, $q_{\rm DM} = 1.2$, $inc = 85^o$, $M_\star/L_{\rm B} = 4$, $\beta_z^{\rm GC,\ blue} = -0.2$, $\beta_z^{\rm GC,\ red} = 0.1$, $\kappa_z^{\rm GC,\ blue} = 0$, $\kappa_z^{\rm GC,\ red} = 0$.

6.5.2 Two parameter grid model

Next, we explored the covariances by co-varying 2 parameters (θ_i, θ_j) and keeping the others fixed ($\{\theta\}_k$, where $i \neq j \neq k$). The summary of the $\{\theta\}_k^{\rm (m,fix)}$, the ranges of parameters (i, j) and number of grid points in each parameter is presented in Table 6.7. The first column shows the iteration step - m, columns (2) - (10) contain the values of the $\theta_k^{m,\rm fix}$ in the top row and grid range for (θ_i, θ_j) in the bottom row of each iteration. The last column shows the number of linearly-spaced grid points for each θ_i and θ_j. If the covariance is not explored for a given parameter at a given iteration step, then the range row is left empty (–).

In iterations 1-6, we set the rotation of both red and blue GCs to 0 ($\kappa = 0$) and we introduce rotation in iterations 7 and 8. This is motivated by an increased computational time when $\kappa^{\rm GC} \neq 0$ and a recent study that showed that β_z and κ_z have negligible impact on the enclosed mass measurements from GCS with similar methodology (Veršič et al., 2024).

In iteration step 5, we introduce the literature mass-concentration relation (Correa et al., 2015) using the Python package COMMAH to assign c_{200} given M_{200} and the cosmological parameters from Planck Collaboration et al. (2016). This choice was driven by two observations of the 2D χ^2 surfaces in the iterations 1-4: first, the strong degeneracy of c_{200} with both $\log_{10} M_{200}$ and $M_\star/L_{\rm B}$ and second, the fact that the minimum χ^2 c_{200} is consistent with the literature studies of mass-concentration relation as shown in Fig. 6.7. The literature $M_{200} - c_{200}$ relations are shown as black dotted and dashed lines for relaxed and non-relaxed haloes respectively (Neto et al., 2007), dash-dotted line (Prada et al., 2012) and black and red solid lines (Correa et al., 2015) using cosmological parameters from two different studies, Komatsu et al. (2009, WMAP5) and Planck Collaboration et al. (2016, Planck15). We adopt the latter relation highlighted in red.

Table 6.7: Overview of the parameters used in different iteration steps for the two-parameter optimisation. Column (1) contains the number of iterations m. For each of the parameters used in this work, columns (2) - (10) contain the information on its best approximation and the range explored at the corresponding iteration step. For these columns, each row corresponding to a given iteration is split in two. The top contains the values of the corresponding parameter ($\theta_k^{(\mathrm{m,fix})}$) that was kept constant when exploring the χ^2 surface in parameters (i, j). The bottom contains the range of values we explored for a given parameter and is marked with (–) if that parameter is fixed at a given iteration step. When the parameters were changed between subsequent iteration steps we highlight them in bold and remark with † the change in range. The last column shows the number of grid points linearly distributed for each of the parameters in the corresponding range.

it.	$\log_{10} M_{200}$ [M$_\odot$]	c_{200}	q_{DM}	inc [deg]	$M_\star/L_\mathrm{B}$ [M$_\odot$/L$_\odot$]	$\beta_{\mathrm{z,blue}}$	$\beta_{\mathrm{z,red}}$	κ_{blue}	κ_{red}	no. grid points
1	12	10	1.2	85	4.5	-0.12	0.1	0	0	
	10 - 13	2 - 20	0.6 - 2	60 - 90	1 - 8	-0.3 - 0.3	-0.3 - 0.3	–	–	30
2	12	10	1.2	85	4.5	**-0.2**	0.1	0	0	
	10 - 13	2 - 20	0.6 - 2	60 - 90	1 - 8	-0.3 - 0.3	-0.3 - 0.3	–	–	30
3	**12.3**	**8.5**	1.2	85	4.5	-0.2	0.1	0	0	
	10 - 13	2 - 20	0.6 - 2	60 - 90	1 - 8	-0.3 - 0.3	-0.3 - 0.3	–	–	30
4	12.3	8.5	1.2	85	**3.5**	-0.2	0.1	0	0	
	10 - 13	2 - 20	0.6 - 2	60 - 90	1 - 8	-0.3 - 0.3	-0.3 - 0.3	–	–	40
5	12.3	COMMAH [a)]	1.2	**90** [b)]	3.5	-0.2	0.1	0	0	
	10 - 13	COMMAH	0.6 - 2	–	1 - 8	-0.5 - 0.5†	-0.5 - 0.5†	–	–	40
6	12.3	COMMAH	1.2	90	**3.0**	-0.2	**0.05**	0	0	
	10 - 13	COMMAH	0.6 - 3†	–	1 - 8	-0.5 - 0.5	-0.5 - 0.5	–	–	40
7	12.3	COMMAH	1.2	90	3.0	-0.2	0.05	**-0.1**	**-0.20**	
	–	COMMAH	0.6 - 3	–	–	-0.5 - 0.5	-0.5 - 0.5	-0.5 - 0.5†	-0.5 - 0.5†	10
8	12.3	COMMAH	1.2	90	3.0	**-0.15**	**0.15**	**-0.15**	-0.20	
	10 - 13	COMMAH	0.4 - 3.5†	–	1 - 8	-0.8 - 0.4†	-0.8 - 0.4†	-0.7 - 0.4†	-0.7 - 0.4†	30

† Parameter range modified from the previous step,
a) Correa et al. (2015) with Planck Collaboration et al. (2016) cosmology
b) Hui et al. (1995)

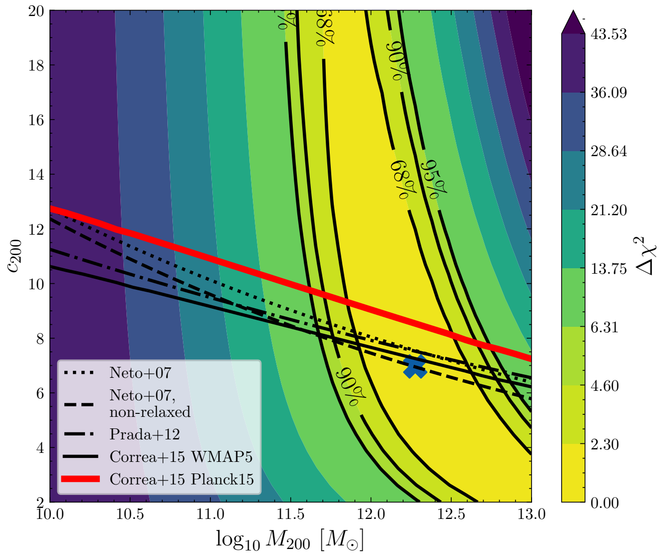

Figure 6.7: $\Delta\chi^2$ surface for $\log_{10} M_{200}{-}c_{200}$ plane in iteration 4 (see Table 6.7 for a summary of the parameters). The black contour lines show the 68th, 90th and 95th percentile confidence levels, with minimal χ^2 solution shown with the blue cross. Dotted, dashed, dot-dashed black lines and solid red and black lines show the different literature $M_{200} - c_{200}$ relations. The solid lines show the $M_{200} - c_{200}$ computed with COMMAH code from Correa et al. (2015) using the cosmological parameters from Planck Collaboration et al. (2016) in red and the cosmological parameters from Komatsu et al. (2009) in black.

6

We set two criteria for the convergence of the solution. First, $\theta_i^{(m)} \approx \theta_i^{(m,\mathrm{fix})}$ for a given parameter i in all 2-dimensional slices of the χ^2 surface. Second, $\chi^2(\theta_i^{(m)}, \theta_j^{(m)}) \approx \chi^2(\theta_k^{(m)}, \theta_l^{(m)})$ for all (i, j), (k, l) parameter pairs as shown in Fig. 6.8. Once both criteria were met, we are confident to have found the global minimum. We used only the blue GCs to locate the minimum in this step. The constraints from the red GCs were used only to inform the population-specific parameters: velocity anisotropy β_z and rotation κ. We chose this approach because, in this way, the convergence of the parameters from the red GCs provides an independent verification of our method and the location of the global minimum.

The iterative process for the blue GCs is demonstrated in Fig. 6.8 for blue and Fig. 6.9 for red GCs, where each row corresponds to a different free parameter θ_i. The left panels show the difference between the minimum value of χ^2 statistics at iteration step m and the global minimum value. The right panels show the difference in the best-fit value of the corresponding free parameter at a given step and the fixed value at each iteration. The θ_j components are shown with different symbols and each colour corresponds to a given iteration. On the left panels, the convergence trend is evident, with the minimum value of χ^2 decreasing with each subsequent iteration. Additionally, the spread of the minimum of the χ^2 is decreasing, suggesting that all the parameter pairs are converging to the same global minimum. A similar trend is seen in the right panels as the value of the parameter at the minimum χ^2 becomes more consistent among the different (i, j) pairs and gets closer to the value assumed at a given iteration.

A comparison of the initial run marked with blue symbols and the final set-up with black symbols shows improved consistency between parameter pairs. Based on this, we conclude that we identified the global minimum in the 5D parameter space.

6.5.3 BEST FIT PARAMETERS AND UNCERTAINTIES

For the quantification of the uncertainties, we start by taking the 2D likelihood surface and, by marginalising over one of the dimensions, we come to the marginalised posterior, which is equivalent to the probability. For each of the θ_i, we obtain four independent constraints on the

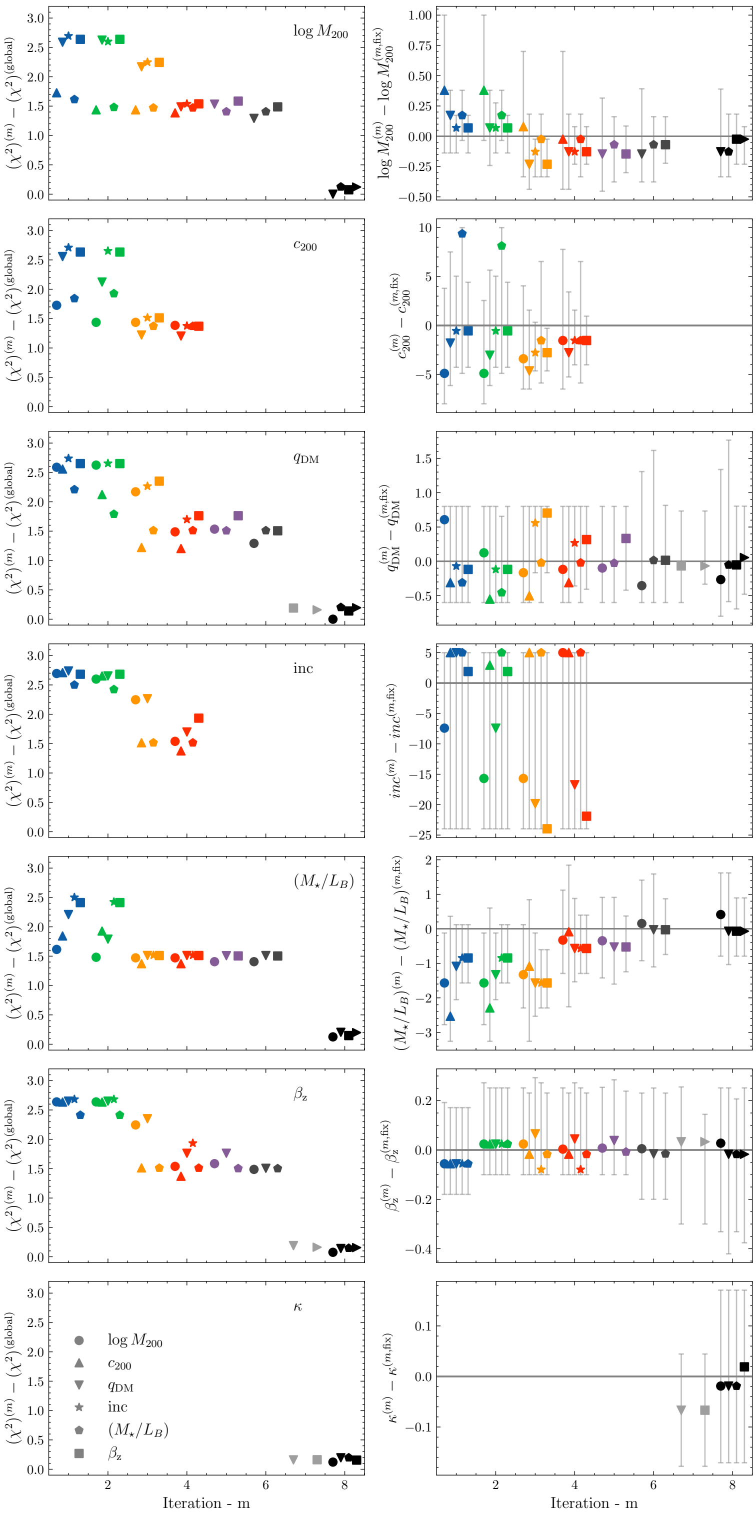

Figure 6.8: Convergence of the parameters and minimal χ^2 for the **blue** GCs. The panels in the left column show the evolution of the minimal value of the statistics in each of the two-parameter grids. The right panels show the difference between the value of the corresponding parameter at the minimum and the value of the parameter shown in Table 6.7 at a given iteration. The error bars show 1σ uncertainty intervals. Each colour highlights the iteration step and the symbols correspond to the different parameters covarying in the 2D grid. The grey horizontal line is shown as a guide.

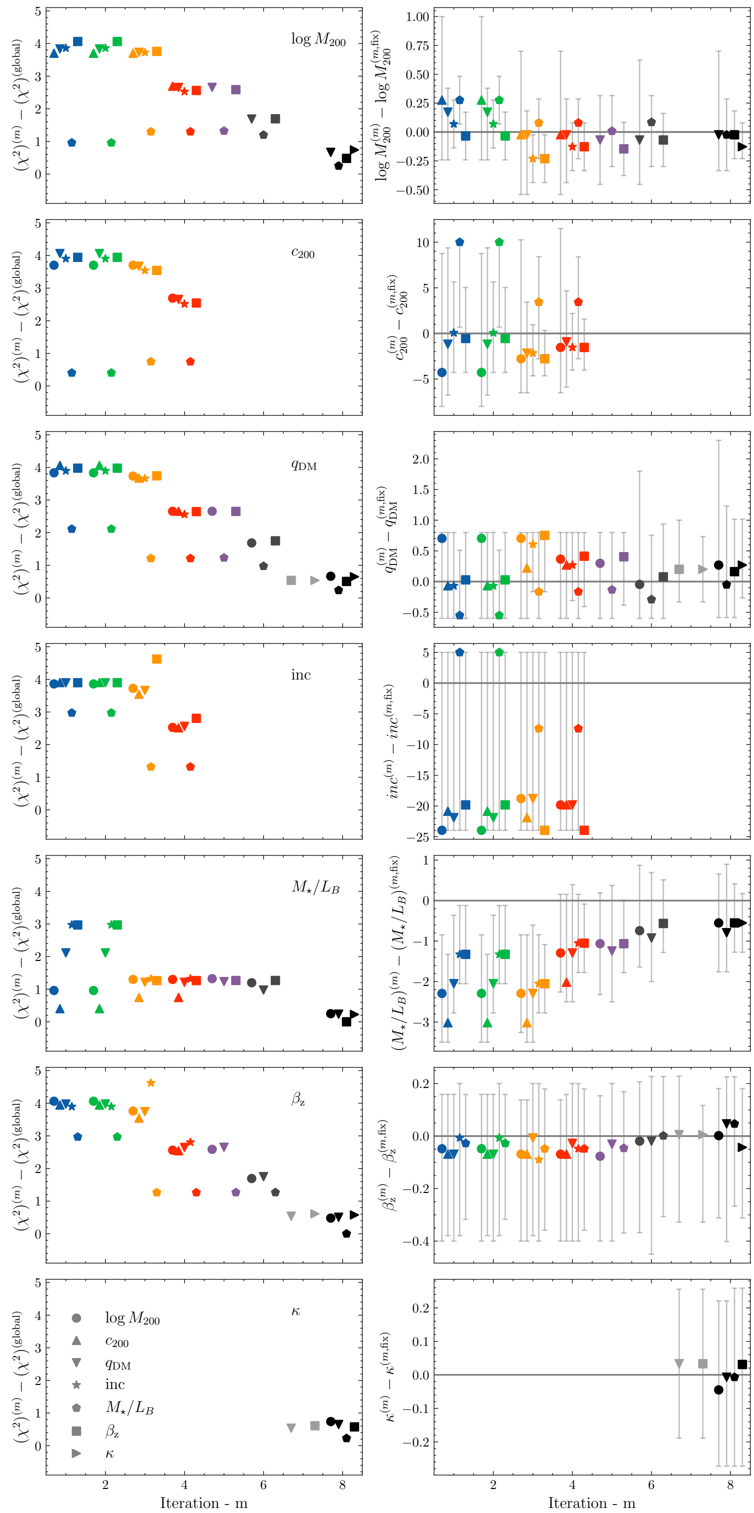

Figure 6.9: Convergence of the parameters and minimal χ^2 for the **red** GCs. The symbols and colours correspond to those in Fig. 6.8.

parameter from the blue GCs and another four from red GCs. We use the joint posterior to quantify the best-fit solution and the 16th and 84th-percentile uncertainties.

6.6 Results

In this section, we present the results from the final iteration – iteration 8. The convergence in both the minimum χ^2 and the values of the parameters at the minimum support the conclusion that iteration 8 has converged. This is, therefore, our final iteration. We first focus on the $\Delta\chi^2$ surface followed by the combined constraints from independent modelling of the red and blue GCs and finally, we present the results of the modelling.

6.6.1 $\Delta\chi^2$ surface

The $\Delta\chi^2$ surface for the 5 parameters explored in iteration 8 (see Table 6.7) is shown in Fig. 6.10 for the constraints from the blue GCs and constraints from red GCs show similar trends. Each panel shows the smoothed $\Delta\chi^2$ surface on a grid of parameter pairs. The black contours highlight the 68.3th, 90th and 95th percentiles, where the 68.3th percentile approximately corresponds to the 1σ region. The blue cross highlights the location of the minimum χ^2.

This figure provides useful insight into the correlations between the different parameters. However, combining the constraints on each of the parameters coming from the $\Delta\chi^2$ surface is not trivial, so we take advantage of the evaluated likelihoods instead. We show this figure for demonstrative purposes and the black contours help to guide the eye.

There are several degeneracies between the parameters. The parameter best constrained by the data is $\log_{10} M_{200}$, which has tight constraints and shows minimal degeneracy with the parameters of the velocity distribution of the GCs, β_z and κ. The total dark matter mass is strongly anticorrelated with the stellar $M_\star/L_\mathrm{B}$, in such a way that models with lower $\log_{10} M_{200}$ prefer higher $M_\star/L_\mathrm{B}$. The flattening of the dark matter halo is positively correlated with $\log_{10} M_{200}$, with more massive haloes preferring stronger elongation of the isodensity contours along the minor axis of the stellar and GC distribution of NGC 5128.

The flattening of the DM halo depends very weakly on both the virial dark matter mass and $M_\star/L_\mathrm{B}$. The strongest constraints on this parameter come from the properties of the GC velocity distribution. As can be seen in the second column, κ provides the strongest constraints on the flattening q_DM, disfavouring an oblate or spherical halo. The velocity anisotropy provides somewhat weaker constraints. The parameters of the velocity distribution are not correlated.

6.6.2 Combining constraints from red and blue GCs

Following the methodology outlined in Sect. 6.5.3, we compute the marginalised probability for each of the parameters θ_i. Combining the probabilities we arrive at the joint posterior distribution for all free parameters. The final results are shown in Fig. 6.11. The red and blue lines correspond to the constraints from the corresponding population of GCs, and the black lines show the joint posterior. The faint lines show the probability distributions coming from the individual parameters.

The top row shows the parameters of the stellar and dark matter distributions, which should be consistent between both GC populations. The bottom row shows population-specific parameters. The median, 16th and 84th percentiles of the bold joint probabilities are presented in Table 6.8.

The total dark matter mass is best constrained by the data, with very consistent posteriors coming from both GC populations. The flattening of the dark matter halo in the top-middle panel shows a broader posterior, with the red population slightly favouring a more prolate halo. The top-right panel shows that the stellar $M_\star/L_\mathrm{B}$ results differ slightly in that the red population favours lower values than the blue population. However, these differences are within the 1σ uncertainties.

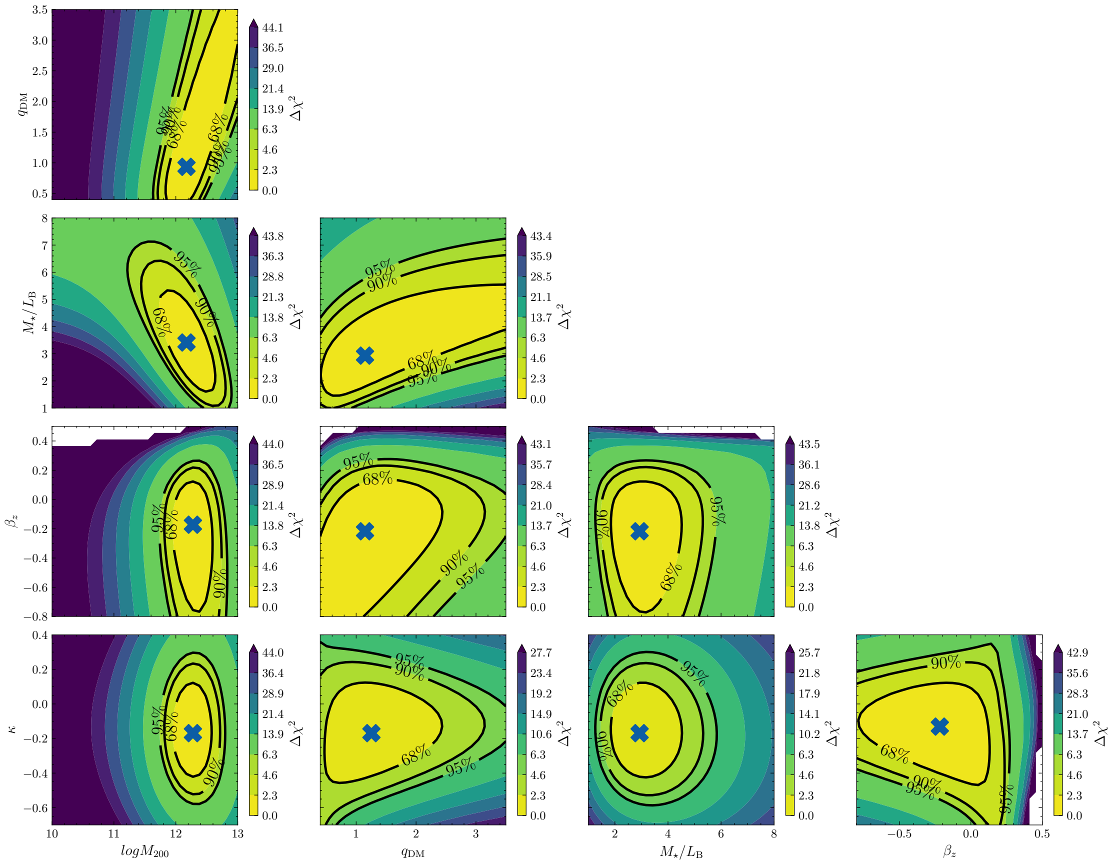

Figure 6.10: The smoothed $\Delta\chi^2$ surfaces for the different combinations of parameters from iteration 8 from the blue GCs. The black lines highlight the 68th, 90th and 95th percentile corresponding to $\Delta\chi^2$ levels of 2.3, 4.6 and 6.3 respectively. The minimal χ^2 solution is highlighted with the blue cross.

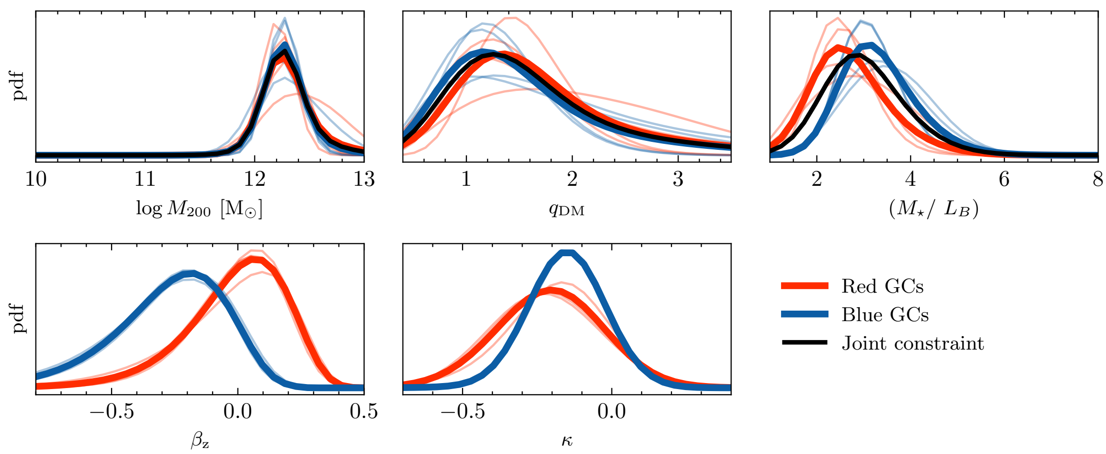

Figure 6.11: Posterior distributions of the individual parameters for the final iteration. Red and blue coloured lines correspond to the constraints from the corresponding GC subpopulation and black shows the joint posterior. Thin lines are the marginalised posteriors from the different parameter pairs shown in Fig. 6.10 and the thick lines are the joint probabilities from all of the parameter pairs. The parameters in the bottom row are intrinsic to the two GC populations and we do not combine them.

Table 6.8: The final results from the marginalised probabilities seen in Fig. 6.11.

θ_i^m	Joint	red GCs	blue GCs
$\log M_{200}$	$12.27^{+0.21}_{-0.20}$	$12.27^{+0.23}_{-0.20}$	$12.27^{+0.20}_{-0.19}$
$q_{\rm DM}$	$1.45^{+0.78}_{-0.53}$	$1.52^{+0.77}_{-0.53}$	$1.38^{+0.79}_{-0.51}$
$(M/L)_B$	$2.98^{+0.96}_{-0.78}$	$2.66^{+0.91}_{-0.72}$	$3.26^{+0.90}_{-0.69}$
β_z	–	$0.02^{+0.16}_{-0.22}$	$-0.24^{+0.19}_{-0.24}$
κ	–	$-0.21^{+0.18}_{-0.18}$	$-0.15^{+0.13}_{-0.13}$

The bottom-left panel shows that the red population prefers an isotropic to mild radial velocity anisotropy, while the blue population strongly disfavours isotropy, showing a preference for negative cylindrical anisotropy. The bottom-right panel shows strong consistency in the rotation parameters of both GC populations, with the red GCs preferring a slightly stronger rotation.

6.6.3 Best fit model

Now that we have established the best-fit parameters, we can compare the resulting velocity fields of the globular clusters with that of the best-fitting model. Figure 6.12 shows the velocity field of the blue GCs in the left column and the velocity dispersion field in the right column. The first row shows the smooth velocity and dispersion fields of the observed GCs, the second row shows the model predictions, the third shows the residuals, and the final row the histogram of the residuals. The smoothing parameters are the same as discussed in Sect. 6.3.2.

In the top-left panel, both major and minor axis rotation is strongly visible, indicative of a triaxial potential. Axisymmetric modelling cannot reproduce this feature as can be seen in the panel below. Instead, the model is sensitive to the average rotation between the major and minor axis rotation and compensates by lowering the rotational amplitude. This can be seen as the negative residuals close to the minor axis, where the axisymmetric rotation has the opposite sign, and as the underestimation close to the major axis, where the residuals are positive.

The right column shows the velocity dispersion maps. The smoothed data shows signs of a drop in the velocity dispersion along the minor axis, which is even more prominently visible in the model panel below. The velocity dispersion residuals, which are of the order of ∼25%, do not show coherent patterns, unlike in the left panel, and their distribution is much lower compared with the velocity field residuals.

Both top panels show signs of clustering, which are partially driven by the smoothing procedure adopted in this work. As the smooth velocity fields are only used for demonstration purposes and were not used in the model, a full investigation is beyond the scope of this work.

6.7 Discussion

6.7.1 Enclosed mass

Based on the best-fit model, the parameters of the NFW distribution are: $M_{200} = 1.86^{+1.61}_{-0.69} \times 10^{12}$ M$_\odot$, $c_{200} = 8.58^{+0.35}_{-0.41}$, $r_s = 29.94^{+6.95}_{-5.21}$ kpc, and $r_{200} = 257.11^{+44.10}_{-36.23}$ kpc. Figure 6.13 shows the comparison between the constraints for the enclosed mass from this work and literature studies. The lines show results from this work with the stellar mass in grey, dark matter mass in red and combined baryonic and non-baryonic in black. The shaded regions span the 16th to 84th percentiles. The green point shows the measurement with the whole sample of GCs from Woodley et al. (2007), the yellow point shows the most robust measurement from Woodley et al. (2010b), and the light blue point shows the measurement from Hughes et al. (2023). Blue and red circles show the enclosed mass estimates from blue and red GCs respectively from Hughes et al. (2023). The stars show constraints from PNe, with yellow showing estimate from Hui et al. (1995), light

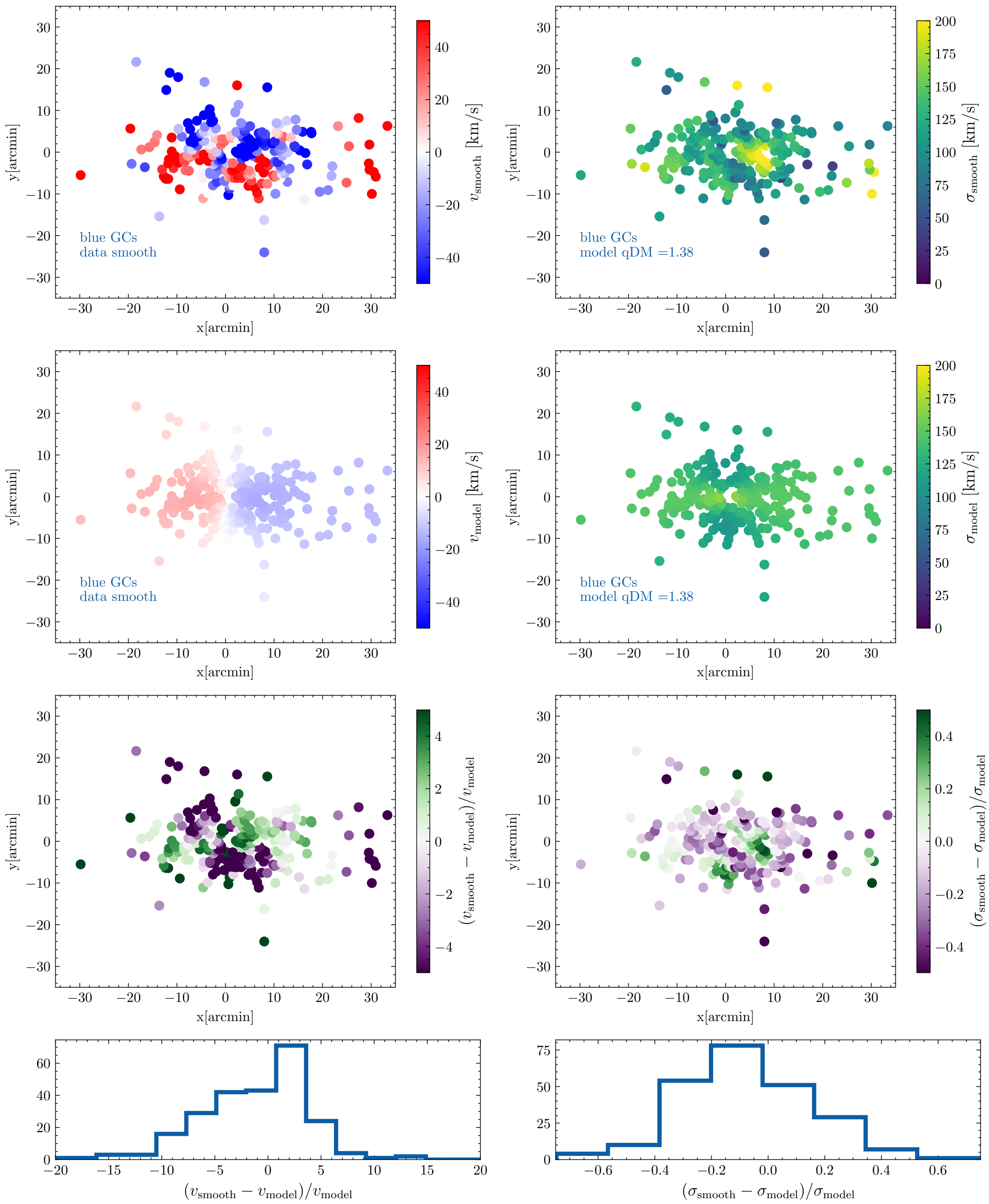

Figure 6.12: Comparison between the smooth velocity field of blue GCs and the model. The left column shows the mean velocity and the right column velocity dispersion. The first row shows the data and the second row the CJAM model evaluation for the best-fit values as given in Table 6.8. The third row shows the residuals between the smooth data and the model; the histogram of the residuals is shown in the bottom row.

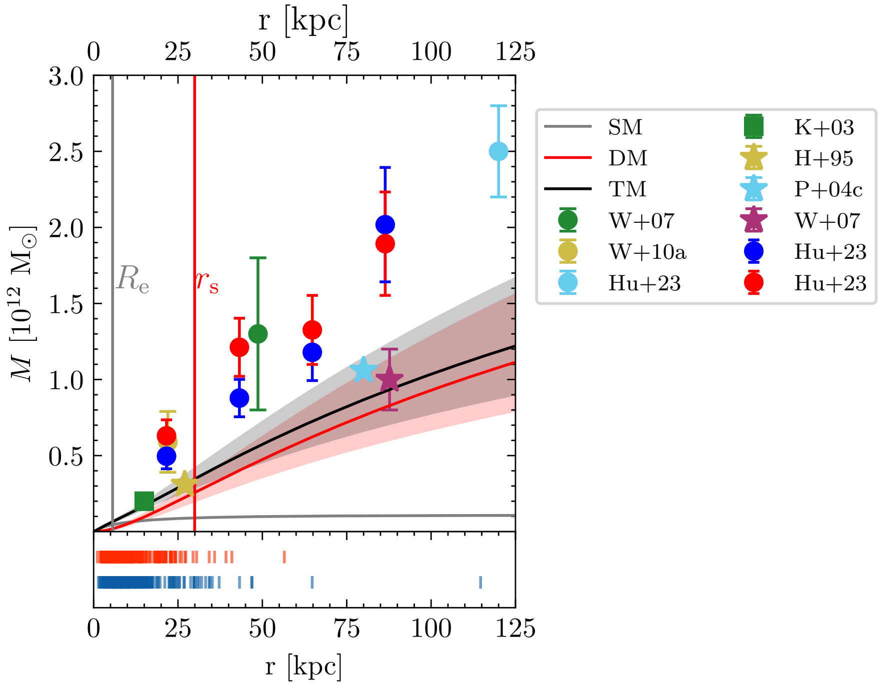

Figure 6.13: Enclosed mass measurements from this work are shown with lines and literature studies with symbols. The grey line shows the stellar enclosed mass, with $M_\star/L_B$ determined in this work. The red line with the associated shaded 1σ uncertainty region shows the enclosed dark matter mass integrated in spherical shells with r_s the scale radius of an NFW halo. The black line shows the total mass. Circles show literature measurements of the total mass with GCs as dynamical tracers, stars show PN-based measurements, and the square shows measurements from X-ray gas from Kraft et al. (2003). The location of the red and blue GCs used in this work is shown in the bottom panel.

blue from Peng et al. (2004a), with correction from Woodley et al. (2007), and the measurement from the latter study is shown in purple.

Our enclosed mass measurement is on average lower than the literature estimates from other dynamical modelling of GCs. The origin of the discrepancy could be the difference in the slope of the tracer density profile. Woodley et al. (2007) reanalysed the enclosed mass from Peng et al. (2004a) and found a factor of 2 higher mass, when using the de-projected 3D tracer density profile instead of the 2D one used in the original study. The slope used in Woodley et al. (2007) is steeper than that used in our work.

Woodley et al. (2007) modelled the pressure- and rotationally-supported masses of PNe and GCs separately, making no separation based on GC colour. To avoid biases in the inner regions obscured by the dust they excluded $R < 5$ arcmin. They adopted a distance of 3.9 Mpc to CenA and we account for the different distances between our and the literature study. Later, Woodley et al. (2010b) applied a tracer mass estimator (TME, Evans et al., 2003) to the whole sample of GCs to estimate the enclosed mass within 20 arcmin. They found the total mass of $(5.9 \pm 2.0) \times 10^{11}$ M$_\odot$, which agrees within 2σ with our result at 20 arcmin. They excluded eight outliers based on their projected velocity and radius (v^2R), which could inflate the mass estimate, and their robust measurements exclude GCs within 1 R_e ($R < 5$ arcmin). Relaxing the latter criteria results in increased mass estimate at all radii almost by a factor of 2, hinting at the sensitivity of this method to outliers.

Hughes et al. (2023) used the most spatially extended sample of GCs to provide enclosed mass estimates separately for the blue and red GCs. Our measurements agree within 2σ, but are systematically lower. They also used a TME (corrected for rotational support) to estimate the total enclosed mass within a given radius assuming spherical symmetry in the total mass distribution. In

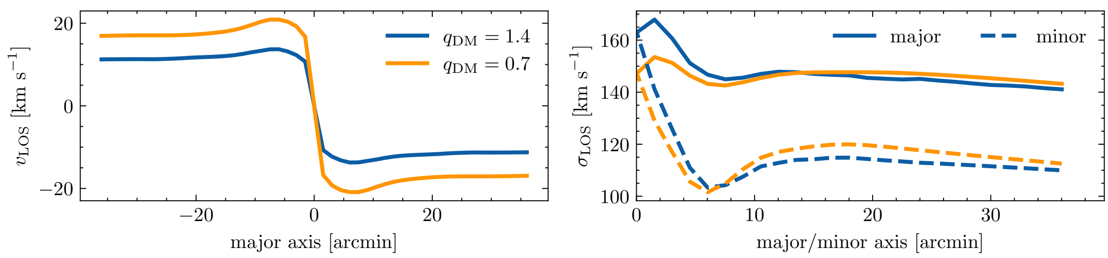

Figure 6.14: Comparing best-fit prolate (blue) and oblate (orange) CJAM model results. The left panel shows the mean LOS velocity along the major axis. The right panel shows the velocity dispersion along the major axis (solid lines) and along the minor axis (dashed lines). The LOS velocity is shown symmetrically along the major and minor axes, to highlight the asymmetric rotational signature. However, the velocity dispersion on the right panel is shown for positive values of the axes due to the symmetry of $\sigma_{\rm LOS}$.

their modelling, GCs are spherically distributed with a single power-law profile with an isotropic distribution of orbits. Their measurements are in good agreement with mass estimates from GCs, but are higher than the estimates using PNe. They postulate that the simplified assumption of isotropy in their estimates could be one of the reasons for this, as also commented in Woodley et al. (2007), but the mass-anisotropy degeneracy in spherical symmetry (Binney and Tremaine, 2008) prevents them from making a conclusive determination.

Pearson et al. (2022) used simulations to model stream formation due to a disruption of a dwarf galaxy. They sampled different masses of the host galaxy and found a lower limit on the mass of $M_{200} > 4.7 \times 10^{12}$ M$_\odot$. They compared the visual appearance of the stream observed by Crnojević et al. (2016) and a single RV along the stream with their simulation results to identify the gravitational potential needed for the observed stream morphology and kinematics. Because of covariances between the mass of the disrupted galaxy, the infall velocity and the line-of-sight position, more RV measurements along the stream are needed to provide stronger constraints on the mass.

Müller et al. (2022) used the satellite galaxies of the CenA to determine the dynamical mass within $R_{\rm max} \sim 800$ kpc (the maximal extent of their tracers). Using the mean circular velocity of 27 dwarfs, they estimated a spherical enclosed mass and determined $M_{200} = (5.3 \pm 3.5) \times 10^{12}$ M$_\odot$. This agrees with our measurements within the uncertainties. The dynamical time scales at such large distances, where the satellites are distributed, are longer than the Hubble time and non-virialised motion could inflate the enclosed mass estimate.

The best fit $M_\star/L_{\rm B}$ from this work is lower than that of Hui et al. (1995) and Mathieu et al. (1996), which could be attributed to the different treatment of the DM component in the modelling. Cappellari et al. (2009) modelled the central region of CenA to determine the mass of the central BH and found $M_\star/L_K = 0.65 \pm 0.15$.

6.7.2 Limitations of the modelling assumptions

In the context of CJAM, the flattening of $q_{\rm DM} > 1$ that we recover corresponds to the elongation of the dark matter distribution along the minor axis of the stellar and GC distribution. Literature investigations (Hui et al., 1995; Mathieu et al., 1996; Peng et al., 2004a) have identified clear signs of a triaxial halo and, in this section, we compare the modelling results from a prolate and oblate halo to identify the features in the observing plane that favour $q_{\rm DM} > 1$.

Figure 6.14 compares the projected velocity moments from the minimum χ^2 solution for our fiducial result $q_{\rm DM} = 1.45$ in blue and an oblate case with $q_{\rm DM} = 0.7$ in orange. For the latter, we recomputed the other parameters from the 2D χ^2 grids shown in Fig. 6.10. We chose a value of $q_{\rm DM} = 0.7$ as an intermediate flattening between the outer stellar halo flattening of 0.54 and the flattening of the GCS (0.72 for red and 0.82 for blue GCs). The left panel shows the mean LOS velocity and the right panel the velocity dispersion profile. We present simplified velocity moments along the major and minor axis only followed by a more detailed analysis of the 2D velocity moments.

The mean velocity along the major axis is higher in the oblate solution, however, the difference is smaller than the typical measurement uncertainty of 33 km s^{-1}. Beyond 10 arcmin the velocity dispersion profiles of the oblate and prolate DM haloes are very similar for both major and minor axes, where the majority of the kinematic tracers lie. To match the velocity dispersion at these radii, the resulting M_{200} and $M_{\star}/L_{\rm B}$ estimates for the oblate halo are lower compared with the prolate halo. This anti-correlation between the flattening and mass can be seen in Fig. 6.10. A lower total mass results in a central value of the velocity dispersion that is lower for the oblate solution (~ 150 km s^{-1}), compared with the prolate solution (~ 165 km s^{-1}). The latter value is in better agreement with the central stellar root-mean-square velocity of ~ 170 km s^{-1} in the inner 0.2 arcsec of CenA observed by Cappellari et al. (2009).

A drop in the velocity dispersion along the minor axis is also seen in the smooth velocity field in Fig. 6.12. Such a drop is consistent with the projected dispersion map of a triaxial system with short and long-axis tube orbits as seen in van den Bosch and van de Ven (2009). The full details of how measured flattening constrained with axisymmetric modelling can be mapped to the intrinsic shape and orientation of the DM halo is a topic for a future study.

2D velocity moments

Now that we understand the impact flattening has on the projected velocity components along the major and minor axis, we looked into the 2D maps of the LOS moments in Fig. 6.15. Such comparison is very informative as the discrete dynamical modelling approach used here is sensitive to the differences in the 2D velocity field originating from the different flattening of the DM potential.

To make the plots in Fig. 6.15 we evaluated CJAM on a grid of points linearly spaced in R and φ for the best fit parameters shown in Table 6.8. The left column shows the maps of the first moment projected along the line-of-sight and the right column shows the second moment. The first two rows show the model results from the blue GCs best-fit solutions for the prolate (top) and the oblate (bottom) cases shown inFig. 6.14. The bottom two rows show the residual of the prolate map with respect to the oblate case for the blue GC in the top and red GCs in the bottom. The streaks along the major axis are an artefact of the plotting and not a real feature.

The 2D maps reveal the full complexity of the velocity moments which can be probed by discrete dynamical modelling. The residuals for both blue (in the third row) and red GCs (in the bottom row) show that the best fit oblate model favours a stronger rotational signature. The residuals in the left column are higher for red than blue GCs and they consistently show higher residuals along the semimajor axis. This means that the gradient of the mean velocity from the minor to major axis depends on the flattening of the dark matter halo. Velocity dispersion maps in the right column show a similarly complex signature, with the opposite sign of the residuals. The prolate solution shows on average higher dispersion compared with the best-fit oblate solution. These maps highlight the importance and strength of discrete dynamical modelling, where the position of each GC is used to constrain the 2D velocity distribution, which shows distinct signatures for oblate and prolate solutions.

6.7.3 Extremely misaligned dark matter haloes in cosmological simulations

Within the axisymmetric modelling approach used in this work, the dark matter halo shape with $q_{\rm DM} > 1$ corresponds to its elongation along the minor axis of the stellar distribution. This raises a question of how frequent are such misalignments between the minor axes of the stellar and DM profiles. For example, in the Milky Way evidence disfavours a configuration in which the minor axis of the disc and DM halo are parallel (e.g. Debattista et al., 2013; Han et al., 2023; Law et al., 2009). In the Auriga analogues of the Milky Way, Prada et al. (2019, see their Fig. 6) found that

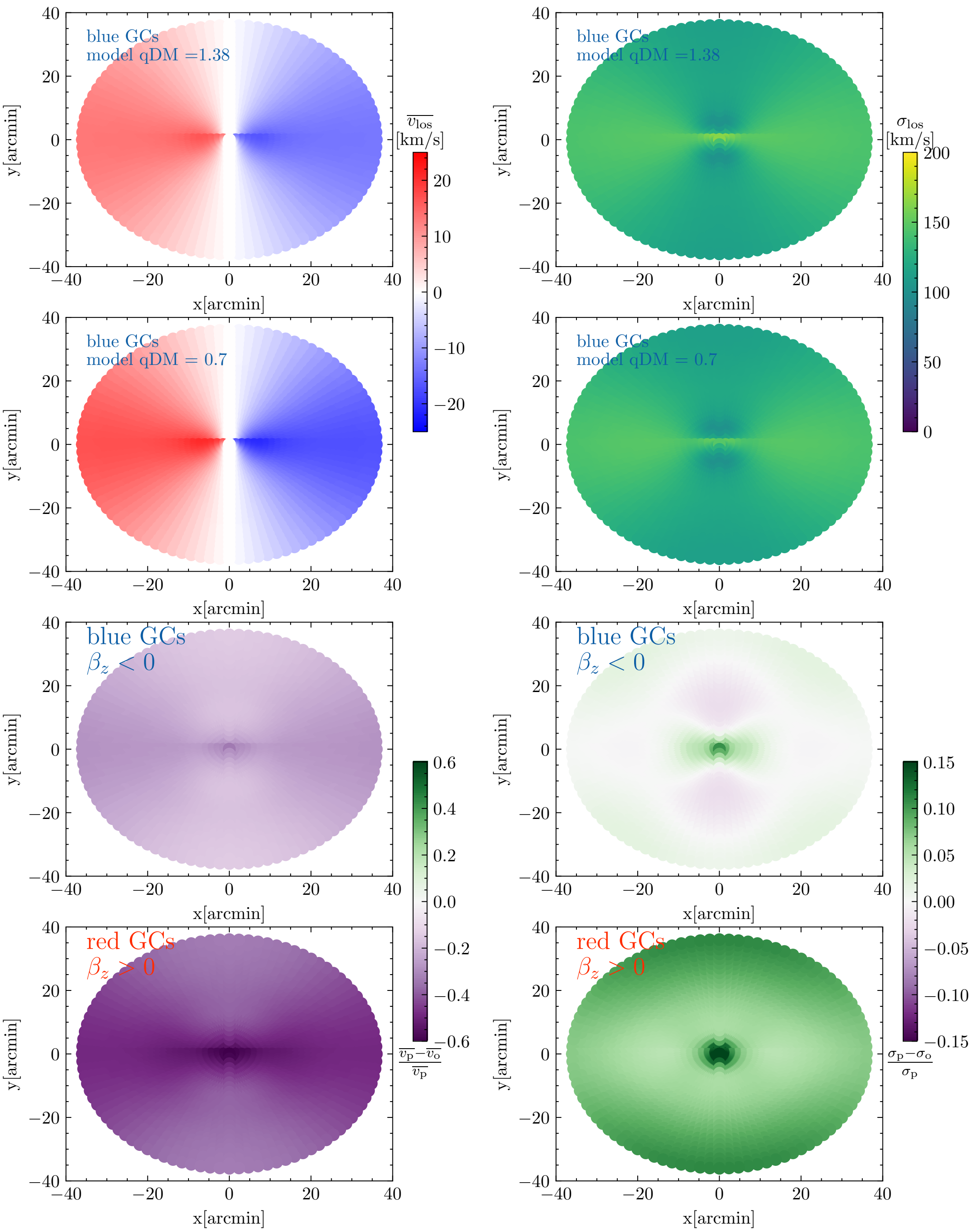

Figure 6.15: Comparison between the first and second moment velocity maps for axisymmetric Jeans modelling in the left and right column, respectively. The first two rows show the best-fit models for blue GCs, with the best fit $q_{\rm DM} = 1.38$ in the top $q_{\rm DM} = 0.7$ below. The bottom two rows show the residuals for the blue GCs on the top and red GCs on the bottom. The parameters used to evaluate the model were taken from Table 6.8 and for $q_{\rm DM} = 0.7$ we take the other parameters at the minimal χ^2 based on the 2D χ^2 grids as shown in Fig. 6.10.

the minor axes of the DM haloes and angular momentum vector of the stellar discs are aligned for most of their 30 haloes, with 2 haloes showing misalignment $> 70^o$ at 1/16 R_{200}.

In this section, we conduct a qualitative investigation to examine the frequency of highly-misaligned distributions in two cosmological simulations. This analysis aims to enhance our understanding of the results by employing radial regimes analogous to the sensitivity observed in the CenA study. For this purpose, we use IllustrisTNG (Nelson et al., 2019, and references therein) and Magneticum pathfinder[5] simulations to find analogues of CenA with a central oblate stellar component hosted in a prolate DM halo elongated along the stellar minor axis. We follow a procedure similar to Pulsoni et al. (2021) and Valenzuela et al. (in prep.) to measure the shapes of the simulated galaxies, corresponding to method S1 from Zemp et al. (2011). This is not carried out through dynamical modelling, but instead by computing the eigenvalues of the inertial tensor calculated using the positions of the simulated particles and their masses within ellipsoidal shells.

In both simulations, we selected galaxies in the mass range of CenA as a first step: $M_{\rm vir} = 3\times10^{12} - 3\times10^{13}$ $\mathrm{M_\odot}$ and $M_\star = 1 - 5\times10^{11}$ $\mathrm{M_\odot}$. Secondly, we selected those that have oblate stellar distributions embedded in prolate haloes. We then looked at the angle between the stellar minor axis and DM major axis and inspected the frequency of small misalignments between these two axes. We use the definition for triaxiality: $T \equiv (1-q^2)/(1-p^2)$, where $q = b/a$ and $p = c/a$ are the axis ratios between the major (a), intermediate (b) and minor (c) axis. A completely prolate halo has $T = 1$ ($a > b = c$), and perfectly oblate halo has $T = 0$ with ($a = b > c$). We first selected galaxies with $T_\star < 1/3$ and that are hosted in a halo with $T_{\rm DM} > 2/3$. To mimic the configuration of stellar and dark matter in line with CenA as presented in this work, we compute the shape of the stellar component at $3r_{\star,\rm half}$ (stellar half-mass radius) and the shape of the dark matter halo at $5r_{\star,\rm half}$. For those, we compute the angle between the minor axis of the stellar distribution and the major axis of the dark matter.

Magneticum

From Box4 (uhr) of the Magneticum Pathfinder simulation suite, which has side length of 68 Mpc, DM particle mass of $m_{\rm DM} = 5.1\times10^7$ $\mathrm{M_\odot}$ and average stellar particle mass of $m_* = 1.8\times10^6$ $\mathrm{M_\odot}$ (Teklu et al., 2015; Valenzuela and Remus, 2022), we find 111 galaxies that match the mass criteria, of which 94 have a modest star formation rate $\mathrm{SFR} < 3\ \mathrm{M_\odot\,yr^{-1}}$. Of these, 12 galaxies meet the shape criteria laid out above, of which 10 have modest star formation rates; only one of these galaxies has a small angle of 17° between the stellar minor axis and the DM major axis, whereas the rest have angles above 80°. That galaxy is at the lower end of the mass selection limits with $M_\star = 1.0\times10^{11}$ $\mathrm{M_\odot}$ and $M_{\rm vir} = 4.6\times10^{12}$ $\mathrm{M_\odot}$. It has no star formation and shows signs of recent interaction in the stellar halo. It should be noted, however, that the stellar component has a relatively spherical shape, such that the orientation of its axes are not very well defined.

IllustrisTNG

We considered the TNG100 simulation run, with a simulation box of 110.7 Mpc on a side, DM particle mass of 7.5×10^6 $\mathrm{M_\odot}$ and mean baryonic particle mass of 1.4×10^6 $\mathrm{M_\odot}$ (Nelson et al., 2019). From the redshift $z = 0$ snapshot, we identified 455 galaxies in the mass range around CenA. Of these, 121 have a prolate DM halo ($\sim 27\%$), but only 17 have an oblate stellar component within $3\ r_{\star,\rm half}$. Most of the 121 prolate DM haloes have the major axis close to the plane defined by the intermediate and major axis of the stellar component within 20°. Out of the 17 galaxies selected, only in 1 case there is significant misalignment. This is a clear merger, as shown by the presence of substructures or strong asymmetries in the stellar distribution and velocities. This galaxy has a moderate SFR of $1.8\ \mathrm{M_\odot}/yr$. The similarities between the simulated galaxy in the Magneticum simulation and CenA as well as the consistent merger imprints and low probability of such extreme misalignment found in both simulation suite suggest that it is likely a transient phenomenon. This work opens up possibilities for further studies of how the dark matter halo shape is influenced by the merger history of its host and the environment.

[5] www.magneticum.org

6.7.4 CONNECTION WITH THE CENA SATELLITES DISTRIBUTION

Recent studies of CenA satellites have found evidence of a corotating plane of satellites around CenA (Müller et al., 2018). In their latest study, Müller et al. (2021) showed that 21 out of 28 dwarf galaxies, which have both distance and radial velocity measurements that make them satellites of CenA, share a coherent motion within a flattened planar structure.

This plane of satellites is almost perpendicular to the dust disk and lies very close to the line connecting CenA and its nearest massive neighbour M83. Müller et al. (2019) used the accurate distances of CenA satellites using the tip of the RGB to determine the intrinsic 3D shape of the satellite system. They find a PA= $60^\circ\ ^{+21}_{-23}$ and determine the axis ratios $b/a = 0.71$ and $c/a = 0.41$, which results in a triaxiality of $T = 0.6$, close to prolate shape. They find that the long axis is aligned along the line-of-sight, in contrast with the stellar shape measurements traced by PNe within 25 kpc by Hui et al. (1995) and within 80 kpc by Peng et al. (2004a). The former found $T = 0.4$ (triaxial, but more oblate) and determined the viewing angles, such that the intermediate axis lies along the line-of-sight. Using these viewing angles, Peng et al. (2004a) found that the kinematics of the PNe at larger distances favour a significantly more prolate shape of $T = 0.98$.

Müller et al. (2021) explored the frequency of similar flattened structures in TNG100 (Nelson et al., 2019). Such flattened and coherently moving structures are found in only 0.3% of CenA analogues in dark-matter-only simulations and in 0.2% in hydrodynamical simulations. More generally, the distribution of satellite galaxies in ΛCDM is not expected to be completely random, i.e. isotropic (e.g. Zentner et al., 2005), due to the anisotropic accretion from cosmic filaments.

In this framework, the DM halo of CenA is expected to be elongated along the major axis of the PNe and the satellite system, which is in contrast with the results of our modelling under axisymmetric assumptions. On the other hand, the triaxial shape of the satellite system with $T = 0.6$ (Müller et al., 2019) and of PNe with $T = 0.98$ (Peng et al., 2004a) strongly disfavour spherical or oblate distributions, which is in line with our findings.

6.8 SUMMARY AND CONCLUSIONS

We carried out axisymmetric dynamical modelling of the blue and red GCs in the CenA galaxy to measure the total mass and the intrinsic shape of its dark matter halo. The axisymmetric JAM modelling used in this work requires a relaxed system. Given that CenA shows signatures of past mergers, special care was taken to identify a sample of GCs that shows a point-symmetric distribution indicative of a relaxed distribution. The dataset that constrains the model is composed of the photometric dataset from (T17) and the radial velocity sample from Hughes et al. (2021a), which extend out to 115 kpc and include 225 red and 257 blue GCs. We note that 90% of the kinematic dataset is within 40 kpc.

We used axisymmetric JAM modelling together with a discrete Gaussian likelihood analysis to determine the best-fitting parameters of the gravitational potential and orbital properties of the GCs. The gravitational potential is composed of both an axisymmetric stellar surface brightness out to 140 kpc (25 $R_{\rm e}$), a mass-to-light ratio $M_\star/L_{\rm B}$, and an axisymmetric dark matter distribution. We assumed an NFW form for the dark matter profile, parametrised by M_{200} and used the latest literature mass-concentration relation to determine the c_{200}. By varying $q_{\rm DM}$ we explored the deviation of DM halo from spherical symmetry. To find the best-fit model, we maximise the Gaussian likelihood. The best-fit parameters were determined in an iterative approach, accounting for the covariances in the modelled parameters. We modelled the blue and red GCs separately and used them as two independent samples to verify our approach and determine the highest likelihood solution for the parameters of the gravitational potential. The need to treat them separately was further motivated by the intrinsically different spatial distribution and orbital properties.

We derive a dark matter mass of $M_{200} = 1.86^{1.61}_{-0.69} \times 10^{12}$ M$_\odot$ and $M_\star/L_{\rm B}$= $2.98^{+0.96}_{-0.78}$, resulting in a total stellar mass of $M_\star \approx 0.9 \times 10^{11}$ M$_\odot$. The total halo mass is lower than literature investigations using GC kinematics, but in agreement with measurements from PNe as discussed in Sect. 6.7.1. Our flattening of $q_{\rm DM} = 1.45^{+0.78}_{-0.53}$ disfavours an oblate or spherical DM halo. We explored the implications of $q_{\mathrm{DM}} > 1$ under the axisymmetry assumption of the JAM modelling by examining the frequency of prolate DM haloes that host an oblate stellar distribution in the Magneticum and TNG simulations. We found that in both simulation suites, DM elongated along the minor axis of the stellar distribution is very rare and identified only in galaxies with strong signatures of active or recent mergers. Comparing the smooth velocity field of the GCs, we identified a difference in the velocity dispersion along the major and minor axes that can also arise in intrinsically triaxial potentials (Sect. 6.7.3). This suggests that GCs, and the modelling carried out in this work, are sensitive to deviations from spherical and cylindrical symmetry.

We find that the orbital properties of blue and red GCs are different. While both populations show mild rotation, we find that the rotation parameter κ is larger for red GCs than blue GCs. The blue population also shows negative orbital anisotropy in cylindrical coordinates while the red population is consistent with being isotropic. Both results highlight the need for incorporating rotation and anisotropy in future dynamical modelling.

Future work should include more complex modelling that can account for triaxial symmetry and non-relaxed structures such as streams. To enable such modelling, RV measurements in the outer halo need to include the full extent of the galaxy potential. This will allow us to gain a better understanding of the global potential of the host and its assembly history.

Chapter 7

Thesis conclusions

7.1 SUMMARY

Mass is the dominant driver of galaxy formation and evolution and according to ΛCDM cosmology, ∼80% of it is made up of dark matter (DM), which only interacts with luminous matter through gravity (chapter 1). The surface brightness of luminous matter is low in regions of the galaxies where dark matter dominates. Dynamical modelling is sensitive to the properties of the gravitational potential, and thus luminous and DM mass, out to the outermost kinematic tracer. Thus constraints on the nature of dark matter using stellar kinematics in baryon-dominated centres of galaxies $\leqslant 1\ R_{\mathrm{e}}$[1] rely on extrapolation out to the halo. The halo of every galaxy is populated by globular clusters (GCs). The total mass of the globular clusters systems (GCS) is correlated with the virial mass of the halo and can be observed out to $5 - 10\ R_{\mathrm{e}}$. Therefore these are ideal kinematic tracers in the regions dominated by DM.

Throughout this thesis, I used discrete dynamical modelling based on Jeans equations (JAM) (chapter 2) to constrain the parameters of the gravitational potential with spatially extended GCS. In particular, I focused on the radial profile of the gravitational potential and on determining the shape of the dark matter halo in NGC 5128, a nearby elliptical galaxy. By probing the spatial distribution of DM in areas where it dominates over the luminous matter, we can get a deeper understanding of its nature.

The research questions, datasets and stellar systems I studied were different throughout the thesis but were connected by a joint dynamical modelling approach. Discrete dynamical modelling alleviates the need for binning the kinematic dataset and offers unique advantages when modelling intrinsically sparse systems, such as GCs in galactic haloes. I used the CJAM implementation of the Jeans anisotropic MGE modelling in a cylindrical coordinate system that can account for the flattening of the kinematic tracers and mass distribution.

The gravitational potential is comprised of dark and luminous components. Driven by different research questions I characterised it either as a single total mass profile, combining dark and luminous matter distribution, or by considering only one of the two components. I used different functional forms (NFW, Einasto and generalised Hernquist profile) to parameterise the dark matter distribution and stellar surface brightness profile scaled by the mass-to-light ratio (M/L). Together with the gravitational potential I also modelled the orbital properties of the tracer population, i.e., the cylindrical velocity anisotropy β_z and rotation parameter κ.

Accurate modelling is based on accurate characterisation of the spatial distribution of the kinematic tracers. For the heterogeneous datasets of GCs used in this thesis, I developed a two-step approach to assess the spatial and magnitude completeness of a photometric dataset. I used both simulated data of mock dwarf galaxies and observed kinematics of GCs and PNe. I used both χ^2 analysis and Bayesian statistics to find the best-fit parameters of the gravitational potential. Both were based on the assumption of Gaussian line-of-sight velocity distribution (LOSVD) which acted as a likelihood. The posterior was computed from the likelihood of individual kinematic tracers.

In what follows I summarise the main conclusions of this thesis based on the open questions posed in Sect. 1.5.

OBSERVATIONAL REQUIREMENTS TO RESOLVE THE CORE-CUSP PROBLEM

In chapter 3, I find that both line-of-sight velocities (LOSVs) and proper motions (PMs) of stellar tracers are needed to robustly recover the inner and outer slope of a cored DM profile in a dwarf spheroidal galaxy. The mock LOSV sample that can best robustly constrain the true slopes is comprised of ∼2000 tracers, and with high precision $\epsilon_i \sim 10V_{200}$ in the radial region where most tracers are located ($0.2 \leqslant R/R_c \leqslant 2.5$). A smaller number of tracers in the very inner and outer regions are also needed. High precision in these radial ranges can bias the results due to the stochasticity of small-number statistics. That is why a lower precision of LOSV measurements in these regions yields better results. The associated mock PM sample of ~ 100 tracers across the whole body of the stellar system and with a typical precision $\epsilon_i \sim 10V_{200}$ is also needed.

[1]Radius enclosing 50% of the total stellar light.

7

ADVANTAGES AND CAVEATS OF DISCRETE DYNAMICAL MODELLING

In chapter 4, I developed a two-step approach to determine an accurate tracer density profile of GCs (presented in Sect. 2.3) and determined how complementary observing campaigns and kinematic tracers can be used to carry out robust discrete dynamical modelling. The low number of kinematic tracers spread over a large radial range of the galactic haloes warrants a careful approach to ensure robust measurements. I used a combination of two GC datasets and a PNe dataset to demonstrate that discrete dynamical modelling is strongly sensitive to interlopers. Their presence can result in multimodal posterior distributions and combining independent kinematic tracers and datasets can mitigate their effect to produce robust dynamical modelling results.

IS THE TOTAL MASS PROFILE OF EARLY-TYPE GALAXIES ISOTROPIC AND UNIVERSAL?

In chapter 5, I present the discrete dynamic modelling of 19 SLUGGSs galaxies with a flexible density profile with a fixed outer slope (-3) and free inner slope α. To break the degeneracy between the density and scale radius of the total mass profile, I imposed informative priors without impacting the parameters of interest M_{200}[2] and α.

I modelled GCs as a single population and found biased results for massive cD galaxies in the galaxy sample. By studying NGC 1407, I confirmed that the different orbital properties of blue and red GCs in such galaxies is the source of the bias. Galaxies with fewer than ~ 50 GCs also tend to show biased results.

From the 12 galaxies with robust measurements presented here, I recovered a value for the inner slope of $\overline{\alpha} = 1.9 \pm 0.01$. This is lower than the outer slope, therefore the single power law is not a good description of their total mass density profile. By fitting a single power-law slope $\gamma_{\rm tot}$ to the profile I find a value of $\langle\gamma_{\rm tot}\rangle = -2.22 \pm 0.14$, stepper than isotropic $\gamma_{\rm tot} = -2$.

The universality of the isotropic slope is identified by a small scatter in the spread across many orders of magnitude in stellar mass. Our measurement uncertainties prevent us from making such a statement and we demonstrate that the number of GCs is the strongest driver in the uncertainties of the $\gamma_{\rm tot}$ measurements.

7

ARE DARK MATTER HALOES CONSISTENT WITH SPHERICAL?

I used the kinematics of GCs around the nearby galaxy NGC 5128 to model the DM shape with the axisymmetric CJAM. I find that a spherical halo is strongly disfavored and a prolate halo is preferred by the data. I modelled blue and red GCs separately and both favour such values of the shape parameter. The strongest constraints on the shape parameter come from the orbital properties of the kinematic tracers. Net rotation and anisotropy impact the projected 2D velocity field of the GCs in the presence of a non-spherical DM halo, and discrete dynamical modelling is sensitive to such signatures.

Since the axis of symmetry is fixed in the Jeans modelling that I carried out, a prolate halo corresponds to a halo with a major axis aligned with the minor axis of the oblate kinematic tracers. We find that in the cosmological simulations such configuration is rare and when it occurs there is strong evidence for a recent merger, suggesting a transient configuration. Our modelling assumptions limit a concussive answer on the exact orientation of the halo, however, the data strongly disfavours a spherical distribution and future studies need to take this into account to avoid biased measurements.

7.2 PROSPECTS FOR THE FUTURE

There are three avenues to expand this work:

[2]Mass of a spherical overdensity with average density 200$\times$ the critical density of the universe.

Increased sample size

Novel wide-field photometric surveys like with the LSST, the Roman telescope, and the recently launched Euclid telescope will provide large databases from which candidate GCs can be selected for spectroscopic follow-up observations. This will increase the number of galaxies that can be modelled using discrete dynamical modelling, thereby increasing the statistical sample available to constrain cosmological models by providing a good observational handle on a large number of M_{200} measurements as well as dark matter mass distribution (e.g. Dold and Fahrion, 2022).

Combining GCs with other kinematic tracers

While GCs offer possibilities to trace the gravitational potential in the halo, modelling only GCs can lead to poor constraints in the inner regions of the galaxy. By combining halo tracers and stellar kinematics we can provide stronger constraints on both the total halo mass and inner DM slope.

Most galaxies host more PNe than GCs and because they are stellar remnants their orbital properties and spatial distribution trace the stellar halo. They are distinct dynamical tracers of the potential and provide complementary information on the dynamical mass. By combing GCs, PNe and stellar kinematics we can provide tighter constraints on the stellar mass-to-light ratio, on halo mass M_{200}, on the inner and outer slope of the dark matter halo, as well as on the shape of the halo.

Triaxial dynamical modelling

The haloes of galaxies are expected to deviate from simple oblate or prolate shapes and are expected to be triaxial. The statistical distribution of axis ratios can constrain dark matter models and inform feedback processes in hydrodynamic simulations. Triaxial modelling offers the opportunity to constrain the shape of the dark matter haloes.

While solutions to the triaxial Jeans equations exist (van de Ven et al., 2003), they have yet to be implemented in a freely available open-source software like CJAM. More flexible triaxial Schwarzschild modelling (Chanamé et al., 2008; Schwarzschild, 1979) can account for deviations from cylindrical or spherical symmetry. Either open-source triaxial Jeans modelling or the discrete triaxial Schwarzschild method would open up possibilities to use the discrete halo tracers to their full potential and measure the intrinsic distribution of dark matter in galaxies to bring us closer to addressing the question of its nature.

BIBLIOGRAPHY

Alabi, Adebusola B. et al. (Aug. 2016). "The SLUGGS survey: the mass distribution in early-type galaxies within five effective radii and beyond". In: MNRAS 460.4, pp. 3838–3860. DOI: 10.1093/mnras/stw1213. arXiv: 1605.06101 [astro-ph.GA].

Alam, Shadab et al. (Sept. 2017). "The clustering of galaxies in the completed SDSS-III Baryon Oscillation Spectroscopic Survey: cosmological analysis of the DR12 galaxy sample". In: MNRAS 470.3, pp. 2617–2652. DOI: 10.1093/mnras/stx721. arXiv: 1607.03155 [astro-ph.CO].

Allgood, Brandon et al. (Apr. 2006). In: *mnras* 367.4, pp. 1781–1796. DOI: 10.1111/j.1365-2966.2006.10094.x. arXiv: astro-ph/0508497 [astro-ph].

Aprile, E. et al. (Sept. 2018). "Dark Matter Search Results from a One Ton-Year Exposure of XENON1T". In: Phys. Rev. Lett. 121.11, 111302, p. 111302. DOI: 10.1103/PhysRevLett.121.111302. arXiv: 1805.12562 [astro-ph.CO].

Auger, M. W. et al. (Nov. 2010). "The Sloan Lens ACS Survey. X. Stellar, Dynamical, and Total Mass Correlations of Massive Early-type Galaxies". In: ApJ 724.1, pp. 511–525. DOI: 10.1088/0004-637X/724/1/511. arXiv: 1007.2880 [astro-ph.CO].

Bailin, Jeremy and Matthias Steinmetz (July 2005). "Internal and External Alignment of the Shapes and Angular Momenta of ΛCDM Halos". In: ApJ 627.2, pp. 647–665. DOI: 10.1086/430397. arXiv: astro-ph/0408163 [astro-ph].

Barnabè, Matteo et al. (Aug. 2011). "Two-dimensional kinematics of SLACS lenses - III. Mass structure and dynamics of early-type lens galaxies beyond z $\simeq$ 0.1". In: MNRAS 415.3, pp. 2215–2232. DOI: 10.1111/j.1365-2966.2011.18842.x. arXiv: 1102.2261 [astro-ph.CO].

Bastian, Nate et al. (May 2020). "The globular cluster system mass-halo mass relation in the E-MOSAICS simulations". In: *arXiv e-prints*, arXiv:2005.05991, arXiv:2005.05991. arXiv: 2005.05991 [astro-ph.GA].

Beasley, Michael A. et al. (May 2008). "A 2dF spectroscopic study of globular clusters in NGC 5128: probing the formation history of the nearest giant elliptical". In: MNRAS 386.3, pp. 1443–1463. DOI: 10.1111/j.1365-2966.2008.13123.x. arXiv: 0803.1066 [astro-ph].

Bedregal, A. G. et al. (Oct. 2006). "S0 galaxies in Fornax: data and kinematics". In: MNRAS 371.4, pp. 1912–1924. DOI: 10.1111/j.1365-2966.2006.10829.x. arXiv: astro-ph/0607434 [astro-ph].

Bellstedt, Sabine et al. (June 2018). "The SLUGGS survey: a comparison of total-mass profiles of early-type galaxies from observations and cosmological simulations, to ∼4 effective radii". In: MNRAS 476.4, pp. 4543–4564. DOI: 10.1093/mnras/sty456. arXiv: 1803.02373 [astro-ph.GA].

Bertone, Gianfranco and Dan Hooper (Oct. 2018). "History of dark matter". In: *Reviews of Modern Physics* 90.4, 045002, p. 045002. DOI: 10.1103/RevModPhys.90.045002. arXiv: 1605.04909 [astro-ph.CO].

Betoule, M. et al. (Aug. 2014). "Improved cosmological constraints from a joint analysis of the SDSS-II and SNLS supernova samples". In: A&A 568, A22, A22. DOI: 10.1051/0004-6361/201423413. arXiv: 1401.4064 [astro-ph.CO].

Bílek, M., S. Samurović, and F. Renaud (May 2019). "Study of gravitational fields and globular cluster systems of early-type galaxies". In: A&A 625, A32, A32. DOI: 10.1051/0004-6361/201834675. arXiv: 1903.05659 [astro-ph.GA].

Binney, James and Scott Tremaine (2008). *Galactic Dynamics: Second Edition*.

Blakeslee, John P. (June 1997). "The Dependence of Globular Cluster Number on Density for Abell Cluster Central Galaxies". In: ApJ 481.2, pp. L59–L62. DOI: 10.1086/310653. arXiv: astro-ph/9703099 [astro-ph].

Blakeslee, John P. et al. (Mar. 2009). "The ACS Fornax Cluster Survey. V. Measurement and Recalibration of Surface Brightness Fluctuations and a Precise Value of the Fornax-Virgo Relative Distance". In: ApJ 694.1, pp. 556–572. DOI: 10.1088/0004-637X/694/1/556. arXiv: 0901.1138 [astro-ph.CO].

Brodie, Jean P. and Jay Strader (Sept. 2006). "Extragalactic Globular Clusters and Galaxy Formation". In: ARA&A 44.1, pp. 193–267. DOI: 10.1146/annurev.astro.44.051905.092441. arXiv: astro-ph/0602601 [astro-ph].

Brodie, Jean P. et al. (Nov. 2014). "The SAGES Legacy Unifying Globulars and GalaxieS Survey (SLUGGS): Sample Definition, Methods, and Initial Results". In: ApJ 796.1, 52, p. 52. DOI: 10.1088/0004-637X/796/1/52. arXiv: 1405.2079 [astro-ph.GA].

Bryan, S. E. et al. (Mar. 2013). "The impact of baryons on the spins and shapes of dark matter haloes". In: MNRAS 429.4, pp. 3316–3329. DOI: 10.1093/mnras/sts587. arXiv: 1207.4555 [astro-ph.CO].

Bullock, J. S. (Mar. 2002). "Shapes of Dark Matter Halos". In: *The Shapes of Galaxies and their Dark Halos*. Ed. by Priyamvada Natarajan, pp. 109–113. DOI: 10.1142/9789812778017_0018. arXiv: astro-ph/0106380 [astro-ph].

Bullock, James S. and Michael Boylan-Kolchin (Aug. 2017). "Small-Scale Challenges to the ΛCDM Paradigm". In: ARA&A 55.1, pp. 343–387. DOI: 10.1146/annurev-astro-091916-055313. arXiv: 1707.04256 [astro-ph.CO].

Cappellari, M. (2002). "Efficient multi-Gaussian expansion of galaxies". In: MNRAS 333, pp. 400–410. DOI: 10.1046/j.1365-8711.2002.05412.x. eprint: arXiv:astro-ph/0201430.

Cappellari, Michele (Oct. 2008). "Measuring the inclination and mass-to-light ratio of axisymmetric galaxies via anisotropic Jeans models of stellar kinematics". In: MNRAS 390.1, pp. 71–86. DOI: 10.1111/j.1365-2966.2008.13754.x. arXiv: 0806.0042 [astro-ph].

Cappellari, Michele et al. (Apr. 2009). "The mass of the black hole in Centaurus A from SINFONI AO-assisted integral-field observations of stellar kinematics". In: MNRAS 394.2, pp. 660–674. DOI: 10.1111/j.1365-2966.2008.14377.x. arXiv: 0812.1000 [astro-ph].

Cappellari, Michele et al. (May 2011). "The ATLAS^{3D} project - I. A volume-limited sample of 260 nearby early-type galaxies: science goals and selection criteria". In: MNRAS 413.2, pp. 813–836. DOI: 10.1111/j.1365-2966.2010.18174.x. arXiv: 1012.1551 [astro-ph.CO].

Cappellari, Michele et al. (July 2013). "The ATLAS^{3D} project - XV. Benchmark for early-type galaxies scaling relations from 260 dynamical models: mass-to-light ratio, dark matter, Fundamental Plane and Mass Plane". In: MNRAS 432.3, pp. 1709–1741. DOI: 10.1093/mnras/stt562. arXiv: 1208.3522 [astro-ph.CO].

Cappellari, Michele et al. (May 2015). "Small Scatter and Nearly Isothermal Mass Profiles to Four Half-light Radii from Two-dimensional Stellar Dynamics of Early-type Galaxies". In: ApJ 804.1, L21, p. L21. DOI: 10.1088/2041-8205/804/1/L21. arXiv: 1504.00075 [astro-ph.GA].

Chanamé, Julio, Jan Kleyna, and Roeland van der Marel (Aug. 2008). "Constraining the Mass Profiles of Stellar Systems: Schwarzschild Modeling of Discrete Velocity Data Sets". In: ApJ 682.2, pp. 841–860. DOI: 10.1086/589429. arXiv: 0710.1872 [astro-ph].

Chaturvedi, Avinash et al. (Jan. 2022). "The Fornax Cluster VLT Spectroscopic Survey. III. Kinematical characterisation of globular clusters in the Fornax galaxy cluster". In: A&A 657, A93, A93. DOI: 10.1051/0004-6361/202141334. arXiv: 2109.08694 [astro-ph.GA].

Chua, Kun Ting Eddie et al. (Mar. 2019). In: *mnras* 484.1, pp. 476–493. DOI: 10.1093/mnras/sty3531. arXiv: 1809.07255 [astro-ph.GA].

Ciotti, L. and G. Bertin (Dec. 1999). "Analytical properties of the R$^{1/m}$ law". In: A&A 352, pp. 447–451. arXiv: astro-ph/9911078 [astro-ph].

Coccato, L., M. Arnaboldi, and O. Gerhard (Dec. 2013). "Signatures of accretion events in the haloes of early-type galaxies from comparing PNe and GCs kinematics". In: MNRAS 436.2, pp. 1322–1334. DOI: 10.1093/mnras/stt1649. arXiv: 1209.0356 [astro-ph.CO].

Cole, Shaun and Cedric Lacey (July 1996). "The structure of dark matter haloes in hierarchical clustering models". In: MNRAS 281, p. 716. DOI: 10.1093/mnras/281.2.716. arXiv: astro-ph/9510147 [astro-ph].

Correa, Camila A. et al. (Sept. 2015). "The accretion history of dark matter haloes - III. A physical model for the concentration-mass relation". In: MNRAS 452.2, pp. 1217–1232. DOI: 10.1093/mnras/stv1363. arXiv: 1502.00391 [astro-ph.CO].

Côté, Patrick et al. (July 2004). "The ACS Virgo Cluster Survey. I. Introduction to the Survey". In: ApJS 153.1, pp. 223–242. DOI: 10.1086/421490. arXiv: astro-ph/0404138 [astro-ph].

Courteau, Stéphane et al. (Jan. 2014). "Galaxy masses". In: *Reviews of Modern Physics* 86.1, pp. 47–119. DOI: 10.1103/RevModPhys.86.47. arXiv: 1309.3276 [astro-ph.CO].

Crain, Robert A. and Freeke van de Voort (Aug. 2023). "Hydrodynamical Simulations of the Galaxy Population: Enduring Successes and Outstanding Challenges". In: ARA&A 61, pp. 473–515. DOI: 10.1146/annurev-astro-041923-043618. arXiv: 2309.17075 [astro-ph.GA].

Crnojević, D. et al. (May 2016). "The Extended Halo of Centaurus A: Uncovering Satellites, Streams, and Substructures". In: ApJ 823.1, 19, p. 19. DOI: 10.3847/0004-637X/823/1/19. arXiv: 1512.05366 [astro-ph.GA].

de Blok, W. J. G., Stacy S. McGaugh, and Vera C. Rubin (Nov. 2001). "High-Resolution Rotation Curves of Low Surface Brightness Galaxies. II. Mass Models". In: AJ 122.5, pp. 2396–2427. DOI: 10.1086/323450.

de Blok, W. J. G. et al. (Dec. 2008). "High-Resolution Rotation Curves and Galaxy Mass Models from THINGS". In: AJ 136.6, pp. 2648–2719. DOI: 10.1088/0004-6256/136/6/2648. arXiv: 0810.2100 [astro-ph].

De Lucia, Gabriella and Jérémy Blaizot (Feb. 2007). "The hierarchical formation of the brightest cluster galaxies". In: MNRAS 375.1, pp. 2–14. DOI: 10.1111/j.1365-2966.2006.11287.x. arXiv: astro-ph/0606519 [astro-ph].

de Vaucouleurs, Gerard et al. (1991). *Third Reference Catalogue of Bright Galaxies*.

Deason, A. J. et al. (Mar. 2012). "Elliptical Galaxy Masses Out to Five Effective Radii: The Realm of Dark Matter". In: ApJ 748.1, 2, p. 2. DOI: 10.1088/0004-637X/748/1/2. arXiv: 1110.0833 [astro-ph.CO].

Debattista, Victor P. et al. (Oct. 2013). "What's up in the Milky Way? The orientation of the disc relative to the triaxial halo". In: MNRAS 434.4, pp. 2971–2981. DOI: 10.1093/mnras/stt1217. arXiv: 1301.2670 [astro-ph.GA].

Derkenne, Caro et al. (Sept. 2021). "Total mass density slopes of early-type galaxies using Jeans dynamical modelling at redshifts 0.29 ¡ z ¡ 0.55". In: MNRAS 506.3, pp. 3691–3716. DOI: 10.1093/mnras/stab1996. arXiv: 2107.05206 [astro-ph.GA].

Derkenne, Caro et al. (July 2023). "The MAGPI Survey: impact of environment on the total internal mass distribution of galaxies in the last 5 Gyr". In: MNRAS 522.3, pp. 3602–3626. DOI: 10.1093/mnras/stad1079.

Di Valentino, Eleonora et al. (July 2021). "In the realm of the Hubble tension-a review of solutions". In: *Classical and Quantum Gravity* 38.15, 153001, p. 153001. DOI: 10.1088/1361-6382/ac086d. arXiv: 2103.01183 [astro-ph.CO].

Ding, Y. et al. (Apr. 2023). "The Fornax3D project: Environmental effects on the assembly of dynamically cold disks in Fornax cluster galaxies". In: A&A 672, A84, A84. DOI: 10.1051/0004-6361/202244558. arXiv: 2301.05532 [astro-ph.GA].

Dodelson, Scott (2003). *Modern Cosmology*.

Dold, Dominik and Katja Fahrion (July 2022). "Evaluating the feasibility of interpretable machine learning for globular cluster detection". In: A&A 663, A81, A81. DOI: 10.1051/0004-6361/202243354. arXiv: 2204.00017 [astro-ph.GA].

Dufour, R. J. et al. (Mar. 1979). "Picture processing analysis of the optical structure of NGC 5128 (Centaurus A)." In: AJ 84, pp. 284–301. DOI: 10.1086/112421.

Dumont, Antoine et al. (Apr. 2022). "A Population of Luminous Globular Clusters and Stripped Nuclei with Elevated Mass to Light Ratios around NGC 5128". In: ApJ 929.2, 147, p. 147. DOI: 10.3847/1538-4357/ac551c. arXiv: 2112.04504 [astro-ph.GA].

Dumont, Antoine et al. (June 2023). "Investigating the Dark Matter Halo of NGC 5128 using a Discrete Dynamical Model". In: *arXiv e-prints*, arXiv:2306.11786, arXiv:2306.11786. DOI: 10.48550/arXiv.2306.11786. arXiv: 2306.11786 [astro-ph.GA].

Dutton, Aaron A. and Andrea V. Macciò (July 2014). "Cold dark matter haloes in the Planck era: evolution of structural parameters for Einasto and NFW profiles". In: MNRAS 441.4, pp. 3359–3374. DOI: 10.1093/mnras/stu742. arXiv: 1402.7073 [astro-ph.CO].

Dutton, Aaron A. and Tommaso Treu (Mar. 2014). "The bulge-halo conspiracy in massive elliptical galaxies: implications for the stellar initial mass function and halo response to baryonic processes". In: MNRAS 438.4, pp. 3594–3602. DOI: 10.1093/mnras/stt2489. arXiv: 1303.4389 [astro-ph.CO].

Dutton, Aaron A. et al. (June 2019). "NIHAO XX: the impact of the star formation threshold on the cusp-core transformation of cold dark matter haloes". In: MNRAS 486.1, pp. 655–671. DOI: 10.1093/mnras/stz889. arXiv: 1811.10625 [astro-ph.GA].

Dutton, Aaron A. et al. (Dec. 2020). "NIHAO - XXV. Convergence in the cusp-core transformation of cold dark matter haloes at high star formation thresholds". In: MNRAS 499.2, pp. 2648–2661. DOI: 10.1093/mnras/staa3028. arXiv: 2011.11351 [astro-ph.GA].

Eggen, O. J., D. Lynden-Bell, and A. R. Sandage (Nov. 1962). "Evidence from the motions of old stars that the Galaxy collapsed." In: ApJ 136, p. 748. DOI: 10.1086/147433.

Einasto, J. (Jan. 1965). "On the Construction of a Composite Model for the Galaxy and on the Determination of the System of Galactic Parameters". In: *Trudy Astrofizicheskogo Instituta Alma-Ata* 5, pp. 87–100.

Ellis, John et al. (June 1984). "Supersymmetric relics from the big bang". In: *Nuclear Physics B* 238.2, pp. 453–476. DOI: 10.1016/0550-3213(84)90461-9.

Emsellem, E., G. Monnet, and R. Bacon (May 1994). "The multi-gaussian expansion method: a tool for building realistic photometric and kinematical models of stellar systems I. The formalism". In: A&A 285, pp. 723–738.

Ene, Irina et al. (Sept. 2018). "The MASSIVE Survey - X. Misalignment between kinematic and photometric axes and intrinsic shapes of massive early-type galaxies". In: MNRAS 479.2, pp. 2810–2826. DOI: 10.1093/mnras/sty1649. arXiv: 1802.00014 [astro-ph.GA].

Evans, N. W. et al. (Feb. 2003). "New Mass Estimators For Tracer Populations". In: ApJ 583.2, pp. 752–757. DOI: 10.1086/345400. arXiv: astro-ph/0210255 [astro-ph].

Fahrion, K. et al. (May 2020). "The Fornax 3D project: Globular clusters tracing kinematics and metallicities". In: A&A 637, A26, A26. DOI: 10.1051/0004-6361/202037685. arXiv: 2003.13705 [astro-ph.GA].

Forbes, Duncan A. et al. (Aug. 2014). "Extended star clusters in NGC 1023 from HST/ACS mosaic imaging". In: MNRAS 442.2, pp. 1049–1053. DOI: 10.1093/mnras/stu940. arXiv: 1405.2578 [astro-ph.GA].

Forbes, Duncan A. et al. (Mar. 2017). "The SLUGGS Survey: A Catalog of Over 4000 Globular Cluster Radial Velocities in 27 Nearby Early-type Galaxies". In: AJ 153.3, 114, p. 114. DOI: 10.3847/1538-3881/153/3/114. arXiv: 1701.04835 [astro-ph.GA].

Foreman-Mackey, Daniel et al. (Mar. 2013). "emcee: The MCMC Hammer". In: PASP 125.925, p. 306. DOI: 10.1086/670067. arXiv: 1202.3665 [astro-ph.IM].

Forouhar Moreno, Victor J. et al. (Dec. 2022). "Galactic satellite systems in CDM, WDM and SIDM". In: MNRAS 517.4, pp. 5627–5641. DOI: 10.1093/mnras/stac3062. arXiv: 2208.07376 [astro-ph.GA].

Foster, C. et al. (Nov. 2017). "The SAMI Galaxy Survey: the intrinsic shape of kinematically selected galaxies". In: MNRAS 472.1, pp. 966–978. DOI: 10.1093/mnras/stx1869. arXiv: 1709.03585 [astro-ph.GA].

Foster, Caroline et al. (Mar. 2016). "The SLUGGS Survey: stellar kinematics, kinemetry and trends at large radii in 25 early-type galaxies". In: MNRAS 457.1, pp. 147–171. DOI: 10.1093/mnras/stv2947. arXiv: 1512.06130 [astro-ph.GA].

Gaia Collaboration et al. (Aug. 2018). "Gaia Data Release 2. Summary of the contents and survey properties". In: A&A 616, A1, A1. DOI: 10.1051/0004-6361/201833051. arXiv: 1804.09365 [astro-ph.GA].

Gaia Collaboration et al. (May 2021). “Gaia Early Data Release 3. Summary of the contents and survey properties”. In: A&A 649, A1, A1. DOI: 10.1051/0004-6361/202039657. arXiv: 2012.01533 [astro-ph.GA].

Gao, Liang et al. (June 2008). “The redshift dependence of the structure of massive Λ cold dark matter haloes”. In: MNRAS 387.2, pp. 536–544. DOI: 10.1111/j.1365-2966.2008.13277.x. arXiv: 0711.0746 [astro-ph].

Georgiev, Iskren Y. et al. (Aug. 2010). “Globular cluster systems in nearby dwarf galaxies - III. Formation efficiencies of old globular clusters”. In: MNRAS 406.3, pp. 1967–1984. DOI: 10.1111/j.1365-2966.2010.16802.x. arXiv: 1004.2039 [astro-ph.CO].

Gerhard, Ortwin (July 2013). “Dark matter in massive galaxies”. In: *The Intriguing Life of Massive Galaxies*. Ed. by Daniel Thomas, Anna Pasquali, and Ignacio Ferreras. Vol. 295, pp. 211–220. DOI: 10.1017/S174392131300481X. arXiv: 1212.2768 [astro-ph.CO].

Goodman, Jonathan and Jonathan Weare (Jan. 2010). “Ensemble samplers with affine invariance”. In: *Communications in Applied Mathematics and Computational Science* 5.1, pp. 65–80. DOI: 10.2140/camcos.2010.5.65.

Han, Jiwon Jesse, Charlie Conroy, and Lars Hernquist (Sept. 2023). “A tilted dark halo origin of the Galactic disk warp and flare”. In: *Nature Astronomy*. DOI: 10.1038/s41550-023-02076-9. arXiv: 2309.07209 [astro-ph.GA].

Han, Jiwon Jesse et al. (Dec. 2022). “The Stellar Halo of the Galaxy is Tilted and Doubly Broken”. In: AJ 164.6, 249, p. 249. DOI: 10.3847/1538-3881/ac97e9. arXiv: 2208.04327 [astro-ph.GA].

Harris, Gretchen L. H. (Oct. 2010). “NGC 5128: The Giant Beneath”. In: PASA 27.4, pp. 475–481. DOI: 10.1071/AS09063. arXiv: 1004.4907 [astro-ph.GA].

Harris, Gretchen L. H., Marina Rejkuba, and William E. Harris (Oct. 2010). In: PASA 27.4, pp. 457–462. DOI: 10.1071/AS09061. arXiv: 0911.3180 [astro-ph.GA].

Harris, William E. (Mar. 2023). “A Photometric Survey of Globular Cluster Systems in Brightest Cluster Galaxies”. In: ApJS 265.1, 9, p. 9. DOI: 10.3847/1538-4365/acab5c. arXiv: 2212.06174 [astro-ph.GA].

Harris, William E., John P. Blakeslee, and Gretchen L. H. Harris (Feb. 2017a). “Galactic Dark Matter Halos and Globular Cluster Populations. III. Extension to Extreme Environments”. In: ApJ 836.1, 67, p. 67. DOI: 10.3847/1538-4357/836/1/67. arXiv: 1701.04845 [astro-ph.GA].

Harris, William E. et al. (Nov. 2006). “Structural Parameters for Globular Clusters in NGC 5128. II. Hubble Space Telescope ACS Imaging and New Clusters”. In: AJ 132.5, pp. 2187–2197. DOI: 10.1086/507579. arXiv: astro-ph/0607269 [astro-ph].

Harris, William E. et al. (Dec. 2014). “Globular Cluster Systems in Brightest Cluster Galaxies: A Near-universal Luminosity Function?” In: ApJ 797.2, 128, p. 128. DOI: 10.1088/0004-637X/797/2/128. arXiv: 1410.6291 [astro-ph.GA].

Harris, William E. et al. (Jan. 2017b). “Globular Cluster Systems in Brightest Cluster Galaxies. III: Beyond Bimodality”. In: ApJ 835.1, 101, p. 101. DOI: 10.3847/1538-4357/835/1/101. arXiv: 1612.08089 [astro-ph.GA].

Harris, William E. et al. (Dec. 2020). “Measuring Dark Matter in Galaxies: The Mass Fraction within Five Effective Radii”. In: ApJ 905.1, 28, p. 28. DOI: 10.3847/1538-4357/abc429. arXiv: 2010.14372 [astro-ph.GA].

Haşegan, Monica et al. (July 2005). “The ACS Virgo Cluster Survey. VII. Resolving the Connection between Globular Clusters and Ultracompact Dwarf Galaxies”. In: ApJ 627.1, pp. 203–223. DOI: 10.1086/430342. arXiv: astro-ph/0503566 [astro-ph].

Hayashi, Eric, Julio F. Navarro, and Volker Springel (May 2007). “The shape of the gravitational potential in cold dark matter haloes”. In: MNRAS 377.1, pp. 50–62. DOI: 10.1111/j.1365-2966.2007.11599.x. arXiv: astro-ph/0612327 [astro-ph].

Hayashi, Kohei, Masashi Chiba, and Tomoaki Ishiyama (Nov. 2020). “Diversity of Dark Matter Density Profiles in the Galactic Dwarf Spheroidal Satellites”. In: ApJ 904.1, 45, p. 45. DOI: 10.3847/1538-4357/abbe0a. arXiv: 2007.13780 [astro-ph.GA].

Hénault-Brunet, V. et al. (Feb. 2019). “Mass modelling globular clusters in the Gaiaera: a method comparison using mock data from an N-body simulation of M 4”. In: MNRAS 483.1, pp. 1400–1425. DOI: 10.1093/mnras/sty3187.

Hudson, Michael J., Gretchen L. Harris, and William E. Harris (May 2014). “Dark Matter Halos in Galaxies and Globular Cluster Populations”. In: ApJ 787.1, L5, p. L5. DOI: 10.1088/2041-8205/787/1/L5. arXiv: 1404.1920 [astro-ph.GA].

Hughes, A. K. et al. (Aug. 2022). “New Velocity Measurements of NGC 5128 Globular Clusters out to 130 kpc: Outer Halo Kinematics, Substructure and Dynamics”. In: *arXiv e-prints*, arXiv:2208.08997, arXiv:2208.08997. arXiv: 2208.08997 [astro-ph.GA].

Hughes, Allison K. et al. (June 2021a). “NGC 5128 Globular Cluster Candidates Out to 150 kpc: A Comprehensive Catalog from Gaia and Ground-based Data”. In: ApJ 914.1, 16, p. 16. DOI: 10.3847/1538-4357/abf63c. arXiv: 2104.02719 [astro-ph.GA].

Hughes, Allison K. et al. (Apr. 2023). “New Velocity Measurements of NGC 5128 Globular Clusters Out to 130 kpc: Outer Halo Kinematics, Substructure, and Dynamics”. In: ApJ 947.1, 34, p. 34. DOI: 10.3847/1538-4357/acbf43. arXiv: 2208.08997 [astro-ph.GA].

Hughes, Meghan E. et al. (Apr. 2021b). In: *mnras* 502.2, pp. 2828–2844. DOI: 10.1093/mnras/stab196. arXiv: 2101.08282 [astro-ph.GA].

Hui, Xiaohui et al. (Aug. 1995). “The Planetary Nebula System and Dynamics of NGC 5128. III. Kinematics and Halo Mass Distributions”. In: ApJ 449, p. 592. DOI: 10.1086/176082.

Humphrey, Philip J. (Jan. 2009). “Low-Mass X-ray Binaries and Globular Clusters in Early-Type Galaxies. II. Globular Cluster Candidates and Their Mass-Metallicity Relation”. In: ApJ 690.1, pp. 512–525. DOI: 10.1088/0004-637X/690/1/512. arXiv: 0809.0698 [astro-ph].

Iodice, E. et al. (Mar. 2003). “Polar Ring Galaxies and the Tully-Fisher Relation: Implications for the Dark Halo Shape”. In: ApJ 585.2, pp. 730–738. DOI: 10.1086/346107. arXiv: astro-ph/0211281 [astro-ph].

Iodice, E. et al. (Mar. 2019a). “The Fornax Deep Survey with the VST. V. Exploring the faintest regions of the bright early-type galaxies inside the virial radius”. In: A&A 623, A1, A1. DOI: 10.1051/0004-6361/201833741. arXiv: 1812.01050 [astro-ph.GA].

Iodice, E. et al. (July 2019b). “The Fornax3D project: Tracing the assembly history of the cluster from the kinematic and line-strength maps”. In: A&A 627, A136, A136. DOI: 10.1051/0004-6361/201935721. arXiv: 1906.08187 [astro-ph.GA].

Iorio, Giuliano and Vasily Belokurov (Jan. 2019). “The shape of the Galactic halo with Gaia DR2 RR Lyrae. Anatomy of an ancient major merger”. In: MNRAS 482.3, pp. 3868–3879. DOI: 10.1093/mnras/sty2806. arXiv: 1808.04370 [astro-ph.GA].

Jeans, J. H. (Jan. 1922). “The Motions of Stars in a Kapteyn Universe”. In: MNRAS 82, pp. 122–132. DOI: 10.1093/mnras/82.3.122.

Jin, Yunpeng et al. (Jan. 2020). “SDSS-IV MaNGA: Internal mass distributions and orbital structures of early-type galaxies and their dependence on environment”. In: MNRAS 491.2, pp. 1690–1708. DOI: 10.1093/mnras/stz3072. arXiv: 1911.00777 [astro-ph.GA].

Jordán, Andrés et al. (Dec. 2005). “The ACS Virgo Cluster Survey. X. Half-Light Radii of Globular Clusters in Early-Type Galaxies: Environmental Dependencies and a Standard Ruler for Distance Estimation”. In: ApJ 634.2, pp. 1002–1019. DOI: 10.1086/497092. arXiv: astro-ph/0508219 [astro-ph].

Jordán, Andrés et al. (Nov. 2006). “Trends in the Globular Cluster Luminosity Function of Early-Type Galaxies”. In: ApJ 651.1, pp. L25–L28. DOI: 10.1086/509119. arXiv: astro-ph/0609371 [astro-ph].

Jordán, Andrés et al. (Apr. 2007a). “The ACS Fornax Cluster Survey. I. Introduction to the Survey and Data Reduction Procedures”. In: ApJS 169.2, pp. 213–224. DOI: 10.1086/512778. arXiv: astro-ph/0702320 [astro-ph].

Jordán, Andrés et al. (July 2007b). “The ACS Virgo Cluster Survey. XII. The Luminosity Function of Globular Clusters in Early-Type Galaxies”. In: ApJS 171.1, pp. 101–145. DOI: 10.1086/516840. arXiv: astro-ph/0702496 [astro-ph].

Jordán, Andrés et al. (Jan. 2009). "The ACS Virgo Cluster Survey XVI. Selection Procedure and Catalogs of Globular Cluster Candidates". In: ApJS 180.1, pp. 54–66. DOI: 10.1088/0067-0049/180/1/54.

Jordán, Andrés et al. (Nov. 2015). "The ACS Fornax Cluster Survey. XI. Catalog of Globular Cluster Candidates". In: ApJS 221.1, 13, p. 13. DOI: 10.1088/0067-0049/221/1/13.

Kabasares, Kyle M. et al. (Aug. 2022). "Black Hole Mass Measurements of Early-type Galaxies NGC 1380 and NGC 6861 through ALMA and HST Observations and Gas-dynamical Modeling". In: ApJ 934.2, 162, p. 162. DOI: 10.3847/1538-4357/ac7a38. arXiv: 2206.09043 [astro-ph.GA].

Kartha, Sreeja S. et al. (Jan. 2014). "The SLUGGS survey: the globular cluster systems of three early-type galaxies using wide-field imaging". In: MNRAS 437.1, pp. 273–292. DOI: 10.1093/mnras/stt1880. arXiv: 1310.1979 [astro-ph.CO].

Kartha, Sreeja S. et al. (May 2016). "The SLUGGS survey*: exploring the globular cluster systems of the Leo II group and their global relationships". In: MNRAS 458.1, pp. 105–126. DOI: 10.1093/mnras/stw185. arXiv: 1602.01838 [astro-ph.GA].

Kazantzidis, Stelios et al. (Aug. 2004). "The Effect of Gas Cooling on the Shapes of Dark Matter Halos". In: ApJ 611.2, pp. L73–L76. DOI: 10.1086/423992. arXiv: astro-ph/0405189 [astro-ph].

Khoperskov, S. A. et al. (July 2014). In: *mnras* 441.3, pp. 2650–2662. DOI: 10.1093/mnras/stu692.

Kirby, Evan N. et al. (Feb. 2011). "Multi-element Abundance Measurements from Medium-resolution Spectra. IV. Alpha Element Distributions in Milky Way Satellite Galaxies". In: ApJ 727.2, 79, p. 79. DOI: 10.1088/0004-637X/727/2/79. arXiv: 1011.5221 [astro-ph.GA].

Kissler-Patig, M. (Mar. 1997). "The dichotomy of early-type galaxies from their globular cluster systems." In: A&A 319, pp. 83–91. DOI: 10.48550/arXiv.astro-ph/9610019. arXiv: astro-ph/9610019 [astro-ph].

Komatsu, E. et al. (Feb. 2009). "Five-Year Wilkinson Microwave Anisotropy Probe Observations: Cosmological Interpretation". In: ApJS 180.2, pp. 330–376. DOI: 10.1088/0067-0049/180/2/330. arXiv: 0803.0547 [astro-ph].

Kraft, R. P. et al. (July 2003). "X-Ray Emission from the Hot Interstellar Medium and Southwest Radio Lobe of the Nearby Radio Galaxy Centaurus A". In: 592.1, pp. 129–146. DOI: 10.1086/375533. arXiv: astro-ph/0304363 [astro-ph].

Krajnović, Davor et al. (Mar. 2005). "Dynamical modelling of stars and gas in NGC 2974: determination of mass-to-light ratio, inclination and orbital structure using the Schwarzschild method". In: MNRAS 357.4, pp. 1113–1133. DOI: 10.1111/j.1365-2966.2005.08715.x. arXiv: astro-ph/0412186 [astro-ph].

Law, David R., Steven R. Majewski, and Kathryn V. Johnston (Sept. 2009). "Evidence for a Triaxial Milky Way Dark Matter Halo from the Sagittarius Stellar Tidal Stream". In: ApJ 703.1, pp. L67–L71. DOI: 10.1088/0004-637X/703/1/L67. arXiv: 0908.3187 [astro-ph.GA].

Leung, Gigi Y. C. et al. (Jan. 2021). In: *mnras* 500.1, pp. 410–429. DOI: 10.1093/mnras/staa3107. arXiv: 2104.04273 [astro-ph.GA].

Lynden-Bell, D. (Jan. 1967). "Statistical mechanics of violent relaxation in stellar systems". In: MNRAS 136, p. 101. DOI: 10.1093/mnras/136.1.101.

Macciò, Andrea V., Aaron A. Dutton, and Frank C. van den Bosch (Dec. 2008). "Concentration, spin and shape of dark matter haloes as a function of the cosmological model: WMAP1, WMAP3 and WMAP5 results". In: MNRAS 391.4, pp. 1940–1954. DOI: 10.1111/j.1365-2966.2008.14029.x. arXiv: 0805.1926 [astro-ph].

Malin, D. F., P. J. Quinn, and J. A. Graham (Sept. 1983). "Shell structure in NGC 5128." In: ApJ 272, pp. L5–L7. DOI: 10.1086/184106.

Martín-Navarro, I. et al. (June 2019). "Fornax 3D project: a two-dimensional view of the stellar initial mass function in the massive lenticular galaxy FCC 167". In: A&A 626, A124, A124. DOI: 10.1051/0004-6361/201935360. arXiv: 1903.10514 [astro-ph.GA].

Massari, D. et al. (Nov. 2018). "Three-dimensional motions in the Sculptor dwarf galaxy as a glimpse of a new era". In: *Nature Astronomy* 2, pp. 156–161. DOI: 10.1038/s41550-017-0322-y. arXiv: 1711.08945 [astro-ph.GA].

Massari, D. et al. (Jan. 2020a). “Stellar 3D kinematics in the Draco dwarf spheroidal galaxy”. In: A&A 633, A36, A36. DOI: 10.1051/0004-6361/201935613. arXiv: 1904.04037 [astro-ph.GA].
— (Jan. 2020b). “Stellar 3D kinematics in the Draco dwarf spheroidal galaxy”. In: A&A 633, A36, A36. DOI: 10.1051/0004-6361/201935613. arXiv: 1904.04037 [astro-ph.GA].
Mathieu, A., H. Dejonghe, and X. Hui (May 1996). “Probing the halo of Centaurus A: a merger dynamical model for the PN population”. In: A&A 309, pp. 30–42. DOI: 10.48550/arXiv.astro-ph/9510079. arXiv: astro-ph/9510079 [astro-ph].
Mayer, Lucio et al. (Oct. 2002). “Tidal debris of dwarf spheroidals as a probe of structure formation models”. In: MNRAS 336.1, pp. 119–130. DOI: 10.1046/j.1365-8711.2002.05721.x. arXiv: astro-ph/0110386 [astro-ph].
Merritt, D. (June 1985). “Spherical stellar systems with spheroidal velocity distributions”. In: AJ 90, pp. 1027–1037. DOI: 10.1086/113810.
Mieske, S. et al. (Sept. 2008). “The nature of UCDs: Internal dynamics from an expanded sample and homogeneous database”. In: A&A 487.3, pp. 921–935. DOI: 10.1051/0004-6361:200810077. arXiv: 0806.0374 [astro-ph].
Mo, Houjun, Frank C. van den Bosch, and Simon White (2010). *Galaxy Formation and Evolution*.
Moskowitz, A. G. and M. G. Walker (Mar. 2020). “Stellar Density Profiles of Dwarf Spheroidal Galaxies”. In: ApJ 892.1, 27, p. 27. DOI: 10.3847/1538-4357/ab7459. arXiv: 1910.10134 [astro-ph.GA].
Müller, Oliver et al. (Feb. 2018). “A whirling plane of satellite galaxies around Centaurus A challenges cold dark matter cosmology”. In: *Science* 359.6375, pp. 534–537. DOI: 10.1126/science.aao1858. arXiv: 1802.00081 [astro-ph.GA].
Müller, Oliver et al. (Sept. 2019). “The dwarf galaxy satellite system of Centaurus A”. In: A&A 629, A18, A18. DOI: 10.1051/0004-6361/201935807. arXiv: 1907.02012 [astro-ph.GA].
Müller, Oliver et al. (Jan. 2021). “The coherent motion of Cen A dwarf satellite galaxies remains a challenge for ΛCDM cosmology”. In: A&A 645, L5, p. L5. DOI: 10.1051/0004-6361/202039973. arXiv: 2012.08138 [astro-ph.GA].
Müller, Oliver et al. (June 2022). “The Cen A galaxy group: Dynamical mass and missing baryons”. In: A&A 662, A57, A57. DOI: 10.1051/0004-6361/202142351. arXiv: 2111.10306 [astro-ph.GA].
Naidu, Rohan P. et al. (Dec. 2021). “Reconstructing the Last Major Merger of the Milky Way with the H3 Survey”. In: ApJ 923.1, 92, p. 92. DOI: 10.3847/1538-4357/ac2d2d. arXiv: 2103.03251 [astro-ph.GA].
Napolitano, Nicola R. et al. (Mar. 2014). “The SLUGGS survey: breaking degeneracies between dark matter, anisotropy and the IMF using globular cluster subpopulations in the giant elliptical NGC 5846”. In: MNRAS 439.1, pp. 659–672. DOI: 10.1093/mnras/stt2484. arXiv: 1401.1501 [astro-ph.GA].
Navarro, J. F. et al. (Apr. 2004). “The inner structure of ΛCDM haloes - III. Universality and asymptotic slopes”. In: MNRAS 349.3, pp. 1039–1051. DOI: 10.1111/j.1365-2966.2004.07586.x. arXiv: astro-ph/0311231 [astro-ph].
Navarro, Julio F., Carlos S. Frenk, and Simon D. M. White (May 1996). “The Structure of Cold Dark Matter Halos”. In: ApJ 462, p. 563. DOI: 10.1086/177173. arXiv: astro-ph/9508025 [astro-ph].
— (Dec. 1997). “A Universal Density Profile from Hierarchical Clustering”. In: ApJ 490.2, pp. 493–508. DOI: 10.1086/304888. arXiv: astro-ph/9611107 [astro-ph].
Nelson, Dylan et al. (May 2019). “The IllustrisTNG simulations: public data release”. In: *Computational Astrophysics and Cosmology* 6.1, 2, p. 2. DOI: 10.1186/s40668-019-0028-x. arXiv: 1812.05609 [astro-ph.GA].
Nelson, Dylan et al. (Nov. 2023). “Introducing the TNG-Cluster Simulation: overview and physical properties of the gaseous intracluster medium”. In: *arXiv e-prints*, arXiv:2311.06338, arXiv:2311.06338. DOI: 10.48550/arXiv.2311.06338. arXiv: 2311.06338 [astro-ph.GA].
Neto, Angelo F. et al. (Nov. 2007). “The statistics of Λ CDM halo concentrations”. In: MNRAS 381.4, pp. 1450–1462. DOI: 10.1111/j.1365-2966.2007.12381.x. arXiv: 0706.2919 [astro-ph].

O'Neil, Stephanie et al. (Sept. 2023). "Endothermic self-interacting dark matter in Milky Way-like dark matter haloes". In: MNRAS 524.1, pp. 288–306. DOI: 10.1093/mnras/stad1850. arXiv: 2210.16328 [astro-ph.GA].

Oliva-Altamirano, Paola et al. (June 2015). "The accretion histories of brightest cluster galaxies from their stellar population gradients". In: MNRAS 449.4, pp. 3347–3359. DOI: 10.1093/mnras/stv475. arXiv: 1503.01465 [astro-ph.GA].

Oser, Ludwig et al. (Jan. 2012). "The Cosmological Size and Velocity Dispersion Evolution of Massive Early-type Galaxies". In: ApJ 744.1, 63, p. 63. DOI: 10.1088/0004-637X/744/1/63. arXiv: 1106.5490 [astro-ph.CO].

Osipkov, L. P. (Jan. 1979). "Spherical systems of gravitating bodies with an ellipsoidal velocity distribution". In: *Soviet Astronomy Letters* 5, pp. 42–44.

Pearson, Sarah et al. (Jan. 2015). "Tidal Stream Morphology as an Indicator of Dark Matter Halo Geometry: The Case of Palomar 5". In: ApJ 799.1, 28, p. 28. DOI: 10.1088/0004-637X/799/1/28. arXiv: 1410.3477 [astro-ph.GA].

Pearson, Sarah et al. (Dec. 2022). "Mapping Dark Matter with Extragalactic Stellar Streams: The Case of Centaurus A". In: ApJ 941.1, 19, p. 19. DOI: 10.3847/1538-4357/ac9bfb. arXiv: 2205.12277 [astro-ph.GA].

Peng, Eric W., Holland C. Ford, and Kenneth C. Freeman (Feb. 2004a). In: *apj* 602.2, pp. 685–704. DOI: 10.1086/381160. arXiv: astro-ph/0311236 [astro-ph].

— (Feb. 2004b). "The Globular Cluster System of NGC 5128. II. Ages, Metallicities, Kinematics, and Formation". In: ApJ 602.2, pp. 705–722. DOI: 10.1086/381236. arXiv: astro-ph/0311265 [astro-ph].

Planck Collaboration et al. (Sept. 2016). "Planck 2015 results. XIII. Cosmological parameters". In: A&A 594, A13, A13. DOI: 10.1051/0004-6361/201525830. arXiv: 1502.01589 [astro-ph.CO].

Planck Collaboration et al. (Sept. 2020). "Planck 2018 results. VI. Cosmological parameters". In: A&A 641, A6, A6. DOI: 10.1051/0004-6361/201833910. arXiv: 1807.06209 [astro-ph.CO].

Poci, Adriano, Michele Cappellari, and Richard M. McDermid (May 2017). "Systematic trends in total-mass profiles from dynamical models of early-type galaxies". In: MNRAS 467.2, pp. 1397–1413. DOI: 10.1093/mnras/stx101. arXiv: 1612.05805 [astro-ph.GA].

Posti, L. and S. M. Fall (May 2021). "Dynamical evidence for a morphology-dependent relation between the stellar and halo masses of galaxies". In: A&A 649, A119, A119. DOI: 10.1051/0004-6361/202040256. arXiv: 2102.11282 [astro-ph.GA].

Posti, Lorenzo, Filippo Fraternali, and Antonino Marasco (June 2019). "Peak star formation efficiency and no missing baryons in massive spirals". In: A&A 626, A56, A56. DOI: 10.1051/0004-6361/201935553. arXiv: 1812.05099 [astro-ph.GA].

Posti, Lorenzo and Amina Helmi (Jan. 2019). "Mass and shape of the Milky Way's dark matter halo with globular clusters from Gaia and Hubble". In: A&A 621, A56, A56. DOI: 10.1051/0004-6361/201833355. arXiv: 1805.01408 [astro-ph.GA].

Pota, Vincenzo et al. (July 2015). "The SLUGGS survey: multipopulation dynamical modelling of the elliptical galaxy NGC 1407 from stars and globular clusters". In: MNRAS 450.3, pp. 3345–3358. DOI: 10.1093/mnras/stv831. arXiv: 1504.03325 [astro-ph.GA].

Prada, Francisco et al. (July 2012). "Halo concentrations in the standard Λ cold dark matter cosmology". In: MNRAS 423.4, pp. 3018–3030. DOI: 10.1111/j.1365-2966.2012.21007.x. arXiv: 1104.5130 [astro-ph.CO].

Prada, Jesus et al. (Dec. 2019). "Dark matter halo shapes in the Auriga simulations". In: MNRAS 490.4, pp. 4877–4888. DOI: 10.1093/mnras/stz2873. arXiv: 1910.04045 [astro-ph.GA].

Pulsoni, C. et al. (Oct. 2018). "The extended Planetary Nebula Spectrograph (ePN.S) early-type galaxy survey: The kinematic diversity of stellar halos and the relation between halo transition scale and stellar mass". In: A&A 618, A94, A94. DOI: 10.1051/0004-6361/201732473. arXiv: 1712.05833 [astro-ph.GA].

Pulsoni, C. et al. (Sept. 2020). "The stellar halos of ETGs in the IllustrisTNG simulations: The photometric and kinematic diversity of galaxies at large radii". In: A&A 641, A60, A60. DOI: 10.1051/0004-6361/202038253. arXiv: 2004.13042 [astro-ph.GA].

Pulsoni, C. et al. (Mar. 2021). "The stellar halos of ETGs in the IllustrisTNG simulations. II. Accretion, merger history, and dark halo connection". In: A&A 647, A95, A95. DOI: 10.1051/0004-6361/202039166. arXiv: 2009.01823 [astro-ph.GA].

Puzia, T. H. et al. (Feb. 2004). "VLT spectroscopy of globular cluster systems. I. The photometric and spectroscopic data set". In: A&A 415, pp. 123–143. DOI: 10.1051/0004-6361:20031448. arXiv: astro-ph/0505448 [astro-ph].

Read, J. I., M. G. Walker, and P. Steger (Mar. 2019). "Dark matter heats up in dwarf galaxies". In: MNRAS 484.1, pp. 1401–1420. DOI: 10.1093/mnras/sty3404. arXiv: 1808.06634 [astro-ph.GA].

Read, J. I. et al. (Mar. 2006). "The importance of tides for the Local Group dwarf spheroidals". In: MNRAS 367.1, pp. 387–399. DOI: 10.1111/j.1365-2966.2005.09959.x. arXiv: astro-ph/0511759 [astro-ph].

Read, J. I. et al. (Feb. 2021). "Breaking beta: a comparison of mass modelling methods for spherical systems". In: MNRAS 501.1, pp. 978–993. DOI: 10.1093/mnras/staa3663. arXiv: 2011.09493 [astro-ph.GA].

Rejkuba, M. (Sept. 2012). "Globular cluster luminosity function as distance indicator". In: Ap&SS 341.1, pp. 195–206. DOI: 10.1007/s10509-012-0986-9. arXiv: 1201.3936 [astro-ph.CO].

Rejkuba, M. et al. (Feb. 2011). "How old are the stars in the halo of NGC 5128 (Centaurus A)?" In: A&A 526, A123, A123. DOI: 10.1051/0004-6361/201015640. arXiv: 1011.4309 [astro-ph.CO].

Rejkuba, M. et al. (Jan. 2022). "The outermost stellar halo of NGC 5128 (Centaurus A): Radial structure". In: A&A 657, A41, A41. DOI: 10.1051/0004-6361/202141347. arXiv: 2111.02945 [astro-ph.GA].

Rejkuba, Marina et al. (Sept. 2005). "Deep ACS Imaging of the Halo of NGC 5128: Reaching the Horizontal Branch". In: ApJ 631.1, pp. 262–279. DOI: 10.1086/432462. arXiv: astro-ph/0505622 [astro-ph].

Remus, Rhea-Silvia et al. (Apr. 2013). "The Dark Halo—Spheroid Conspiracy and the Origin of Elliptical Galaxies". In: ApJ 766.2, 71, p. 71. DOI: 10.1088/0004-637X/766/2/71. arXiv: 1211.3420 [astro-ph.GA].

Remus, Rhea-Silvia et al. (Jan. 2017). "The co-evolution of total density profiles and central dark matter fractions in simulated early-type galaxies". In: MNRAS 464.3, pp. 3742–3756. DOI: 10.1093/mnras/stw2594. arXiv: 1603.01619 [astro-ph.GA].

Robison, Bailey et al. (Aug. 2023). "The shape of dark matter haloes: results from weak lensing in the ultraviolet near-infrared optical Northern survey (UNIONS)". In: MNRAS 523.2, pp. 1614–1628. DOI: 10.1093/mnras/stad1519. arXiv: 2209.09088 [astro-ph.GA].

Rocha, Miguel et al. (Mar. 2013). "Cosmological simulations with self-interacting dark matter - I. Constant-density cores and substructure". In: MNRAS 430.1, pp. 81–104. DOI: 10.1093/mnras/sts514. arXiv: 1208.3025 [astro-ph.CO].

Romanowsky, Aaron J. et al. (June 2009). "Mapping The Dark Side with DEIMOS: Globular Clusters, X-Ray Gas, and Dark Matter in the NGC 1407 Group". In: AJ 137.6, pp. 4956–4987. DOI: 10.1088/0004-6256/137/6/4956. arXiv: 0809.2088 [astro-ph].

Rubin, Vera C. and Jr. Ford W. Kent (Feb. 1970). "Rotation of the Andromeda Nebula from a Spectroscopic Survey of Emission Regions". In: ApJ 159, p. 379. DOI: 10.1086/150317.

Santucci, Giulia et al. (May 2022). "The SAMI Galaxy Survey: The Internal Orbital Structure and Mass Distribution of Passive Galaxies from Triaxial Orbit-superposition Schwarzschild Models". In: ApJ 930.2, 153, p. 153. DOI: 10.3847/1538-4357/ac5bd5. arXiv: 2203.03648 [astro-ph.GA].

Sarzi, M. et al. (Aug. 2018). "Fornax3D project: Overall goals, galaxy sample, MUSE data analysis, and initial results". In: *aap* 616, A121, A121. DOI: 10.1051/0004-6361/201833137. arXiv: 1804.06795 [astro-ph.GA].

Schaye, Joop et al. (Jan. 2015). "The EAGLE project: simulating the evolution and assembly of galaxies and their environments". In: MNRAS 446.1, pp. 521–554. DOI: 10.1093/mnras/stu2058. arXiv: 1407.7040 [astro-ph.GA].

Schlafly, Edward F. and Douglas P. Finkbeiner (Aug. 2011). “Measuring Reddening with Sloan Digital Sky Survey Stellar Spectra and Recalibrating SFD”. In: ApJ 737.2, 103, p. 103. DOI: 10.1088/0004-637X/737/2/103. arXiv: 1012.4804 [astro-ph.GA].

Schlegel, David J., Douglas P. Finkbeiner, and Marc Davis (June 1998). “Maps of Dust Infrared Emission for Use in Estimation of Reddening and Cosmic Microwave Background Radiation Foregrounds”. In: ApJ 500.2, pp. 525–553. DOI: 10.1086/305772. arXiv: astro-ph/9710327 [astro-ph].

Scholz-Díaz, Laura, Ignacio Martín-Navarro, and Jesús Falcón-Barroso (Feb. 2023). “The dark side of galaxy stellar populations - II. The dependence of star-formation histories on halo mass and on the scatter of the main sequence”. In: MNRAS 518.4, pp. 6325–6339. DOI: 10.1093/mnras/stac3422. arXiv: 2211.11779 [astro-ph.GA].

Schwarzschild, M. (Aug. 1979). “A numerical model for a triaxial stellar system in dynamical equilibrium”. In: *apj* 232, pp. 236–247. DOI: 10.1086/157282.

Serra, Paolo et al. (Aug. 2016). “Linear relation between H I circular velocity and stellar velocity dispersion in early-type galaxies, and slope of the density profiles”. In: MNRAS 460.2, pp. 1382–1389. DOI: 10.1093/mnras/stw1010. arXiv: 1604.07902 [astro-ph.GA].

Sersic, Jose Luis (1968). *Atlas de Galaxias Australes*.

Sesar, Branimir, Mario Jurić, and Željko Ivezić (Apr. 2011). “The Shape and Profile of the Milky Way Halo as Seen by the Canada-France-Hawaii Telescope Legacy Survey”. In: ApJ 731.1, 4, p. 4. DOI: 10.1088/0004-637X/731/1/4. arXiv: 1011.4487 [astro-ph.GA].

Simon, Joshua D. (Aug. 2019). “The Faintest Dwarf Galaxies”. In: ARA&A 57, pp. 375–415. DOI: 10.1146/annurev-astro-091918-104453. arXiv: 1901.05465 [astro-ph.GA].

Simon, Joshua D. et al. (Mar. 2005). “High-Resolution Measurements of the Halos of Four Dark Matter-Dominated Galaxies: Deviations from a Universal Density Profile”. In: ApJ 621.2, pp. 757–776. DOI: 10.1086/427684. arXiv: astro-ph/0412035 [astro-ph].

Sonnenfeld, Alessandro et al. (Nov. 2013). “The SL2S Galaxy-scale Lens Sample. IV. The Dependence of the Total Mass Density Profile of Early-type Galaxies on Redshift, Stellar Mass, and Size”. In: ApJ 777.2, 98, p. 98. DOI: 10.1088/0004-637X/777/2/98. arXiv: 1307.4759 [astro-ph.CO].

Spitler, L. R. and D. A. Forbes (Jan. 2009). “A new method for estimating dark matter halo masses using globular cluster systems”. In: MNRAS 392.1, pp. L1–L5. DOI: 10.1111/j.1745-3933.2008.00567.x. arXiv: 0809.5057 [astro-ph].

Spriggs, T. W. et al. (May 2020). “Fornax 3D project: Automated detection of planetary nebulae in the centres of early-type galaxies and first results”. In: *aap* 637, A62, A62. DOI: 10.1051/0004-6361/201936862. arXiv: 2003.10456 [astro-ph.GA].

Springel, Volker, Carlos S. Frenk, and Simon D. M. White (Apr. 2006). “The large-scale structure of the Universe”. In: Nature 440.7088, pp. 1137–1144. DOI: 10.1038/nature04805. arXiv: astro-ph/0604561 [astro-ph].

Strader, Jay et al. (Dec. 2011). “Wide-field Precision Kinematics of the M87 Globular Cluster System”. In: ApJS 197.2, 33, p. 33. DOI: 10.1088/0067-0049/197/2/33. arXiv: 1110.2778 [astro-ph.CO].

Taylor, Matthew A. et al. (Aug. 2016). “The Survey of Centaurus A's Baryonic Structures (SCABS). I. Survey Description and Initial Source Catalogues”. In: *arXiv e-prints*, arXiv:1608.07285, arXiv:1608.07285. DOI: 10.48550/arXiv.1608.07285. arXiv: 1608.07285 [astro-ph.GA].

Taylor, Matthew A. et al. (Aug. 2017). “The Survey of Centaurus A's Baryonic Structures (SCABS) - II. The extended globular cluster system of NGC 5128 and its nearby environment”. In: MNRAS 469.3, pp. 3444–3467. DOI: 10.1093/mnras/stx1021. arXiv: 1608.07288 [astro-ph.GA].

Teklu, Adelheid F. et al. (Oct. 2015). “Connecting Angular Momentum and Galactic Dynamics: The Complex Interplay between Spin, Mass, and Morphology”. In: ApJ 812.1, 29, p. 29. DOI: 10.1088/0004-637X/812/1/29. arXiv: 1503.03501 [astro-ph.GA].

Tenneti, Ananth et al. (Oct. 2015). “Galaxy shapes and alignments in the MassiveBlack-II hydrodynamic and dark matter-only simulations”. In: MNRAS 453.1, pp. 469–482. DOI: 10.1093/mnras/stv1625. arXiv: 1505.03124 [astro-ph.CO].

Thater, Sabine et al. (May 2023). "Dynamical modelling of ATLAS^{3D} galaxies". In: *arXiv e-prints*, arXiv:2305.09344, arXiv:2305.09344. DOI: 10.48550/arXiv.2305.09344. arXiv: 2305.09344 [astro-ph.GA].

Tolstoy, Eline, Vanessa Hill, and Monica Tosi (Sept. 2009). "Star-Formation Histories, Abundances, and Kinematics of Dwarf Galaxies in the Local Group". In: ARA&A 47.1, pp. 371–425. DOI: 10.1146/annurev-astro-082708-101650. arXiv: 0904.4505 [astro-ph.CO].

Tortora, C. et al. (Nov. 2014). "Systematic variations of central mass density slopes in early-type galaxies". In: MNRAS 445.1, pp. 115–127. DOI: 10.1093/mnras/stu1616. arXiv: 1409.0538 [astro-ph.GA].

Valenzuela, Lucas M. and Rhea-Silvia Remus (Aug. 2022). "A Stream Come True – Connecting tidal tails, shells, streams, and planes with galaxy kinematics and formation history". In: *arXiv e-prints*, arXiv:2208.08443, arXiv:2208.08443. DOI: 10.48550/arXiv.2208.08443. arXiv: 2208.08443 [astro-ph.GA].

van de Ven, G. et al. (July 2003). "General solution of the Jeans equations for triaxial galaxies with separable potentials". In: MNRAS 342.4, pp. 1056–1082. DOI: 10.1046/j.1365-8711.2003.06501.x. arXiv: astro-ph/0302172 [astro-ph].

van de Ven, G. et al. (Jan. 2006). "The dynamical distance and intrinsic structure of the globular cluster ω Centauri". In: A&A 445.2, pp. 513–543. DOI: 10.1051/0004-6361:20053061. arXiv: astro-ph/0509228 [astro-ph].

van den Bosch, Remco C. E. and Glenn van de Ven (Sept. 2009). "Recovering the intrinsic shape of early-type galaxies". In: MNRAS 398.3, pp. 1117–1128. DOI: 10.1111/j.1365-2966.2009.15177.x. arXiv: 0811.3474 [astro-ph].

Varghese, A., R. Ibata, and G. F. Lewis (Oct. 2011). "Stellar streams as probes of dark halo mass and morphology: a Bayesian reconstruction". In: MNRAS 417.1, pp. 198–215. DOI: 10.1111/j.1365-2966.2011.19097.x. arXiv: 1106.1765 [astro-ph.GA].

Veršič, Tadeja et al. (May 2023). "The flattening of dark matter halo of Centaurus A galaxy (NGC 5128) out to 40 kpc". In: *arXiv e-prints*, arXiv:2305.09822, arXiv:2305.09822. DOI: 10.48550/arXiv.2305.09822. arXiv: 2305.09822 [astro-ph.GA].

Veršič, Tadeja et al. (Jan. 2024). "Total mass slopes and enclosed mass constrained by globular cluster system dynamics". In: A&A 681, A46, A46. DOI: 10.1051/0004-6361/202347413.

Viaene, S. et al. (Feb. 2019). "The Fornax 3D project: dust mix and gas properties in the centre of early-type galaxy FCC 167". In: A&A 622, A89, A89. DOI: 10.1051/0004-6361/201834465. arXiv: 1812.07582 [astro-ph.GA].

Villegas, Daniela et al. (July 2010). "The ACS Fornax Cluster Survey. VIII. The Luminosity Function of Globular Clusters in Virgo and Fornax Early-type Galaxies and Its Use as a Distance Indicator". In: ApJ 717.2, pp. 603–616. DOI: 10.1088/0004-637X/717/2/603. arXiv: 1004.2883 [astro-ph.CO].

Vogelsberger, Mark et al. (Aug. 2016). "ETHOS - an effective theory of structure formation: dark matter physics as a possible explanation of the small-scale CDM problems". In: MNRAS 460.2, pp. 1399–1416. DOI: 10.1093/mnras/stw1076. arXiv: 1512.05349 [astro-ph.CO].

Vogelsberger, Mark et al. (Jan. 2020). "Cosmological simulations of galaxy formation". In: *Nature Reviews Physics* 2.1, pp. 42–66. DOI: 10.1038/s42254-019-0127-2. arXiv: 1909.07976 [astro-ph.GA].

Voggel, Karina T. et al. (Aug. 2020). "A Gaia-based Catalog of Candidate Stripped Nuclei and Luminous Globular Clusters in the Halo of Centaurus A". In: ApJ 899.2, 140, p. 140. DOI: 10.3847/1538-4357/ab6f69. arXiv: 2001.02243 [astro-ph.GA].

Walker, Matthew G., Mario Mateo, and Edward W. Olszewski (Feb. 2009). "Stellar Velocities in the Carina, Fornax, Sculptor, and Sextans dSph Galaxies: Data From the Magellan/MMFS Survey". In: AJ 137.2, pp. 3100–3108. DOI: 10.1088/0004-6256/137/2/3100. arXiv: 0811.0118 [astro-ph].

Walsh, J. R., M. Rejkuba, and N. A. Walton (Feb. 2015). In: *aap* 574, A109, A109. DOI: 10.1051/0004-6361/201424316. arXiv: 1501.01853 [astro-ph.GA].

Wang, Jianling et al. (Oct. 2020). In: *mnras* 498.2, pp. 2766–2777. DOI: 10.1093/mnras/staa2508. arXiv: 2008.13418 [astro-ph.GA].

Watkins, Laura L., N. Wyn Evans, and Jin H. An (July 2010). "The masses of the Milky Way and Andromeda galaxies". In: MNRAS 406.1, pp. 264–278. DOI: 10.1111/j.1365-2966.2010.16708.x. arXiv: 1002.4565 [astro-ph.GA].

Watkins, Laura L. et al. (Dec. 2013). "Discrete dynamical models of ω Centauri". In: MNRAS 436.3, pp. 2598–2615. DOI: 10.1093/mnras/stt1756. arXiv: 1308.4789 [astro-ph.GA].

Wechsler, Risa H. and Jeremy L. Tinker (Sept. 2018). "The Connection Between Galaxies and Their Dark Matter Halos". In: ARA&A 56, pp. 435–487. DOI: 10.1146/annurev-astro-081817-051756. arXiv: 1804.03097 [astro-ph.GA].

Wechsler, Risa H. et al. (Mar. 2002). "Concentrations of Dark Halos from Their Assembly Histories". In: ApJ 568.1, pp. 52–70. DOI: 10.1086/338765. arXiv: astro-ph/0108151 [astro-ph].

Weijmans, Anne-Marie et al. (Nov. 2014). "The ATLAS ^{3D} project - XXIV. The intrinsic shape distribution of early-type galaxies". In: MNRAS 444.4, pp. 3340–3356. DOI: 10.1093/mnras/stu1603. arXiv: 1408.1099 [astro-ph.GA].

White, S. D. M. and M. J. Rees (May 1978). "Core condensation in heavy halos: a two-stage theory for galaxy formation and clustering." In: MNRAS 183, pp. 341–358. DOI: 10.1093/mnras/183.3.341.

Woodley, Kristin A. et al. (Aug. 2007). "The Kinematics and Dynamics of the Globular Clusters and Planetary Nebulae of NGC 5128". In: AJ 134.2, pp. 494–510. DOI: 10.1086/518788. arXiv: 0704.1189 [astro-ph].

Woodley, Kristin A. et al. (Jan. 2010a). "The Ages, Metallicities, and Alpha Element Enhancements of Globular Clusters in the Elliptical NGC 5128: A Homogeneous Spectroscopic Study with Gemini/Gemini Multi-Object Spectrograph". In: ApJ 708.2, pp. 1335–1356. DOI: 10.1088/0004-637X/708/2/1335. arXiv: 0911.0955 [astro-ph.GA].

Woodley, Kristin A. et al. (May 2010b). "The Kinematics of the Globular Cluster System of NGC 5128 with a New Large Sample of Radial Velocity Measurements". In: AJ 139.5, pp. 1871–1888. DOI: 10.1088/0004-6256/139/5/1871. arXiv: 1002.3142 [astro-ph.GA].

Yıldırım, Akın et al. (July 2017). "The structural and dynamical properties of compact elliptical galaxies". In: MNRAS 468.4, pp. 4216–4245. DOI: 10.1093/mnras/stx732. arXiv: 1701.05898 [astro-ph.GA].

Zemp, Marcel et al. (Dec. 2011). "On Determining the Shape of Matter Distributions". In: ApJS 197.2, 30, p. 30. DOI: 10.1088/0067-0049/197/2/30. arXiv: 1107.5582 [astro-ph.IM].

Zentner, Andrew R. et al. (Aug. 2005). "The Anisotropic Distribution of Galactic Satellites". In: ApJ 629.1, pp. 219–232. DOI: 10.1086/431355. arXiv: astro-ph/0502496 [astro-ph].

Zepf, Stephen E., Doug Geisler, and Keith M. Ashman (Nov. 1994). "The Richness of the Globular Cluster System of NGC 3923: Clues to Elliptical Galaxy Formation". In: ApJ 435, p. L117. DOI: 10.1086/187608. arXiv: astro-ph/9408098 [astro-ph].

Zhao, D. H. et al. (Feb. 2003). "The growth and structure of dark matter haloes". In: MNRAS 339.1, pp. 12–24. DOI: 10.1046/j.1365-8711.2003.06135.x. arXiv: astro-ph/0204108 [astro-ph].

Zhu, Kai et al. (Apr. 2023). "MaNGA DynPop – III. Accurate stellar dynamics vs. stellar population relations in 6000 early-type and spiral galaxies: fundamental plane, mass-to-light ratios, total density slopes, and dark matter fractions". In: *arXiv e-prints*, arXiv:2304.11714, arXiv:2304.11714. DOI: 10.48550/arXiv.2304.11714. arXiv: 2304.11714 [astro-ph.GA].

Zhu, Ling et al. (Nov. 2016). "A discrete chemo-dynamical model of the giant elliptical galaxy NGC 5846: dark matter fraction, internal rotation, and velocity anisotropy out to six effective radii". In: MNRAS 462.4, pp. 4001–4017. DOI: 10.1093/mnras/stw1931. arXiv: 1608.08238 [astro-ph.GA].

Zhu, Ling et al. (Aug. 2022). "The Fornax3D project: Discovery of ancient massive merger events in the Fornax cluster galaxies NGC 1380 and NGC 1427". In: A&A 664, A115, A115. DOI: 10.1051/0004-6361/202243109. arXiv: 2203.15822 [astro-ph.GA].

Zwicky, F. (Jan. 1933). "Die Rotverschiebung von extragalaktischen Nebeln". In: *Helvetica Physica Acta* 6, pp. 110–127.

ABSTRACT

In this thesis, I focus on constraining the gravitational potential of early-type galaxies (ETGs) with discrete dynamical modelling to shed light on the nature of dark matter (DM). To that end, I used CJAM, an implementation of discrete Jeans anisotropic MGE (JAM) modelling of globular clusters (GCs) and planetary nebulae (PNe), both tracers found in the DM-dominated haloes. Additionally, I worked with simulated datasets of dwarf galaxies to provide observational guidelines for breaking the so-called core-cusp problem.

I find that both line-of-sight velocities (LOSVs) and proper motions (PMs) are needed to recover the inner slope of the density profile in mock datasets of dwarf spheroidal galaxies. The mock dataset for which the true inner and outer slope can be best recovered is characterized by a radial variation in the number and precision of the LOSVs. A lower number of tracers and larger measurement uncertainties, paired with a large number of precise measurements yield the best results for cored DM haloes.

I developed a two-step approach to determine the tracer density profile from a heterogeneous photometric dataset of GCs. It is based on the measurements of the position angle and flattening together with comparing the observed and theoretical GC luminosity function. I employ it to make a clean dataset of photometric tracers and generate a tracer density profile for dynamical modelling.

I used different prescriptions for the gravitational potential, by using different dark matter density profiles, stellar surface brightness, or modelling both with one total mass density profile. I constrained the best-fit parameters by combining Gaussian line-of-sight velocity distribution (LOSVD) as likelihood and informative as well as uninformative priors in a Bayesian analysis.

I find that GCs offer a unique possibility to constrain the dark matter density distribution beyond the scale radius of the halo. However, galaxies with fewer than 20 GCs can result in strongly biased measurements. Treating blue and red GCs as a single population does not introduce biases for most galaxies. Nevertheless, in central dominant galaxies, the blue GCs tend to trace the group/cluster potential and treating blue and red GCs as a single population will result in an overestimation of the total mass.

The radial distribution of the total mass profile is not consistent with a single power law profile and I find a steeper slope than the isothermal one of -2. Dark matter in galaxies is not spherically distributed and with GCs we can measure the deviations from spherical symmetry that are expected in both DM-only and hydrodynamical cosmological simulations.

ZUSAMMENFASSUNG

Zu diesem Zweck habe ich Kugelsternhaufen (globular clusters - GCs) und Planetarische Nebel (planetary nebulae - PNe) als Tracer für die Verteilung der dunklen Materie in den Halos der Galaxien benutzt und mittels “discrete Jeans anisotropic MGE” (JAM) modelliert. Darüber hinaus habe ich mit simulierten Datensätzen von Zwerggalaxien gearbeitet, um Beobachtungsrichtlinien zur Lösung des “Core-Cusp-Problems” zu erstellen.

Der Fokus dieser Arbeit liegt darauf, das Gravitationspotenzial von frühen Typen von Galaxien (Early Type Galaxies - ETGs) mit diskreter dynamischer Modellierung einzugrenzen, um Licht in die Natur der dunklen Materie zu bringen. Zu diesem Zweck habe ich Kugelsternhaufen (Globular Clusters - GCs) und Planetarische Nebel (Planetary Nebulae - PNe) als Tracer für die Verteilung der dunklen Materie in den Halos der Galaxien benutzt und mit mit CJAM, einer Implementierung von diskretem ”Jeans anisotropic MGE modelling”(JAM) modelliert. Darüber hinaus habe ich mit simulierten Datensätzen von Zwerggalaxien gearbeitet, um Beobachtungsrichtlinien zur Lösung des Core-Cusp-Problems zu erstellen.

Es stellt sich heraus, dass sowohl Geschwindigkeiten entlang der Sichtachse (Line Of Sight Velocities - LOSV) als auch Eigenbewegungen (Proper Motions - PM) benötigt werden, um die korrekte innere Steigung des Dichteprofils in Mock-Datensätzen von spheroidalen Zwerggalaxien zu erhalten. Der Mock-Datensatz, für den die beste Übereinstimmung mit der wahren inneren und äußeren Steigung erzielt werden kann, zeichnet sich durch eine radiale Änderung der Anzahl und Präzision der LOSVs aus. Eine geringere Anzahl von Tracern und größere Messunsicherheiten, gepaart mit einer großen Anzahl von präzisen Messungen, liefern die besten Ergebnisse für cored”DM-Halos.

Ich habe eine zweistufige Methode entwickelt, um das Dichteprofil der Tracer aus einem heterogenen photometrischen Datensatz von GCs zu bestimmen. Diese basiert auf der Messung des Positionswinkels und der Abflachung zusammen mit dem Vergleich der beobachteten und theoretischen Leuchtkraftfunktion von GCs. Damit kann ein homogener Datensatz von photometrischen Tracern erstellt werden und ein Tracer-Dichteprofil für die dynamische Modellierung erzeugt werden.

Ich habe verschiedene Ansätze für das Gravitationspotenzial verwendet, indem ich verschiedene Dichteprofile der dunklen Materie oder die stellare Flächenhelligkeit verwendet habe, oder beides mit einem Dichteprofil für die Gesamtmasse modelliert habe. Ich konnte die am besten passenden Parameter durch die Kombination von Gauß’schen LOSV Verteilungen (LOSVD) als Wahrscheinlichkeit und informativen sowie nicht-informativen A-priori-Verteilungen in einer Bayes’schen Analyse eingrenzen.

Es zeigt sich, dass GCs eine einzigartige Möglichkeit bieten, die Dichteverteilung der dunklen Materie über den Skalenradius des Halos hinaus zu bestimmen. Allerdings können Galaxien mit weniger als 20 GCs zu stark verzerrten Messungen führen. Die Behandlung von blauen und roten GCs als eine einzige Population führt bei den meisten Galaxien nicht zu Verzerrungen. Bei Galaxien im Zentrum von Galaxienhaufen hingegen neigen die blauen GCs dazu, das Gruppen-/Haufenpotenzial nachzuzeichnen, und ihre Behandlung als eine einzige Population führt zu einer Überschätzung der Gesamtmasse.

Die radiale Verteilung der Gesamtmasse stimmt nicht mit einem einfachen Potenzgesetzprofil überein und ich finde eine steilere Steigung als die isotherme Steigung von -2. Dunkle Materie in Galaxien ist nicht kugelförmig verteilt, und mit GCs können wir die Abweichungen von der sphärischen Symmetrie messen, die sowohl bei reiner dunkler Materie als auch bei hydrodynamischen Simulationen erwartet wird.

Povzetek za navdušence

Tekom doktorske disertacije sem preiskovala porazdelitev snovi v galaksijah zgodnjega tipa (angl. early-type galaxy, ETG). Galaksije vsebujejo vidno (barionsko) snov, zvezde, plin in prah, ter halo temne snovi (ne-barionsko). Celotna masa haloja najmočneje vpliva na razvoj in evolucijo galaksije in temna snov predstvalja 80% vse mase v vesolju. Kljub temu, je njena narava še neraziskana saj je ne moremo direktno opazovat, temveč jo lahko preučujemo z dinamičnim modeliranje.

Število galaksij določene mase se razlikuje glede na različne teorije o naravi temne snovi, kot sta to topla temna snow (angl. warm dark matter, WDM) ali hladna temna snov (angl. cold dark matter). Prav tako narava temne snovi vpliva na obliko haloja temne snovi (okrogla/sferična ali elipsoidna) in na porazdelitev mase znotraj haloja (strmo naraščanje gostote temne snovi v središču ali konstantna gostota). Preko preučevanja porazdelitve temne snovi lahko preučujemo teorije o njeni naravi in to je cilj te dizertacije.

Uporabila sem posebno metodo za dinamično modeliranje: Jeansov anizotropično modeliranje z razstvaljenjem na Gaussove funkcije (angl. Jeans anisotropic MGE, JAM). To metodo sem uporabila v posebni: diskretni implementaciji. Ta omogoča, da izkoristimo vse podatke brez da bi jih zdržužili ter s tem zmanjšali razdaljo od središča galaksije kjer lahko z gotovosto preučujemo porazdelitev snovi. Ker so galaksije v samih središčih halojev moremo uporabit objekte ki so bolj oddaljeni od središča gravitatiskega potenciala. Kroglaste kopice so skupki več deset tisoč zvezd, in so bolj oddaljene od središča haloja kot večina zvezd. Opazujemo jih lahko v bližnjih galaksijah in omogočajo edinstven vpogled v porazdelitev temne snovi.

V tej dizertaciji sem uporabila JAM metodo in z izmerjenimi hitrostmi kroglastih kopic sem izmerila porazdelitev snovi (zvezd in temne snovi) v 18 galaksijah in izmerila obliko haloja galaksije CenA (NGC 5128). Moji rezultati nakazujejo, da so kroglaste kopice zelo močno orodje, s katerim lahko bolje razumemo porazdelitev snovi. Naklon gostote snovi ni preprosta potenčna funkcija temveč je bolj kompleksna in velik radijska porazdelive kroglastih kopic je bila ključna za to potrditev.

Prav tako sem z JAM modeli potrdila, da haloji temne snovi niso okrogli in gibanje kroglastih kopic je občutljivo na to odstopanje od preproste sferične simetrije. Ta potrditev je zelo pomemebno za nadaljno modeliranje galaksij, saj lahko pripelje do napačnih sklepov v kolikor modeliranje temelji na predpostavki sferične simetrije.

Zaključki te disertacije so odlična iztočnica za nadaljne študije ne-sferične porazdelitve temne snovi s kroglastimi kopicami.

Acknowledgements

This project has received funding from the European Research Council (ERC) under the European Union's Horizon 2020 research and innovation programme under grant agreement No 724857 (Consolidator Grant ArcheoDyn). I would like to acknowledge the studentship support from the European Southern Observatory and the VISESS Completion Grant support. The computational results presented have been achieved (in part) using the Vienna Scientific Cluster (VSC).

Now that I have dispensed with the formalities lets get to the good stuff. While the thesis bears the name of only one person it is a result of a joint effort and I would like to acknowledge the support of everyone who has helped and supported me, thereby contributing to this work that is a culmination of the past 4 years.

First and foremost I would like to thank my supervisor Glenn van de Ven, for taking the time at 11 PM after a 3-day workshop to listen and provide encouraging words that put me on the path to this thesis. And of course, for all the support, advice, guidance, freedom and so much patience you have shown since then. Thank you.

We all have official and unofficial co-supervisors, and I would like to thank Laura Watkins for our continuous chats on scientific and non-scientific topics, despite the time-zone constraints. Thank you for your candid and kind nature that helped ground me when I got lost. Thank you Sabine Thater for always having the time to talk and the kind words. I would like to thank Marina Rejkuba for the long scientific discussions at ESO and for somehow always knowing when I was unsure of my statements. Hvala za zrcalo, ki sem ga potrebovala. The group meetings with Magda Arnaboldi were always exciting and full of science, thank you for the engaging and rigorous discussions and for always being so enthusiastic about science, it is wonderfully infectious.

I would also like to thank Ryan and Prash who were always up to discuss science with me. I greatly enjoyed every time you shared your wide knowledge and skills with me. Claudia, talking with you about science was the first time I felt like I had a collaborator. It was amazing, thank you, I hope science "makes sense"for you, for a long time. Lucas thank you for the great time investigating the shapes of simulated galaxies. I now have more questions that I have answers to, what a great feeling.

Thank you Laurane for all our chats about science, life and philosophy. Thank you for your enthusiasm and drive which inspired me on more than one occasion. It was great fun to share the office with you. I hope we keep laughing together so much that our cheeks hurt.

Alice (Zocchi). Your honesty, dedication, kindness and smile have changed me. That is all I need to say.

My colleagues and friends from ESO, well my volleyball and board games friends. Samuel, Ivanna, Josh, KEVIN, Aish, Paul, Keegan, Linus, Alice (ESO), Malte, Sandra, (not Simon!) you made my time at ESO unforgettable. Samuel, there will be a day when I dethrone you. Ivanna, I want Huggsy too. Josh, never stop parkouring. Pierrick, I still haven't met Kevin. Aish, thank you for bringing me into the volleyball group. Linus, keep up the volleyball spirit. Malte, never stop fixing things, it is amazing. Alice (ESO, your smile always brightened my day.

The PLEES team, Laurane, Gwenael, Paula. I had an absolute blast working together with you. I learned so much and I felt we made something unique and positive. I hope we continue.

To my friends and colleagues. Agata, thank you for babysitting the plants. Alina, you crack me up every time. Carina, ♪... Tell me why ... ♪. Christine, your German courses were so much fun, you are an amazing teacher. Edward, I hope you go sledging again, you are a natural. Francisco, I finally got a 3070, now I can play Jedi Survivor. Iris, your singing is beautiful. James, your dedication and drive continue to inspire me. Katerina, edinstvena izkušnja je rast z nekom tako kot sem s tabo. Nika, vsak dan s tabo je poseben. Pavel and Andrea, you should charge for all the comedy you provide. Pritam, you are just magical. Silvia and Taï, I cannot enjoy pizzas and coffee anymore. Simon, I forgive you for the bike. Steffi, no spoilers, please. Sü, **ZL + X + YYYYYYYYYY** and your cats are super cute. Tatiana, even daydreaming about the perfect set and spike with you was fun. Tea in Kaja, vedno sem uživala v naših klepetih in vem da jih bo še veliko. Vajino prijateljstvo me je spremljajo čez vse moje selitve in bo še kar vztrajalo. Verena, I loved our lunch breaks. Yanina and Pam, can I have seconds please?

I would not be where I am without my family, so this is for you. Mami, ati, Metka, Barbara, David, Domen in Muri. Najlepša hvala za vso podporo, za vse nasvete, za vse selitve, da ste vedno bili veter v mojih krilih in varno pristanišče v nevihti.

Last, but most certainly not least. Smaran, I cannot imagine having so much fun during my PhD without you. You taught me the importance of expressing discontent and ritual complaining. You set me free and yet you made a home for me, I couldn't be more grateful. I cannot thank you enough and all I can say is that I will cook pasta-pesto-sausages for dinner.

Ko hodiš, pojdi zmeraj do konca.
Spomladi do rožne cvetice,
poleti do zrele pšenice,
jeseni do polne police,
pozimi do snežne kraljice,
v knjigi do zadnje vrstice,
v življenju do prave resnice.
A če ne prideš ne prvič ne drugič
do krova in pravega krova,
poskusi vnovič in zopet in znova.

– Tone Pavček

–